VNIVERSITAT DE VALÈNCIA

Programa de Doctorado en Física

Tesis Doctoral

Polymorphism of rare-earth orthovanadates under high pressure

Doctorando:

Tomás Marqueño Villanueva

Directores:

Dr. Daniel Errandonea Ponce

Dr. Julio Pellicer Porres

Dr. David Santamaría Pérez

Marzo, 2022

Dedication

To my grandfather Hilario.

Acknowledgements

The work reported in this dissertation was supported by the Spanish Ministerio de Ciencia e Innovación under Grants No. MAT2016-75586-C4-1/3-P, PID2019-106383GB-C41/43, and PGC2018-097520-A-I00 (cofinanced by EU FEDER funds), and by Generalitat Valenciana under Grant Prometeo/2018/123 (EFIMAT). I specially acknowledge the Spanish Ministerio de Ciencia e Innovación for the BES-2017-079651 predoctoral fellowship. Also thanks to the ALBA-CELLS and ESRF synchrotrons for providing beam time for the XRD experiments.

I am grateful to my three thesis advisors, Daniel Errandonea, Julio Pellicer and David Santamaria for their outstanding willingness and remarkable patience. Thanks for attending me every time I knocked at your doors. Without your help nothing of this would have happened. Thanks to Alfonso Muñoz and Plácida Rodrígez from the University of La Laguna (Tenerife) for providing me with theoretical calculations when I needed them. Also thanks to Alfredo Segura, Domingo Martínez, Javier Ruiz, Akun Liang, Daniel Díaz, Enrico Bandiello, Robin Turnbull and other many other collaborators for helping me with the experiments and for the fruitful discussions.

To Catalin Popescu for his incomparable help during the beam times at ALBA.

To my mates at the Applied Physics Department. Thanks for the good times that we spent together.

To my family. Specially to my mother María del Mar, my grandmother María and my grandfather Hilario, who passed away too early.

To Cristina, the love of my life.

Abstract

Rare-earth orthovanadates constitute a paradigmatic family of ternary oxides, due to their striking properties and their manifold polymorphs. Many of their different phases can be achieved by submitting these crystal structures under extreme pressure and temperature conditions. In this dissertation we study the behaviour of $NdVO_4$, $GdVO_4$, $PrVO_4$ and $TbVO_4$ under high pressures and different temperature conditions. Different samples of these compounds were characterized by means of several experimental techniques such as X-ray diffraction (XRD), Raman scattering and optical absorption. In addition to this, many of our experimental results are also supported by *ab initio* calculations, which allowed a better understanding of the pressure behaviour of these compounds. With regard to $NdVO_4$, our experiments under quasi-hydrostatic conditions showed that there is a zircon-to-scheelite phase transition at $\sim$ 6.5 GPa and a scheelite-to-fergusonite phase transition at $\sim$ 20 GPa. Similar findings were found in $GdVO_4$ at 7.0 and 20 GPa respectively by means of XRD, Raman spectroscopy and optical absorption measurements. Moreover, the Raman scattering measurements found a third phase transition to a post-fergusonite phase at $\sim$ 30 GPa. With respect to $PrVO_4$, XRD experiments at high pressures found a zircon-to-monazite and a monazite-to-$PbWO_4$-III phase transition at $\sim$ 5.5 and $\sim$ 12.7 GPa, respectively. Motivated by theoretical predictions, we also synthesized the scheelite phase of $PrVO_4$ at high pressures and high temperatures in a Paris-Edinburgh large volume press cell. The recovered scheelite phase was later studied upon compression by using Raman spectroscopy. In general, the equations of state of the different phases observed for $NdVO_4$, $GdVO_4$ and $PrVO_4$ are also reported, as well as

the pressure evolution of the Raman active modes. The experiments and calculations on these orthovanadates show that kinetic barriers play a crucial role in the zircon-scheelite/monazite systematics of RVO$_4$ compounds. By gathering the data available in the most recent literature as well as our *ab initio* calculations we could unveil the mechanisms that govern in these structural sequences. In particular, the zircon-to-scheelite and zircon-to-monazite phase transitions are triggered by dynamical and mechanical instabilities respectively. Finally, we explored the Jahn-Teller effect of TbVO$_4$ at low temperatures (and high pressures). Optical absorption experiments at low temperatures and room pressure show a progressive widening of the electronic band gap below 35 K as a consequence of the Jahn-Teller distortion. XRD measurements at low temperatures and low pressures show that the transition temperature considerably increases with pressure. A tentative pressure-temperature phase diagram is proposed for TbVO$_4$.

Contents

Dedication **3**

Acknowledgments **5**

Abstract **7**

Resumen **3**

I Objetivos 3

II Metodología 5

II.1 Métodos experimentales 5

II.2 Cálculos *ab initio* 10

III Conclusiones 13

III.1 Ortovanadato de neodimio 13

III.2 Ortovanadato de gadolinio 14

III.3 Ortovanadato de praseodimio 16

III.4 Mecanismos de transición 17

III.5 Ortovanadato de terbio 18

III.6 Final 19

1 Introduction **21**

1.1 Historical background 21

1.2 Crystal structures . . . 27
1.3 Physical properties . . . 34
1.3.1 Compressibility . . . 35
1.3.2 Vibrational properties . . . 37
1.3.3 Electronic band structure . . . 41
1.4 Technological applications . . . 44

2 Theoretical background **47**
2.1 Thermodynamics of crystals under high pressure . . . 47
2.2 Classification of phase transitions in solids . . . 51
2.2.1 Landau Theory of phase transitions . . . 52
2.3 Finite strains . . . 55
2.3.1 Eulerian strain . . . 56
2.3.2 Lagrangian strain . . . 58
2.4 Equation of State . . . 59
2.5 The Stiffness Tensor . . . 61
2.5.1 Symmetries . . . 65
2.5.2 Stability criteria and distortion . . . 66
2.6 Interband absorption . . . 67
2.6.1 Direct transitions . . . 68
2.6.2 Indirect transitions . . . 71
2.7 The cooperative Jahn-Teller effect . . . 74
2.8 Principles of X-ray difraction . . . 78
2.8.1 Bragg's law . . . 78
2.8.2 The stucture factor . . . 80

3 Experimental methods 83

3.1 The Diamond Anvil Cell . . . 83

3.2 Powder X-ray diffraction . . . 88

3.2.1 Sources of X-rays . . . 89

3.2.1.1 Conventional X-ray sources . . . 89

3.2.1.2 Synchrotron Radiation sources . . . 91

3.2.2 Refinement of the crystal structrure . . . 99

3.3 Raman spectroscopy . . . 104

3.4 Optical absorption . . . 107

3.4.1 Optical absorption at high pressures . . . 109

3.4.2 Optical absorption at low temperatures . . . 110

3.5 The Paris-Edinburgh large volume press . . . 110

4 Neodymium orthovanadate under high pressure 115

4.1 Experimental details . . . 117

4.2 Simulation details . . . 118

4.3 Powder XRD experiments . . . 119

4.4 Raman spectroscopy experiments . . . 132

4.5 *Ab initio* calculations . . . 139

4.6 Conclusions . . . 145

5 Gadolinium orthovanadate under high pressure 147

5.1 Experimental details . . . 148

5.2 Simulation details . . . 152

5.3 Powder XRD experiments . . . 152

5.4 Raman spectroscopy experiments . . . 160

5.5 Optical absorption experiments . . . 171

5.6 *Ab initio* calculations . . . 175
5.7 Conclusions . . . 183

6 Praseodymium orthovanadate under high pressure 185
6.1 Experimental details . . . 187
6.2 Simulation details . . . 189
6.3 Powder XRD experiments . . . 190
6.4 Scheelite phase synthesis and characterization . . . 199
6.5 Raman scattering experiments on the scheelite phase . . . 205
6.6 *Ab initio* calculations . . . 208
6.6.1 Polyhedral contribution to compressibility . . . 213
6.7 Conclusions . . . 216

7 Transition mechanisms in RVO$_4$ compounds 219

8 The Jahn-Teller effect in Terbium Orthovanadate 229
8.1 Experimental details . . . 230
8.2 Optical absorption experiments . . . 233
8.3 Low-Temperature-High-Pressure XRD experiments . . . 237
8.4 Conclusions . . . 242

9 Conclusions 243

Bibliography 247

Resumen

I Objetivos

Los compuestos RVO$_4$, también llamados ortovanadatos de tierras raras (R = átomo de tierra rara), constituyen un subgrupo particular de óxidos ternarios, los cuales han suscitado un interés generalizado, principalmente debido a las numerosas aplicaciones tecnológicas para las cuales han demostrado ser útiles, tales como centelleadores, termofósforos, láseres de estado sólido, materiales para el almacenamiento de residuos nucleares, materiales fotocatalíticos para la purificación de agua, etc. Además de esto, los compuestos RVO$_4$ muestran una gran variedad de fases cristalinas en función de las condiciones de presión y temperatura a la que se encuentren sometidos. Este amplio polimorfismo hace todavía más interesante el estudio de tales compuestos, ya que algunas de sus fases de alta presión pueden ser recuperadas en condiciones ambiente en un estado metaestable. En términos generales, se puede decir que los ortovanadatos de tierras raras constituyen un paradigma dentro de los óxidos ternarios, por lo que su estudio bajo diferentes condiciones termodinámicas puede arrojar luz sobre el comportamiento de un grupo mucho más amplio de compuestos.

De esta manera, los objetivos fundamentales de esta tesis doctoral pueden resumirse en los siguientes puntos: (i) identificación y caracterización de las diferentes estructuras cristalinas en varios compuestos RVO$_4$ sometidos a condiciones de extrema presión y/o temperatura, (ii) comprensión de los mecanismos físicos que subyacen a las transiciones de fase observadas y (iii)

búsqueda de sistemáticas en la familia RVO$_4$. Para ello no solo caracterizaremos nuestras muestras mediante diferentes técnicas experimentales, sino que también dispondremos de cálculos *ab initio* que nos permitirán obtener una mejor comprensión de los fenómenos observados. Nuestro trabajo se centrará en aquellos compuestos en el que el átomo de tierra rara pertenece a la serie de los lantánidos, en particular, estudiaremos experimentalmente los compuestos en los que R = Pr, Nd, Gd y Tb bajo altas presiones y, ocasionalmente, altas o bajas temperaturas.

En primer lugar, el estudio experimental de estos materiales permite la obtención de diferentes parámetros físicos característicos de cada estructura cristalina. Por ejemplo, la difracción de rayos X permite identificar la fase, hallar experimentalmente la ecuación de estado presión-volumen y evaluar la anisotropía que el material presenta bajo compresión. Por otra parte, gracias a la técnica de espectroscopia Raman es posible encontrar la dependencia de la frecuencia de algunos modos de vibración con la presión. Asimismo, puesto que se trata de materiales semiconductores, la caracterización óptica de la banda prohibida puede ser especialmente relevante para detectar cambios en la estructura electrónica del material.

Sin lugar a duda, la obtención de sistemáticas constituye una de las motivaciones principales en el estudio de los compuestos RVO$_4$ bajo presión. Previamente a nuestros estudios, la sistemática establecida en la literatura relacionaba la estructura de alta presión con el tamaño del catión de la tierra rara. Más concretamente, la sistemática se expresaba en los siguientes términos: excepto el LaVO$_4$, todos los compuestos RVO$_4$ cristalizan en la estructura tipo zircón (grupo espacial $I4_1/amd$) en condiciones ambiente; cuando estos compuestos se comprimen lo suficiente a temperatura ambiente, sufren una transformación de fase a una estructura tipo scheelita (grupo espacial $I4_1/a$) cuando R^{3+} es un catión pequeño (R = Sm - Lu) o a una estructura tipo monacita (grupo espacial $P2_1/n$) cuando se trata de cationes grandes (R = Ce, Pr y Nd). Esta sencilla sistemática, sin embargo, no da cuenta de algunas excepciones a ella cuando se modifican ciertas condiciones experimentales. Por ejemplo, diferentes condiciones en la hidrostaticidad del medio pueden alterar el resultado final, como demostraron nuestros experimentos. Por ello, es

conveniente también realizar un estudio teórico acerca de los fenómenos físicos que subyacen en los procesos de transformación de una estructura en otra, de modo que podamos encontrar una sistemática relacionada de una manera más directa con los mecanismos de transición.

II Metodología

II.1 Métodos experimentales

Puesto que nuestra investigación es principalmente de carácter experimental, conviene hacer una exposición resumida de los métodos y materiales empleados. La mayor parte de nuestros experimentos requieren la compresión de muestras cristalinas, generalmente en polvo, mediante el uso de celdas de alta presión. En este caso, los dos tipos de celdas empleadas han sido la celda de yunques de diamante o DAC (del inglés *Diamond Anvil Cell*) y la celda de gran volumen París-Edimburgo. Comenzaremos nuestra exposición por la primera, puesto que has sido la más utilizada en nuestros experimentos.

La celda de yunques de diamante es posiblemente el aparato más empleado hoy en día para someter materiales a presiones extremas. La principal característica de este dispositivo es que, a diferencia de otras celdas de presión, proporciona una excelente ventana óptica para los rayos X y la radiación comprendida entre el infrarrojo lejano y el ultravioleta en el espectro electromagnético. Además, el tamaño usual de estas celdas es lo suficientemente pequeño como para caber en la palma de la mano, lo cual facilita su uso en multitud de montajes. Más específicamente, este tipo de celdas consiste en un par de yunques de diamante contrapuestos, cuyos «culets» tienen diámetros comprendidos entre 200 y 500 micras. La reducida superficie que ofrecen estos yunques permite alcanzar presiones muy elevadas, generalmente de decenas de gigapascales (GPa) o incluso de cientos en algunos casos particulares, aplicando una fuerza mucho menor que en el caso de las celdas de gran volumen. Por lo tanto, pese a las increíbles ventajas que proporciona,

la principal limitación de este mecanismo es que requiere cantidades muy pequeñas de muestra. Entre ambos diamantes se sitúa una junta de metal (generalmente acero, wolframio o renio), previamente preindentada a un grosor adecuado y perforada en la zona central. En esta junta se introduce la cantidad de muestra deseada (en polvo o monocristal), un medio transmisor de presión para optimizar las condiciones hidrostáticas (generalmente una mezcla de etanol-metanol-agua o gases nobles como el helio, neón o argón) y un estándar para determinar la presión de la cámara. Como estándar de presión pueden emplearse rubíes, cuyos picos de luminiscencia tienen longitudes de onda calibradas con la presión. Es decir, los rubíes pueden excitarse empleando un láser y medir los picos de luminiscencia con un espectrómetro convencional. El desplazamiento de estos picos hacia mayores longitudes de onda con la presión está ampliamente estudiado en la literatura ($\sim$ 3,65 nm/GPa en el rango del visible). También puede emplearse algún material cuyo comportamiento bajo presión sea conocido. Por ejemplo, en difracción de rayos X, puede emplearse NaCl, Pt, Au, Cu u otro material cuyos picos de Bragg estén calibrados con la presión. La presión en la cámara donde se encuentran los materiales aumenta al aproximar los diamantes. En función del tipo de celda de diamante, esto puede hacerse de diferentes formas. En nuestro caso particular, el tipo de celdas de diamante empleadas son las llamadas celdas de membrana. Estas celdas están constituidas por tres partes principales: el cuerpo de la celda y el pistón, cada uno de ellos con un diamante, y la membrana. El principio por el que funcionan este tipo de celdas es sencillo: el pistón se desplaza progresivamente contra el cuerpo gracias al empuje de la membrana, la cual se hincha empleando gas a presiones moderadas ($<$ 100 bar). Esto permite el acercamiento de los diamantes, así como un mayor control de la presión a la cual se somete la muestra. La relación entre la presión de membrana y la presión de la muestra depende de cada experimento.

El hecho de que el diamante sea un material transparente a los rayos X de alta energía ($E > 10$ eV) permite estudiar la evolución estructural bajo presión empleando la difracción de rayos X (DRX). Esta técnica constituye uno de los métodos más comunes de caracterización de materia-

les. Consiste en un proceso de dispersión elástica coherente, en el cual la radiación dispersada por los átomos se amplifica por interferencia constructiva en determinadas direcciones, dando lugar a un patrón de difracción característico. En los materiales cristalinos estas direcciones están relacionadas con las distancias entre los diferentes planos cristalinos según la ley de Bragg. En nuestro caso particular, se emplearon muestras policristalinas en los experimentos de DRX. Debido a que el polvo contiene una gran cantidad de pequeños cristales orientados en múltiples direcciones arbitrarias, algunos de ellos se encuentran en posiciones en las que uno de sus planos cristalinos cumple la condición de Bragg. Como consecuencia se generan una serie de conos de difracción que se registran como un conjunto de anillos concéntricos en el detector bidimensional. Cada uno de estos anillos corresponde a una determinada distancia interplanar del cristal. Para realizar el análisis, estos anillos concéntricos se integran en patrones de difracción bidimensionales que representan la Intensidad frente al ángulo 2θ. Puesto que la posición de los picos en los patrones integrados está relacionada con las distancias interplanares del cristal, es posible deducir los parámetros de la celda unidad del cristal. El proceso mediante el cual se refinan los parámetros de red en función de la posición de los picos de difracción es conocido como indexación (refinamiento LeBail). Por otro lado, la intensidad relativa de estos picos está relacionada con la posición de los átomos dentro de la celda unidad, por lo que es posible determinar estas posiciones. Este tipo de refinamiento se denomina método Rietveld. No obstante, este proceso solo puede llevarse a cabo cuando el patrón de difracción tiene una buena calidad, lo cual implica, entre otras cosas, que el polvo esté molido muy finamente, que no existan orientaciones preferenciales y que la muestra se encuentre en condiciones hidrostáticas. Si, por el contrario, no se cumplen estas condiciones, se alterará de forma espuria la intensidad relativa de los picos de difracción y solo será posible realizar la indexación de los patrones de difracción y obtener los parámetros de red.

Respecto a las fuentes de rayos X empleadas en los experimentos, podemos describir dos tipos fundamentales: las fuentes convencionales y los sincrotrones. Con respecto a las primeras, los rayos X se suelen obtener acelerando electrones que posteriormente impactan contra un blanco

metálico, normalmente de cobre ($\lambda_{K\alpha}$ = 1,5406 Å) o molibdeno ($\lambda_{K\alpha}$ = 0,7093 Å). La radiación se produce como consecuencia del decaimiento de electrones del átomo del metal desde niveles superiores a niveles internos menos vacantes. Aunque hoy en día siguen siendo muy útiles, este tipo de fuentes convencionales cuentan con una serie de limitaciones. Por ejemplo, el brillo proporcionado por estas fuentes es mucho menor del que pueden proporcionar las fuentes de radiación sincrotrón. De hecho, un sincrotrón de tercera generación, puede suministrar radiación entre 12 y 16 órdenes de magnitud más brillante que un tubo de rayos X convencional. En los sincrotrones, la radiación electromagnética se produce acelerando electrones mediante un campo eléctrico y curvando su trayectoria mediante campos magnéticos. Cuando las partículas cargadas se encuentran girando a velocidades relativistas se produce un haz de radiación electromagnética colimada en la dirección tangencial. Mediante el empleo de dos tipos de dispositivos conocidos como «wigglers» y onduladores, los cuales consisten en un conjunto de imanes que «ondulan» la trayectoria de los electrones, es posible aumentar aún más el brillo, gracias a la superposición coherente de la radiación emitida. Tras pasar por estos dispositivos de inserción, el haz electromagnético incide sobre un conjunto de espejos de sílice que actúan como monocromador, de forma que es posible seleccionar una determinada longitud de onda. A continuación el haz pasa por una serie de filtros y espejos que focalizan el haz monocromático sobre la muestra. Los haces difractados por la muestra son recogidos por un detector bidimensional. Habitualmente, el procedimiento de medida consiste en insertar la celda de yunques de diamante cargada, de modo que el haz se focalice sobre la muestra.

Por otro lado, el estudio de las vibraciones de la red cristalina resulta crucial para la comprensión del comportamiento de los compuestos $R\mathrm{VO_4}$ bajo presión. Por ello, una de las técnicas que más relevancia han adquirido durante la investigación ha sido la espectroscopia Raman. Esta técnica se basa en el fenómeno de dispersión Raman, en la que se caracterizan modos de vibración en el centro de la zona de Brillouin cuya simetría induce una variación no nula en el tensor de susceptibilidad. Como consecuencia, además de la luz dispersada elásticamente, obtenemos dos

contribuciones de menor intensidad, cuya frecuencia es la resta y otra la suma de la frecuencia de la radiación incidente y la frecuencia de los fonones. En estos casos hablamos de dispersión Stokes y Anti-Stokes, respectivamente. Se trata, por lo tanto, de un fenómeno de dispersión inelástica. Para estos experimentos hemos empleado un montaje que incluye un láser de He-Ne (λ = 632,8 nm), un monocromador con una red de 600 lineas/mm y un detector CCD multi-canal con un sistema de refrigeración termoeléctrico . Además de ello, la línea láser se eliminó mediante el uso de diferentes tipos de filtros. Este sistema permite obtener espectros Raman con una precisión de 1 cm^{-1} aproximadamente. La calibración de este montaje se realiza tomando como referencia las líneas de plasma del laser He-Ne.

Además de las dos técnicas mencionadas, algunas de las muestras fueron estudiadas mediante la técnica de absorción óptica, la cual permite estimar el tamaño del la banda prohibida de estos materiales, así como su evolución con la presión o la temperatura. Para ello se seleccionan monocristales delgados ($\alpha d \sim 3$) de caras plano-paralelas, de modo que el grosor de la muestra sea uniforme. Mediante un sencillo montaje en el que empleamos una fuente de luz cuyo espectro está comprendido entre el ultravioleta y el infrarrojo y un espectrómetro, es posible medir el espectro de transmitancia de la muestra, para después obtener el espectro de absorción. La dependencia del frente de absorción con la energía muestra de qué tipo son las transiciones desde la banda de valencia a la banda de conducción, es decir, si son directas o indirectas. En las medidas bajo presión, la celda de diamante se inserta en el montaje de forma que mediante un microscopio puede observarse la muestra contenida en su interior. En el caso de las medidas a presión casi cero y baja temperatura, los monocristales se dispondrán en el interior de un criostato de helio comprimido, que permite enfriar muestras hasta los 14 K.

Durante nuestra investigación, se llevaron a cabo diferentes síntesis en la celda de gran volumen París-Edimburgo. A diferencia de la celda de yunques de diamante, esta celda permite la compresión de cantidades mucho mayores de muestra (3 mm^3 aproximadamente) hasta un máximo de 15 GPa. Además, este tipo de celda cuenta con un sistema de calentamiento eléctrico

controlado por ordenador, por lo que es posible realizar síntesis de compuestos a altas presiones y altas temperaturas (hasta 10 GPa y 1500 K empleando un horno de grafito) y conseguir un volumen considerable de muestra. Pese a que no permite un acceso óptico a la muestra, este tipo de celdas pueden emplearse en experimentos *in situ* tales como medidas de transporte o difracción. Este tipo de celda de gran volumen está equipada con dos yunques cónicos de carburo de tungsteno contrapuestos. Entre ambos yunques se sitúa la junta o *gasket* de pirofilita, la cual contiene la muestra en su interior y se halla rodeada de un anillo de teflón que evita una posible extrusión lateral del material. La muestra compactada en un cilindro se introduce en un pequeño tubo de nitruro de boro, el cual actúa como medio transmisor de la presión. A su vez, éste es introducido en un cilindro hueco de grafito, empleado para aumentar la temperatura de la muestra. Este conjunto de elementos se introducen en la junta de pirofilita y se tapan con unos anillos de molibdeno que actúan como electrodos. La presión de la celda se aumenta mediante un sistema manual de bombeo de aceite que desplaza el pistón, aproximando los yunques. La temperatura de la muestra se eleva calentando el horno de grafito mediante una corriente eléctrica controlada. Para evitar el sobrecalentamiento de los yunques, éstos disponen de un sistema de refrigeración de agua fría. Las condiciones de temperatura y presión de la muestra están previamente calibradas con la potencia eléctrica y la presión del aceite respectivamente.

De forma muy sintetizada, el cuadro 1 muestra un resumen de los detalles experimentales con los que se estudió cada compuesto. Se incluye el nombre del compuesto, el tipo de muestra (polvo o monocristal), la técnica empleada, los dispositivos utilizados para cambiar la presión y/o temperatura, las condiciones a las que se sometió la muestra y el medio en el que se encontraba.

II.2 Cálculos *ab initio*

Gran parte de nuestro estudio, en concreto el de los compuestos $NdVO_4$, $GdVO_4$ y $PrVO_4$ incluye también un análisis teórico mediante el empleo de cálculos *ab initio* en el marco de la teoría del funcional de la densidad o DFT (del inglés *Density Functional Theory*). Este tipo de

Cuadro 1: Resumen de los detalles experimentales según cada compuesto. Las condiciones a las que se sometió las muestras se denotan como AP (Alta Presión), AT (Alta Temperatura) y BT (Baja temperatura).

Compuesto	Muestra	Técnica	Dispositivos	Condiciones	Medio
$NdVO_4$	Polvo	DRX	DAC	AP	He
	Polvo	Raman	DAC	AP	Ne
$GdVO_4$	Polvo	DRX	DAC	AP	Ar
	Polvo	Raman	DAC	AP	Ne
	Monocristal	Abs. óptica	DAC	AP	MEW
$PrVO_4$	Polvo	DRX	DAC	AP	Ne
	Polvo	Síntesis fase scheelita	Celda gran volumen París-Edimburgo	AT-AP	BN
$PrVO_4$ (scheelita)	Polvo	Raman	DAC	AP	Ne
$TbVO_4$	Monocristal	Abs. óptica	Criostato	BT	Vacío
	Polvo	DRX	Criostato + DAC	BT-AP	Aceite de silicona

cálculos se realizan con el objetivo de complementar a los resultados experimentales, de forma que sea posible obtener una explicación más completa y precisa de los fenómenos observados.

La estabilidad de los diferentes polimorfos de un compuesto sometido a altas presiones puede estudiarse mediante el cálculo de sus curvas de energía libre de Gibbs. El cruce de estas curvas coincidiría con las presiones de transición. En estos cálculos se debería tener en cuenta tanto la contribución de los efectos térmicos como de la presión. No obstante, es común despreciar los primeros (asumir que $T = 0$), por lo que las curvas de energía libre serían equivalentes a las curvas de entalpía. Esta aproximación se ha demostrado razonable en una gran cantidad de casos, pues suele introducir variaciones muy pequeñas en las presiones de transición. Empleando estos cálculos es posible además relajar una determinada estructura y hallar la correspondiente presión para un conjunto de volúmenes de la celda unidad. Esto permite analizar desde un punto teórico la evolución de los parámetros de red y posiciones atómicas con la presión así como hallar la

ecuación de estado teórica de una determinada estructura.

Por otra parte, una transición de fase no tiene porqué necesariamente verse reflejada en las curvas de entalpía. Es posible que la estructura, a determinada presión, sea dinámica o mecánicamente inestable. Para analizar el primero de los casos, es necesario calcular la dependencia de la frecuencia de los fonones con la presión. Además de esto, los cálculos permiten estimar la evolución de los modos que no son activos Raman, como los modos infrarrojos o los modos silenciosos. Los cálculos son especialmente interesantes en este último caso, ya que los modos silenciosos no son detectables mediante las técnicas convencionales de espectrocopia. Las inestabilidades dinámicas se producen por el ablandamiento de un fonón, lo que significa que su frecuencia de vibración se hace cero a una determinada presión. Como consecuencia, se produce un desplazamiento de algunos átomos o estructuras poliédricas dentro de la celda unidad, lo que puede introducir cambios en la simetría del cristal. Por otra parte, las inestabilidades mecánicas están relacionadas con las propiedades elásticas de la celda unidad. Por ello, es necesario calcular el tensor de constantes elásticas a diferentes presiones, el cual relaciona una determinada deformación con un determinado estrés. Asumiendo condiciones de presión hidrostática, es posible calcular a qué presión se produce una deformación finita con un estrés adicional nulo. Dicho de otra manera, los cálculos permiten hallar a qué presión se produce una deformación espontánea de la estructura cristalina. Este tipo de inestabilidad suele dar lugar a transiciones de segundo orden, en las que no se produce una discontinuidad en los parámetros de orden. No obstante, si estas inestabilidades se producen en una estructura metaestable, es posible que sirvan para disminuir la barrera de activación entre esta fase y la fase termodinámicamente estable. En otras palabras, las inestabilidades dinámicas y mecánicas pueden favorecer una transición de primer orden.

III Conclusiones

En esta tesis se muestran los resultados obtenidos sobre diferentes tipos de compuestos $R\mathrm{VO_4}$ en condiciones extremas de presión. El orden establecido en este trabajo comienza con la exposición de los resultados obtenidos para los compuestos $\mathrm{NdVO_4}$, $\mathrm{GdVO_4}$ y $\mathrm{PrVO_4}$ bajo presión en tres capítulos diferentes. En el capítulo que sigue a continuación, exploramos la sistemática de los compuestos $R\mathrm{VO_4}$ tipo zircón sometidos a altas presiones, mediante el uso de cálculos así como de los resultados experimentales obtenidos en nuestros experimentos y aquellos disponibles en la literatura más actual. Por último, la tesis cierra su exposición con el estudio del efecto Jahn-Teller cooperativo en el $\mathrm{TbVO_4}$ a bajas temperaturas y altas presiones.

III.1 Ortovanadato de neodimio

Respecto al compuesto $\mathrm{NdVO_4}$, nuestros experimentos de DRX y dispersión Raman bajo presión en condiciones quasi-hidrostáticas (empleando He y Ne como medios transmisores respectivamente) confirman el comienzo de una transición de fase zircón-scheelita a 6.5 GPa aproximadamente. Esto constituye una diferencia notable con estudios experimentales previos, donde la fase monacita, en lugar de la scheelita, aparecía a altas presiones. Este resultado pone de relieve la enorme influencia de las condiciones hidrostáticas en la secuencia estructural que los compuestos $R\mathrm{VO_4}$ muestran bajo compresión. Además de ello, experimentalmente se observa un colapso de volumen del $\sim 11\,\%$, lo cual es típico en las transiciones zircón-scheelita, ya que la estructura scheelita es mucho más compacta. Asimismo, los cálculos *ab initio* predicen inestabilidades dinámicas y mecánicas a presiones similares a la observada experimentalmente, por lo que es posible que alguna de ellas intervenga en la disminución de la barrera cinética entre las fases zircón y scheelita. Se observa también una segunda transición de fase a 20 GPa, la cual se correspondería con una distorsión monoclínica de la fase scheelita que da lugar a la fase fergusonita. Según los cálculos esta distorsión se produciría como resultado de una inestabilidad mecánica relacionada

con el tensor de constantes elásticas. Con respecto a las ecuaciones de estado, se obtienen módulos de incompresibilidad de $B_0 = 118(2)$ y $143(8)$ GPa para las fases zircón y scheelita respectivamente, lo que supone un aumento del 20 % después de la transición. Los valores experimentalmente obtenidos tienen una buena compatibilidad en general con los valores teóricos. Por otro lado, para la fase fergusonita se obtiene el mismo módulo que para la fase scheelita, lo cual es razonable teniendo en cuenta que se trata de una versión distorsionada (monoclínica) de ésta. En referencia a los experimentos de dispersión Raman, la distribución de los modos Raman de las fases zircón y scheelita presentan algunas similitudes. En ambos casos los espectros se encuentran divididos en dos regiones separadas por un gap en el que no existen modos Raman. En la estructura zircón, los modos en la región de alta energía, los cuales corresponden a vibraciones internas del tetraedro VO_4, poseen coeficientes de presión sustancialmente mayores a la del resto. Asimismo, la frecuencia y el valor de los coeficientes de presión de los modos internos disminuye de una fase a otra (de $d\omega/dP \sim 5$ a ~ 3 - 4 cm^{-1}/GPa en la fase zircón y scheelita, respectivamente). Ello se debe principalmente a que existen ligeros cambios en la dirección de vibración y una menor contribución del átomo V al movimiento. Por otro lado, en la fase zircón es necesario destacar que el modo B_{2g} posee un coeficiente de presión negativo ($d\omega/dP = -1{,}1$ cm^{-1}/GPa), el cual está asociado a la inestabilidad de la fase zircón a altas presiones. Asimismo, los cálculos *ab initio* predicen el ablandamiento de un modo silencioso BV_{1u} a 7 GPa. Por otro lado, con respecto a la fase scheelita, solo la frecuencia de los modos $E_g^{(1)}$ y $B_g^{(1)}$ tiene una dependencia negativa con la presión a partir de la transición. Una vez se descomprime la muestra, se recupera la fase scheelita en condiciones ambiente, lo cual demuestra la irreversibilidad de la transición zircón-scheelita y la existencia de una barrera cinética entre ambas estructuras.

III.2 Ortovanadato de gadolinio

Por un lado, los experimentos de difracción y espectroscopia Raman confirman la transición de fase zircón-scheelita en el $GdVO_4$ por debajo de 7,0 GPa. Como en general sucede en las transi-

ciones zircón-scheelita, se produce un considerable colapso de volumen ($\Delta V/V_0 \sim 11\,\%$) asociado al aumento de la eficiencia de empaquetamiento en la fase scheelita. El análisis experimental de las ecuaciones de estado da como resultado un valor del módulo de incompresibilidad de $B_0 = 122(5)$ y 137(2) GPa para las fases zircón y scheelita, respectivamente. Estos valores son similares a los obtenidos en el caso del $NdVO_4$ y concuerdan mejor con los cálculos *ab initio* que los valores previamente reportados para muestras dopadas. Por otra parte, los cálculos predicen el ablandamiento del fonón silencioso B_{1u} a 8,2 GPa, cerca de la presión de transición observada. Como se muestra en capítulos posteriores, el ablandamiento de este fonón está directamente relacionado con la transición entre las estructuras tipo zircón y scheelita. Al igual que ocurre en el $NdVO_4$, se observa una segunda transición de fase a 20 GPa, en la que la fase scheelita se transforma en fergusonita. Además de esto, en los experimentos Raman se observa una tercera transición de fase a 29 GPa. Según los cálculos, una estructura con grupo espacial *Cmca* es más estable a partir de $\sim$ 30 GPa, por lo que esta fase es una buena candidata para la nueva estructura. Por lo que respecta a la evolución de los modos con la presión, se observa un comportamiento similar al $NdVO_4$. En particular, se observa un aumento de la frecuencia de todos los modos en la fase zircón, con excepción de los modos $E_g^{(2)}$ y B_{2g}, los cuales tienen una dependencia negativa con la presión. Por otra parte, en la estructura scheelita, la mayoría de los modos se endurecen bajo compresión, salvo los modos $E_g^{(1)}$ y $B_g^{(1)}$. La evolución con la presión de este último modo $B_g^{(1)}$ es particularmente interesante, pues permite identificar la transición scheelita-fergusonita. Más específicamente, la frecuencia de este modo disminuye desde 8 hasta 20 GPa, punto a partir del cual pasa a convertirse en el modo A_g de la estructura fergusonita, cuya frecuencia aumenta ligeramente con la presión. Tras la descompresión de la muestra, se obtiene la fase scheelita en condiciones ambiente, en un estado metaestable, lo cual demuestra la irreversibilidad de la primera transición de fase y pone de manifiesto la existencia de barreras cinéticas.

III.3 Ortovanadato de praseodimio

En lo que respecta al $PrVO_4$, el polimorfismo de este compuesto ha sido estudiado a altas presiones y temperaturas. En primer lugar, se llevaron a cabo experimentos de DRX de muestras en polvo bajo compresión a temperatura ambiente, empleando gas neón como medio transmisor de la presión. Los experimentos mostraron una primera transición zircón-monacita a 5,5 GPa, lo cual concuerda con estudios previos. Esta transición tiene asociado un colapso de volumen del $\Delta V/V_0 \sim 8\,\%$, ligeramente inferior a la transición zircón-scheelita. Una segunda transición de fase es observada por encima de 12,2 GPa. Para esta nueva fase hemos propuesto una estructura isomorfa a la fase $PbWO_4$-III, la cual muestra una mayor compatibilidad con los datos experimentales que otras estructuras previamente sugeridas en la literatura. En particular, el patrón de difracción simulado y el experimental muestran un alto grado de semejanza, así como la evolución experimental y teórica de los parámetros de red con la presión. Con respecto a la estabilidad termodinámica de las diferentes estructuras, las curvas de entalpía calculadas predicen las transiciones de fase a 5,3 y 11,1 GPa, lo cual es compatible con las observaciones empíricas. A su vez, los cálculos también predicen una inestabilidad mecánica en la fase zircón a 5,1 GPa, lo que sugiere una posible influencia de la distorsión en la transición. Con respecto a los módulos de incompresibilidad de las diferentes fases, las estructuras zircón y monacita muestran valores muy similares ($B_0 = 117(4)$ y 114,8(1,4) GPa respectivamente), lo cual contrasta con las transiciones zircón-scheelita. Por el contrario, sí que se observa un aumento sustancial del valor de B_0 en la fase $PbWO_4$-III ($B_0 = 175(15)$ GPa), aunque este valor podría estar sobrestimado debido a la poca cantidad de medidas experimentales en este rango. Por otra parte, los cálculos también predicen que la fase scheelita es energéticamente competitiva con la fase monacita a altas presiones, lo cual motivó intentar sintetizar la fase scheelita a altas presiones y altas temperaturas en la celda de gran volumen París-Edimburgo. Se realizaron cuatro síntesis en total, a 7 GPa todas ellas, tres de 1h de duración a 600, 800 y 1000 ℃ y una de 6h a 800 ℃. Como resultado obtuvimos muestras

en condiciones ambiente consistentes en una mezcla de fases zircón y scheelita. Mediante refinamientos Rietveld se obtuvieron tanto los parámetros de red como las posiciones atómicas de la fase scheelita en condiciones ambiente. Los refinamientos también permitieron estimar la proporción de la fase scheelita, la cual crece considerablemente con la duración del proceso de síntesis. Así pues, mientras en las síntesis de 1h la proporción de scheelita apenas supera el 50 %, tras la síntesis de 6 horas ℃ la proporción de fase scheelita era del ∼ 80 % en la muestra recuperada. También se observó en las síntesis de 1h que, mientras la proporción de scheelita era del ∼ 50 % cuando la muestra se calentaba a 600 y 800 ℃, la proporción caía al 35 % cuando la temperatura se elevaba a 1000 ℃. Puesto que la compresión no hidrostática de la muestra precede a su calentamiento, es posible que parte de la fase monacita que aparece se transforme en scheelita y que otra parte retorne a la fase zircón al elevar considerablemente la temperatura. Estos experimentos muestran la enorme relevancia de las barreras cinéticas en los compuestos $R\mathrm{VO_4}$. La muestra con una mayor proporción de fase scheelita fue estudiada bajo compresión mediante la técnica de dispersión Raman. Como en el resto de compuestos tipo scheelita estudiados, la mayoría de los modos poseen una dependencia positiva y casi lineal con la presión, a excepción de los modos $E_g^{(1)}$ y $B_g^{(1)}$. En este caso, los coeficientes de presión de los modos internos son ligeramente mayores que las del resto. Por otra parte, los experimentos demostraron que alrededor de 16.7 GPa se produce una transición de fase a una estructura tipo $\mathrm{PbWO_4}$-III, lo cual es coherente con las predicciones teóricas. Bajo descompresión, la fase scheelita reaparece y es recuperada posteriormente en condiciones ambiente, lo cual demuestra la reversibilidad de la transición scheelita-$\mathrm{PbWO_4}$-III y la imposibilidad de recuperar la fase zircón (estable en condiciones ambiente) sin emplear calentamiento (barreras cinéticas).

III.4 Mecanismos de transición

Después de estos tres capítulos, es evidente que una de las cuestiones aún por resolver era establecer las condiciones en las que se producen las transiciones zircón-scheelita y zircón-monacita

en los compuestos RVO$_4$. Es por ello que en el capitulo siguiente mostramos un análisis más general de la sistemática de las transiciones zircón-scheelita/monacita. Reuniendo los datos experimentales disponibles en la literatura y nuestros cálculos *ab initio* hemos sido capaces de desvelar los mecanismos que subyacen a este tipo de transiciones de fase. Con anterioridad a nuestro estudio, la sistemática de estos compuestos se explicaba en términos del tamaño del catión de la tierra rara. Además de ello, la estabilidad de los diferentes polimorfos se discute habitualmente en términos de entalpía, mientras que el papel que juegan las inestabilidades dinámicas o mecánicas queda fuera del análisis. Por contra, nuestros cálculos claramente sugieren que la barrera cinética entre las fases zircón y scheelita disminuye gracias al ablandamiento del modo silencioso B_{1u} (inestabilidad dinámica). Además de esto, los cálculos también muestran que la transición zircón-monacita se desencadena como consecuencia de una inestabilidad mecánica asociada al tensor de constantes elásticas. De hecho, esta inestabilidad conlleva una distorsión monoclínica de la fase zircón compatible con los desplazamientos atómicos necesarios para la transición. La relación entre estos dos fenómenos y la estabilidad relativa de las fases involucradas (curvas de entalpía) explica la sistemática observada en los compuestos RVO$_4$. Esta familia constituye un ejemplo particular y, por lo tanto, el tipo de análisis que hemos propuesto podría extrapolarse a otros óxidos ternarios y a otras familias de compuestos.

III.5 Ortovanadato de terbio

Finalmente, en el último capítulo de esta tesis antes de las conclusiones, estudiamos el efecto Jahn-Teller cooperativo en el TbVO$_4$ a bajas temperaturas. Por un lado, las medidas de absorción óptica en monocristal revelaron que el el TbVO$_4$ tipo zircón posee una banda prohibida de $\sim$ 2,8 eV en la que las transiciones se producen de manera indirecta. Según la temperatura de la muestra desciende, el tamaño de la banda prohibida aumenta hasta los 100 K. Entre 100 y 35 K, el tamaño de la banda prohibida permanece aproximadamente constante. Este comportamiento sigue la tendencia descrita por la función de Bose-Einstein. Sin embargo, entre 35 y 30 K el tamaño de la

banda prohibida comienza a crecer según la muestra se enfría. Esto es coherente con la transición de segundo orden asociada al efecto Jahn-Teller cooperativo que tiene lugar en el $TbVO_4$ a 33 K. Por otra parte, los experimentos de difracción de rayos X a altas presiones y bajas temperaturas mostraron que la temperatura de transición aumenta notablemente con la presión hasta los $\sim$ 3 GPa, para después disminuir ligeramente. Estos experimentos permitieron hallar dos puntos de la línea del diagrama de fases: el primero a 120(11) K y 3,2 GPa y el segundo a 107(10) K y 4,8 GPa. En otras palabras, la temperatura de transición es entre tres y cuatro veces superior al valor observado en condiciones de presión ambiente. Puesto que la distorsión que se produce durante la transición tiene una simetría B_{2g}, el ablandamiento parcial del modo de vibración correspondiente (el cual es activo Raman) según aumenta la presión, podría explicar por qué el efecto Jahn-Teller puede ocurrir a temperaturas considerablemente más altas.

III.6 Final

En resumen, durante la investigación se han desarrollado diferentes tipos de experimentos en compuestos RVO_4 bajo condiciones de presión y temperatura extremas. Ello nos ha permitido identificar al menos seis tipos de estructuras cristalinas: zircón, scheelita, monacita, fergusonita, $PbWO_4$-III y la fase ortorrómbica del $TbVO_4$ a bajas temperaturas. Algunas de estas estructuras, como la scheelita y la monacita pueden recuperarse en condiciones ambiente en un estado metaestable. Las técnicas experimentales de medida empleadas para caracterizar las muestras han sido la difracción de rayos X, dispersión Raman y absorción óptica. Los resultados obtenidos se han complementado con cálculos *ab initio*, los cuales sirvieron para tener una mejor comprensión de los fenómenos físicos estudiados. Además, los cálculos también permitieron el análisis de los mecanismos de transición en los compuestos RVO_4 tipo zircón bajo presión. En concreto, los cálculos, junto con los datos experimentales de la literatura, revelaron que las transiciones zircón-scheelita y zircón-monacita están gobernadas por inestabilidades dinámicas y mecánicas respectivamente.

1 Introduction

1.1 Historical background

The interest for new and useful materials has been a constant feature in all human history. As a matter of fact, many ancient and prehistoric societies are anthropologically distinguished in accordance with the type of material that defined the lives of their individuals [1], so that nowadays we refer to them as the stone, bronze, iron... ages. In more recent centuries and decades, tremendous scientific advances in physics and chemistry lead to the discovery of many new exotic materials with striking properties. These properties can also be altered by disturbing the original electronic configuration of the atoms that constitute a particular material, by submitting it to different external conditions such as high pressures or high/low temperatures. For instance, some solids have shown that, below a certain temperature, their resistivity shrinks to zero and become superconductors. Other materials become (anti)ferromagnetic or get distorted (Jahn-Teller effect) at low temperatures. With regard to high pressures, these allow to considerably change the interatomic distances between the constitutive atoms of the solid. As a consequence, the chemical bonding between atoms is radically modified. These changes may disrupt the physical behaviour of the original material or give rise to different structures with other optical, vibrational, electronic, magnetic, etc. characteristics. Moreover, some of structures that can be synthesized at high pressures can be quenched at ambient conditions in a metastable state, which is potentially useful for obtaining materials which are hard to find in nature. The best example of this are dia-

monds, which can be synthesized by submitting carbon to high pressures and temperatures and are subsequently recovered at room conditions. Hence, high pressures have been proven to be a fundamental tool for materials research and for the development of new technologies.

The history of high-pressure research has its beginning with the investigations carried out by Percy W. Bridgman during the first half of the 20th century, for which he received the Nobel prize in 1946 [2]. Prof. Bridgman was the first scientist that developed an apparatus that was able to compress matter up to 10 GPa, which allowed him to perform many experiments on a huge number of compounds [3]. Latter advancements lead to the design of the first diamond-anvil cell (DAC), which was much more smaller than precedent presses and easier to carry [4]. It also allowed the optical access to the sample, which was not possible with previous devices. Depending on the DAC model, the maximum pressure that can be achieved range from 10 and 500 GPa typically. Further developements revealed that pressures up to 1 TPa can be achieved with nanocrystalline diamonds [5]. Since diamonds are transparent to X-rays and IR-VIS-UV radiation, many techniques can be used to characterize samples under high pressure conditions, such as X-ray diffraction, Raman scattering or optical absorption measurements. The development of high brilliance radiation facilities like synchrotrons considerably boosted the number of high pressure experiments around the globe. Furthermore, these astonishing developments have also been relevant not only to material science but to other fields such as biochemistry, medicine, geology or food processing [6].

In recent years, ternary oxides (AXO_4, where X = V, P, W, Nb, Mo, As, etc. and A is a trivalent element) have displayed striking properties that made them suitable for industrial and technological application. As an example of this, orthophosphates are potentially useful as nuclear waste storage materials because of their resistance to corrosion by geological fluids [7]. On the other hand, (ortho)tantalates, niobates, molybdenates and tungstenates have shown excellent scintillation properties which make them suitable as radiation detectors [8, 9]. In our particular case, this dissertation is focused in the study of a subset of the ternary oxides family known as rare-earth

orthovanadates (where X = V and A = R = rare-earth atom) [10] under extreme conditions. RVO$_4$ compounds have also proven to be potentially useful as scintillators [11, 12], as well as many other applications such as thermophosphors [13], laser host-materials [14, 15] or photocatalytic materials for water purification [16, 17]. On the other hand, orthovanadates undergo different kinds of phase transitions at high pressures, some of which can be quenched to ambient conditions in a metastable state. The physical properties of these new polymorphs are different from the original ones, which make them suitable for other technological purposes. For instance, scheelite structured BiVO$_4$ can be used in lithium-based batteries as electrode material [18]. Therefore, the experimental and theoretical study of the RVO$_4$ family at different pressures and temperatures is fundamental to improve our knowledge of the varied and outstanding properties of orthovanadates.

The interest in the high pressure polymorphs of SiO$_2$, an abundant material in nature, motivated the study at high temperatures and pressures of metal orthovanadates in the beginning of the 60s, due to their structural similarities. In particular, both Si and V are tetrahedrally coordinated with O atoms in silica and in zircon-type orthovanadates, respectively. The first study of this kind was reported by Young and Schwartz [19] in 1962, in which they studied the high pressure polymorphs CrVO$_4$ and FeVO$_4$. In their study, the authors submitted their samples to pressures near 6 GPa and temperatures close to 1000 K for 24h by using a belt-apparatus. An additional study on FeVO$_4$ was performed by the same authors [20] in 1964. The recovered products at room conditions were characterized by means of X-ray diffraction (XRD), which revealed that different unknown polymorphs had been synthesized. Nonetheless, their structures were not fully determined until a decade later by Muller and Joubert [21] and Kanamaru *et al* [22]. Also in the 60s decade, Stubican and Roy [23] reported a wide study on several rare-earth ternary oxides, including orthovanadates, under high pressures and temperatures. With regard to RVO$_4$ compounds, the authors characterized the whole family at room conditions via XRD. Their results confirmed that these compounds crystallize in the zircon-type structure [Space Group (S.

G.): $I4_1/amd$] at ambient conditions, with the only exception of $LaVO_4$, which crystallized in the monazite-type phase (S. G.: $P2_1/n$). Their samples were compressed up to 8 GPa and heated at 600 ℃ during several hours. After quenching them at ambient conditions, the samples were analyzed by means of XRD. These experiments revealed that new polymorphs had been recovered as a consequence of an irreversible phase transition at high pressures and temperatures. For R = La and Ce, a monazite-type structure was recovered, whereas the rest of RVO_4 compounds transformed into a scheelite-type structure (S.G.: $I4_1/a$). However, the lattice parameters of only a few compounds are reported and the atomic positions are not refined in any case. In these early decades, most of ternary oxides high-pressure polymorphs were studied in recovered samples at ambient conditions, after submitting them to high pressures. *In situ* high pressure experiments on orthovanadates will take place for the first time two decades later. With regard to temperature-induced transformations, several studies in the 70s reported a second order phase transition in $DyVO_4$ and $TbVO_4$ at low temperatures and ambient pressure [24–27]. According to these studies, the zircon structure of both compounds gets distorted below 14 and 33 K respectively, as a consequence of a cooperative Jahn-Teller effect [28].

In the 80s decade, one of the most studied orthovanadates was $BiVO_4$. *In situ* high-pressure and high-temperature experiments revealed that this compound undergoes a second-order ferroelastic phase transition from the fergusonite (S.G.: $I2/a$) to the scheelite phase [29, 30]. In contrast to previous decades, these experiments were performed with ta DAC instead of a belt-type apparatus. The use of this novel technology allowed to characterize the vibrational structure and the optical absorption properties of YVO_4 under high pressure [31]. These experiments lead to the discovery of a phase transition from the zircon to the scheelite structure over 7.5 GPa. Some other rare-earth orthovanadates were also studied during this decade. For instance, $DyVO_4$ and $TbVO_4$ were studied at high-pressure conditions by means of Raman scattering experiments, which revealed changes compatible with a zircon-to-scheelite phase transition [32].

The development of synchrotron facilities and the spread of this technology to many coun-

tries allowed to perform angle-dispersive single-crystal and powder XRD experiments with high resolution. The huge increase in brilliance that these facilities provided in comparison to conventional X-ray sources allowed to collect better XRD patterns in much smaller time lapses. As a consequence, the XRD studies on the structural evolution of orthovanadates under high pressure hugely multiplied. For instance, the previously mentioned zircon-to-scheelite phase transition found in YVO_4 under high pressure was confirmed by means of *in situ* XRD experiments in 2004 by Wang *et al.* [33] and Manjón *et al.* [34]. With regard to the RVO_4 compounds where R is a lanthanide, *in situ* high-pressure room-temperature experiments determined that these oxides, with the exception of $LaVO_4$, undergo a zircon-to-scheelite phase transformation when R cations are small (Sm - Lu) [35–38] whereas for those with larger rare-earth cations (Ce - Nd) the zircon structure transforms into the monazite-type phase [39–42]. In this particular case, scientific consensus established a systematic that related the size of the rare-earth cation with the high-pressure structure. Radioactive $PmVO_4$ has been left out of the scope of high pressure studies for obvious reasons. This systematic is slightly different from that observed by Stubican and Roy [23] in the 60s. However, according to our experimental and theoretical studies, both results can be reconciled by taking into account the hydrostatic conditions and kinetic barriers [43, 44]. Under further compression, these compounds have been observed to have other phase transitions. For instance, some scheelite compounds have been observed to transform into a fergusonite phase at approximately 20 GPa [37]. Moreover, monazite-type structures like $CeVO_4$ (at high pressures) and $LaVO_4$ have been observed to transform into different monoclinic structures when submitted to further compression [39, 43, 45, 46].

In addition to experimental achievements, *ab initio* calculations in the framework of the Density Functional Theory (DFT) also had a decisive contribution to the study of rare-earth orthovanadates under high pressures. Theoretical models allowed to study the thermodynamical stability of high pressure phases, as well as many of their physical properties such as compressibility, vibrational and electronic structures, elastic stability, etc [35–37, 40]. Calculations not only

showed a very good compatibility with experimental results, but also helped to identify some mechanisms that may have a decisive influence on the phase transitions.

Regarding experimental conditions, several works on orthovanadates have shown that non-hydrostatic effects can substantially alter the structural sequence or the transition pressure. For instance, when $ScVO_4$ is compressed under poor hydrostatic conditions, a different kind of structure is recovered at ambient conditions [47]. Similarly, experiments in a large volume press showed that the scheelite structure of $CeVO_4$ can be recovered at ambient conditions when the sample is compressed using boron nitride as pressure transmitting medium, which does not provide good hydrostatic conditions at ambient temperatures [40]. In line with these observations, our high pressure experiments on $NdVO_4$ showed that hydrostatic conditions can play a decisive role in the high pressure structural sequence [44, 46] (see Chapter 4). Moreover, in the case of $HoVO_4$, non-hydrostatic stresses lead to a reduction of the transition pressure from 8 to 4 GPa [37].

The structural behaviour of RVO_4 compounds under high pressure conditions has also motivated the study of the pressure evolution of their electronic band gap. In fact it has been experimentally observed that during the zircon-to-scheelite phase transition there is a substantial band gap collapse [48, 49]. In particular, there is a reduction of $\sim$ 0.5 - 1 eV at the transition pressure. Since the scheelite phase can be recovered in a metastable state due to the irreversible character of the transition, it is possible to obtain scheelite structured orthovanadates with smaller band gaps at room conditions. According to literature, the band gap energy of most scheelite-type orthovanadates is below 3 eV [48].

To sum up, the behaviour of rare-earth orthovanadates and related compounds under extreme conditions has been a very prolific field of research. Our experimental and theoretical contribution to this field is summarized in this dissertation, which has been partially published in Refs. [43, 44, 46, 49]. The body of this doctoral thesis is structured in the following order. In this chapter, we have provided a basic introduction on the topic and we will describe the crys-

talline structures that are relevant in our study. Chapter 2 contains a summary of the theoretical concepts that are necessary to understand the behaviour of solids under extreme pressures and temperatures. A brief description of the different experimental techniques used during our research is provided in Chapter 3. After these first three chapters, we deep into the results of our research. Chapter 4 describes our XRD and Raman scattering experiments on $NdVO_4$ under high pressure. The obtained results are supported by *ab initio* calculations. In chapter 5 we describe an extensive experimental and theoretical research on $GdVO_4$ under high pressure, which includes XRD, Raman and optical absorption measurements as well as DFT calculations. The theoretical and experimental high-pressure evolution of $PrVO_4$ is studied in chapter 6, where we also report the synthesis of the scheelite phase of this compound using the Paris-Edinburgh large volume press. The systematics of the RVO_4 family are discussed in chapter 7. Calculations allowed us to unveil the mechanisms that underlay the pressure-induced phase transitions in the rare-earth orthovanadate family. The cooperative Jahn-Teller effect in $TbVO_4$ at low temperatures is studied in Chapter 8 by means of optical absorption measurements. In addition to this, we also studied this compound at low temperatures and high pressures by means of angle-dispersive powder XRD. Finally, in Chapter 9 we condensed the main conclusions from our studies in a few paragraphs.

1.2 Crystal structures

In this section of the Introduction, we will provide an accurate description of the crystal structures that are relevant in our study. With the exception of $LaVO_4$, all RVO_4 compounds, as well as many other ternary oxides, crystallize in the tetragonal zircon structure at ambient conditions, which is depicted in Fig. 1.1 in different spatial projections. This type of structure has been named after the widely-known natural mineral zircon ($ZrSiO_4$) for being isomorphic to it. This crystal structure is characterized for having a tetragonal unit-cell in which the position of the vanadium and rare-earth atoms fixed by symmetry. In the 50s decade, Milligan and Vernon [50]

solved the crystalline structure of rare-earth orthovanadates using neutron diffraction measurements. In their study, the authors reported the unit-cell lattice parameters of these compounds as well as their atomic positions at ambient conditions. Later works provided much more accurate measurements of these parameters by the end of the twentieth century [51].

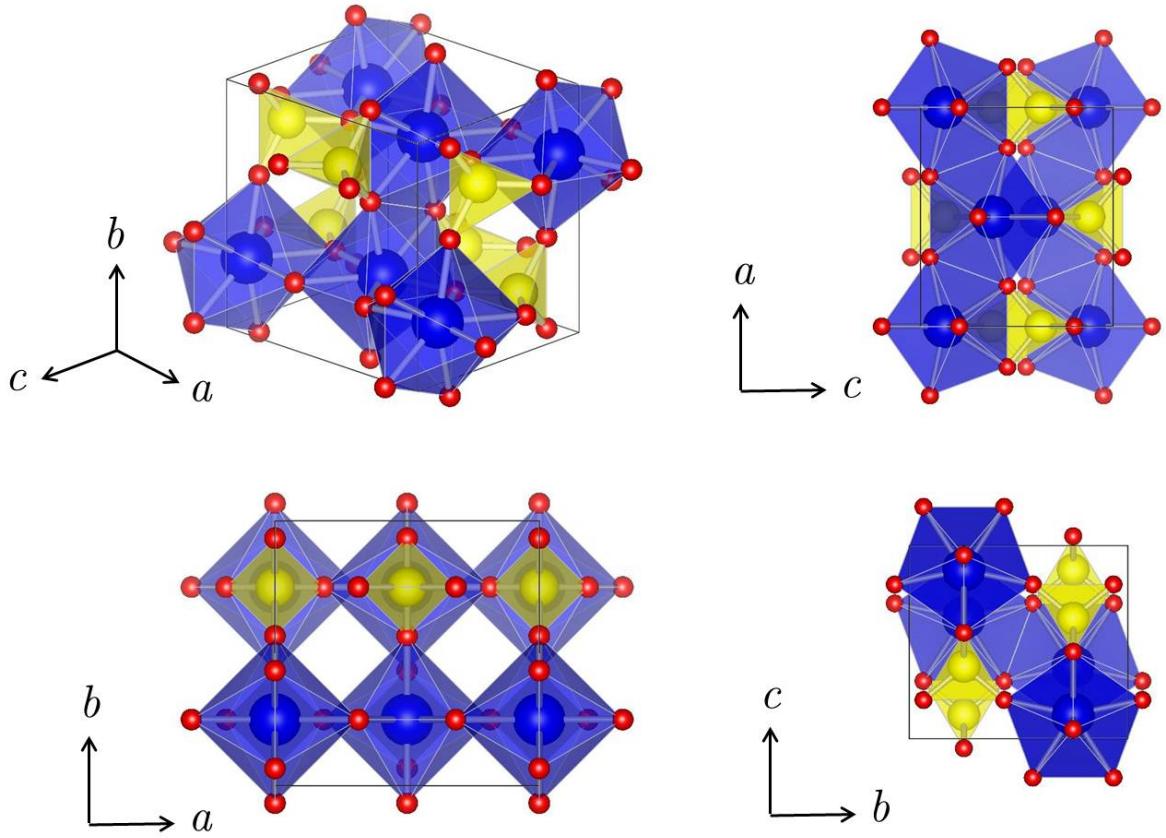

Figure 1.1: Unit-cell of the zircon structure in different orientations (S.G.: $I4_1/amd$, $Z = 4$). Red, yellow and blue spheres represent the oxygen, vanadium and rare-earth atoms respectively. The coordination of vanadium and the rare-earth atom are depicted as yellow and blue polyhedral structures respectively.

As we previously mentioned, the zircon crystal structure (Fig. 1.1), has a tetragonal symmetry. In particular, its space group is $I4_1/amd$ (Schoenflies: D_{4h}^{19}, No. 141, $Z = 4$), usually described with origin at $2/m$ in the literature (setting 2). The atomic positions in this structure are given in Table 1.1 for $GdVO_4$ at ambient conditions. The R and V cations are located at the high-symmetry positions corresponding to 4a and 4b Wyckoff sites, respectively. By contrast, the position of the

oxygen atoms corresponds to the 16h Wyckoff position, described by the vector $(0 \quad y \quad z)$. This structure can be visualized as constituted by a set of isolated VO_4 regular tetrahedra surrounding the rare-earth cation R, forming distorted eight-vertex RO_8 triangular dodecahedra. These RO_8 polyhedral units are sometimes referred as bidisphenoids in literature. The V–O distance in RVO_4 compounds is $\sim$ 1.7 Å, showing a very small variation upon compression, which means that the VO_4 are quite rigid structures. In fact, in our works we estimated that the contribution of these units to the total compressibility is 1% [43]. On the other hand, in the RO_8 bidisphenoids, the rare-earth cation is surrounded by eight oxygen atoms with two different lengths i.e. four short and four long R–O bonds, which range typically between 2.2 and 2.5 Å. Therefore, according to these polyhedral description of the crystal, the zircon structure can be described as a set of alternating VO_4 and RO_8 polyhedra distributed along the direction given by the crystallographic c-axis. This particular distribution of the polyhedra explains the anisotropic behaviour of the zircon structure under compression [37, 49] as well as the remarkable birrefringence of this kind of crystals.

Table 1.1: Refined atomic positions of zircon-type $GdVO_4$ (S.G.: $I4_1/amd$) at ambient conditions (reported by Mullica *et al.* [52]). The unit-cell parameters are $a = 7.2122(7)$ and $c = 6.346(2)$ Å.

Element	Wyckoff position	x	y	z
Gd	4a	0	0.75	0.125
V	4b	0	0.25	0.375
O	16h	0	0.4323(5)	0.2028(7)

At low temperatures, some compounds like $TbVO_4$, undergo a phase transition due a cooperative Jahn-Teller effect in which the zircon structure gets distorted [26, 27]. This leads to an orthorhombic structure with a space group $Fddd$ (Schoenflies: D_{2h}^{24}, No. 70, $Z = 8$). The distortion takes place in the ab basal plane of the zircon structure along the $[1 \quad 1 \quad 0]$ and $[1 \quad -1 \quad 0]$ directions. These directions are taken as the a- and b-axes of the orthorhombic phase respectively.

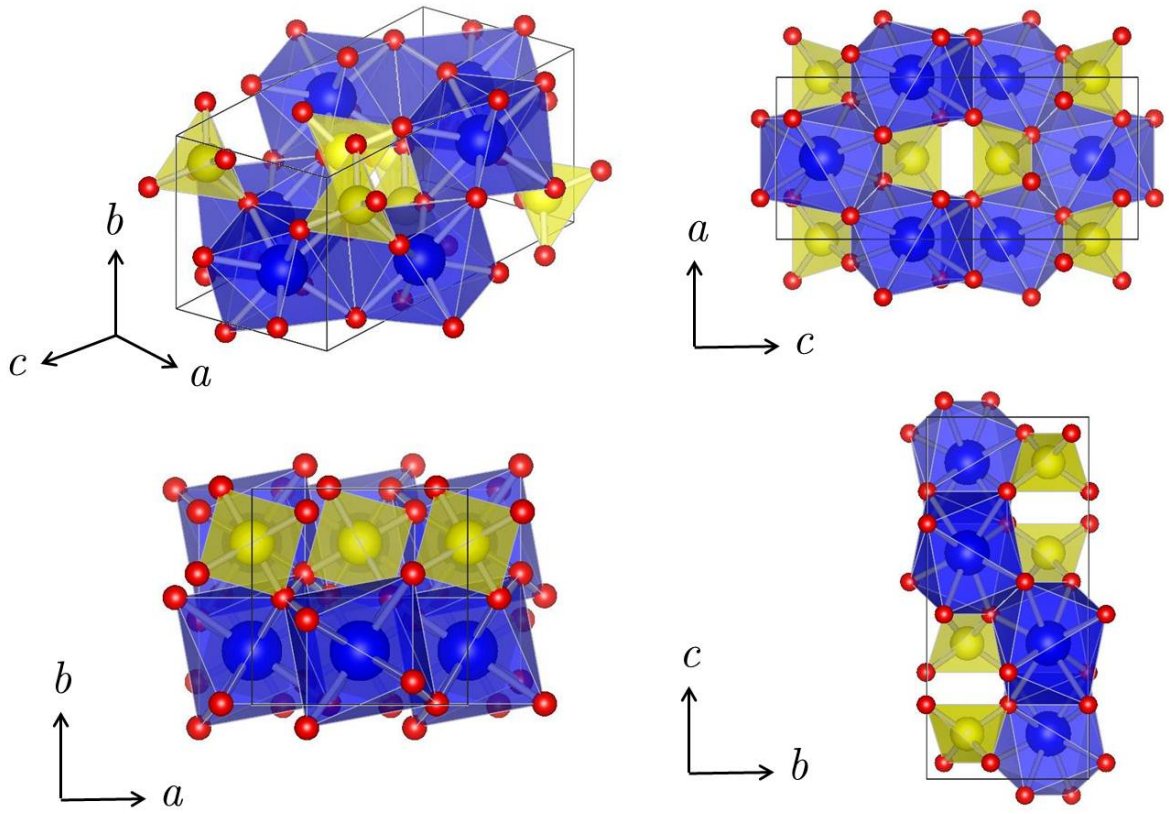

Figure 1.2: Unit-cell of the scheelite structure in different orientations (S.G.: $I4_1/a$, $Z = 4$). The structural elements follow the same description given in Fig. 1.1.

Table 1.2: Refined atomic positions of scheelite-type $ErVO_4$ (S.G.: $I4_1/a$) at room conditions (Range and Meister [53]). The unit-cell parameters are $a = 5.003(1)$ and $c = 11.143(2)$ Å.

Element	Wyckoff position	x	y	z
Er	4b	0	0.25	0.625
V	4a	0	0.25	0.125
O	16f	0.1460(6)	0.5050(6)	0.2054(3)

The scheelite polymorph, shown in Fig. 1.2, has been found in many RVO_4 compounds as a high-pressure phase that can be quenched to ambient conditions in a metastable state. This structure was firstly reported in a RVO_4 compound ($ErVO_4$) by Range and Meister [53] in 1990.

The refined atomic positions are given in Table 1.2. Similarly to the zircon phase, the scheelite structure has a tetragonal symmetry, with the space group being in this case $I4_1/a$ (Schoenflies: C_{4h}^6, No. 88, $Z = 4$). The R and V cations are located at the high-symmetry sites described by the Wyckoff positions 4b and 4a, respectively. On the contrary, the position of the oxygen atoms is not fixed by symmetry, but located at the Wickoff positions 16f $(x \quad y \quad z)$. As in the zircon structure, this polymorph is constituted by VO_4 regular tetrahedra and RO_8 bidisphenoids. The latter are much less distorted than in the zircon phase, since the two different R–O distances become much more similar. Moreover, the scheelite crystal structure can be also described as a set of alternating VO_4 and RO_8 polyhedral units running parallel to the c-axis direction. However, these chains are vertex- instead of edge-shared as in the zircon structure. This phase has also a larger packing efficiency than the zircon structure. Actually, the zircon-to-scheelite phase transition is characterized by a huge volume collapse of $\Delta V/V_0 \sim 11\%$ [54]. On the other hand, the fergusonite crystal structure (S.G.: $I2/a$, Schoenflies: C_{2h}^6, No. 15, $Z = 4$) can be considered as a monoclinic distortion of the scheelite phase along the direction defined by the ab base diagonal. In fact, both structures are related by a group-subgroup relation.

Table 1.3: Refined atomic positions of monazite-type $LaVO_4$ (S.G.: $P2_1/n$) at ambient conditions (Errandonea *et al.* [45]). The unit-cell parameters are $a = 7.044(2)$ Å, $b = 7.283(2)$ Å, $c = 6.714(2)$ Å and $\beta = 104.86(5)$ °.

Element	Wyckoff position	x	y	z
La	4e	0.2771(4)	0.1570(2)	0.1038(2)
V	4e	0.2995(4)	0.1648(2)	0.6145(6)
O_1	4e	0.2425(5)	−0.0009(5)	0.4253(8)
O_2	4e	0.3866(7)	0.3434(7)	0.4944(8)
O_3	4e	0.4815(9)	0.1506(5)	0.8247(9)
O_4	4e	0.1190(5)	0.2206(6)	0.7305(9)

$LaVO_4$ crystallize in the monazite structure at ambient conditions (S.G.: $P2_1/n$, Schoenflies: C_{2h}^5 , No. 14, $Z = 4$), which is depicted in Fig. 1.3. The corresponding atomic positions reported

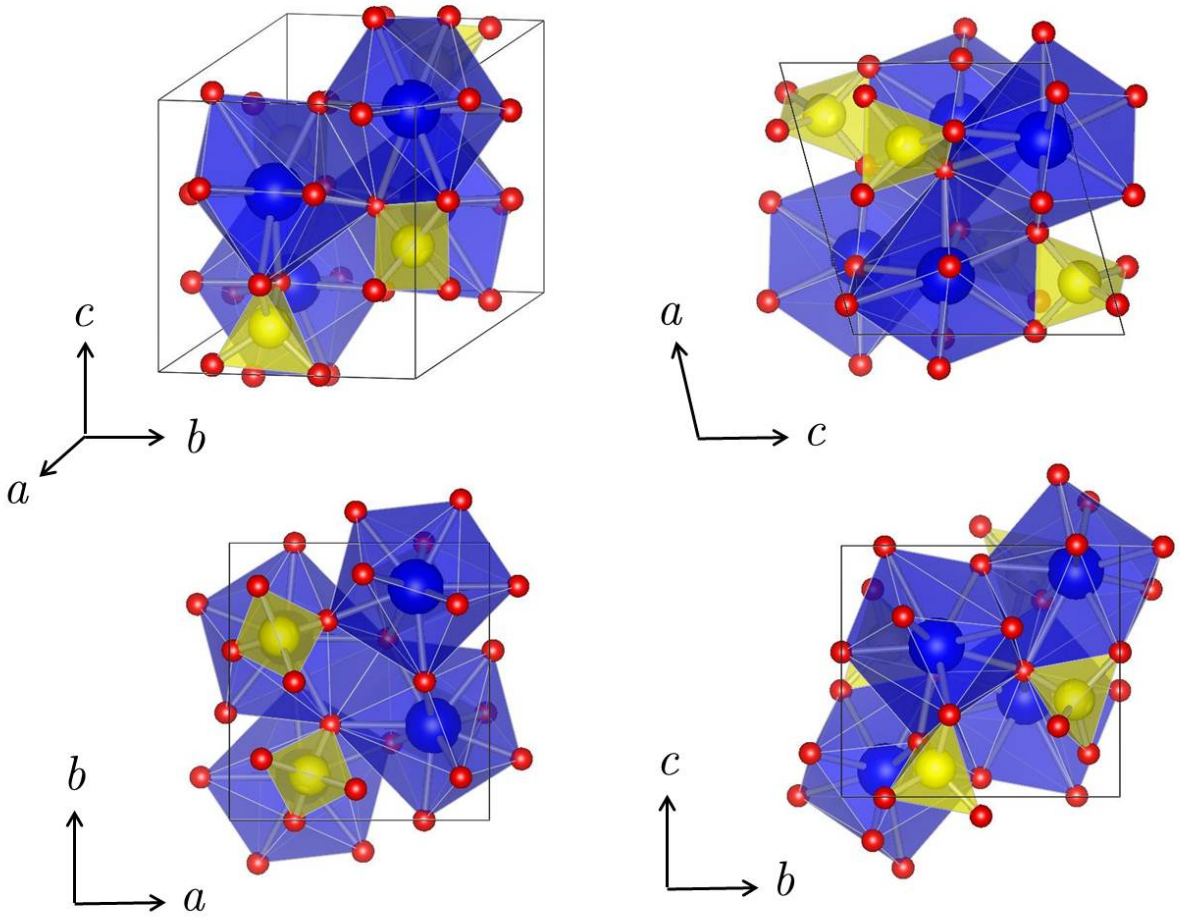

Figure 1.3: Unit-cell of the monazite structure in different (S.G.: $P2_1/n$, $Z = 4$). The structural elements follow the same description given in Fig. 1.1.

by Errandonea *et al.* [45] are summarized in Table 1.3. This structure has also been observed as the high pressure phase of $CeVO_4$ and $PrVO_4$ [39, 42, 43]. Just like the zircon and scheelite structures, the V atoms are four-coordinated, although the VO_4 tetrahedra are slightly distorted. A full description of the monazite crystal structure for rare-earth ternary oxides was provided by Beall *et al.* [55] and Mullica *et al.* [56, 57] . With respect to the *R* atom, these are nine-fold coordinated, forming an equatorial pentagon (constituted by 5 oxygen atoms belonging to VO_4 monodentate tetrahedra) interpenetrated by a tetrahedron (formed by 4 oxygen atoms which belong to two bidentate VO_4 tetrahedra). The VO_4 tetrahedra out of the equatorial plane can be

considered as the link between the RO_9 units, which leads to the formation of chains along the c-axis direction. Moreover, in the case of rare-earth elements, the RO_9 polyhedrons are distorted, with nine different bond lengths between the rare-earth cation and the oxygen atoms. A complete review of the structural properties and relations of the monazite structure can be found in Clavier *et al.* [58].

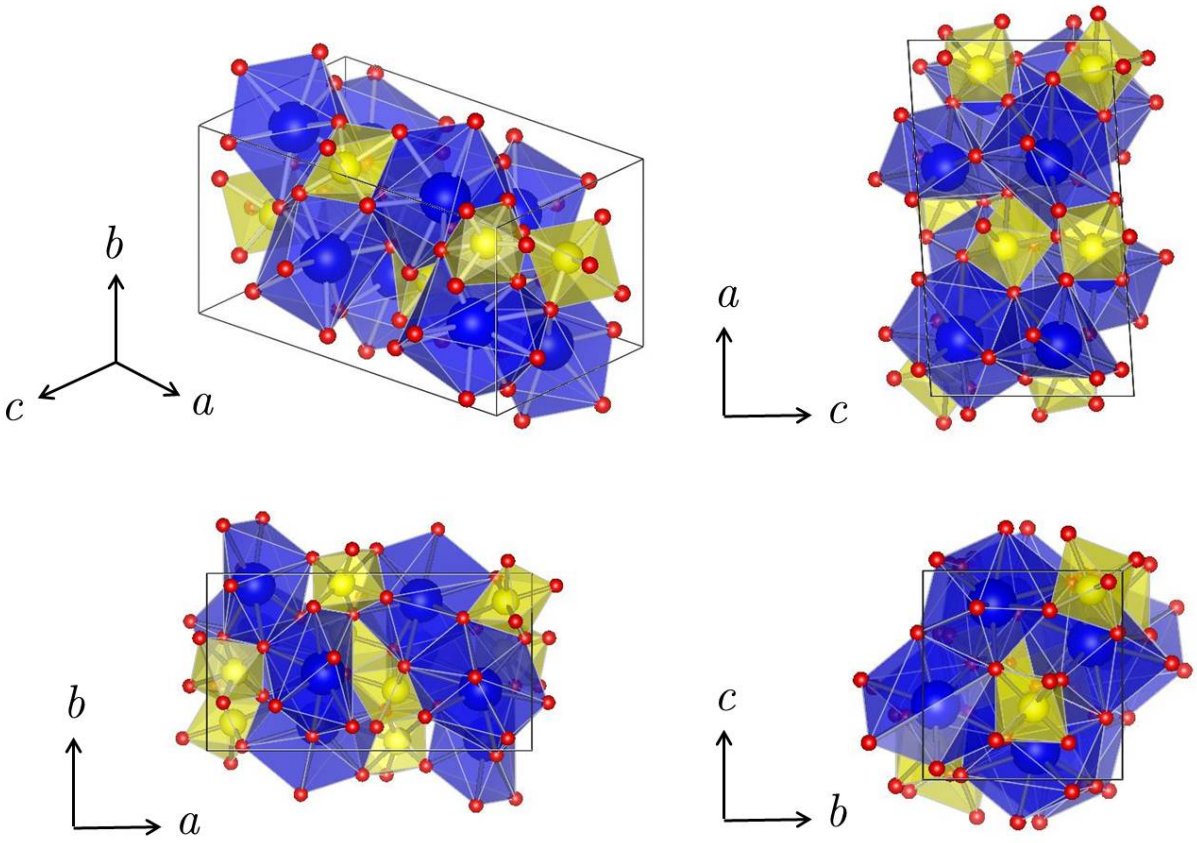

Figure 1.4: Unit-cell of the $BaWO_4$-II-type structure in different orientations (S.G.: $P2_1/n$, $Z = 8$). The structural elements follow the same description given in Fig. 1.1.

When compressed, the monazite structure transforms into the $BaWO_4$-II-type structure (S.G.: $P2_1/n$, Schoenflies: C_{2h}^5 , No. 14, $Z = 8$), depicted in Fig. 1.4 [45]. The calculated atomic positions for $LaVO_4$ at 16.4 GPa reported by Errandonea *et al.* are shown in Table 1.4. The main difference

Table 1.4: Calculated atomic positions of $BaWO_4$-II-type $LaVO_4$ (S.G.: $P2_1/n$) at 16.4 GPa (Errandonea *et al.* [45]). The unit-cell parameters are a = 12.319 Å, 6.443 Å, c = 6.775 Å and β = 95.80 °.

Element	Wyckoff position	x	y	z
La_1	4e	0.89138	0.34364	0.11856
La_2	4e	0.87725	0.05433	0.11856
V_1	4e	0.86896	0.83095	0.17888
V_1	4e	0.83191	0.55824	0.60671
O_1	4e	0.93820	0.04308	0.31838
O_2	4e	0.79212	0.35971	0.77788
O_3	4e	0.90611	0.40060	0.47845
O_4	4e	0.77509	0.63949	0.09695
O_5	4e	0.91628	0.69045	0.87024
O_6	4e	0.81457	0.77366	0.42413
O_7	4e	0.99659	0.70000	0.15006
O_8	4e	0.82884	0.01541	0.98855

with the other shown structures, is that the V atoms are six-coordinated i.e. the coordination increases from 4 to 6 during the monazite-to-$BaWO_4$-II phase transition. The rare-earth cations are typically surrounded by 9 to 10 oxygen atoms, although this depends on the particular compound. This phase is sometimes referred as the $PbWO_4$-III structure, since they are formally isomorphic [59]. The structure can be viewed as a set of zigzag layers of slightly distorted VO_6 octahedra distributed along the a-axis direction, linked by R atoms [60]. Each layer is constituted of eigth- and four-membered rings of VO_6 octahedra; in the former type of ring each pair of edge-shared octahedra is linked with another by corner-sharing, whereas in the latter all octahedra are connected by corner-sharing.

1.3 Physical properties

In this section, we will provide a basic description of some of the physical properties of different crystal structures of RVO_4 compounds. In particular, we focus our explanations in their

structural response to pressure (compressibility), their vibrational properties and their electronic band structure.

1.3.1 Compressibility

These crystal structures display an anisotropic behaviour upon compression, which can be explained in terms of the distribution of the different constitutive polyhedral structures. In particular, this explanation is clearer in the cases of the zircon and scheelite polymorphs, since their polyhedral structures are much more simple and less distorted. Table 1.5 summarizes the linear axial compressibilities of some RVO$_4$ compounds. As it can be observed in the table, the a-axis is more compressible than the c-axis in the zircon phase, whereas the opposite happens in the scheelite phase.

Table 1.5: Unit-cell lattice parameters and linear axial compressibilities for some selected RVO$_4$ compounds. The conditions under which the lattice parameters were obtained are indicates between brackets (AC = Ambient Conditions). Data extracted from Refs. [36, 44, 54, 61].

Compound	Phase	a (Å)	c (Å)	κ_a (GPa^{-1})	κ_c (GPa^{-1})
NdVO$_4$	Zircon	7.333(1)	6.438(1) [AC]	$3.081(8) \times 10^{-3}$	$1.554(4) \times 10^{-3}$
	Scheelite	5.0376(5)	11.4105(7) [9.1 GPa]	$1.621(6) \times 10^{-3}$	$2.038(8) \times 10^{-2}$
ErVO$_4$	Zircon	7.09595(3)	6.27105(3) [AC]	$2.0(1) \times 10^{-3}$	$1.6(2) \times 10^{-3}$
	Scheelite	5.01466(3)	11.17009(10) [AC]	$1.7(1) \times 10^{-3}$	$2.3(1) \times 10^{-3}$
EuVO$_4$	Zircon	7.2408(5)	6.3681(3) [AC]	2.5×10^{-3}	1.3×10^{-3}
	Scheelite	5.0004(2)	11.128(5) [15.3 GPa]	1.3×10^{-3}	1.9×10^{-3}
DyVO$_4$	Zircon	7.1540(3)	6.31360(4) [AC]	1.77×10^{-2}	1.08×10^{-2}
	Scheelite	5.0144(9)	11.0274(1) [9.9 GPa]	0.58×10^{-2}	1.87×10^{-2}

With respect to the zircon phase, this structure can be described as a set of chains constituted by alternating edge-sharing RO$_8$ dodecahedra (bidisphenoids) and VO$_4$ tetrahedra running parallel to the c-axis direction. These chains are joined laterally by edge-sharing RO$_8$ dodeca-

hedra along the crystallographic *a*-axis (Fig. 1.1). Thus, the fact that the RO_8 polyhedral units are much more compressible than the VO_4 tetrahedra makes the *a*-axis more compressible than the *c*-axis. A similar explanation holds for the scheelite phase. However, in this case, the RO_8 and VO_4 polyhedral units are corner-shared. This allows to find the same RO_8 - VO_4 alternating pattern in the *a* and *b* crystallographic directions (tetragonal symmetry). On the other hand, we find that slightly twisted chains of edge-connected RO_8 are distributed along the *c*-axis direction. Therefore, the *c*-axis is much more compressible than the *a*-axis, since there is no contribution of the VO_4 tetrahedra to the compressibility of the former.

Table 1.6: Birch-Murnaghan equation of state parameters of some RVO_4 compounds. V_0, B_0 and B_0' represent the unit-cell volume, bulk modulus and bulk modulus derivative at zero pressure, respectively. The Pressure Transmitting Medium (PTM) is indicated for each case. ME = Methanol-Ethanol; MEW = Methanol-Ethanol-Water.

Compound	Phase	PTM	V_0 (Å^3)	B_0 (GPa)	B_0'	Ref.
$LaVO_4$	Zircon (Nano Rods)	ME	364.0(2)	93(2)	4 (fixed)	[62]
	Monazite	MEW	333.2(1)	106(1)	4 (fixed)	[45]
	$BaWO_4$-II	Theory	609.2	154	4.2	[45]
$CeVO_4$	Zircon	Ne	352.9	125(9)	4 (fixed)	[39]
	Monazite	Ne	326.2(8)	133(5)	4.4(6)	[39]
$SmVO_4$	Zircon	MEW	336.5(9)	129(4)	4 (fixed)	[35]
	Scheelite	MEW	227.7(1.2)	133(5)	4 (fixed)	[35]
$EuVO_4$	Zircon	MEW	333.8(4)	150(7)	5.3(6)	[36]
	Scheelite	MEW	296.2(6)	195(8)	5.5(9)	[36]
$TbVO_4$	Zircon	Ne	324.4(9)	122(5)	4	[39]
	Scheelite	Ne	288.2	163(9)	4 (fixed)	[39]
$ErVO_4$	Zircon	MEW	316.4(7)	158(13)	4 (fixed)	[54]
	Scheelite	MEW	280.2(8)	158(17)	4 (fixed)	[54]

On the other hand, the incompressibility of a crystal structure is given by the magnitude of its

bulk modulus. To put it in another way, the bulk modulus provides an estimation of the hardness of the material. In order to measure this parameter, it is necessary to estimate the Equation of State (EOS) of the material. In our case, we use the Birch-Murnaghan EOS, which is explained in more detail in Chapter 2. The EOS parameters of some selected rare-earth orthovanadates are shown in Table 1.6. These include the unit-cell volume (V_0), the bulk modulus (B_0) and its derivative at zero pressure. The data included in the table was obtained from XRD experiments, which were reported in the indicated references. As it can be seen in Table 1.6, in the zircon-type compounds there is a tendency of B_0 to grow as the the unit-cell volume decreases, with some exceptions like $TbVO_4$. In addition to this, the bulk modulus of the scheelite polymorphs tends to be substantially higher. This is a direct consequence of the associated large volume collapse ($\Delta V/V \sim 10\%$) in the zircon-to-scheelite phase transition, which considerably increases the packing efficiency. By contrast, the bulk moduli of the monazite and zircon phases of the same compound tend to be quite similar. Even though the volume decrease at the zircon-to-monazite phase transition is remarkably large ($\sim 8\%$), the flexibility of the RO_9 polyhedral unit allows the contraction, which counteracts the effects of the volume collapse. On the contrary, in the $BaWO_4$-II-type structure, the bulk modulus is predicted to increase by $\sim 50\%$ with respect to the monazite phase.

1.3.2 Vibrational properties

Here we will briefly describe some of the most important characteristics of the lattice vibrations of the zircon and scheelite crystal structures. Table 1.7 shows the representation of the Raman, Infrared (IR) and silent modes of the zircon and scheelite structures in the center of the Brillouin zone, according to group theory. [63].

Since these two phases have been extensively studied in this dissertation by means of the Raman scattering technique, we will focus in the Raman active modes symmetries and how they change from one structure to the other. Tables 1.8 and 1.9 show the frequencies of the Raman

active modes of some zircon- and scheelite-type $R\mathrm{VO_4}$ compounds, respectively.

Table 1.7: Symmetry and activity of the vibrational modes of the zircon and scheelite structures at the Γ point.

Activity	Zircon	Scheelite
Raman	$\Gamma_R = 2A_{1g} + 4B_{1g} + B_{2g} + 5E_g$	$\Gamma_R = 3A_g + 5B_g + 5E_g$
Infrared (IR)	$\Gamma_{IR} = 3A_{2u} + 4E_u$	$\Gamma_{IR} = 4A_u + 4E_u$
Silent	$\Gamma_S = B_{1u} + A_{1u} + A_{2g} + 2B_{2u}$	$\Gamma_S = 3B_u$
Acoustic	$\Gamma_A = A_{2u} + E_u$	$\Gamma_A = A_u + E_u$

Table 1.8: Experimental Raman frequencies for some selected zircon-type $R\mathrm{VO_4}$ compounds at ambient conditions (units in $\mathrm{cm^{-1}}$). Data extracted from Refs. [64–66]

Compound	$E_g^{(1)}$	$B_{1g}^{(1)}$	$E_g^{(2)}$	$E_g^{(3)}$	$B_{1g}^{(2)}$	B_{2g}	$E_g^{(4)}$	$A_{1g}^{(1)}$	$B_{1g}^{(3)}$	$B_{1g}^{(4)}$	$E_g^{(5)}$	$A_{1g}^{(2)}$
$\mathrm{YVO_4}$	137	157	163	260	267	260	378	444	490	817	840	891
$\mathrm{SmVO_4}$	112	123	151	238	261	–	379	–	473	805	816	878
$\mathrm{GdVO_4}$	110	123	156	246	252	261	376	438	483	809	825	884
$\mathrm{TbVO_4}$	–	120	154	246	–	260	–	381	483	809	826	885

Table 1.9: Experimental Raman frequencies for some selected scheelite-type $R\mathrm{VO_4}$ compounds (units in $\mathrm{cm^{-1}}$). Except $\mathrm{TbVO_4}$, whose phonon frequencies where measured at 1.6 GPa, all measurements correspond to ambient conditions. Data extracted from Refs. [31, 49, 65, 66].

Compound	$E_g^{(1)}$	$B_g^{(1)}$	$B_g^{(2)}$	$E_g^{(2)}$	$A_g^{(1)}$	$E_g^{(3)}$	$A_g^{(2)}$	$B_g^{(3)}$	$B_g^{(4)}$	$E_g^{(4)}$	$E_g^{(5)}$	$B_g^{(5)}$	$A_g^{(3)}$
$\mathrm{YVO_4}$	–	148	165	199	242	317	347	368	413	434	747	812	828
$\mathrm{SmVO_4}$	116	149	198	206	251	334	366	382	435	450	770	820	855
$\mathrm{GdVO_4}$	115	140	178	189	236	309	348	374	401	428	744	808	833
$\mathrm{TbVO_4}$	107	132	175	190	236	309	346	368	408	431	745	803	831

The main similarity between the Raman spectra of both structure is that they are divided into two frequency regions separated from each other by a large gap, which typically ranges from 450 to 750 $\mathrm{cm^{-1}}$ in $R\mathrm{VO_4}$ compounds. The modes within the high frequency region ($\omega > 700$ $\mathrm{cm^{-1}}$)

can be considered as internal vibrations of the VO_4 tetrahedra in good approximation. This means that in this kind of vibration, only the oxygen atoms can move, whereas the R and V atoms are nearly at rest. On the other hand, although the modes in the lower frequency region ($\omega < 500$ cm^{-1}) cannot be strictly classified in terms of the tetrahedral vibration.

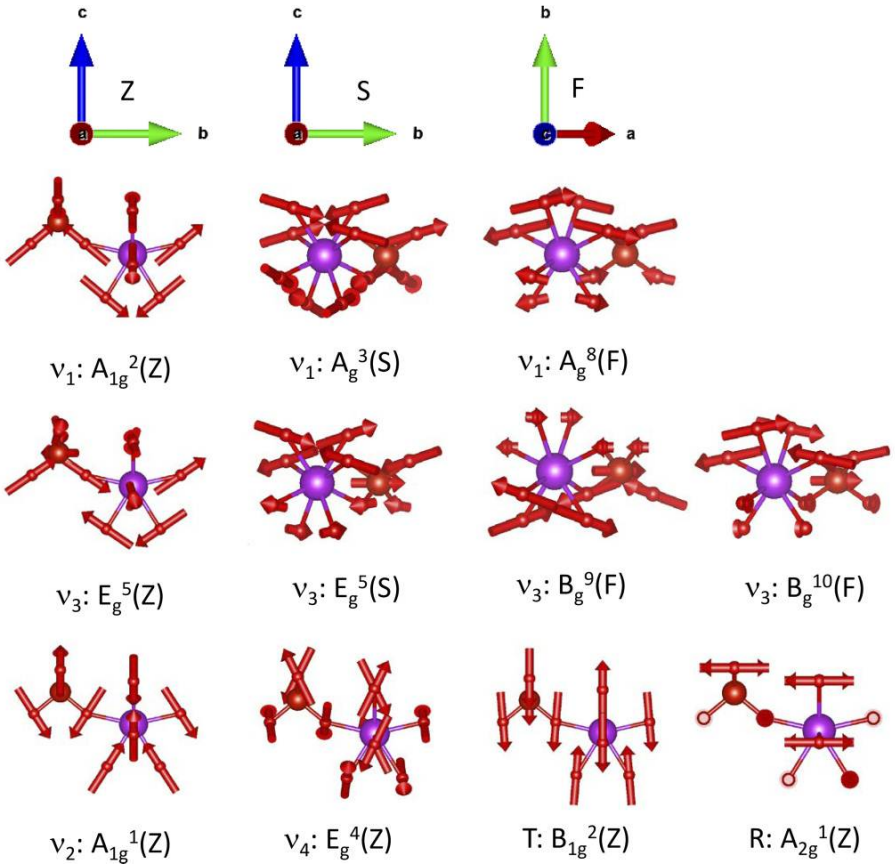

Figure 1.5: Selected vibration patterns at Γ for the zircon (Z), scheelite (S) and fergusonite (F) phases. Bi, V and O atoms are represented by large, medium and small spheres. Only first neighbours are represented. The direction and magnitude of the vibration are represented by red vectors. The ν, T and R labels indicate wether the mode is internal, translational or rotational, respectively. Extracted from Pellicer-Porres *et al.* [67] with permission of the authors.

In both structures, the mode located at the highest frequency, which also gives rise to the most intense Raman peak, corresponds to a symmetric stretching mode of the VO_4 tetrahedra (labeled as ν_1). In particular, this is the $A_{1g}^{(2)}$ mode in the zircon and the $A_g^{(3)}$ mode in the scheelite structure (see Tables 1.8 and 1.9). These modes have the highest frequency of all due to the fact

that they involve a more effective change in the V–O bond length, which also represents the strongest bond in the structure. In addition to this, these vibration modes mainly affect oxygen atoms, which are very light. However, the frequency of this mode decreases from the zircon to the scheelite structure. In some compounds, like $BiVO_4$, this occurs as a consequence of the change in the contribution of the R–O bonds [67]. Besides, the expansion of the VO_4 tetrahedra at the transition (increase in the V–O length) also favours the frequency decrease [37]. When the scheelite structure gets distorted and transforms into the fergusonite phase, the most energetic Raman mode corresponds to the $A_g^{(8)}$ vibration. In this case, the R and the V atoms can move, but the amplitude of their displacements is smaller than that of the oxygen atoms by an order of magnitude. The symmetries of these modes in the zircon, scheelite and fergusonite phases are displayed in Fig. 1.5

Regarding the second highest Raman modes, these are the $B_{1g}^{(4)}$ mode in the zircon and the $B_g^{(5)}$ mode in the scheelite phase, which both represent asymmetric stretching modes. In this case, the former shows a greater frequency thanks to the contribution of the V atoms to the stretching. Finally, the third highest Raman mode of both zircon and scheelite phases correspond to the $E_g^{(5)}$ degenerate mode (Fig. 1.5). This degeneracy is broken after the scheelite-to-fergusonite phase transition, in which the phonon splits into the $B_g^{(9)}$ and $B_g^{(10)}$ modes. The vibration pattern of these modes is also depicted in Fig. 1.5. With respect to the modes in the lower frequency region, some of these display some particular vibration patterns, which can be described as blend of bending (ν_3, scissorν_4), translational (T), or rotational modes (R). Fig. 1.5 shows the vibrational pattern of some of these modes for the zircon structure. In addition to this, the modes with the lowest frequencies involve considerable atomic displacements of the rare-earth cation that cannot be neglected. For instance, the R atoms move along the c-axis direction in the $B_{1g}^{(1)}$ and $B_g^{(1)}$ modes of the zircon and scheelite phases, respectively. These can also vibrate in the perpendicular directions, as in the $E_g^{(1)}$ mode. A more detailed explanation of these vibration patterns can be found in Pellicer-Porres *et al.* [67] for the case of $BiVO_4$.

1.3.3 Electronic band structure

Table 1.10: Experimental and calculated values of the bandgap energy for several zircon-type orthovanadates near ambient conditions (units in eV).

Compound	Experimental	Theory	Bandgap type	Reference
YVO_4	3.78	2.79	Direct	[48]
	–	2.98	Indirect	[68]
$LuVO_4$	3.76	2.86	Direct	[48]
	–	2.95	Indirect	[69]
$NdVO_4$	3.72	2.86	Direct	[48]
	–	3.02	Indirect	[70]
$GdVO_4$	3.82	–	Direct	[49]
	–	2.98	Direct	[71]
	–	2.77	Direct	[72]

According to calculations [48, 72], in zircon-type rare-earth orthovanadates like YVO_4, $NdVO_4$, $GdVO_4$ and $LuVO_4$, the maximum of the valence band and the minimum of the conduction band are both located in the Γ point, which means that these are all direct-gap crystal structures. Table 1.10 shows the experimental and calculated bandgaps for these compounds reported in literature. The theoretical values reported in the Materials Project website [73, 74] are also included for the sake of comparison. Fig. 1.6 (a) shows the calculated electronic band structure for zircon-type $LuVO_4$, which shows that the dispersion of the valence bands is rather small in general. In the same picture, we show the associated density of states and the corresponding contribution of each atom. The lower part of the valence band is mainly composed of V3d–O2p bonding states, whereas the the upper part of the valence band basically consists in O2p states. The main contribution of the rare-earth atom is strongly localized in the half of the valence band. With respect to

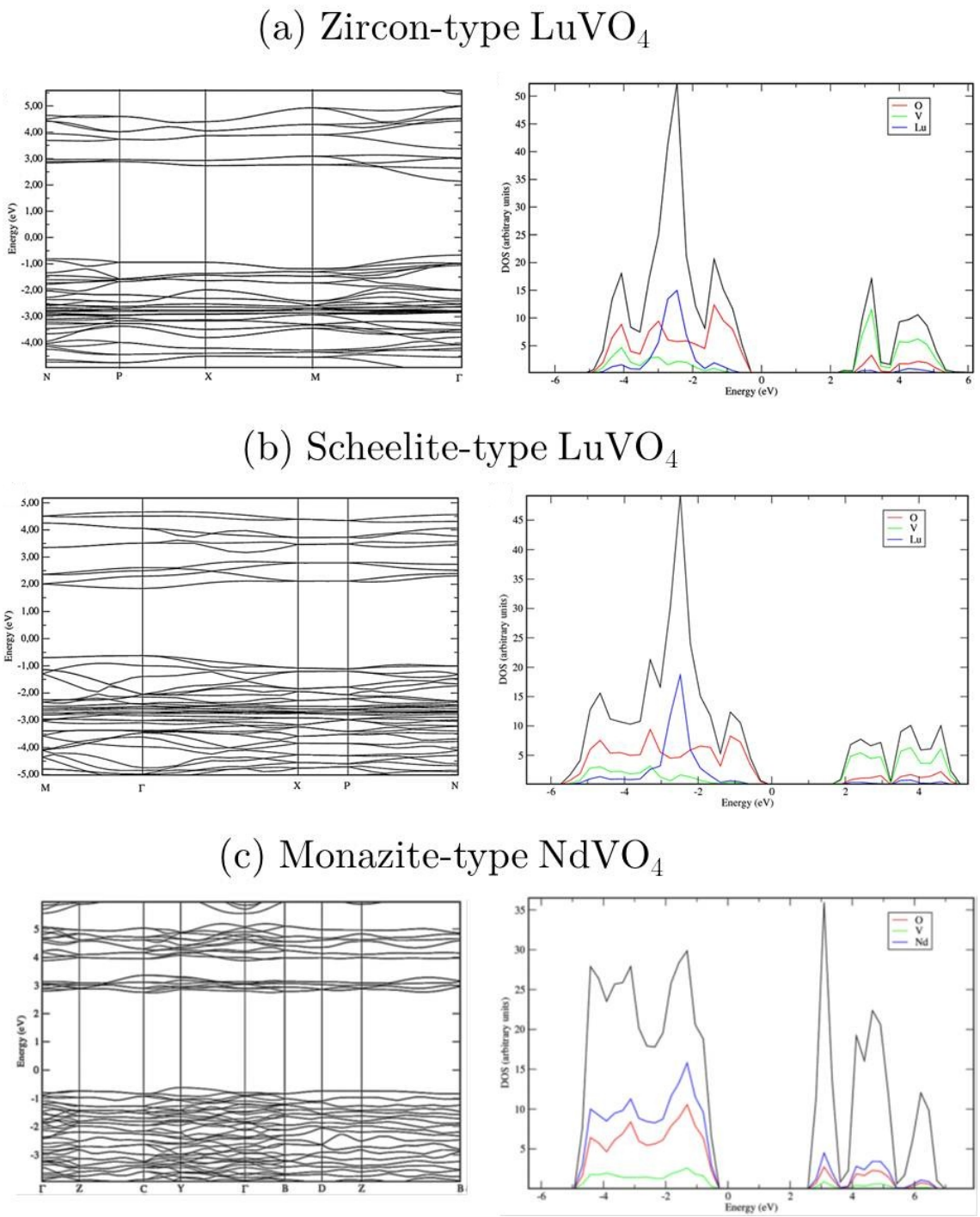

Figure 1.6: Calculated electronic band structure (*left*) and density of states (*right*) of the zircon (a) and scheelite (b) phases of $LuVO_4$ and the monazite (c) phase of $NdVO_4$ (ambient pressure). Extracted from Panchal *et al.* [48] with permission of the authors.

the conduction band, this is mostly composed of antibonding V3d–O2p states. Thus, the changes in the bandgap size induced by pressure are mainly a consequence of the contraction of the VO_4 tetrahedra. In some compounds like $LuVO_4$ and $NdVO_4$, there is also a small contribution to the conduction band from the 6s electrons of the rare-earth cation. This leads to a $\sim$ 0.2 eV decrease in the bandgap with respect to other vanadates like YVO_4, in which these states do not exist [48]. Experimental measurements of the bandgap energy yield results which are substantially larger than the predicted value. In particular, DFT calculations tend to underestimate the value of the bandgap by 1 eV approximately. For instance, whereas the predicted value for $LuVO_4$ is E_{gap} = 2.86 eV [48], experimental measurements yield a value of E_{gap} = 3.87 eV [75].

Regarding the scheelite phase, the calculated electronic band structure and the corresponding density of states are depicted in Fig. 1.6 (b). Broadly speaking, this phase shares many similarities with the zircon phase. As in the zircon structure, in the scheelite phase there is a direct bandgap in which the maximum of the valence band and the minimum of the conduction band are both located at the Γ point. The predicted value of the bandgap energy is E_{gap} = 2.31 eV. Thus, there is a 0.5 eV bandgap collapse from the zircon to the scheelite structure. This sudden decrease in the bandgap size has been experimentally reported to occur at the zircon-to-scheelite phase transition, which takes place upon compression [48, 49]. Similarly to the zircon phase, the states near the Fermi level are mainly composed of V3d and O2p states. This can be observed in Fig. 1.6 (b), where the partial contributions to the DOS are depicted.

Several scenarios have been proposed in order to explain the bandgap collapse at the zircon-to-scheelite transformation. For instance, it has been suggested that the reduction of the site symmetry of the R cation (from D_{2d} in the zircon to S_4 in the scheelite phase) leads to a smaller electronic localization in the scheelite phase, which is correlated with the huge drop in the size of the bandgap. Moreover, the expansion of the VO_4 tetrahedra at the transition also contributes to the bandgap reduction. In particular, the increase of the V–O bonds ($\sim$ 6%) reduces the Coulomb attraction of the O2p orbitals to the V^{+3} ions, which leads to a reduction of the splitting of the

O2p and V3d states and consequently, to the reduction of the bandgap energy.

On the other hand, the calculated band structure and DOS of monazite-type $NdVO_4$ is depicted in Fig. 1.6 (c). In contrast to the previous described structures, this is an indirect bandgap semiconductor, in which the maximum of the valence band and the minimum of the conduction band are located at the Z and Y points of the Brillouin zone, respectively. Furthermore, in this phase the 4f electrons of Nd become partially delocalized. As a consequence, there is a relevant contribution of these orbitals in the region close to the Fermi level, as it can be seen in Fig. 1.6 (c), which is even superior to that of the V3d and O2p orbitals. Besides this, there is some hybridization of these orbitals, which reveals the covalent character of the chemical bonds.

1.4 Technological applications

With respect to technological applications, rare-earth orthovanadates and orthophosphates can be used as nuclear waste storage materials [76]. The reason for this is that some part of the nuclear fission products is constituted by actinide elements, which are chemically similar to lanthanides. Thus, the study of the structural and mechanical properties of these elements constitute an underpinning part in their use as the solid-state warehouse of radioactive waste.

On the other hand, doped rare-earth orthovanadates are widely used as solid-state lasers. A well-known subset of these are neodymium-doped vanadate lasers, which use zircon-type Nd:YVO_4 (λ = 1064 nm), Nd:$GdVO_4$ (λ = 1063 nm) or Nd:$LuVO_4$ (λ = 1089 nm). These structures provide an efficient energy transfer from the VO_4^{3-} levels (bandgap transitions) to the excited electronic states of the doping element, which subsequently produces the emission of NIR radiation. This also makes doped RVO_4 compounds useful as phosphors [77] and scintillators [11]. Since the light emission properties of these materials depend on the local environment of the doping rare-earth cation, different crystalline structures can substantially alter these properties [78]. In this regard, some phases like scheelite and monazite can be recovered at ambient conditions in a

metastable state after submitting zircon-type RVO$_4$ compounds at high pressure conditions. This means that high pressure studies may have an important role in the development of new lasers or other different technological applications in photonics [79].

In addition to this, high pressure studies have shown that there is a bandgap collapse in the zircon-to-scheelite, zircon-to-monazite and monazite-to-postmonazite phase transitions [48, 49], in which the value of E_{gap} shifts from the UV to the visible. Since these high pressure phases can be quenched to room conditions, this allows to synthesize RVO$_4$ compounds with lower values of E_{gap}, making them suitable in green technologies like sunlight assisted photocatalysis. The fact that the bandgap enery of these phases is in the 2 - 3 eV range makes them excellent candidates for pollutant decomposition and water purification [80]. Moreover, orthovanadates can be also synthesized as nanoparticles, which is known to increase the catalysis efficiency [81]. Besides this, research has shown that doped orthovanadate nanparticles are also useful for biomedical purposes, thanks to their low chemical reactivity and their tuneable luminescence properties. For instance, Dy:GdVO$_4$ nanoparticles can be used as anti-cancer drug carriers [82].

2 | Theoretical background

In this chapter we provide a basic scope on the main theoretical concepts necessary to understand our research. First of all, we present a very brief summary on the basic thermodynamics of solids in relation with phase transitions and how these are classified into first- and second-order. In the next subsection, we discuss in a little more detail some relevant concepts related to the physical properties of crystals under compression, mainly, the Equation of State (EOS) and the Stiffness tensor. In order to understand the nature of optical absorption experiments, we also included a subsection explaining the light absorption mechanisms in direct and indirect semiconductors. Finally, this chapter ends with a phenomenological explanation of the cooperative Jahn-Teller effect with $TbVO_4$ at low temperatures as an example.

2.1 Thermodynamics of crystals under high pressure

First of all, let us write the differential form of the first law of thermodynamics,

$$dU = \delta Q + \delta W \tag{2.1}$$

In the first law, the variation of the internal energy U depends on the variation of the heat Q that goes into the crystal and the work W done on it. The symbol δ means that these quantities are inexact differentials, that is to say, they depend on the path taken by the thermodynamic process.

At the same time, both quantities can be expressed as

$$\delta Q = TdS \tag{2.2}$$

$$\delta W = -PdV \tag{2.3}$$

where S, T, P and V are the entropy, temperature, pressure and volume of the system respectively. Hence, the differential form of the internal energy can take the form

$$dU = TdS - PdV \tag{2.4}$$

Thus, the internal energy of a crystal is a function of S and V i.e. $U = U(S, V)$. Experiments at constant entropy and volume are difficult to carry on. Therefore, it is useful to define other thermodynamic potentials for different combinations of independent natural variables, such as

$$H(S, P) = U + PV \tag{2.5}$$

$$F(T, V) = U - TS \tag{2.6}$$

$$G(P, T) = U + PV - TS = H - TS = F + PV \tag{2.7}$$

where H, F and G are the enthalpy, the Helmholtz potential and the Gibbs free energy respectively. By combining these definitions with the fundamental equation 2.4 it is possible to express such thermodynamic potentials in their differential form, i.e.

$$dH = TdS + VdP \tag{2.8}$$

$$dF = -SdT - PdV \tag{2.9}$$

$$dG = -SdT + VdP \tag{2.10}$$

The necessary requirement for any material to be in its equilibrium state is that the free energy must be in its minimum. As a consequence, materials can be found in different phases depending on the particular empirical conditions under which such materials are submitted. Considering crystalline solids, it is possible to find different crystalline structures, i.e., different phases at different P and T conditions, as it is shown in Fig. 2.1, where we show a basic example of a phase diagram.

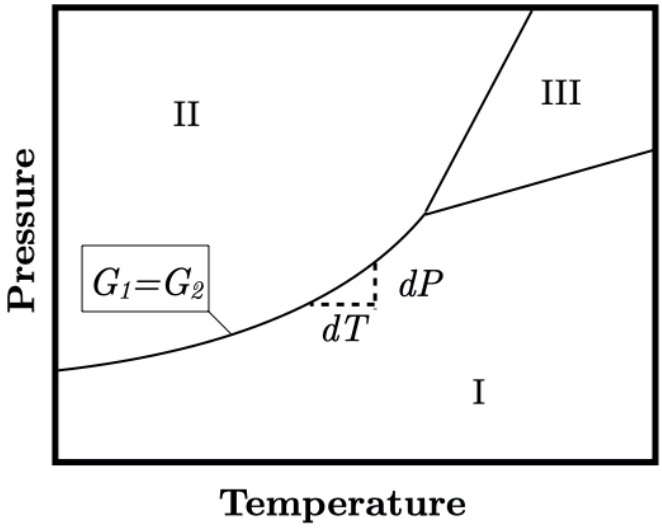

Figure 2.1: Schematic example of a P-T phase diagram with three different phases.

The Gibbs free energy is a continuous function of these external variables, which means that two phases of the same compound have the same free energy at the phase transition, as shown in Fig. 2.2(a). In other words, if we consider a crystal under a certain transition pressure P_t under isothermal conditions, we can write that

$$G_1(P = P_t) = G_2(P = P_t) \Rightarrow F_1 + P_t V_1 = F_2 + P_t V_2. \tag{2.11}$$

Thus, the transition pressure can be expressed as

$$P_t = -\frac{F_2 - F_1}{V_2 - V_1} = -\frac{\Delta F}{\Delta V} = -\left.\frac{\partial F_1}{\partial V_1}\right|_{V_1} = -\left.\frac{\partial F_2}{\partial V_2}\right|_{V_2} \tag{2.12}$$

Hence, according to Eqn. 2.12, the value of P_t can also be calculated as the slope of the common tangent line of the $F_1(V)$ and $F_2(V)$ functions. The thermal contribution to the Gibbs energy is usually neglected in energy calculations. However, this is sometimes reasonable, since entropic effects at room temperature only account for less than 10% of the value of P_t in most cases, as we will show later on.

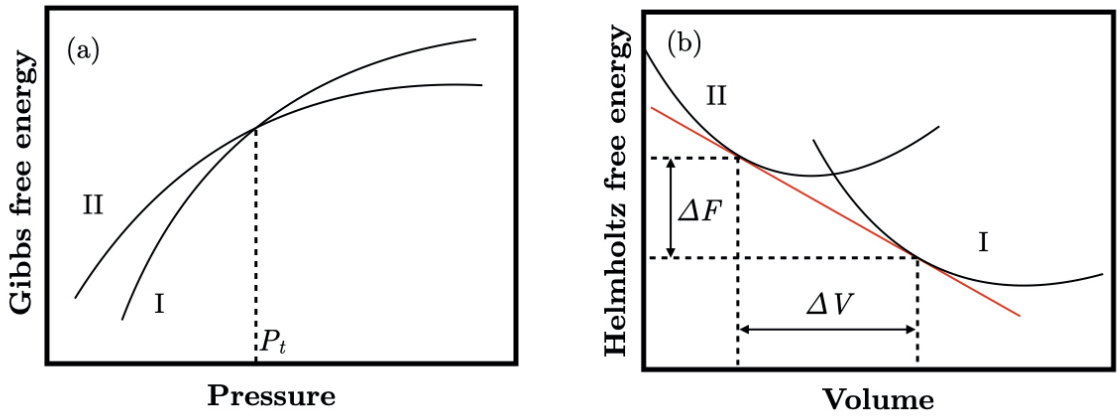

Figure 2.2: Schematic examples of (a) free energy-pressure and (c) energy-volume curves.

A schematic example of this is shown in Fig. 2.2(b). Let us focus on the P-T phase diagram shown in Fig. 2.1. The Gibbs free energy of both phases is the same for all the point over the phase line i.e. $G_1 = G_2$. The slope of such line can be calculated in the following manner

$$dG_{1,2} = -S_{1,2}dT + V_{1,2}dP \Rightarrow \frac{dP}{dT} = \frac{S_1 - S_2}{V_1 - V_2} = \frac{\Delta S}{\Delta V} \tag{2.13}$$

where we applied $dG_1 = dG_2$. This equation is the widely known **Clausius-Clapeyron** relation, where the slope of the line dividing two phase domains is related with the changes in entropy

and volume during the transition. This equation allows us to indirectly estimate the change in entropy, since the slope of the phase line and the change in volume can be measured experimentally.

2.2 Classification of phase transitions in solids

The concept of phase can be defined as a thermodynamic system of a homogeneous chemical composition and physical structure, which can be mechanically separated from a non-homogeneous mixture [83]. The process of transformation between two systems of this kind, from one to another, is commonly known as phase transition. These are identified by a change in the order parameter of the system, which can be the magnetization, volume, resistivity, etc. If there is a discontinuity in the order parameter the transitions is considered **first-order** whereas if the change is continuous, the transition is **second-order**. The most well-known phase transitions are solid-liquid or liquid-gas transitions. However, this dissertation is focused in the solid-solid phase transitions, in which crystalline solids change their structural configuration under high pressure and high or low temperatures. Table 2.1 shows the classification of phase transitions considering the S and V as order parameters and T and P as external variables. Third order phase transitions, in which the discontinuity is found in the second derivatives, are also possible. However, these are far from the scope of this dissertation and won't be discussed.

Table 2.1: Classification of phase transitions.

Order	Discontinuity	
First	S	V
Second	$(\partial S/\partial T)_P$	$(\partial V/\partial T)_P$
	$(\partial S/\partial P)_T$	$(\partial V/\partial P)_T$

2.2.1 Landau Theory of phase transitions

In this subsection we present a qualitative description of first- and second-order transitions according to Landau theory of phase transitions. The approach given by most textbooks only considers phase transitions as a consequence of temperature changes, and therefore choose the Helmholtz free energy as the suitable thermodynamic potential. However, since we are concerned about changes with both pressure and temperature, the following explanations are based in those presented in Umantsev, A. [84], in which the Landau-Gibbs potential is used instead.

The Landau-Gibbs free energy function $G(P, T, \eta)$ used to describe the phase transition between two phases (from α to β for instance) must fulfill the following conditions: it must have at least two different minima (global and local), separated by a maximum, which is the free-energy barrier between both states. A four-order polynomial function posseses these two properties. Thus, it is useful to expand the free-energy potential as a function of the order parameter η near the α phase with $\overline{\eta}_0 = 0$ as

$$G(P, T, \eta) = G_0(P, T) + \frac{1}{2}A(P, T)\eta^2 - \frac{2}{3}B(P, T)\eta^3 + \frac{1}{4}\eta^4 \tag{2.14}$$

where $G_0(P, T)$ is the free-energy of the α phase and $A(P, T)$ and $B(P, T)$ are smooth functions of P and T. The equilibrium states of the Landau-Gibbs function can be easily found considering that

$$\left(\frac{\partial G}{\partial \eta}\right)_{A,B} = \overline{\eta}(A - 2B\overline{\eta} + \overline{\eta}^2) = 0 \tag{2.15}$$

Besides the trivial solution $\overline{\eta}_0 = 0$, there are two more roots

$$\overline{\eta}_{\pm} = B \pm \sqrt{B^2 - A} \tag{2.16}$$

Equilibrium states will only exist if $\overline{\eta}_{\pm}$ is real. Thus, the conditions $A \leq B^2$ must be always

fulfilled. On the other hand, equilibrium states may be stable or unstable. The stability condition can be expressed as

$$\left(\frac{\partial^2 G}{\partial \eta^2}\right)_{A,B} = A - 4B\overline{\eta} + 3\overline{\eta}^2 > 0 \tag{2.17}$$

According to this equation, the state $\overline{\eta}_0$ will be stable (unstable) only if $A > 0$ ($A < 0$). In other words, the stability region of the state $\overline{\eta}_0$ is delimited by the condition $A = 0$.

With regard to the possible values of B, considering $B > 0$, the state $\overline{\eta}_0$ will always be stable (if it exist, that is to say, if $A < B^2$) whereas $\overline{\eta}_-$ is unstable for $0 < A < B^2$ and stable for $A < 0$. The situation is just the opposite for $B < 0$.

We have discussed the stability conditions of the different equilibrium states $\overline{\eta}$. Now, our purpose is to determine which equilibrium state is dominant or *globally stable* to speak properly. Therefore, we need to calculated the free-energy at the $\overline{\eta}_0$ and $\overline{\eta}_\pm$ states. Depending on the values of B and A there are different cases, which can be useful to understand the difference between first- and second-order phase transitions.

For $B = 0$, which is known as the Landau condition, there is only one solution for $\overline{\eta}_0$ and $A > 0$ and three roots $\overline{\eta}_0 = 0$, $\overline{\eta}_\pm = \pm\sqrt{-A}$ for $A < 0$. In the former case, there is only one minimum at $\overline{\eta}_0 = 0$ whereas in the latter case, there is a maximum at this point and two minima at $\overline{\eta}_\pm$, as it can be seen in Fig. 2.3 (a). This diagram is particularly useful to explain second-order phase transitions. If the transition is due to a pressure increase the sign of A should be the opposite of $P - P_t$, where P_t is the transition pressure. In other words, if $A > 0$ then $P - P_t < 0$. This is a progressive transition, since it excludes the possibility of simultaneous stable states for the α and β phases. Nonetheless, it allows two different stable configurations in the β phase i.e. $\overline{\eta}_\pm$. It can explain how, for instance, some unit-cells can become distorted along two equivalent directions. An example of this would be the scheelite-fergusonite phase transition reported in some RVO_4 compounds.

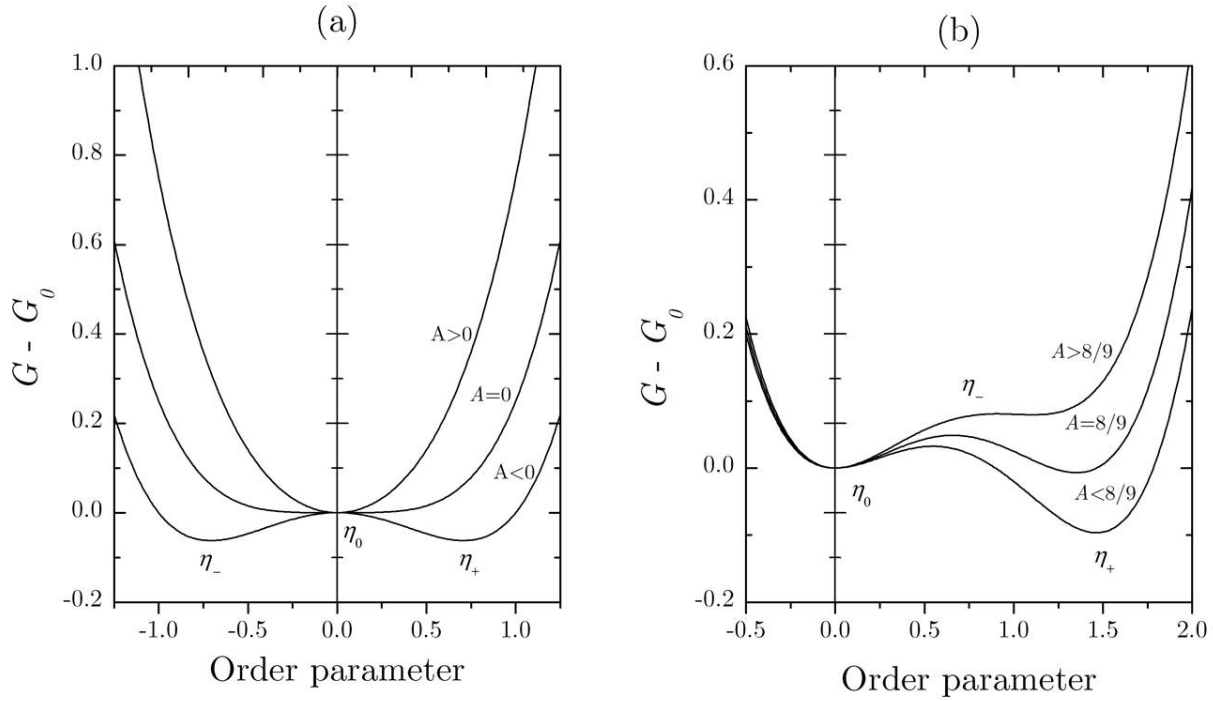

Figure 2.3: Landau potential versus order parameter for (a) $B = 0$ (second-order phase transition) and (b) $B = 1$ (first-order phase transition) [84]

On the other hand, if $B > 0$ a different scenario appears, as it can be observed in Fig. 2.3 (b). In this case, there is a coexistence of the equilibrium states $\overline{\eta}_0$ and $\overline{\eta}_\pm$. Similarly to the previous case, there is only one state $\overline{\eta}_0$ for $A > B^2$ and three states i.e. $\overline{\eta}_0$ and $\overline{\eta}_\pm$ for $A < 0$. As the function A takes different values, there is an exchange between the two absolute minima $\overline{\eta}_0$ and $\overline{\eta}_+$, where $\overline{\eta}_-$ is a maximum between both and constitutes a free-energy barrier. It can be demonstrated that the point where both mimimums are equally stable is defined by the condition $A = 8/9$ when $B = 1$ [84]. Considering high pressure experiments, this situation would correspond to $P = P_t$. This means that the order parameter at the stable state can have two different values i.e. $\overline{\eta}_0$ and $\overline{\eta}_+$. This introduces a discontinuity in $\overline{\eta}$. Therefore, this situation would be characteristic of first-order phase transitions. For larger (smaller) values of A, the dominating minimum will be located at $\overline{\eta}_0$ ($\overline{\eta}_+$). In these scenarios, both minima are locally stable. This means that the non-dominating minimum constitutes a *metastable state* of the system. Experimentally this would be observed as

a coexistence of both phases α and β, with the former disappearing as pressure increases. A good example of this would be the zircon-to-monazite and zircon-to-scheelite phase transitions studied in this dissertation. The situation for $B < 0$ is the same but with $\overline{\eta}_-$ replacing $\overline{\eta}_+$.

2.3 Finite strains

Let us consider a crystal in which two different elements of mass separated by an infinitesimal distance ds^0 are located in the points A of coordinates x_i^0 and B of coordinates $x_i^0 + dx_i^0$. The superscript "0" means that we are dealing with original positions. Thus have that

$$(ds^0)^2 = \sum_i (dx_i^0)^2 \tag{2.18}$$

Imagine that such points are displaced to A' and B' according to a displacement vector $\mathbf{u}$ that is a function of the coordinates of the points. In other words, let us assume that $A(x_i^0) \longrightarrow A'(x_i^0 + u_i)$ and $B(x_i^0 + dx_i^0) \longrightarrow B'(x_i^0 + dx_i^0 + u_i + du_i)$. The distance between A' and B' is ds, which is different from ds^0. Therfore we say that the crystal has experimented strain.

The analysis of finite strains can follow two different schemes. In the Eulerian scheme the reference is defined by the post-compression state, whereas in the Lagrangian scheme the pre-compression is used. In other words, in the former scheme the initial coordinates x_i^0 of a point are expressed as a function of the final coordinates x_i whereas the opposite happens in the latter [85, 86]. More specifically,in the Eulerian scheme:

$$x_i^0 = x_i - u_i \tag{2.19}$$

whereas in the Lagrangian scheme,

$$x_i = x_i^0 + u_i \tag{2.20}$$

Although both are equivalent for infinitesimal strains, they are not for finite strains, since

changes are expanded in square length before and after compression. The Eulerian scheme is more commonly used, since the quantities are expressed in the coordinates of the points of the strained solid, which are experimentally accessible. In fact, most developments on the $P - V$ Equation of State (EOS) of crystals are based on the Eulerian scheme. On the other hand, the Lagrangian scheme is useful in the cases in which we are dealing with structures in its original configuration, such as in the analysis of the stiffness tensor.

2.3.1 Eulerian strain

Considering the Eulerian scheme ($x_i^0 = x_i - u_i$), the difference between the squared distances ds and ds^0 can be expressed as

$$(ds)^2 - (ds^0)^2 = \sum_i (dx_i)^2 - \sum_i (dx_i^0)^2 = 2\sum_i dx_i du_i - \sum_i (du_i)^2 \tag{2.21}$$

The displacements u_i are continous and differentiable functions of the coordinates, hence

$$du_i = \sum_j \frac{\partial u_i}{\partial x_j} dx_j = \sum_j u_{ij} dx_j \tag{2.22}$$

where we defined $u_{ij} = \partial u_i / \partial x_j$. Now we can rewrite Eqn. 2.21 as

$$(ds)^2 - (ds^0)^2 = 2\sum_{ij} \varepsilon_{ij} dx_i dx_j \tag{2.23}$$

with ε_{ij} being the elements of the **Eulerian strain**, defined as

$$\varepsilon_{ij} = \frac{1}{2}\left(u_{ij} + u_{ji} - \sum_k u_{ki} u_{kj}\right) \tag{2.24}$$

The Eulerian strain can also be written in the following manner,

$$\varepsilon_{ij} = \frac{1}{2}\left(\delta_{ij} - \sum_k \frac{\partial x_k^0}{\partial x_i}\frac{\partial x_k^0}{\partial x_j}\right) \tag{2.25}$$

where δ_{ij} is the Kronecker delta. Now, let us consider the case of isotropic strain induced by hydrostatic pressure. In such conditions,

$$u_{ii} = \frac{\phi}{3} \tag{2.26}$$

with $\phi = \sum_i u_{ii} = \Delta V/V_0$ being the trace of the matrix. Combining Eqns. 2.26 and 2.24 we can express the Eulerian strain as

$$\varepsilon_{ij} = \left(\frac{\phi}{3} - \frac{1}{2}\frac{\phi^2}{9}\right)\delta_{ij} = \varepsilon\delta_{ij} \tag{2.27}$$

The volumes of an elementary cube in the stressed and in the original state are

$$V = (dx_1)^3 \tag{2.28}$$

$$V_0 = [dx_1\,(1 - u_{11})]^3 \tag{2.29}$$

respectively. Hence, the ratio between these magnitudes takes the form

$$\begin{aligned}\frac{V}{V_0} = (1-u_{11})^3 = \left(1-\frac{\phi}{3}\right)^3 = \left[\left(1-\frac{\phi}{3}\right)^2\right]^{3/2} \\ = \left(1 - \frac{2\phi}{3} - \frac{\phi^2}{9}\right)^{3/2} = (1-2\varepsilon)^{3/2}\end{aligned} \tag{2.30}$$

Since ε is negative for positive pressures, we use $f = -\varepsilon$ instead in order describe finite strains under compression. Therefore, the previous equation can be rewritten as

$$\frac{V}{V_0} = (1+2f)^{3/2} \tag{2.31}$$

2.3.2 Lagrangian strain

Now, let us consider the Lagrangian scheme ($x_i = x_i^0 + u_i$), in which the strain is expressed as a function of the original coordinates. Thus, the difference between the squared distances is

$$(ds)^2 - (ds^0)^2 = \sum_i (dx_i)^2 - \sum_i (dx_i^0)^2 = 2\sum_i dx_i^0 du_i + \sum_i (du_i)^2 \tag{2.32}$$

As we previously stated, the displacement vector is a continuous and differenciable variable of the coordinates. Therefore we can write

$$du_i = \sum_j \frac{\partial u_i}{\partial x_j^0} dx_j^0 = \sum_j u_{ij}^0 dx_j^0 \tag{2.33}$$

where we defined $u_{ij}^0 = \partial u_i / \partial x_j^0$. Whith this, we can rewrite Eqn. 2.32 in the following manner:

$$(ds)^2 - (ds^0)^2 = 2\sum_{ij} \eta_{ij} dx_i^0 dx_j^0 \tag{2.34}$$

where η_{ij} are the elements of the **Lagrangian strain**, which are defined as

$$\eta_{ij} = \frac{1}{2}\left(u_{ij}^0 + u_{ji}^0 + \sum_k u_{ki}^0 u_{kj}^0 \right) \tag{2.35}$$

Note that the Lagrangian strain is a symmetric tensor by definition. On the other hand, the Lagrangian strain can also be expressed as

$$\eta_{ij} = \frac{1}{2}\left(\sum_k \frac{\partial x_k}{\partial x_i^0} \frac{\partial x_k}{\partial x_j^0} - \delta_{ij} \right) \tag{2.36}$$

Once we have arrived at this point, the differences and similarities between the Eulerian and Lagrangian strains are quite evident. In this case, we will not deal with the particular case of isotropic compression in the same way that we did in the case of the Eulerian strain, since it has

no special relevance in our study. These developments can be found in Ref. [86].

2.4 Equation of State

In the field of thermodynamics, the set of physical magnitudes that characterize a system is commonly known as state variables (internal energy, pressure, temperature, enthalpy, etc.). On the other hand, the Equation of State (abbreviated as EOS) is defined as the general expression which relates these different state variables at equilibrium. The most well-known example is $PV = nRT$, which relates the pressure, volume, temperature and number of moles of an ideal gas. In solids, the relationship between pressure and volume is generally described using the isothermal bulk modulus,

$$B = -V\left(\frac{\partial P}{\partial V}\right)_T \tag{2.37}$$

A simple equation of state, proposed by Murnaghan [87], can be obtained by assuming a linear dependence of the bulk modulus with pressure $B(P) \approx B_0 + B_0' P$ and integrating Eqn. 2.37,

$$V(P) = V_0\left(1 + \frac{B_0'}{B_0}P\right)^{-\frac{1}{B_0'}}, \tag{2.38}$$

where the subscript "0" refers to any function evaluated at zero pressure. This EOS can be reversed, so that we can express pressure as a function of volume:

$$P(V) = \frac{B_0}{B_0'}\left[\left(\frac{V_0}{V}\right)^{B_0'} - 1\right] \tag{2.39}$$

When hydrostatic pressure, the Helmholtz free energy of the system changes according to:

$$F(V) = F_0 + \frac{B_0 V}{B_0'}\left[\frac{(V_0/V)^{B_0'}}{B_0' - 1} + 1\right] - \frac{B_0 V_0}{B_0' - 1} \tag{2.40}$$

However, the problem of the Murnaghan equations of state is that they can only reproduce the

compression of the crystal for small changes in volume ($V/V_0 > 0.9$). For higher pressures, more accurate equations of state can be derived from the strain-stress relations. The energy of the system can be expanded in terms of the strain f as

$$F(f) = \sum_{k=0}^{n} c_k f^k. \tag{2.41}$$

The Birch-Murnaghan EOS, which is the one used in our analysis, is based on the Eulerian strain. Therfore, we can rewrite Eqn. 2.31 as

$$f = \frac{1}{2}\left[\left(\frac{V_0}{V}\right)^{2/3} - 1\right]. \tag{2.42}$$

Thus, the energy can be expanded as a n-degree polynomial ($n > 1$), where the different c_k coefficients can be found by imposing the following boundary conditions [88]:

$$\lim_{f\to 0}\left\{F; V; P = -\frac{dF}{dV}; B = -V\frac{dP}{dV}; B' = \frac{dB}{dP}; \dots\right\} = \left\{F_0; V_0; 0; B_0; B_0'; \dots\right\}. \tag{2.43}$$

If we limit the expansion to a third degree polynomial, the energy will take the form

$$\begin{aligned} F(f) &= F_0 + \frac{9}{2}B_0V_0[f^2 + (B_0' - 4)f^3] \\ &= F_0 + \frac{9}{16}V_0B_0\frac{(x^{2/3}-1)^2}{x^{7/3}}[x^{1/3}(B_0' - x(B_0' - 6))] \end{aligned} \tag{2.44}$$

with $x = V_0/V$. In this expression, the linear term vanishes, since $c_1 \propto dF/dV|_{f=0} = -P_0 = 0$. Considering that $P = -dF/dV$, pressure can be written as a function of volume in the following manner

$$P(V) = \frac{3B_0}{2}\left[\left(\frac{V_0}{V}\right)^{7/3} - \left(\frac{V_0}{V}\right)^{5/3}\right]\left\{1 + \frac{3}{4}(B_0' - 4)\left[\left(\frac{V_0}{V}\right)^{2/3} - 1\right]\right\}. \tag{2.45}$$

Eqns. 2.44 and 2.45 are the most used Birch-Murnaghan equations of state in the study of solids under high pressures. These are third-order equations of state, which allow us to estimate V_0, B_0

and B_0' of some material under compression. Occasionally, if the $P-V$ curves are sufficiently flat we can assume that the variation of B with pressure is small and therefore consider a second-order BM EOS ($B_0' \approx 4$). Although higher order equations can be used for the data analysis, we will only use second and third order BM EOS, since these can provide sufficently accurate results.

2.5 The Stiffness Tensor

For the purpose of this section, we will follow the theoretical developments exposed in Wallace [89], since these provide a helpful background for high-pressure physics. The crystal is considered as an homogeneous, anisotropic elastic solid hereinafter. Let us consider a general situation in which a crystal is brought from an arbitrary initial configuration ($\mathbf{x^0}$) to a final one ($\mathbf{x}$) by applying stresses. As a consequence, finite strains arise, which distinguish both configurations. In this regard, most textbooks follow a Lagrangian scheme to derive the stiffness tensor of a crystal. Therefore, we will use the Lagrangian strain in our exposition, which we shall invoke again,

$$\eta_{ij} = \frac{1}{2}\left(\sum_k \frac{\partial x_k}{\partial x_i^0}\frac{\partial x_k}{\partial x_j^0} - \delta_{ij}\right) \tag{2.46}$$

In the absence of pyroelectric and piezoelectric effects, strained bodies experiment "near-action" internal forces, which leads to a symmetric stress tensor σ_{ij} [90]. From the combination of the first and second laws of thermodynamics we have that $dU = TdS - \delta W$, so it is necessary to express δW in terms of the stress and strain vectors in order to be able to continue with the thermodynamic analysis. According to Wallace [89], the differential form of the work can be written as

$$\delta W = -V\sum_{ij}\sigma_{ij}d\eta_{ij}. \tag{2.47}$$

Therefore, the differential forms of the internal energy and the Helmholtz free energy ($F = U - TS$)

are

$$dU = TdS + V\sum_{ij}\sigma_{ij}d\eta_{ij}, \tag{2.48}$$

$$dF = -SdT + V\sum_{ij}\sigma_{ij}d\eta_{ij} \tag{2.49}$$

respectively. These functions are dependent on the configuration of the crystal $\mathbf{x}$. However, the final configurations is achievable through the initial configuration $\mathbf{x^0}$ and the Lagrangian strains η_{ij}. Thus it is advisable to write these functions as

$$U(\mathbf{x}, S) = U(\mathbf{x^0}, \eta_{ij}, S); \tag{2.50}$$

$$F(\mathbf{x}, T) = F(\mathbf{x^0}, \eta_{ij}, T). \tag{2.51}$$

From Eqn. 2.48 for dU we have that

$$\sigma_{ij} = V^{-1}\left(\partial U/\partial\eta_{ij}\right)_{S,\eta'}; \tag{2.52}$$

$$T = \left(\partial U/\partial S\right)_{\eta'}. \tag{2.53}$$

Likewise, for dF Eqn. 2.49 leads to

$$\sigma_{ij} = V^{-1}\left(\partial F/\partial\eta_{ij}\right)_{T,\eta'}; \tag{2.54}$$

$$S = -\left(\partial F/\partial T\right)_{\eta'}. \tag{2.55}$$

The subscript η' implies that all other η_{kl} terms remain constant when differenciating with respect to η_{ij} Considering that the state functions depend on the original configuration $\mathbf{x^0}$ and the

rotation-independent strain η_{ij} (Eqn. 2.50 and 2.51), we can expand both U and F in terms of η_{ij}

$$\begin{aligned} U\left(\mathbf{x^0}, \eta_{ij}, S\right) &= U\left(\mathbf{x^0}, S\right) + \sum_{ij}\left(\frac{\partial U}{\partial \eta_{ij}}\right)_{S,\eta'} \eta_{ij} + \frac{1}{2}\sum_{ijkl}\left(\frac{\partial^2 U}{\partial \eta_{ij}\partial \eta_{kl}}\right)_{S,\eta'} \eta_{ij}\eta_{kl} + \dots \\ &= U\left(\mathbf{x^0}, S\right) + V\sum_{ij}\sigma_{ij}\eta_{ij} + \frac{1}{2}V\sum_{ijkl} C^S_{ijkl}\eta_{ij}\eta_{kl} + \dots \end{aligned} \tag{2.56}$$

$$\begin{aligned} F\left(\mathbf{x^0}, \eta_{ij}, T\right) &= F\left(\mathbf{x^0}, T\right) + \sum_{ij}\left(\frac{\partial T}{\partial \eta_{ij}}\right)_{T,\eta'} \eta_{ij} + \frac{1}{2}\sum_{ijkl}\left(\frac{\partial^2 F}{\partial \eta_{ij}\partial \eta_{kl}}\right)_{T,\eta'} \eta_{ij}\eta_{kl} + \dots \\ &= F\left(\mathbf{x^0}, T\right) + V\sum_{ij}\sigma_{ij}\eta_{ij} + \frac{1}{2}V\sum_{ijkl} C^T_{ijkl}\eta_{ij}\eta_{kl} + \dots \end{aligned} \tag{2.57}$$

where we applied Eqn. 2.52 and 2.54 to the first order term of the expansion. The second order term of the expansion has been rewritten by introducing the elastic constant $C^{S,T}_{ijkl}$ for adiabatic and isothermal processes (superscripts S and T respectively). More explicitly,

$$C^S_{ijkl} = V^{-1}\left(\partial^2 U/\partial \eta_{ij}\partial \eta_{kl}\right)_{S,\eta'}, \tag{2.58}$$

$$C^T_{ijkl} = V^{-1}\left(\partial^2 F/\partial \eta_{ij}\partial \eta_{kl}\right)_{T,\eta'}. \tag{2.59}$$

The matrix $[C_{ijkl}]$ is commonly known as the **stiffness tensor**. Since the strains η_{ij} are symmetric, the stiffness tensor has Voigt symmetry. In other words, its elements C_{ijkl} are invariant under the interchanges $i \leftrightarrow j$, $k \leftrightarrow l$ and $ij \leftrightarrow kl$. Thus, the use of the Voigt notation is sometimes much more convenient. In such notation, each pair of ij indices is replaced by a single index α,

ij	11	22	33	32, 23	31, 13	21, 12
α	1	2	3	4	5	6

Without entering into the details of the demonstration [89], the variation of stress with

isothermal strains can be written as

$$\begin{aligned}\sigma_{ij}\left(\mathbf{x},T\right) &= \sigma_{ij}\left(\mathbf{x^0},T\right) + \sum_{kl}\left[-\sigma_{ij}\left(\mathbf{x^0},T\right)\delta_{kl} + \sigma_{il}\left(\mathbf{x^0},T\right)\delta_{jk} + \sigma_{jk}\left(\mathbf{x^0},T\right)\delta_{il} + C^{T}_{ijkl}\right]\eta_{kl} + \dots \\ &= \sigma_{ij}\left(\mathbf{x^0},T\right) + \sum_{kl} B^{T}_{ijkl}\eta_{kl} + \dots\end{aligned} \tag{2.60}$$

which can also be written for adiabatic strains by changing $T \longrightarrow S$. The symmetric form of B_{ijkl} can be obtained by interchanging k and l in the expression in brackets

$$B_{ijkl} = \frac{1}{2}\left(\sigma_{il}\delta_{jk} + \sigma_{jl}\delta_{ik} + \sigma_{ik}\delta_{jl} + \sigma_{jk}\delta_{il} - 2\sigma_{ij}\delta_{kl}\right) + C_{ijkl}, \tag{2.61}$$

where σ_{ij} and C_{ijkl} are evaluated at $\mathbf{x^0}$. The expression is valid for both isothermal and adiabatic strains. Since this work is focused on high-pressure experiments, the particular case that is worth mentioning is the one in which a crystal is being compress under hydrostatic pressure. In such case, the applied stress at x^0 can be written as

$$\sigma_{ij} = -\delta_{ij}P, \tag{2.62}$$

where P is the absolute magnitude of the applied pressure. This leads to

$$B_{ijkl} = -P\left(\delta_{jl}\delta_{ik} + \delta_{il}\delta_{jk} - \delta_{ij}\delta_{kl}\right) + C_{ijkl}. \tag{2.63}$$

This expression will be used hereon in our analysis for obtaining B_{ijkl} from C_{ijkl} after getting it at different pressures from *ab-initio* calulations.

2.5.1 Symmetries

The stiffness tensor can be written as a 6×6 matrix in the Voigt notation ($ij \rightarrow \alpha$ and $kl \rightarrow \beta$). Since $C_{\alpha\beta}$ is a symmetric tensor there is a maximum of 21 independent elastic constants. In addition to this, the tensor must be invariant under the symmetry operations of its particular point group. Moreover, since this is a four-rank tensor, it is also invariant under inversions. Considering all these features, the stiffness tensor can be classified according to Laue groups. As a result, there are 11 different possible matrices (one for each Laue group), which can be found in Nye [91].

Table 2.2: Stiffness matrices for tetragonal structures (Voigt notation).

Tetragonal I	**Tetragonal II**
Point groups: $4mm, \bar{4}2m, 422, 4/mmm$	Point groups: $4, \bar{4}, 4/m$
$\begin{pmatrix} C_{11} & C_{12} & C_{13} & 0 & 0 & 0 \\ C_{12} & C_{11} & C_{13} & 0 & 0 & 0 \\ C_{13} & C_{13} & C_{33} & 0 & 0 & 0 \\ 0 & 0 & 0 & C_{44} & 0 & 0 \\ 0 & 0 & 0 & 0 & C_{44} & 0 \\ 0 & 0 & 0 & 0 & 0 & C_{66} \end{pmatrix}$	$\begin{pmatrix} C_{11} & C_{12} & C_{13} & 0 & 0 & C_{16} \\ C_{12} & C_{11} & C_{13} & 0 & 0 & -C_{16} \\ C_{13} & C_{13} & C_{33} & 0 & 0 & 0 \\ 0 & 0 & 0 & C_{44} & 0 & 0 \\ 0 & 0 & 0 & 0 & C_{44} & 0 \\ C_{16} & -C_{16} & 0 & 0 & 0 & C_{66} \end{pmatrix}$

In this case we only show the matrices corresponding to tetragonal structures in Table 2.2. These matrices are of special interest in our case, since the zircon (S. G.: $I4_1/amd$) and scheelite (S. G.: $I4_1/a$) structures are considered Tetragonal I and II respectively. The matrices in Table 2.2 are also valid for $B_{\alpha\beta}$.

2.5.2 Stability criteria and distortion

Several publications [92, 93] have shown in various ways , that the general stability criteria is given by the condition that the $[B_{\alpha\beta}]$ matrix must be positive definite. In our case, we will proof this necessary condition in a much simplified way. First of all, let us consider Eqn. 2.57. At constant temperature, the free energy must be minimum with respect to arbitrary homogeneous strains

$$d^2F_T > 0. \tag{2.64}$$

Therefore, when no external stress is applied,

$$\sum_{\alpha\beta} C^T_{\alpha\beta}\eta_\alpha\eta_\beta > 0. \tag{2.65}$$

According to a theorem of linear algebra, this quantity can only be positive if $\det\left([C_{\alpha\beta}]\right) > 0$, which is the stability criteria if we consider zero applied stress. In such conditions $C_{\alpha\beta} = B_{\alpha\beta}$, thus $[B_{\alpha\beta}]$ is also positive definite. Now. let us choose a Lagrangian strain proportional to some eigenvector of the matrix $[B_{\alpha\beta}]$ such that $\eta_\alpha = kv^B_\alpha$ with k being a non-zero arbitrary constant. We can rewrite Eqn. 2.60 using Voigt notation as

$$\Delta\sigma_\alpha(\mathbf{x^0} \rightarrow \mathbf{x}) = \sum_\beta B^T_{\alpha\beta}\eta_\beta = \lambda^B k v^B_\alpha. \tag{2.66}$$

If any eigenvalue $\lambda^B = 0$ we will have that $\Delta\sigma_\alpha = 0$ for a non-zero strain. Therefore the system does not require any further stress to become distorted in the direction given by the eigenvector. To put it more clearly, there is an spontaneous deformation of the crystal. According to this line of argumentation, if $[B_{\alpha\beta}]$ must be positive definite when the applied load is zero and the system becomes unstable once its determinant is zero we can state that the general stability criteria is that $\det([B_{\alpha\beta}]) > 0$.

From this condition we can derive the different necessary relations that the elastic constants must fulfill for each symmetry, commonly known as **the Born criteria** [94, 95]. Since we have shown in this section the symmetry of the stiffness tensors of the Tetragonal I and II structures, in table 2.3 we show the corresponding Born stability criteria wich are necessary and sufficient.

Table 2.3: Born stability criteria for tetragonal structures.

Tetragonal I	**Tetragonal II**
Point groups: $4mm, \bar{4}2m, 422, 4/mmm$	Point groups: $4, \bar{4}, 4/m$
$B_{11} > \lvert B_{12}\rvert;$	$B_{11} > \lvert B_{12}\rvert;$
$2B_{13}^2 < B_{33}(B_{11} + B_{12});$	$2B_{13}^2 < B_{33}(B_{11} + B_{12});$
$B_{44} > 0;$	$B_{44} > 0;$
$B_{66} > 0;$	$2B_{16}^2 < B_{66}(B_{11} - B_{12});$

In this case the Born criteria are the same for both structures with the exception of those involving the B_{66} and B_{16} elastic constants.

2.6 Interband absorption

In isolated atoms, the energy-level diagram is composed of a series of states with discrete energies. The electronic transitions between these levels involve the emission or absorption of photons. As a consequence, the emission or absorption spectra of these atoms consists in a series of sharp lines. In the case of solids, the picture is more complicated. Some of the properties of individual atoms are conserved, but different physical phenomena appear as a consequence of the formation of bands with their delocalized states [96]. Fig. 2.4 shows a simplified scheme of two separated bands in a solid. In this transition, an electron is promoted from the lower to the upper band by the absorption of a photon with an energy higher than the separation of the bands

($\hbar\omega > E_{gap}$). In order for this to happen, the final state in the upper band must be empty, according to Pauli's exclusion principle. The perfect example for this are semiconductors or insulators. Roughly speaking, in an a semiconductor, an electron can jump from the valence band to the conduction band by absorbing a photon whose energy must be higher than the bandgap.

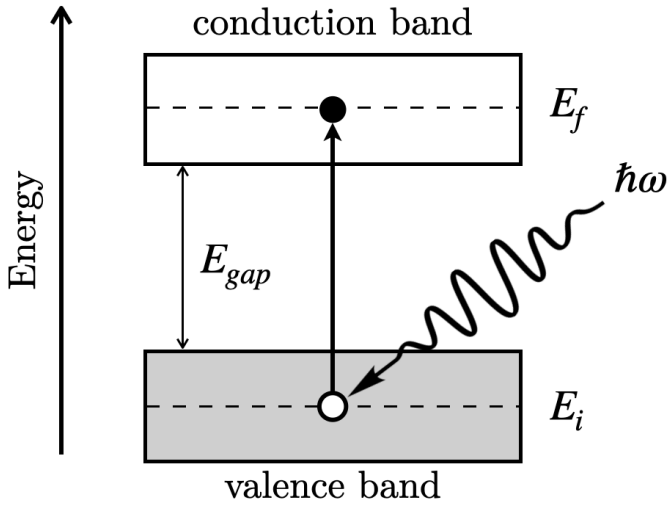

Figure 2.4: Interband electronic transition (from an initial energy E_i to a final state E_f) as the result of the absorption of a photon with energy $\hbar\omega$. The energy difference between the two bands is E_{gap}.

2.6.1 Direct transitions

Firstly, let us focus on **direct absorptions**, in which the minimum of the conduction band and the maximum of the valence band are located at the same point of the Brillouin zone. The laws of the conservation of energy and momentum imply that,

$$E_i(\mathbf{k_i}) + \hbar\omega = E_f(\mathbf{k_f}) \tag{2.67}$$

$$\mathbf{k_i} + \mathbf{k}_\gamma = \mathbf{k_f} \tag{2.68}$$

where E_i and $\mathbf{k_i}$ are the energy and momentum of the electron in the initial state ($i \equiv$ initial) and E_f and $\mathbf{k_f}$ those of the final state ($f \equiv$ final). The momentum of the photon is represented as $\mathbf{k}_\gamma$. In semiconductors, the energy of the absorbed photon is $\sim$ 1 eV (similar to the bandgap energy), which corresponds to a momentum of $|\mathbf{k}_\gamma| \sim 10^4$ cm^{-1}. On the other hand, the size of the Brillouin zone is $G = 2\pi/a$, where a is of the order of magnitude of the lattice parameters (10 Å). This leads to $G \sim 10^8$ cm^{-1}, which is much larger than $\mathbf{k}_\gamma$. Thus, it is possible to neglect the momentum of the photon so that $\mathbf{k_i} \approx \mathbf{k_f}$. This means that the transitions take place without any change in the position in the Brillouin zone. In this section we will follow a semiclassical scheme, in which electromagnetic fields are treated classically whereas electrons are described as quantum mechanical wavefunctions.

The absorption coefficient α can be defined as the ratio of the number of absorbed photons R and the flux of incident photons ϕ,

$$\alpha = \frac{R}{\phi} \tag{2.69}$$

Before calculating the value of R, we must describe the Hamiltonian of the electron in the crystal lattice in the presence of an electromagnetic wave,

$$H = \frac{(\mathbf{p} + e\mathbf{A})^2}{2m} + V \tag{2.70}$$

where $\mathbf{p}$ is the momentum operator, A is the vector potential of the electromagnetic wave, e is the charge of the electron and V is the potential of the crystalline lattice. The vector potential of an electromagnetic wave takes the form

$$\mathbf{A} = A_0 e^{-i(\mathbf{k}_\gamma \mathbf{r} - \omega t)} \mathbf{e} + c.c. \tag{2.71}$$

The quadratic term $\mathbf{A}^2$ in the Hamiltonian can be neglected, since we are dealing with the linear properties of the field. Considering the Coulomb's gauge $\nabla \cdot \mathbf{A} = 0$, the Hamiltonian of the system can be rewritten as

$$H = \frac{\mathbf{p}^2}{2m} + V + \frac{e}{m}\mathbf{A}\cdot\mathbf{p} = H_0 + H' \tag{2.72}$$

where $H' = \frac{e}{m}\mathbf{A}\cdot\mathbf{p}$. If we consider an electromagnetic wave with small intensity, this term of the Hamiltonian can be considered as a perturbation and thus it is possible to apply perturbation theory. In our particular case, we are only interested in the term $e^{-i\omega t}$ of the equation, which leads to transitions in which energy is absorbed. According to Fermi's Golden Rule, the transition rate per unit of volume of electrons from the initial i to the final state f is given by

$$R = \frac{2\pi}{\hbar}\iint \left|\langle\psi_f\,|H'|\,\psi_i\rangle\right|^2 \delta(E_f - E_i - \hbar\omega)\frac{2}{(2\pi)^3}d\tau_{k_f}\frac{2}{(2\pi)^3}d\tau_{k_i} \tag{2.73}$$

where $2/(2\pi)^3$ is the density of states in the reciprocal space. ψ_i and ψ_f represent the Bloch wavefunctions associated to the electron in the initial and final states, respectively:

$$\psi_n(\mathbf{r},\mathbf{k}) = u_{n,k_n}(\mathbf{r})e^{i\mathbf{k_n}\cdot\mathbf{r}} \tag{2.74}$$

Thus, we can expand the matrix element within the integral as follows,

$$\begin{aligned}\left\langle\psi_f\left|\frac{A_0 e^{i\mathbf{k}_\gamma\mathbf{r}}\mathbf{e}\cdot\mathbf{p}}{m}\right|\psi_i\right\rangle &= \frac{eA_0\mathbf{e}}{m}\int e^{i(\mathbf{k_i}+\mathbf{k}_\gamma-\mathbf{k_f})\cdot\mathbf{r}}\left(u^*_{f,\mathbf{k_f}}\mathbf{p}u_{i,\mathbf{k_i}} + \hbar\mathbf{k_i}u^*_{f,\mathbf{k_f}}u_{i,\mathbf{k_i}}\right)dV \\ &= \frac{eA_0\mathbf{e}}{m}\sum_j e^{i(\mathbf{k_i}+\mathbf{k}_\gamma-\mathbf{k_f})R_j}\int_{V_{u.c.}} e^{i(\mathbf{k_i}+\mathbf{k}_\gamma-\mathbf{k_f})\cdot\mathbf{r}}\left(u^*_{f,\mathbf{k_f}}\mathbf{p}u_{i,\mathbf{k_i}} + \hbar\mathbf{k_i}u^*_{f,\mathbf{k_f}}u_{i,\mathbf{k_i}}\right)dV\end{aligned} \tag{2.75}$$

with $V_{u.c.}$ being the volume of the unit-cell and R_j the components of a lattice vector. In this expression, the sum term shrinks to zero unless the relationship $\mathbf{k_i} + \mathbf{k}_\gamma = \mathbf{k_f}$ holds. Thus, the conservation of the momentum is a result of the periodicity of the crystal lattice. By expanding $u_{f,\mathbf{k_f}}$ into a Taylor series of the photon momentum $\mathbf{k}_\gamma$ we have that $u_{f,\mathbf{k_f}} = u_{f,\mathbf{k_i}+\mathbf{k}_\gamma} = u_{f,\mathbf{k_i}} + \mathbf{k}_\gamma\nabla_{\mathbf{k_i}}u_{f,\mathbf{k_i}}$. As we previously stated, $\mathbf{k}_\gamma$ is much smaller than $\mathbf{k_i}$ and $\mathbf{k_f}$. Thus, the corresponding

term in the Taylor series can be neglected so that $u_{f,\mathbf{k_f}} = u_{f,\mathbf{k_i}}$. This approach is usually known as the dipole approximation. The Bloch wavefunctions for the valence ($i \longrightarrow v$) and conduction bands ($f \longrightarrow c$) are orthogonal for the same momentum, hence, the transition rate can be expressed as follows,

$$R = \frac{e^2 A_0^2}{2\pi^2 \hbar m} |P_{cv}|^2 \int \delta\left(E_c(k) - E_v(k) - \hbar\omega\right) d\tau_k \tag{2.76}$$

where $|P_{cv}|^2$ is the momentum matrix element. Considering the effective mass approximation, the term within the Dirac delta can be expressed as

$$E_c(\mathbf{k}) - E_v(\mathbf{k}) - \hbar\omega = E_{c,0} + \frac{\hbar^2 k^2}{2m_c^*} - E_{v,0} + \frac{\hbar^2 k^2}{2m_v^*} - \hbar\omega = E_{gap} + \frac{\hbar^2 k^2}{2\mu^*} - \hbar\omega \tag{2.77}$$

where E_{gap} is the bandgap energy and μ^* is the reduced effective mass. Thanks to this approach, the term inside the Dirac delta can be written as a function of the momentum. For $\hbar\omega > E_{gap}$, R can be written as

$$R = \frac{(2\mu^*)^{3/2} e^2 A_0^2}{\pi \hbar^4 m^2} |P_{cv}|^2 \sqrt{\hbar\omega - E_{gap}} \tag{2.78}$$

In orther to calculate the value of the absorption coefficient, it is necessary to previously obtain the photon flux:

$$\phi = \frac{|\langle \mathrm{S} \rangle|}{\hbar\omega} = \frac{n A_0^2}{2\hbar\mu_0} k_0 \tag{2.79}$$

where $\mathbf{S}$ is the Poynting vector. Considering that $\alpha = R/\phi$ by definition, the absorption coefficient for direct transitions takes the form

$$\alpha = \frac{2^{5/2} (\mu^*)^{3/2} e^2 c \mu_0}{\pi n \hbar^3 \omega m^2} |P_{cv}|^2 \sqrt{\hbar\omega - E_{gap}} \tag{2.80}$$

2.6.2 Indirect transitions

Now, let us consider an indirect transition as the one depicted in Fig. 2.5, in which an electron is excited from an initial state in the valence band to a final state in the conduction band i.e.

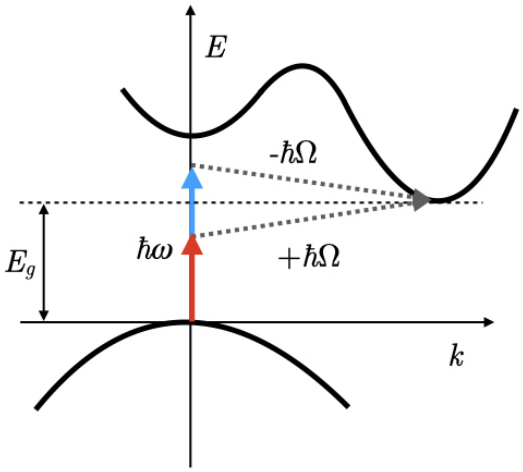

Figure 2.5: Scheme of interband absorption in indirect gap semiconductors.

$E_i, \mathbf{k}_i \rightarrow E_f, \mathbf{k}_f$. Since the maximum of the valence band and the minimum of the conduction band are shifted from each other, these transitions are necessarily mediated by a phonon. Hence, the conservation of the energy and momentum requires that

$$E_f = E_i + \hbar\omega \pm \hbar\Omega \tag{2.81}$$

$$\hbar\mathbf{k}_f = \hbar\mathbf{k}_i \pm \hbar\mathbf{q} \tag{2.82}$$

where Ω and $\mathbf{q}$ are the angular frequency and momentum of the phonon respectively. The photon momentum has been neglected. As the $\pm$ factor reveals, the process can take place as a consequence of phonon absorption (+) and emission (−).

The perturbative term H' in Eqn. 2.72 is now composed of two terms which describe the electron-photon ($H'_{e-\gamma}$) and electron-phonon (H'_{e-q}) interaction. The expression of the latter depends of the type of phonon involved in the transition. Therefore, since the absorption process involve the interaction of three different bodies, in addition to the initial and final states, we must consider an intermediate state m in the analysis. Thus, the electronic transition rate per unit of

volume takes the form

$$R = \frac{2\pi}{\hbar} \iint \left(\frac{2}{(2\pi)^3}\right)^2 \sum_{m:I,II} \frac{\left|\langle f|H_{e-q}|m\rangle\right|^2 \left|\langle m|H_{e-\gamma}|i\rangle\right|^2}{(E_m - E_i - \hbar\omega)^2} \delta(E_f(\mathbf{k_f}) - E_i(\mathbf{k_i}) - \hbar\omega \pm \hbar\Omega) d\tau_{k_f} d\tau_{k_i} \quad (2.83)$$

where the indices I and II represent the two most probable processes through which the transition takes place. In the first one an electron with momentum $\mathbf{k_i}$ promotes from the valence band to the conduction band and subsequently undergoes a transition within the conduction band in which it absorbs or emits a phonon with momentum $\mathbf{k_f} - \mathbf{k_i}$. In the second process an electron from the valence band with momentum $\mathbf{k_f}$ absorbs a photon and promotes to the conduction band. Then, an electron in the valence band with momentum $\mathbf{k_i}$ absorbs or emits a phonon with momentum $\mathbf{k_f} - \mathbf{k_i}$.

As in the direct transition case, the periodicity of the lattice implies that $\mathbf{k_f} = \mathbf{k_i} + \mathbf{k}_\gamma + \mathbf{q} \approx \mathbf{k_i} + \mathbf{q}$ i.e. the law of the conservation of the momentum holds. Assuming that in most semiconductors the matrix elements are near-independent from momentum, this term can be taken out of the integral. Similarly to direct transitions, it is possible to take the parabolic band approximation so that we can express the integrals as a function of energy:

$$\begin{aligned} R &= \sum_{I,II} \iint C_{if} \sqrt{(E_v - E_i)(E_f - E_c)}\, \delta(E_f - E_i - \hbar\omega \pm \hbar\Omega) dE_i dE_f \\ &= \sum_{I,II} C_{if} \int_{E_c}^{E_v + \hbar\omega \pm \hbar\Omega} \sqrt{(E_f - E_c)(E_v + \hbar\omega \pm \hbar\Omega - E_f)}\, dE_f \\ &= \sum_{I,II} C_{if} (\hbar\omega \pm \hbar\Omega - E_{gap})^2 \\ &= C^{abs} (\hbar\omega + \hbar\Omega - E_{gap})^2 + C^{em} (\hbar\omega - \hbar\Omega - E_{gap})^2 \end{aligned} \quad (2.84)$$

Invoking Eqns. 2.69 and 2.79, the absorption coefficient for indirect transitions is expressed as

$$\alpha = \frac{C_0^{abs}}{\hbar\omega} (\hbar\omega + \hbar\Omega - E_{gap})^2 + \frac{C_0^{em}}{\hbar\omega} (\hbar\omega - \hbar\Omega - E_{gap})^2 \quad (2.85)$$

The two terms at the right side of the equation describe the transitions that take place upon the absorption and emission of a phonon. The constants C_0^{abs} and C_0^{em} are proportional to n_q and $(n_q + 1)$ respectively, where $n_q = 1/(e^{\hbar\Omega/k_BT} - 1)$ is the phonon occupation number, which is given by the Bose-Eintein statistics. According to this, phonon absorption is strongly reduced at low temperatures, since it requires the existence of thermally excited phonons. On the contrary, phonon emission can take place at all temperatures. Moreover, for energies close to E_{gap}, the denominator $\hbar\omega$ does not introduce strong variations and can be absorbed into the $C_0^{em,abs}$ constants. Therefore, at low temperatures and energies near E_{gap}, the plot of $\alpha^{1/2}$ versus E should look like a straight line where the intercept with the horizontal axis is $E_{gap} + \hbar\Omega$.

2.7 The cooperative Jahn-Teller effect

The Jahn-Teller (JT) Effect, which was discovered in 1937 by Hermann A. Jahn and Edward Teller, is a well-known mechanism in which molecular or crystal structures undergo a spontaneous breaking of symmetry. More specifically, the Jahn-Teller Theorem states that "any nonlinear molecular system in a degenerate electronic state will be unstable and will undergo a distortion to form a system of lower symmetry and lower energy, thereby removing the degeneracy." [63].

With regard to crystal structures, atoms change their electronic structures when they are surrounded by other atoms, that is to say, the local environment changes their electronic levels. This is caused by the electric field from the surrounding atoms, which is usually referred as "crystal field effect." Therefore, the distribution of the electronic levels depends on the local symmetry (tetrahedral, octahedral, dodecahedral, etc.) and the original electronic configuration of the atom. On the other hand, if some of the electronic levels are degenerate, the polyhedral structure around the atom may undergo an spontaneous distortion as a consequence of the JT effect. This distortion modifies its environment and the JT effect can take place throughout the

whole crystal. This is the so-called cooperative JT effect (CJTE).

In order to explain this phenomena, we must consider a crystal in which some of the regular centers are in degenerate (or pseudodegenerate) states. In molecular aggregates like gases or liquids, the motion of each center does not depend on the motion of other centers. On the contrary, each regular center is influenced by the mean "molecular field" produced by the crystal environment, which is not isotropic at any given moment. Thus, equivalent distortions in free regular centers are no longer equivalent when considering their interactions.

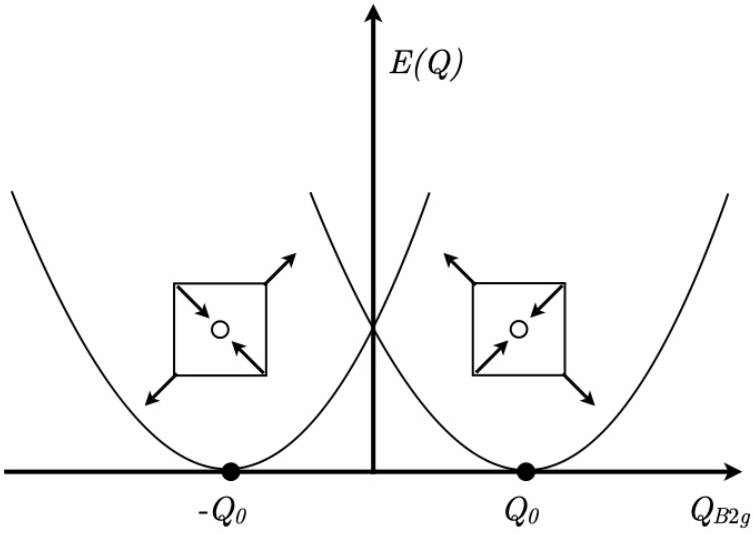

Figure 2.6: Potential energy curves of a square-planar system with a JT $E \otimes b_{2g}$ problem as a function of the Q_{B2g} displacements. The system shows two equivalent minima, with the corresponding distortions depicted over them (adapted from [97]).

In order to provide clearer explanation of this process, let us consider a simple case in which the JT centers in the crystal are characterized by a twofold orbitally degenerate E term coupled to a b_2 phonon (this example is taken from Ref. [97] , where b_2 vibrations are labeled as b_1 and vice versa). For the sake of simplicity we are assuming square planar JT centers. Fig. 2.6 schematically

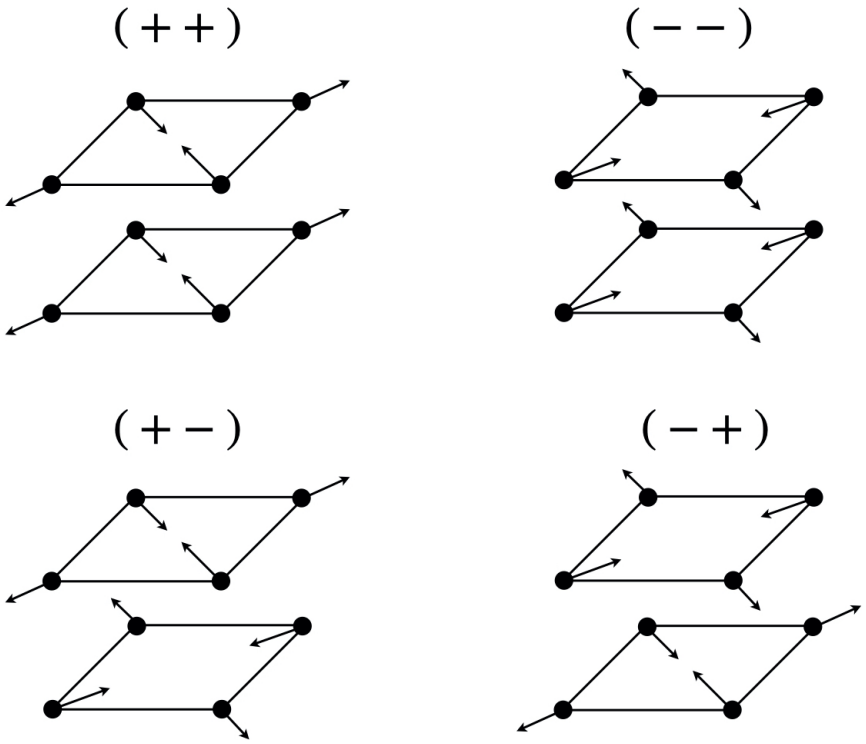

Figure 2.7: Different types of packing of two interacting square-planar JT centers in which the $E \otimes b_{2g}$ problem is realized (adapted from Ref. [97]).

shows the associated potential energy diagram, which has two equivalent minima, each of which corresponds to a rhombic distortion with a b_{2g} symmetry. If the interaction among the JT centers is neglected, both configurations (indicated with (+) and (−) hereon) are equally probable.

However, as we previously stated, interactions between centers cannot be neglected when dealing with crystal structures. If we consider a pair of parallel interacting centers in which the $E \otimes b_2$ problem takes place, four different configurations are possible: (++), (−−), (+−) and (−+), which are depicted in Fig. 2.7. If the energy of the configurations (++) or (−−) is lower, distortions parallel to each other are preferred. Such cases are known as *ferrodistortive* interactions. On the contrary, if the interaction with antiparallel distortions is stronger, the (+−) and (−+) configurations will posses lower energy. These configurations are known as *antiferrodistortive* interactions. In both cases the distortion of each center depends on the other. This kind of

reasoning can be generalized to the interaction of multiple centers and thus, to the whole crystal.

Ferrodistortive interactions lead to the deformation of the whole crystal, which changes its properties, giving rise to structural phase transitions. In addition to this, since the symmetry of the crystal is linked to the symmetry of its regular centers, there is a symmetry breaking after the CJTE takes place.

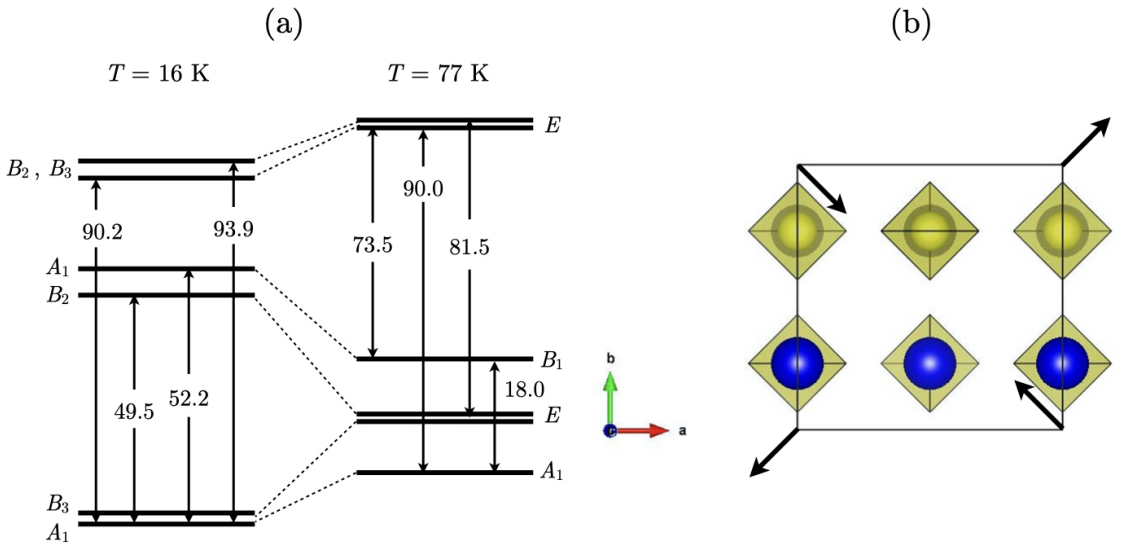

Figure 2.8: (a) Changes in the structure of the electronic low lying levels of Tb^{3+} due to CJTE at low temperatures (from Ref. [27]). Energy units in cm^{-1}. (b) Projection of the unit-cell of zircon-type $TbVO_4$ (Blue spheres represent Tb atoms; VO_4 units are represented by yellow tetrahedra). Axis directions are indicated. The direction of the B_{2g}-distortion is depicted with black arrows.

Zircon-type rare-earth orthovanadates such as $TbVO_4$, $DyVO_4$ and $TmVO_4$ constitute a perfect example of a CJTE in which a twofold degenerate E state is coupled to nondegenerate b_1 or b_2 vibrations ($E \otimes b_1$ or $E \otimes b_2$ problems). Since we studied $TbVO_4$ at low temperatures in this dissertation, we will focus our explanations on this compound, in which the low-lying electronic levels are coupled to a B_{2g} phonon. The changes in the energy levels of the Tb^{3+} cation before and after the CJTE are depicted in Fig. 2.8 (a). At temperatures over 33 K, the Tb^{3+} cation (within the crystal structure) has an orbital doublet E at $\sim$ 8.5 cm^{-1} over the A_1 ground state. Below 33

K, the orbital states at E split into two clearly separate levels (degeneracy breaking) and mix with the other nearby energy levels, which leads to a B_{2g}-type distortion [Fig. 2.8 (b)]. In particular, the distortion of the unit-cell takes place along the [110] and [$\bar{1}$10] directions i.e. the ab base diagonals. As a consequence, the symmetry of the crystal is lowered from the tetragonal zircon structure (S. G.: $I4_1/amd$), in which the site symmetry of the Tb^{3+} cations is $\bar{4}2m$ (D_{2d}), to an orthorhombic structure (S.G.: $Fddd$), where the rare-earth cations are in 222 (D_2) sites.

2.8 Principles of X-ray difraction

X-ray diffraction, usually abbreviated as XRD, is one of the most common techniques for studying and determining crystal structures. We can understand diffraction as an elastic and coherent scattering process produced by the large-range order of a crystalline structure. The reason for using X-rays is that these have a wavelength comparable to the typical interatomic distances.

2.8.1 Bragg's law

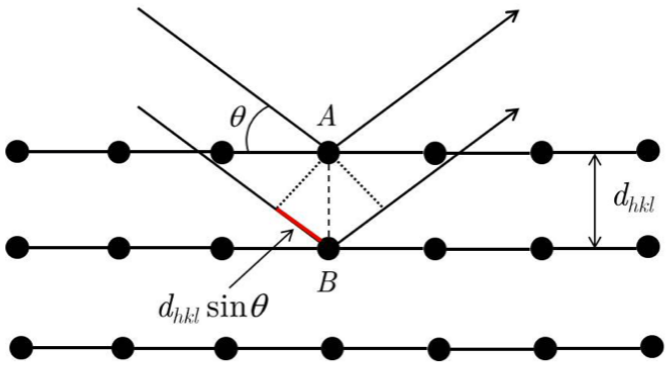

Figure 2.9: Simplified view of the typical Bragg reflection. The longitude of the red segment is $d_{hkl}\sin\theta_{hkl}$
.

The incoming beam of radiation on a crystalline structure can be elastically scattered by the atoms in its crystallographic planes, which are separated by the distance d_{hkl}. Consider Fig. 2.9. The scattered radiation its only possible if the waves reflected by the A and B atoms are in phase. However, that can only happen when the path taken by both rays is equal to a integer number of wavelengths, which can only happen for certain θ_{hkl} angles. More specifically,

$$n\lambda = 2d_{hkl} \sin \theta_{hkl} \tag{2.86}$$

This is the well-known **Bragg's law**, which relates the d-spacing with the incident wavelength and the Bragg angle. We have formulated the Bragg's law using scalars, but it can also be expressed in vector terms. Firstly, we have to consider that the scattered radiation from two charged particles separated by a vector $\mathbf{r}$ has a mismatch equal to $\exp(i\mathbf{Q} \cdot \mathbf{r})$, where $\mathbf{Q}$ is the so-called scattering vector. This vector represents the change in the wave vector of the scattered and incident beams, $\mathbf{Q} = \mathbf{k} - \mathbf{k_0}$. Thus, the **scattering factor** also known as the **form factor** can be expressed as follows,

$$f(\mathbf{Q}) = \int \rho_{el}(\mathbf{r}) \exp(i\mathbf{Q} \cdot \mathbf{r}) d\mathbf{r} \tag{2.87}$$

This factor depends on the electron density ρ_{el} of the particular atoms under study and is a function of $\mathbf{Q}$. In general, the electronic density ρ_{el} of an atom can be well estimated by quantum mechanics calculations, which are beyond the scope of this dissertation though. A particular consequence of this definition is that in the limit $\mathbf{Q} \rightarrow 0$ the form factor is equal to the total number of electrons Z in that particular atom or ion:

$$f(\mathbf{Q} \rightarrow 0) = \int \rho_{el}(\mathbf{r}) d\mathbf{r} = Z \tag{2.88}$$

Now, let us consider a crystal structure defined by the lattice vector $\mathbf{R}$. The scattered radiation by the crystal lattice is only possible if the radiation scattered by each unit-cell is in phase. This

means that the condition $\exp(i\mathbf{Q}\cdot\mathbf{R}) = 1$ must be fulfilled. This can only happen if $\mathbf{Q} = \mathbf{d}^*_{hkl}$, where $\mathbf{d}^*_{hkl} = h\mathbf{a}^* + k\mathbf{b}^* + l\mathbf{c}^*$ is the reciprocal vector, which is perpendicular to the (hkl) plane and its module is $2\pi/d_{hkl}$. Hence, the Bragg's law takes the form,

$$\mathbf{k} - \mathbf{k_0} = 2\pi\frac{\mathbf{s} - \mathbf{s_0}}{\lambda} = \mathbf{d}^*_{hkl} \tag{2.89}$$

where $\mathbf{s_0}$ and $\mathbf{s}$ are unitary vectors.

2.8.2 The stucture factor

The amplitude of the scattered radiation is given by the so-called **structure factor** [98],

$$F(\mathbf{Q}) = \sum_j f_j \exp(i\mathbf{Q}\cdot\mathbf{r}_j) \tag{2.90}$$

Considering that the condition of diffraction is given by the Bragg's law ($\mathbf{Q} = \mathbf{d}^*_{hkl}$) then the structure factor takes the form

$$F(hkl) = \sum_j f_j \exp(2\pi i(hx_j + ky_j + lz_j)) \tag{2.91}$$

This equation is particularly interesting, since it relates the amplitude (and, therefore, the intensity) of a particular hkl reflection with the positions xyz of the atoms in the cell. However, for some of these combinations, $F(hkl)$ may be equal to zero. These cases are known as **systematic extinctions**.

Until now, we have considered the position of the atoms as fixed in the crystal. However, atoms are in a continuous motion due to thermal effects. Thus, it is necessary to introduce these

effects in the structure factor as

$$F(\mathbf{Q}) = \sum_j f_j \exp\left(i\mathbf{Q}\cdot\mathbf{r}_j\right) T_j(\mathbf{Q}) \tag{2.92}$$

Assuming that thermal vibrations are isotropic and harmonic, the average position of the atoms can be accurately described by a Gaussian function. This description is particularly useful, since the width of the distribution depends on the mean-squared atomic displacements $\langle u_j^2 \rangle$. Thus, we can write T_j in terms of $\langle u_j^2 \rangle$ as,

$$T_j(\mathbf{Q}) = \exp(-8\pi^2 \langle u_j^2 \rangle \sin^2\theta/\lambda) = \exp(-B_j \sin^2\theta/\lambda) \tag{2.93}$$

where $B_j = 8\pi^2\langle u_j^2\rangle$ is the so-called **temperature factor**, which has to be taken into account when refining experimental XRD patterns.

3 | Experimental methods

In this chapter we present some of the most used high-pressure devices and techniques used during our research. We start by making a general description of the well-known Diamond Anvil Cell, which allows not only the compression of materials beyond 10 GPa but also the optical access to the sample. After that, we explain the principles of the X-ray diffraction, Raman spectroscopy and optical absorption characterization techniques. With these techniques we could study the crystal structure of $R\mathrm{VO}_4$ compounds under different pressure-temperature conditions, as well as their vibrational structure and band gap energies. We finally present the Paris-Edinburgh large volume press cell, which was used to synthesized larger quantities of scheelite-type RVO_4 samples at high-temperatures and high-pressures.

3.1 The Diamond Anvil Cell

The Diamond Anvil Cell (DAC hereon) is the most used device in high pressure experiments due to its great versatility. The main reason for using DACs instead of other pressure devices (such as the large volume Bridgman cell, multi-anvil presses, etc.) is that they provide an excellent optical window for optical, spectroscopic and x-ray diffraction *in situ* experiments. The reason for this is that diamonds are transparent in the visible-ultraviolet region as well as for hard X-rays ($E > 10$ KeV). However, the main limitation of this kind of cells is the small size of the sample under analysis, since the diameter of the culets are typically around 200-500 μm. The small size of

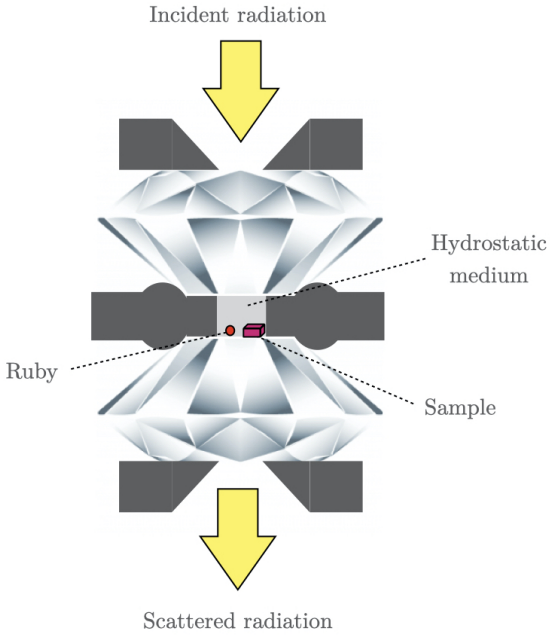

Figure 3.1: Basic sketch of a generic DAC.

the diamonds combined with their extreme hardness, allows to achieve maximum pressures that range from 20 (for diamonds with culet diameters of 500 μm) to 100 GPa (for Bevelled diamonds with culet diameters of 150 μm), typically.

Basically, a DAC consists in a system of two opposing diamonds as shown in Fig. 3.1, in which the sample is confined into the hole of a metallic gasket in between the diamonds. In addition to the sample, the cell is normally loaded with a pressure gauge (usually ruby chips) and a pressure transmitting medium (PTM) to ensure quasi-hydrostatic conditions. Pressure is increased in the cavity by pushing the diamonds one towards each other.

The force necessary to move the diamonds is carried out through different mechanisms. In particular, most of the high-pressure experiments described in this dissertation were performed using membrane DACs. Fig. 3.2 shows a picture of a membrane DAC, which is composed of three main parts: (1) the piston, (2) the cylinder (also known as the body of the cell), and the (3) membrane, which is soldered to (4) the cover. One of the diamonds is fixed in the cylinder

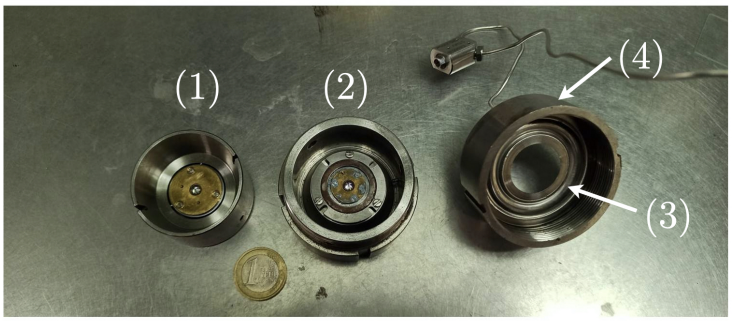

Figure 3.2: Basic pieces of a membrane DAC: (1) piston, (2) body, (3) membrane and (4) cover.

.

and the other one in the piston. The piston slides into the body, which is pushed by the membrane. Pressurized gas is injected into the membrane, whose expansion pushes the cylinder. As a consequence, both diamonds approach towards each other, increasing the pressure in the cavity. With this kind of system it is possible to increase the pressure of the sample to several GPa with moderate membrane pressures (P_m < 100 bar). In fact, we can prove this in terms of orders of magnitude by performing a rough calculation. Considering a membrane pressure of 60 bar, a membrane with external and internal radii of 5.5 and 4.5 cm and a diamond culet diameter of 500 μm we have that, $P = 60$ bar $\times\pi[(5.5)^2 - (4.5)^2]/\pi(0.05)^2 \approx 240$ kbar = 24 GPa. The particular advantage of these type of DAC with respect to other different kinds, such as those in which pressure is increased using screws, is that they allow to better control and monitorize the pressure of the membrane, and thus, of the chamber pressure. Another advantage is that it is not necessary to move the DAC out of the experimental set up to increase pressure.

The metallic gasket placed in between the diamonds needs to be preindented and drilled before the sample loading, so that the cavity has the appropiate size. The necessary membrane pressure for achieving the desired thickness depends on the kind of metal (steel, tungsten or rhenium), the size of the diamonds and the particular cell-membrane combinations.

On the other hand, in order to maintain quasi-hydrostatic conditions, different kind of media are used. These can be solid, liquid or gas. Soft solid media such as solid boron nitride (BN) or cesium iodine (CsI) are not very good PTMs at room temperature. Nonetheless, they have

some advantages for certain experiments. For instance, CsI is transparent to IR radiation, so it can be used in IR absorption experiments under high pressure. On the other hand, one of the most used liquid PTMs is the 16:3:1 mixture of ethanol-methanol-water (MEW) is reasonably hydrostatic below 12 GPa. Besides its good hydrostaticity, the main advantages of MEW is that it is transparent in the VIS-UV region and easy to load in the DAC. Gases, in particular noble gases such as Ne or He, are used for achieving optimal hydrostatic conditions. Their main advantage is that they ensure hydrostatic conditions in a larger range of pressures. As an example of this, table 3.1 shows the hydrostatic limits for different PTMs [99].

Table 3.1: Hydrostatic limits of some pressure transmitting media.

PTM	**Pressure limit for $\sigma_P < 0.2$ GPa**
16:3:1 Methanol-ethanol-water	12 GPa
Nitrogen (N_2)	15 GPa
Argon	20 GPa
Neon	25 GPa
Helium	40 GPa

The pressure under which the sample is submitted can be experimentally determined using the ruby (Cr^{3+}-doped Al_2O_3). luminiscence method. This particular method is based on the shift to higher wavelengths of the R_1 and R_2 luminiscence bands of the fluorescence spectra of ruby, as shown in Fig. 3.3. The pressure dependence of the R_1 line ($\lambda_0 = 697.38$ nm at room conditions) has been widely studied. One of the most used equations describing this dependence was proposed by Mao et al. [100] in 1986:

$$P = \frac{1904}{7.665}\left[1 + \frac{\lambda - \lambda_0}{\lambda_0}\right]^{7.665} \text{ (GPa)} \tag{3.1}$$

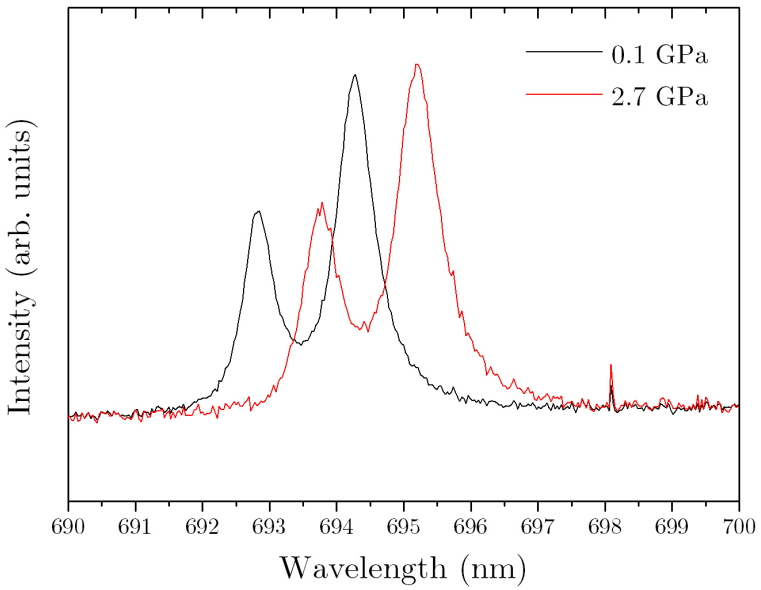

Figure 3.3: Luminiscence spectra of ruby at room temperature near ambient pressure and at 2.7 GPa.

On the other hand, some experimental setups do not allow to use this particular method. For instance, high-pressure experiments at low or high temperatures sometimes require the use of large vessels that do not allow the use of a laser system. However, other alternative methods are available. For instance the DAC can be loaded with a small amount of some kind of material whose pressure evolution is well determined under a particular experimental technique. For instance, in X-ray diffraction, some gold (Au), platinum (Pt), sodium chloride (NaCl) or other substances can be loaded together with the sample in the DAC [101, 102]. These are crystal structures whose equations of state are well determined in literature. Thus, by following the displacement of the corresponding Bragg peaks it is possible to determine the pressure applied on the sample. One of the advantages of this method is that allows to determine pressure in the a particular area of the sample, since the obtained XRD pattern contains the Bragg peaks of the sample as well as those of the pressure gauge. By contrast, the main disadvantage is that this also hinders the refinement of the sample parameters, since both XRD patterns are mixed. This may be worse is the pressure gauge is a much more diffracting structure than the sample.

3.2 Powder X-ray diffraction

Since all of our XRD experiments have been carried out using powder samples, we will restrict our explanations to this particular technique. Crystalline powder is composed of a huge amount of microscopic crystals, usually obtained after grinding bigger single crystals. This fine powder is loaded in a holder i.e. a DAC in our particular case, which is placed in front of a monochromatic x-ray beam. Since the powder is constituted by numerous tiny crystals at random orientations, some of them have one crystallographic plane that fulfils the Bragg's law. In addition to this, this process has cylindrical symmetry around the direction given by the incoming beam $\mathbf{s_0}$, as it is shown in Fig. 3.4. As a consequence, a cone of diffraction is obtained for each crystallographic plane. When a detector is placed in front of the sample, the collected pattern appears as a series of concentric diffraction rings. An example of this is shown in Fig. 3.5 (a) for scheelite-type $GdVO_4$. The integrated intensity as a function of the 2θ-angle is also shown in Fig. 3.5 (b).

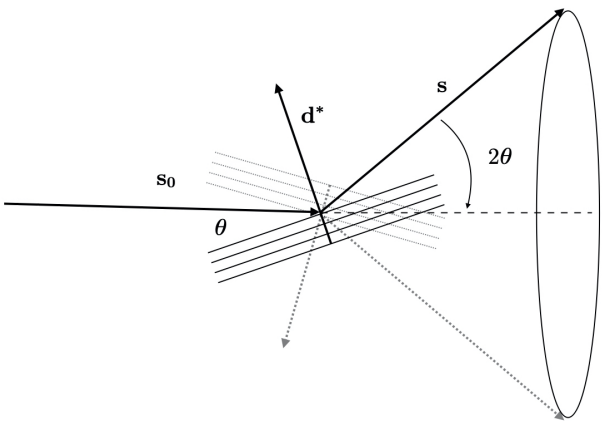

Figure 3.4: Scheme of the diffraction cone generated in powder XRD experiments.

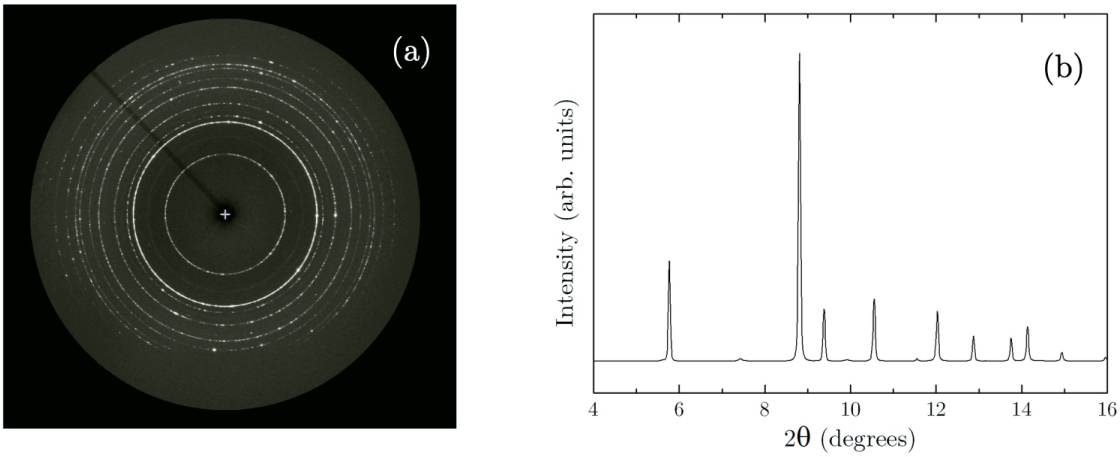

Figure 3.5: (a) Concentric rings pattern of scheelite-type $GdVO_4$ ($\lambda = 0.4642$ Å) and (b) integrated pattern.

3.2.1 Sources of X-rays

3.2.1.1 Conventional X-ray sources

In the electromagnetic spectrum, X-rays are placed in between the ultraviolet and gamma rays, with typical energies in the range of 10^2-10^5 eV ($\lambda = 0.1$-100 Å). In conventional X-ray sources, this radiation is usually obtained by hitting a metallic target (usually Mo or Cu) with a beam of electrons. Many of these electrons lose their kinetic energy when they enter the target, producing a continuum of X-rays due to their deceleration. This braking radiation is commonly referred as **Bremsstrahlung** (from the german *bremsen* "to brake" and *Strahlung* "radiation"). The energy of the incident electrons determines the maximum energy of the Bremsstrahlung distribution, since this corresponds to the energy lost by the electrons which are totally stopped by the metal. This curve is represented in Fig. 3.6 (a).

However, there is also another contribution to the spectra, which is crucial for the experiments. When the electrons strike the target, they strip some inner electrons from the metal atoms. As a consequence, other electrons at more energetic levels in outer shells decay to these

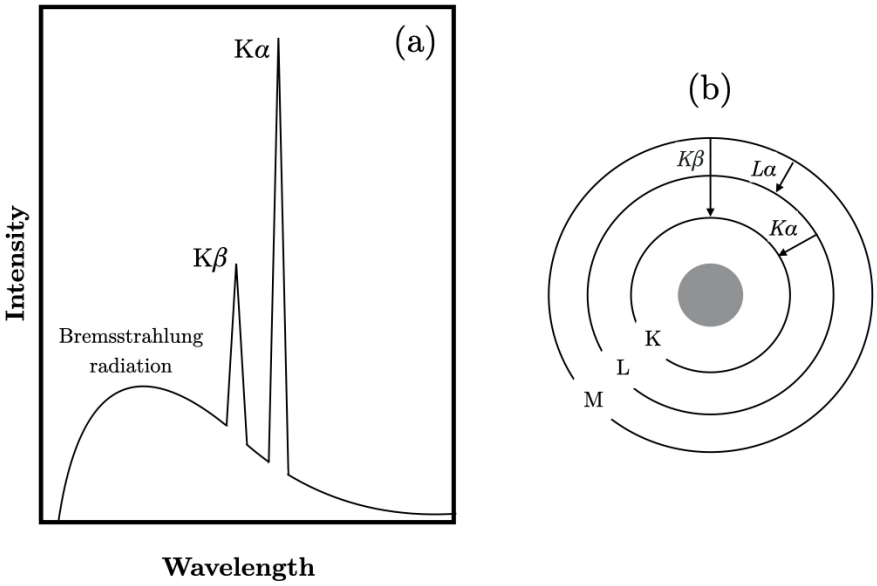

Figure 3.6: Sketchs of (a) the typical X-ray spectrum and (b) the electronic transitions related to X-rays.

empty levels. By doing so, these electrons lose some part of their energy, which is released as X-rays. These kind of transitions are shown in Fig. 3.6 (b). The X-rays produced by this mechanism give rise to sharp peaks in the final spectrum, as it can be observed in Fig. 3.6 (a). For diffraction experiments, the relevant transitions are the ones in which the electrons fall from the L to the K shells, which gives rise to the Kα line, shown in Fig. 3.6. In fact, there are two contributions to this peak, referred as Kα_1 ($2p_{1/2} \rightarrow 2s_{1/2}$ transitions) and Kα_2 ($2p_{3/2} \rightarrow 2s_{1/2}$ transitions), at very similar wavelengths. For instance, the wavelengths for Cu are Kα_1: 1.54059 Å and Kα_2: 1.54441 Å [103]. With regard to the relative intensity, the Kα_2 contribution is approximately half of that of Kα_1. In order to work at a fixed wavelength, the peaks that are not desired for the experiment (such as Kβ) are usually removed using absorbing filters. The Bremsstrahlung radiation is sometimes left as background, since it is very weak compared to the Kα_1) line. Monochromators can also be used as an alternative, which allow to select the Kα line exclusively.

According to the former explanations, it is necessary a source of electrons, a high voltage to accelerate them and a metal target. In addition to that, a cooling system for the target is

necessary in order to avoid melting, since most of the kinetic energy of the electrons is absorbed by the metal, which considerably raises its temperature. A common tool for obtaining X-rays are filament tubes. These consist in a tungsten filament and a water-cooled copper target, which work as cathode and anode respectively. Both pieces are insulated one from the other by an evacuated glass envelope. The electrons are obtained by the thermal excitation of the atoms in the tungsten filament, which is heated by an electrical current, and then accelerated with a high negative potential (30000-50000 V) towards the copper target. The main limitation of sealed X-ray tubes is that most of the supplied energy is transformed into heat, so that the input power (0.5 - 3 kW) is limited by its ability to dissipate heat. On the other hand, the low thermal efficiency of X-ray tubes can be significantly increased by using a rotating anode X-ray source. In this type of sources, the anode is a large disk rotating at high speeds while being cooled down by a cold water stream. The larger bombarded surface and the fact that rotation constantly brings chilled metal to the impact area allow input powers of 15 - 20 kW typically, although in some cases they can arrive to 50 - 60 kW.

Sources like these, although extremely useful, have some intrinsic limitations. For instance, in order to avoid the over-heating of the anode, the intensity must be limited. This means that the required time to get a diffraction pattern is quite large. Moreover, the X-ray wavelength is restricted to the electronic transitions of the particular metal used as target, which is specially problematic when the experimental conditions require small X-ray wavelengths and a more intense and collimated radiation (as in the case of high-pressure experiments). For these reasons, a different and more powerful source of radiation is sometimes required. An example of this are synchrotrons.

3.2.1.2 Synchrotron Radiation sources

Synchrotron constitute a kind of particle accelerators in which the particle beam follows a cyclical closed-loop path. In these facilities, particles are accelerated by an electric field and their

path is curved with magnetic fields. In contrast to cyclotrons, in which these fields are constant, in synchrotrons the electric and magnetic fields change according to the kinetic energy of the charged particles.

Synchrotrons provide a much higher X-ray spectral brilliance than the previously described conventional sources. This magnitude is fundamental when comparing X-ray sources. It accounts for the number of photons per unit of time, the angular divergence and cross-sectional area of the beam and the photons falling within the bandwith (BW) of 0.1% of the central wavelength. Thus, brilliance units are defined as photons/(s·mrad^2·mm^2 · 0.1% BW). The brilliance of a typical third-generation synchrotron, which is characterized by the use of insertion devices such as wigglers or undulators, is 12-16 orders of magnitude higher than that produced by a common X-ray tube. In addition to this, synchrotron radiation can be tuned to the most suitable X-ray wavelength for the experiments. The four main components of these kind of synchrotron facilities are (i) a field emission cathode as the source of the electron beam, (ii) the linear accelerator (iii) the synchrotron (or booster) and (iv) the storage ring, where the bending magnets and insertion devices can be found, which act as sources of radiation. With regard to bending magnets, these are periodically distributed around the storage ring. Their function consists in deflecting the electrons and force them to circulate inside the ring. Insertion devices consist in a closely spaced array of magnets located in the linear sections between the bending magnets. These devices increase the intensity of the radiation by inducing oscillations in the electron beam path.

Electromagnetic radiation can be produced by accelerating charged particles with an electrical field or by curving their path using a magnetic field. In a synchrotron facility, radiation is obtained by the latter method. When a charged particle follows a circular path, as shown in Fig. 3.7, it behaves like an electric dipole with its momentum pointing parallel to the centripetal force (represented with a red arrow). The emitted radiation has cylindrical symmetry around the x axis, and the shape of two lobes, which are represented in the figure with blue lines. As the speed of the particle gets closer to c, the lobes considerably narrow, which produces a more colli-

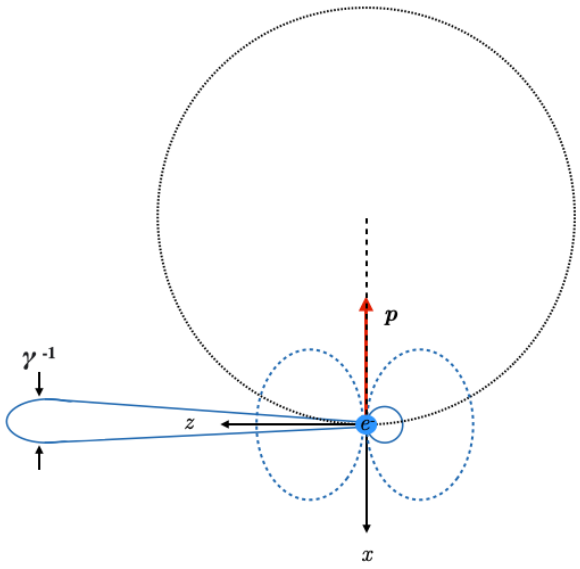

Figure 3.7: Change in the radiation pattern of an electron when accelerated at relativistic speeds.

mated radiation in the direction of the electron movement. The angular aperture of the collimated radiation is inversely proportional to the Lorentz factor $\gamma = 1/\sqrt{1-\beta^2}$ with $\beta = v/c$.

The emission spectrum of the radiation produced by bending magnets is described by the universal curve function, which is shown in Fig. 3.8. The spectral density exponentially grows up to an energy maximum known as the critical energy E_c. Beyond such energy, the intensity rapidly decreases. The value of E_c depends on the energy of the electron beam E_e and the magnitude of the magnetic field B of the bending magnet [104]:

$$E_c[\text{keV}] = 0.665 E_e^2[\text{GeV}] B[\text{T}] \tag{3.2}$$

In order to get a higher E_c value and some extra gain in brilliance, an insertion device (ID) is required. The most common IDs are wigglers and undulators. These consist in large series of magnets periodically ordered so that the magnetic fields alter the movement of the electrons. In particular, these follow a wave-like path, oscillating around of the straightway direction. The

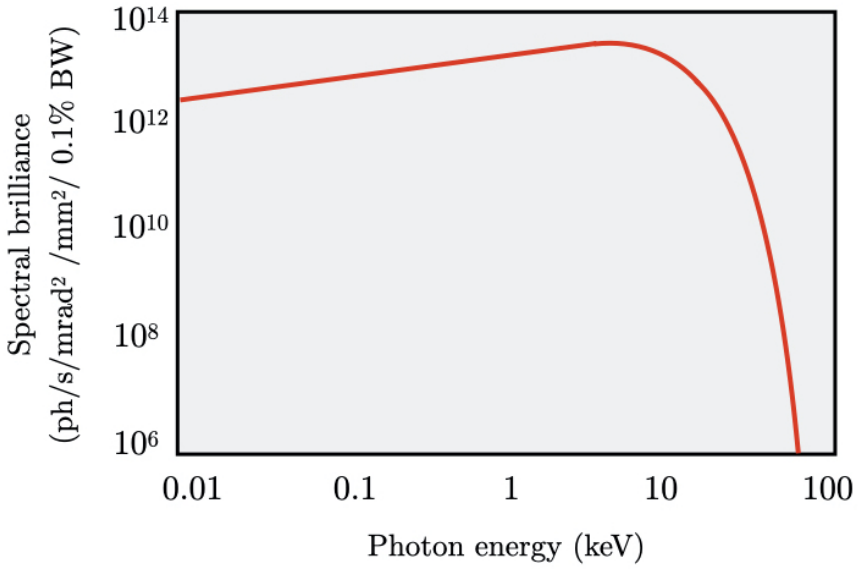

Figure 3.8: Schematic plot of the universal curve function of a bending magnet.

key difference between both IDs is that the undulator has a larger number of periods, so the deviations of the beam along the straight path are smaller. In fact, undulators are constructed in a way such that the emitted radiation at one oscillation is in phase with the one emitted in the following oscillations [104]. As a result, the coherent superposition of the radiation emitted in each oscillation leads to a quasi-monochromatic spectrum with harmonics.

In order to collect X-ray radiation for experiments, it is necessary to use special X-ray optical devices. An essential element in X-ray diffraction lines are X-ray mirrors. Below, we derive the relationship between the refractive index n and the scattering properties of the medium (mirror), which are defined by the electronic density ρ and the scattering length per electron r_0. In this simple approach we will neglect absorption processes and we will assume that the interface between vacuum and the medium is flat and sharp (Fig. 3.9). At high-energies, the refraction index of materials is lower than 1 [104],

$$n = 1 - \delta \tag{3.3}$$

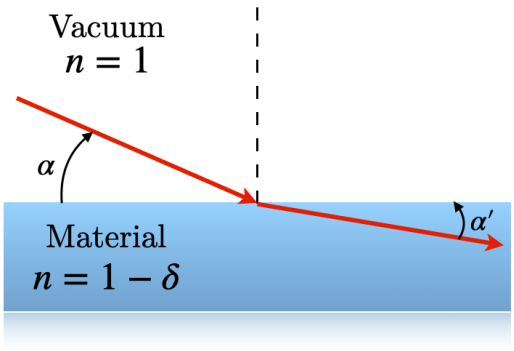

Figure 3.9: Refraction of X-rays in a material under vacuum conditions ($\alpha' < \alpha$).

with

$$\delta = \frac{2\pi\rho r_0}{k^2} \tag{3.4}$$

where k is the wavevector ($k = 2\pi/\lambda$). In condensed matter, the electron density is of order 1 electron/Å^3. Considering that $r_0 = 2.82 \times 10^{-5}$ Å and $k \sim 4$ Å^{-1}, δ is of the order of 10^{-6}. According to Snell's law, the relation between the glancing angles α and α' is

$$\cos\alpha = n\cos\alpha' \tag{3.5}$$

By definition, the critical angle $\alpha = \alpha_c$ is that for which $\alpha' = 0$. Since α_c is small, we can also assume that $\cos\alpha_c \approx 1 - \alpha_c^2/2$. Hence,

$$\alpha_c = \sqrt{2\delta} = \frac{\sqrt{4\pi\rho_0}}{k} \tag{3.6}$$

Therefore, α_c is of order 10^{-3} rad. This means that the angle of incidence in X-ray mirrors must be very close to 90 °. In recent years, multilayered mirrors have been developed, which increases the efficiency of X-ray reflection.

In order to achieve the focusing of X-rays at one point, a system composed of two curved elliptical focalizing mirrors is used, forming the so-called Kirkpatrick-Baez configuration (Fig.

3.10). In this system, the X-ray source is placed in one of the foci of the first mirror. This focalizes radiation in the other focus of the mirror, but only in the plane of the ellipse. Thus, a second mirror with its surface perpendicular to the first one is needed in order to focus X-rays at a point.

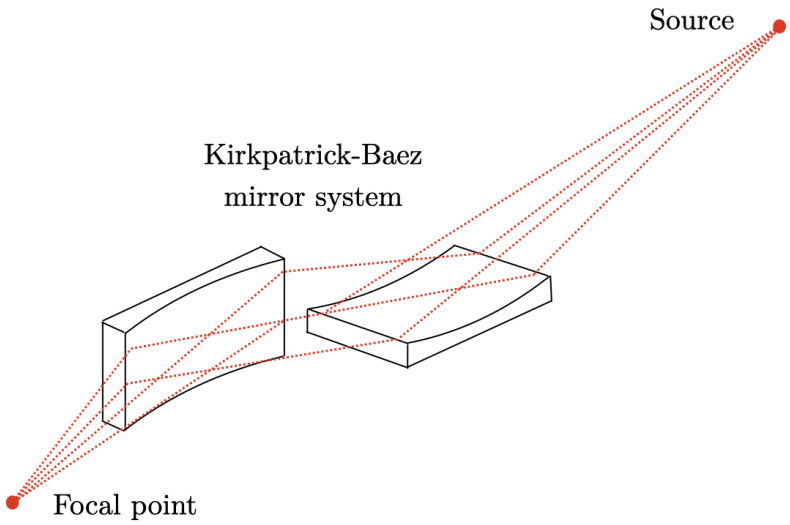

Figure 3.10: Scheme of two elliptical mirror in the Kirkpatrick-Baez configuration.

With regard to monochromators, these usually consist in high crystalline quality (111)-oriented silicon or diamond single crystal. Nonetheless, the former are more widely used due to their lower cost. The polychromatic beam first arrives to a Si-(111) crystal at a θ angle with respect to the surface. A monochromatic beam is subsequently diffracted according to Bragg's law ($\lambda = 2d_{Si(111)} \sin\theta$). This beam is diffracted again by a second Si (111)-oriented single crystal, which improves its monochromatic character. In Fig. 3.11 we show a simplified scheme of a synchrotron beamline, in which all the basic elements are depicted.

A good example of these types of beamlines is the MSPD (Material Science and Powder Diffraction) beamline, at the synchrotron ALBA-CELLS in Spain. Most of the powder XRD experiments under high pressures reported in this dissertation were performed in this beamline. This beamline has a superconducting wiggler (SCW30) as radiation source, whose maximum magnetic

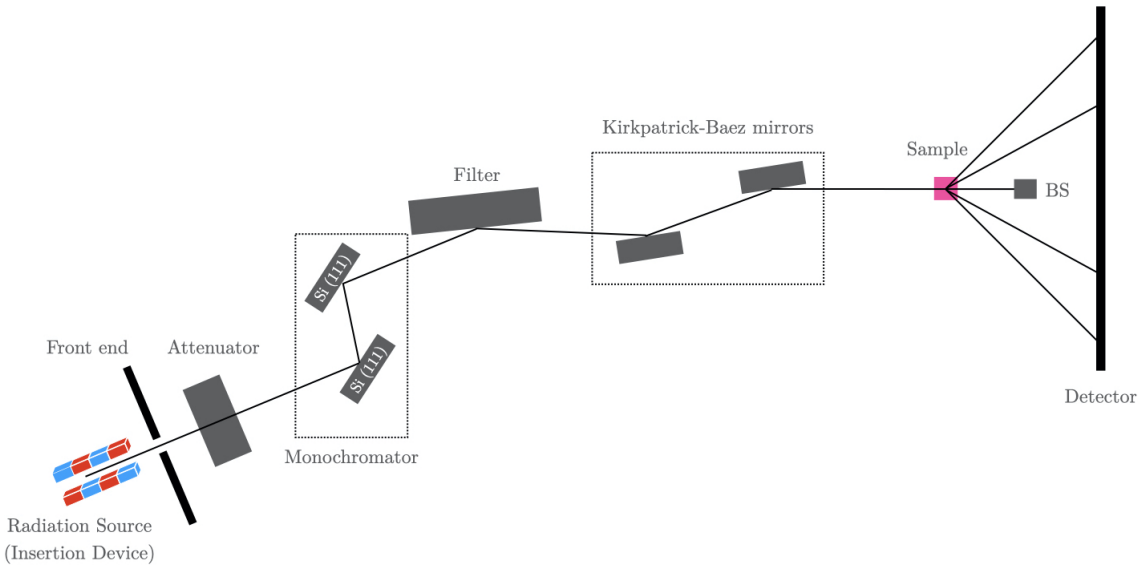

Figure 3.11: Scheme of a typical synchrotron X-ray beamline. Adapted from Ref. [88].

field is $B = 2.15$ T, which corresponds to $K = 6.08$ and a critical energy of $E_c = 12.5$ keV. In MSPD, the SWC30 is operated permanently at its maximum magnetic field. Using a superconductor wiggler implies the use of an attenuator to preclude the overheating of the following elements. After the radiation beam exits from the ID through the front end of the beamline (and passes through the attenuator), it arrives to the monochromator, which is composed of two nitrogen-cooled (111)-oriented silica mirrors. These mirrors are used to select a particular wavelength by applying Bragg's law. In particular, in the MSPD beamline, the photon energy range is 8 - 50 keV (λ = 1.5498 - 0.2479 Å) with a resolution of 2×10^{-4}. Then, the beam arrives to the filter, in which the higher-order harmonics produced by the monochromator vanish. Subsequently, two multilayered mirrors in the Kirkpatrick-Baez configuration focus the beam on the sample. This system of mirrors allows to focus the beam down to a minimum of 15×15 μm^2 FWHM. Finally, the diffracted rays produced by the interaction of the sample (which is inside a DAC in high-pressure experiments) and the radiation beam arrive to the detector, which is a bidimensional Rayonix SX165 charge-coupled device (CCD) equipped with a Beryllium window. The detector

has a round area of 165 mm diameter, works in the 20 - 50 keV energy range and has a dynamic range of 16 bit. The angular resolution of the system is $\Delta 2\theta = 0.0008°$. Beryllium is used to seal off the vacuum areas of the beamline, since it is transparent to X-rays. The non-diffracted part of the beam that pass through the sample is attenuated by a beam stop (BS) in order to avoid any possible detector damage. A photography of the MSPD experimental hutch is shown in Fig. 3.12, where some parts of the beamline can be observed. In this case, a loaded DAC is at the sample position. The sample is located at the focal point with a system of controlled electric drives, which also allow to explore the different parts of the sample. These drives also enable the rocking of the sample, which is essential in the sample centering procedure as well as in the pattern measurement process. The calibration of the experiment is made with a sample whose XRD pattern is well-known. In the case of powder experiments in MSPD, the most used is lanthanum hexaboride (LaB_6).

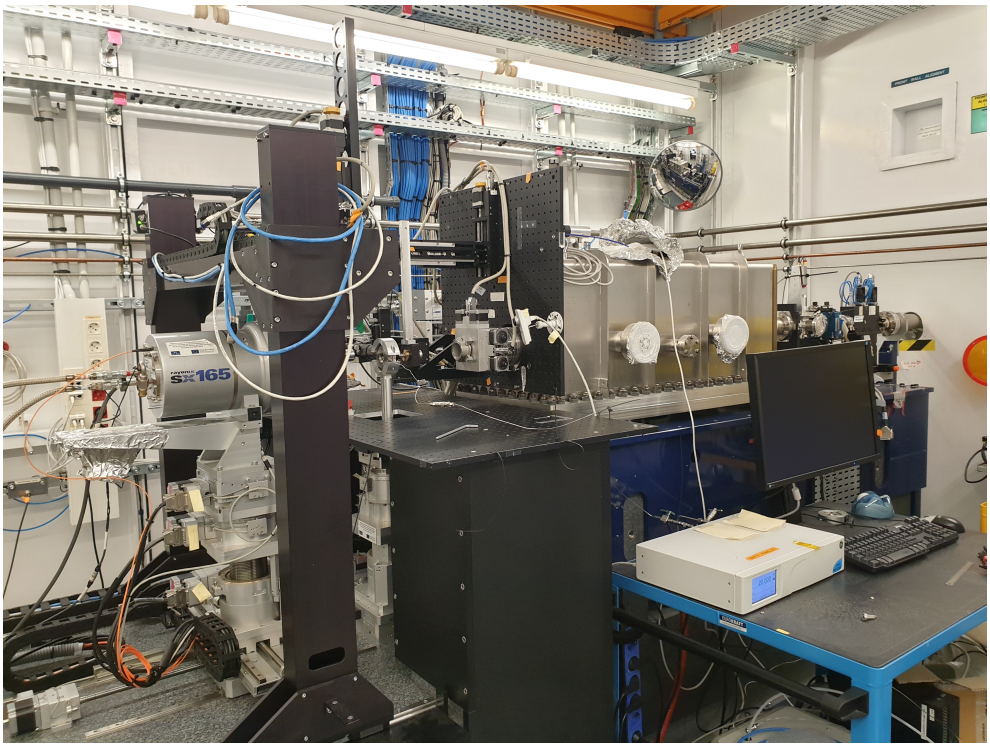

Figure 3.12: Experimental hutch at the MSPD beamline in the ALBA-CELLS synchrotron. Courtesy of Samuel Gallego.

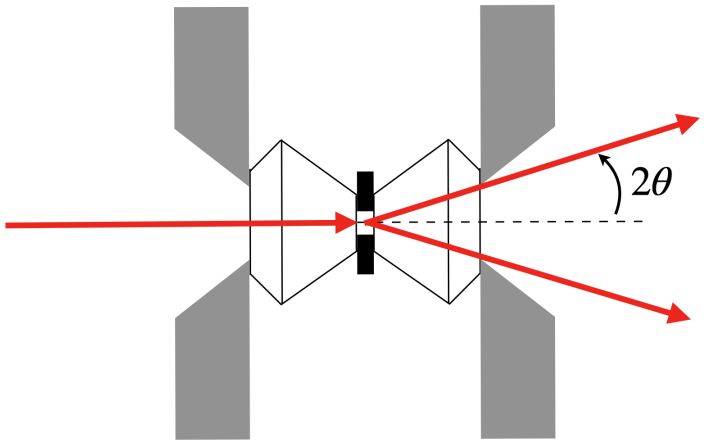

Figure 3.13: Angular limitation of the DAC in XRD experiments.

Synchrotron sources are specially useful for XRD experiments at high pressures. The fact that the sample is loaded within a DAC with an opening angle 2α implies a direct limitation on the 2θ range, as it can be deducted from Fig. 3.13. In particular, in the case of powder diffraction, $2\theta_{max} \leq \alpha$. This situation leads to the observation of a smaller number of diffraction rings. However, in synchrotron beamlines, photon energy can be tuned to the most advantageous wavelength. As an example, the XRD pattern showed in Fig. 3.5 was obtained with $\lambda = 0.4246$ Å. The other crucial fact is brilliance. Since the amount of sample within a DAC is small, a very intense XRD beam is needed to measure patterns in short periods of time (seconds, usually). This also leads to higher quality patterns.

3.2.2 Refinement of the crystal structure

Integrated powder XRD patterns allow us to measure the dimensions of the unit-cell of a crystal and to determine the positions of the atoms within the structure. Nonetheless, this last thing can only be done with a high-quality powder. If the grain size is too large, there may be strong preferential orientations in the sample. As a consequence, the obtained XRD pattern will

show a spotty character, so the concentric rings won't be uniform. Hence, the relative intensities of the peaks in the integrated pattern are not reliable. If this happens, the information about the atomic positions within the unit-cell is lost. Only the unit-cell parameters can be refined, since these can be inferred from the position of the peaks. The methods used in such cases are based in two subsequent separated procedures. The first one consists in the decomposition of the XRD pattern into its component individual diffraction peaks and the indexation of the Bragg reflections. In the second procedure, the crystal structure is refined considering the Bragg intensities of the different reflections as independent from each other. Among all these methods, the **Le Bail refinement** [105] is one of the most used, although other different methods are available, such as those proposed by Will [106], Pawley [107], Langford and Louër [108], etc. These methods allow to refine the unit-cell parameters, the shape and width of the peaks and the instrumental zero error by using least squares analysis.

On the other hand, if fine powder, the diffraction rings are uniform and then it is possible to carry out a **Rietveld refinement**. In this method, least-squares refinements are performed in order to obtain the optimal fit between the whole measured XRD pattern and the entire simulated pattern, based on the simultaneously refined models for the crystal structure, sample characteristics and instrumental factors. More explicitly, this method allows to determine the unit-cell parameters, atomic positions and thermal parameters, as well as many other experimental features, such as the background intensity profile, peaks width and shape factors, zeroshift error, microstrain, grain size, etc. Since the diffraction patterns are recorded in a digital format, these are constituted of several thousand pairs of intensity - scattering angle values (y_i - $2\theta_i$), one for each i increment. Thus, the quantity minimized in the least-squares refinement is the residual S_y,

$$S_y = \sum_i w_i (y_i - y_{ci}) \tag{3.7}$$

where $w_i = 1/y_i$. y_i and y_{ci} are the observed and calculated intensity at the ith step, respectively.

The y_i intensity measured at any point in the pattern is the result of the contribution of many Bragg reflections. The calculated intensities y_{ci} are determined by the squared structure factor $|F_{hkl}|^2$ of the calculated crystal structure, by adding the calculated contributions of the neighbouring reflections and the background [109]:

$$y_{ci} = K \sum_{hkl} L_{hkl} |F_{hkl}|^2 \phi(2\theta_i - 2\theta_{hkl}) P_{hkl} A + y_{bi} \tag{3.8}$$

where K is the scale factor,

L_{hkl} contains the Lorentz polarization and multiplicity factors,

$\phi(2\theta_i - 2\theta_{hkl})$ is the peak profile function,

P_{hkl} is the preferred orientation function,

A is the effective absorption factor, and

y_{bi} is the background intensity at the ith step.

In most cases, the sample is assumed to be flat, so that the absorption coefficient A is constant and can be absorbed into K. Usually, the background intensity y_{bi} can be determined by using a refinable background function, fitted to selected data points. This function can be phenomenological or based in a physical reality, such as an amorphous compound. With regard to L_{hkl}, this term contains the Lorentz multiplier L_θ (which is defined by the geometry of diffraction), the polarization factor P_θ (which accounts for the partial polarization of the scattered beam) and the multiplicity factor p_{hkl} (which accounts for the multiple symmetrically equivalent points in the reciprocal lattice). Preferred orientations are taken into account by the term P_{hkl}. These are generate by the tendency of some crystallites in the sample to be preferentially oriented in one way or set of ways. This type of preferential orientation must not be confused with the preferential orientation caused by "graininess" (such as when powder is not sufficiently fine). In the latter case Rietveld refinements are not possible. Atomic positions and thermal effects are included in the structure factor F_{hkl}. On the other hand, the peak profile function ϕ accounts for the width

and shape of the Bragg peaks. These are usually modelled by using pseudo-Voigt functions [109, 110], which combine both a Gaussian $G(x)$ and Lorentzian function $L(x)$,

$$\phi(x) = \eta \cdot G(x) + (1 - \eta) \cdot L(x) \tag{3.9}$$

where $x = (2\theta_i - 2\theta_k)/H_k$ is the difference between the ith point in the diffraction pattern with respect to the position of the calculated kth peak, divided by the full-witdth at half maximum (FWHM) of such Bragg peak. The Gaussian-Lorentzian character of the peak is given by the η parameter. The FWHM of the Gaussian and Lorentzian functions depend on θ as

$$H_G^2 = U \tan^2\theta + V \tan\theta + W \tag{3.10}$$

$$H_L = X/\cos\theta + Y \tan\theta \tag{3.11}$$

respectively, with (U, V, W) and (X, Y) as free parameters.

In addition to this, the width of the Bragg peaks in the integrated patterns, once the instrumental contribution is substracted, is related to the inhomogeneous strain and grain size of the particular sample under study by the following equations respectively [110, 111]:

$$\beta_\xi = 2\xi \tan\theta \tag{3.12}$$

$$\beta_t = \frac{\lambda}{t\cos\theta} \tag{3.13}$$

where ξ is the microstrain parameter and t is the mean linear dimension of the grain. The sum of both contributions should be determined by a product of convolution. However, this can be simplified by assuming that the convolution can be expressed as a direct sum of both contributions,

$$\beta = \beta_\xi + \beta_t = 2\xi \tan\theta + \frac{\lambda}{t\cos\theta} \tag{3.14}$$

By shifting the term $\cos\theta$ to the left part of the equation we obtain

$$\beta\cos\theta = 2\xi\sin\theta + \lambda/t \tag{3.15}$$

This equation has the shape of a linear function where we have set $y = \beta\cos\theta$ and $x = \sin\theta$. Thus, the strain parameter ξ and the particle size t can be estimated with the slope and the intercept respectively. This method was proposed by G. K. Williamson and W. H. Hall in their famous article [111], for which the graphic representation of $\beta\cos\theta$ against $\sin\theta$ is commonly known as the **Williamson-Hall plot**.

Table 3.2: Figures of merit for Rietveld refinements [109].

Profile residual	$R_p = 100\% \times \sum_i \lvert y_i - y_{ic}\rvert / \sum_i y_{ic}$
Weighted profile residual	$R_{wp} = 100\% \times \sqrt{\sum_i w_i (y_i - y_{ic})^2 / \sum_i w_i (y_{ic})^2}$
Expected profile residual	$R_{exp} = 100\% \times \sqrt{(n-p)/\sum_i w_i (y_{ic})^2}$
Goodness of fit	$\chi^2 = R_{wp}/R_{exp}$

The quality of the refinement is obtained by comparing the observed and calculated intensities for the integrated pattern. Different figures of merit are used to evaluate the goodness of the refinement. Some of these are summarized in Table 3.2. In principle, an accurate refinement of the structure should result in small values of the profile residuals. For example, a refinement can be considered accurate for $R_{wp} < 5\%$ and $\chi < 1.3$. However, these values can sometimes be misleadingly small due to a very high background signal for instance. A deeper discussion about the desired values of the figures of merit in Rietveld refinements can be found in Ref. [109].

3.3 Raman spectroscopy

Raman spectroscopy constitutes an extremely relevant technique for studying elementary excitations in solids in interaction with visible light (usually from a laser source). Raman scattering is produced either by a change in the polarizability of molecules or in the susceptibility tensor of a solid [112]. The relationship between the electric field $\mathbf{E_0}$ of the incident light wave and the induced polarization $\mathbf{P}$ is mediated by the susceptibility tensor χ,

$$\mathbf{P} = \epsilon_0 \chi \mathbf{E_0} \tag{3.16}$$

Different types of collective excitations such as phonons, polaritons, magnons, etc., can induce changes in the susceptibility tensor. However, since the Raman scattering experiments described in this dissertation are all focused in lattice dynamics, we will only consider the changes induced by phonons. These experiments are carried out using visible light, whose momentum is much more smaller than the size of the Brillouin zone: $|k| \lll |\mathbf{G}|$. Therefore, Raman scattering is produced only by the phonons close to the center of the Brillouin zone ($|\mathbf{q}| \approx 0$).

The susceptibility tensor χ is a function of the displacements $X(\omega_q)$ associated with the vibration (whose frequency is ω_q). These displacements are small, so that the two first terms of the Taylor series are enough,

$$\chi = \chi_\mathbf{0} + \left(\frac{\partial \chi}{\partial X}\right)_0 X + \dots \tag{3.17}$$

Assuming that the displacements and the electric field can be written as $X = X_0 \cos \omega_q t$ and $\mathbf{E_0} = \hat{\mathbf{E}}_\mathbf{0} \cos \omega_0 t$, the polarization appears as

$$\mathbf{P} = \epsilon_0 \chi_\mathbf{0} \hat{\mathbf{E}}_\mathbf{0} \cos \omega_0 t + \frac{1}{2}\epsilon_0 \left(\frac{\partial \chi}{\partial X}\right)_0 X_0 \hat{\mathbf{E}}_\mathbf{0} \left[\cos\left(\omega_0 + \omega_q\right)t + \cos\left(\omega_0 - \omega_q\right)t\right] \tag{3.18}$$

Thus, the scattered radiation contains three different contributions. The first one is the elastic

scattered radiation, with the same frequency than the incident light (this process is commonly known as Rayleigh scattering). The other two constitute the Raman bands, with frequencies $\omega_0 - \omega_q$ and $\omega_0 + \omega_q$. These are the Stokes and Anti-Stokes lines respectively. In addition to this, Raman scatterring will take place only if $\partial\chi/\partial X \neq 0$. Hence, only vibrations that induce a change in the susceptibility tensor will be **Raman active**. The three rank matrix $\partial\chi/\partial X$ is commonly known as the **Raman tensor**. Group theory [63] allows to determine which elements of the tensor are zero or finite and thus if a particular mode is Raman active or not. As an example, we show in Tables 3.3 and 3.4 the Raman tensors for two relevant structures in this dissertation, the zircon and scheelite structures (point groups $D_{4h}(4/mmm)$ and $C_{4h}(4/m)$ respectively), extracted from the Bilbao Crystallographic Server [113].

Table 3.3: Raman tensors for a zircon-type structure ($\Gamma_R = 2A_{1g}+4B_{1g}+B_{2g}+5E_g$, where Γ_R is the irreducible representation of the Raman modes).

A_{1g}	B_{1g}	B_{2g}	^1E_g	^2E_g
$\begin{pmatrix} a & 0 & 0 \\ 0 & a & 0 \\ 0 & 0 & b \end{pmatrix}$	$\begin{pmatrix} c & 0 & 0 \\ 0 & -c & 0 \\ 0 & 0 & 0 \end{pmatrix}$	$\begin{pmatrix} 0 & d & 0 \\ d & 0 & 0 \\ 0 & 0 & 0 \end{pmatrix}$	$\begin{pmatrix} 0 & 0 & 0 \\ 0 & 0 & e \\ 0 & e & 0 \end{pmatrix}$	$\begin{pmatrix} 0 & 0 & -e \\ 0 & 0 & 0 \\ -e & 0 & 0 \end{pmatrix}$

Table 3.4: Raman tensors for a scheelite-type structure ($\Gamma_R = 3A_g + 5B_g + 5E_g$).

A_g	B_g	^1E_g	^2E_g
$\begin{pmatrix} a & 0 & 0 \\ 0 & a & 0 \\ 0 & 0 & b \end{pmatrix}$	$\begin{pmatrix} c & d & 0 \\ d & -c & 0 \\ 0 & 0 & 0 \end{pmatrix}$	$\begin{pmatrix} 0 & 0 & e \\ 0 & 0 & f \\ e & f & 0 \end{pmatrix}$	$\begin{pmatrix} 0 & 0 & -f \\ 0 & 0 & e \\ -f & e & 0 \end{pmatrix}$

In Fig. 3.14 we show the basic scheme of the Raman spectroscopy in-house built set up that was used in our experiments. This includes a He-Ne laser ($\lambda = 632.8$ nm), whose plasma lines

are used for the detector calibration. A movable filter is used to remove this lines at the time of measurement. The laser beam is redirected to a beam splitter with a system of mirrors. The light is focused on the pressure chamber of the DAC by using a confocal microscope. The incident power of the laser light on the sample is 10 mW. The load inside of the DAC can be monitored with a video camera. The light scattered backwards, goes back to the beam splitter, passes through the filter, a monochromator with a 600 groves/mm grating (TRH 1000, JobinYvon) and finally arrives to a thermoelectric-cooled multi-channel CCD detector (Synapse, Horiba Jobin Yvon). The resolution of the system is $\sim$ 1 cm^{-1}. In this case, the filter located before the monochromator allows to minimize the elastic scattering contribution to the spectra, which is several orders of magnitude greater than the Raman contribution. The two kinds of available filters in this set up are the multilayer edge filter and the Notch filter. The former acts as a low-pass frequency filter, so that the contribution of the laser line as well as the Antistokes part of the spectra is suppressed. On the contrary, the Antistokes part is visible if a Notch filter is used. This kind of filter is constituted by three Bragg gratings with variable period and allows to go down to 4 cm^{-1} (with respect to the laser frequency) for a sample in air and 30 cm^{-1} if a DAC is used (due to diamond elastic

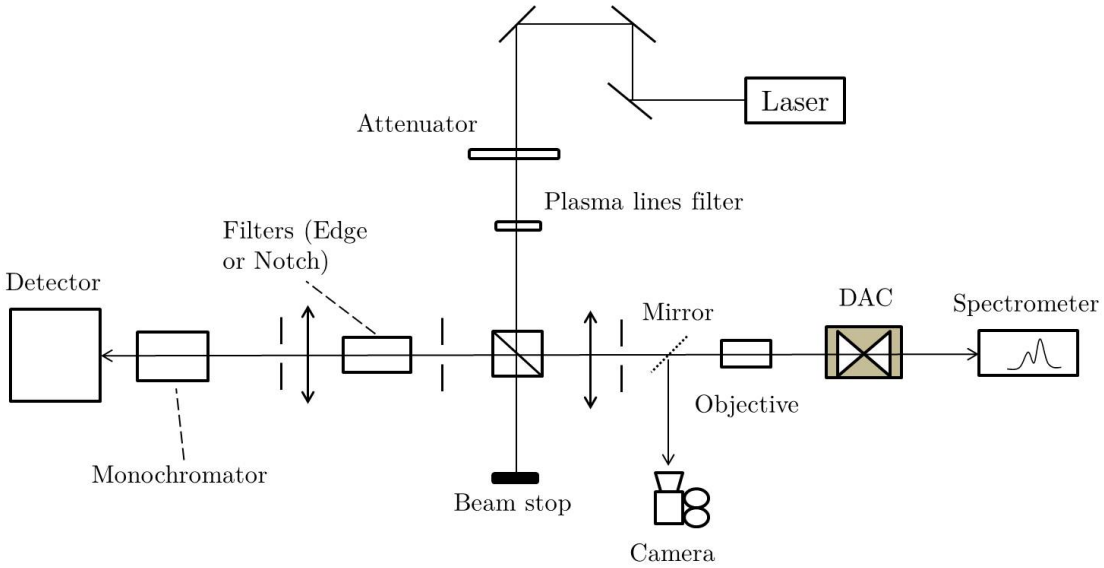

Figure 3.14: Basic scheme of the Raman spectroscopy set up used for the experiments reported in this dissertation.

scattering). The light that pass through the cavity of the DAC is collected by a spectrometer, which is used for measuring the ruby luminiscence (pressure calibrant).

3.4 Optical absorption

The main purpose of optical absorption measurements in solid semiconductors is the characterization of their absorption edge and consequently the determination of their band gap energies. In our experiments, we obtained the transmittance spectra for some thin single-crystals, which allowed us to calculate the optical absorption coefficient. Let us consider an incident monochromatic electromagnetic wave on a plane-parallel semiconductor layer. The electromagnetic wave will undergo a series of internal reflections which depend on the wavelength, the thickness of the layer and the particular optical properties of the sample. As a consequence, the transmittance will take the form

$$T = \frac{(1-R)^2 e^{-\alpha d}}{(1-Re^{-\alpha d})^2 + 4Re^{-\alpha d}\sin^2(\delta/2)} \tag{3.19}$$

where d is the thickness of the layer and α is the absorption coefficient. The phase shift δ and the reflectivity R are given by the following expressions,

$$\delta = \frac{4\pi n d}{\lambda} \tag{3.20}$$

$$R = \frac{(n-n_0)^2 + \kappa}{(n+n_0)^2 + \kappa} \tag{3.21}$$

n and n_0 are the refraction indices of the layer and the surrounding medium, and κ is the extintion coefficient of the sample, which is related to the absorption coefficient:

$$\alpha = \frac{4\pi\kappa}{\lambda} \tag{3.22}$$

The most adequate crystals for optical absorption measurements are those in which $\alpha d \sim 3$. Since in most indirect semiconductors α is of order ~ 5000 cm^{-1} at room conditions, the order of magnitude of d is around 10μm. Considering that the order of magnitude of λ in our experiments is 10^2-10^3 nm, the values of κ should be in the 10^{-2}-10^{-3} range. Thus, in this case we can neglect κ when estimating R. Moreover, if we also assume that for surrounding mediums like air $n_0 \sim 1$, then Eqn. 3.21 may be simplified as

$$R \approx \frac{(n-1)^2}{(n+1)^2} \tag{3.23}$$

By averaging Eqn. 3.19 in the interval between two transmittance maxima, we have

$$\langle T \rangle = \frac{(1-R)^2 e^{-\alpha d}}{1 - R^2 e^{-2\alpha d}} \tag{3.24}$$

Finally, this equation allows to write the absorption coefficient as a function of $\langle T \rangle$ as

$$\alpha = \frac{1}{d} \ln \left(\frac{(1-R)^2}{2\langle T \rangle} + \sqrt{\left(\frac{(1-R)^2}{2\langle T \rangle} \right)^2 + R^2} \right) \tag{3.25}$$

For energies near the band gap the variation of n (and therefore R) with the wavelength is rather small. Accordingly, assuming a constant value of n in the this range introduces a very minor error in the analysis.

Due to some experimental factors, such as the surface quality of the sample, the size of the detector, changes in the intensity of the light, etc, the measured transmittance is not directly $T_0 = I/I_0$. Commonly, the experimental transmittance is related to the theoretical transmittance by a factor that accounts for all the experimental variables

$$T_{theo} = aT_{exp} \tag{3.26}$$

A well-known method for re-escalating the experimental spectra consists in measuring the transmittance in the region where the transmittance (absorbance) is maximum (minimum). Ac-

cording to Eqn. 3.24, when $\alpha \sim 0$, the value of the transmittance should be

$$\langle T \rangle_{theo}^{max} = \frac{(1-R)^2}{1-R^2} = \frac{1-R}{1+R} \tag{3.27}$$

Thus, for escalating our experimental spectra, it is necessary to multiply the experimental transmittance spectra by

$$a = \frac{\langle T \rangle_{theo}^{max}}{\langle T \rangle_{exp}^{max}} = \frac{(1-R)/(1+R)}{\langle T \rangle_{exp}^{max}} \tag{3.28}$$

Once this has been done, we can proceed to calculate the absorption coefficient as expressed in Eqn. 3.25.

3.4.1 Optical absorption at high pressures

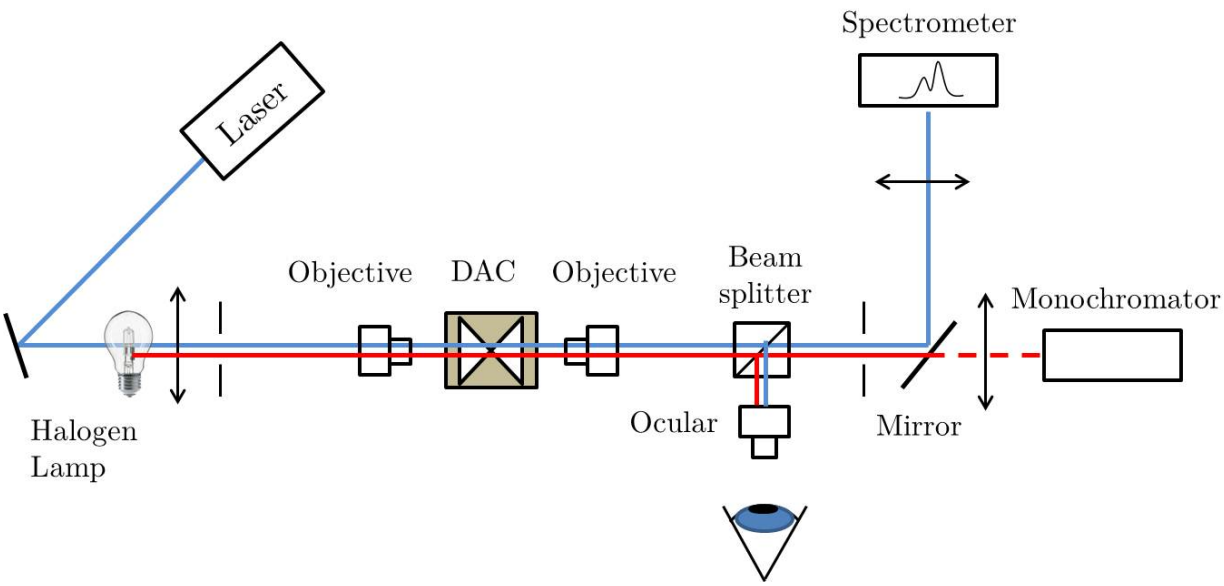

Figure 3.15: In house optical absorption set up for measurements at high pressure.

Fig. 3.15 shows an schematic picture of the typical optical absorption set up for measurements at high pressures. In this set up we combine two different light sources: a halogen lamp, used for the absorption measurements, and laser radiation, used for exciting the rubies, since pressure

is determined by the ruby luminescence method. The path that both kind of radiation follow is depicted in red and blue respectively. The DAC is introduced between two Cassegrain objectives, which are used to focus the light on the sample. Using a beam splitter and an ocular it is possible to observe the pressure chamber of the DAC. By using a movable mirror, it is possible to select if radiation is sent to the spectrometer (laser light) or the monochromator (halogen lamp light).

3.4.2 Optical absorption at low temperatures

On the other hand, Fig. 3.16 shows the optical absorption set up for measurements of single-crystals at low temperatures. In this case, the sample is cooled by using a liquid Helium cryostat, which allows to decrease temperature down to $\sim 13K$. The sample is located in a sample holder attached to a cold finger, through which liquid Helium circulates. The temperature of the surface where the sample is located is measured using a thermocouple and can be heated by a resistive heater, which is connected to a temperature controller. This allows to set the sample to a certain temperature. In order to avoid water condensation and the formation of ice crystals, vacuum conditions must be ensured. Thus, the crysotat is located inside a vessel with optical transparent windows, in which the air is extracted by using a vacuum pump. In contrast to the high pressure set up, the considerable size of the vessel precludes the use of objectives for focusing the light onto the sample, and thus, it is necessary to use a pair of concave mirrors instead. Since the absorption edge of the measured compound ($TbVO_4$) is between 2 and 4 eV, we used a Deuterium lamp as a light source, which provides an excellent light intensity in this spectral range.

3.5 The Paris-Edinburgh large volume press

The diamond anvil cell is a very versatile device in the high pressure sciences field. However, its obvious limitation is the small amount of sample. By contrast, large volume presses allow to work with much larger volumes of sample ($\sim$ 3 mm^3). The problems associated to this kind of

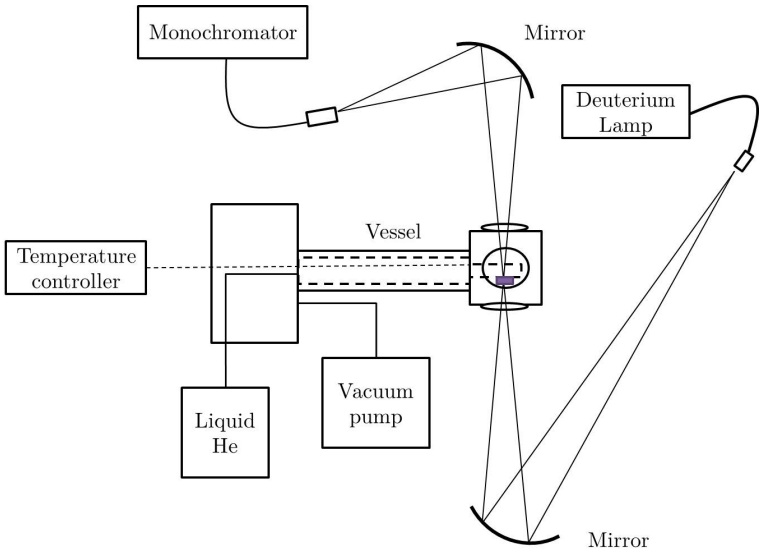

Figure 3.16: In house optical absorption set up for measurements at low temperatures.

cells are: (i) that the range of pressures is quite small ($P < 15$ GPa) compared with a standard DAC and (ii) the lack of optical transparency, although other experiments such as neutron diffraction, resistivity measurements, etc. can be performed. Moreover, large volume presses are especially useful for sample syntheses at high-pressure and high-temperature conditions.

The syntheses described in this dissertation were performed with a Paris-Edinburgh large volume press (model VX, two columns), which is shown in Fig. 3.17 (a). This cell is equipped with two opposite conical tungsten anvils, whose section is shown in Fig 3.17 (b). The pyrophillite gasket that holds the sample is located in between the anvils, surrounded by a teflon ring in order to prevent lateral extrusion. The different parts contained in the gasket are shown in Fig. 3.18. A compacted powder of the sample is introduced in a boron nitride capsule, which acts as a pressure transmitting medium. In turn, this capsule is introduced in a cylindrical graphite heater, which will be used for increasing the temperature of the sample. Two molybdenum rings are placed over and below the graphite oven, acting as electrodes of the heating system.

The pressure of the sample is increased with hand-operated oil pump that moves the cell piston. On the other hand, the temperature of the sample is raised by a computer-controlled

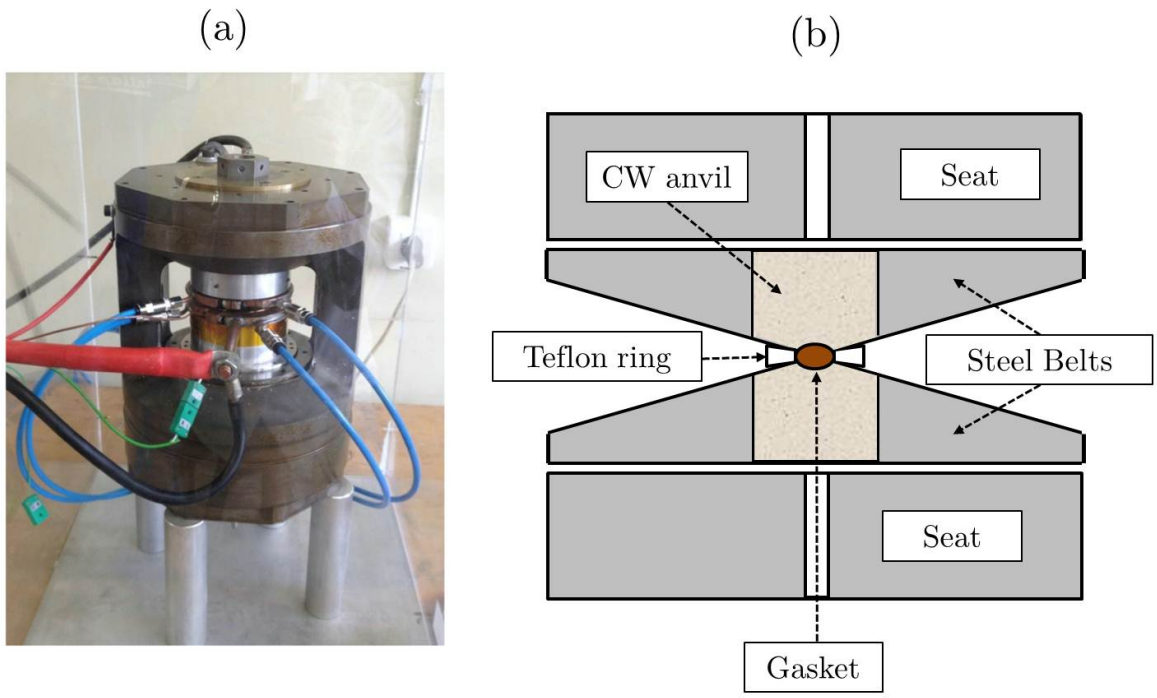

Figure 3.17: Picture of a (a) Paris-Edinburgh large volume cell and (b) section of the pressure anvils.

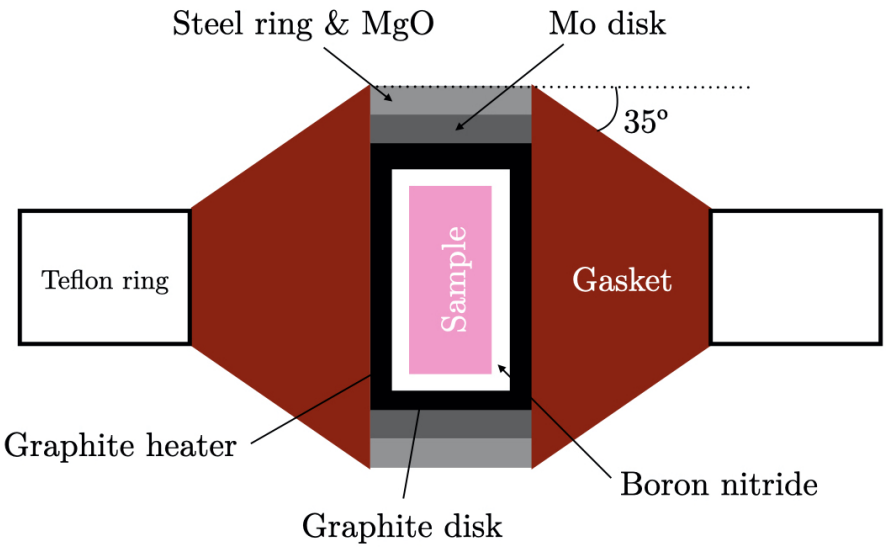

Figure 3.18: Constitutive parts of the pressure chamber in a Paris-Edinburgh large volume press cell.

power supply that heats the graphite oven. The pressure-temperature conditions of the sample can be estimated by the oil-sample pressure and electrical power-temperature calibration curves. In order to avoid an excessive temperature on the tungsten anvils, these are refrigerated using a water cooling system. Under these conditions, the maximum pressure and temperature are 10 GPa and 1500 K. Beyond these conditions, graphite becomes metastable and starts transforming into diamond.

4 | Neodymium orthovanadate under high pressure

Until now, some of the general properties of rare-earth orthovanadates have been described. In particular, we focused our explanations on their different crystal structures (phases), compressibility, vibrational modes and electronic band structure. In addition to this, we also gave detailed information on the theoretical concepts and experimental methods necessary to understand our research. In this Chapter, we start the exposition of our scientific achievements by presenting the obtained results of our study on $NdVO_4$ under high-pressure (HP) conditions. However, before starting with our particular contributions, it seems appropriate to start with a brief summary on earlier studies on $NdVO_4$ under compression.

In this regard, previous experiments confirmed the existence of a first phase transition at 6.5 GPa and suggested a second one at higher pressures. More specifically, powder XRD HP experiments on $NdVO_4$ using a 16:3:1 methanol-ethanol-water (MEW) as PTM reported the existence of a zircon-to-monazite phase transition around 6.5 GPa [41]. This finding was later reinforced by single-crystal optical absorption experiments, in which the band gap of $NdVO_4$ showed two sharp falls at 6 GPa and 11 GPa. These bandgap collapses were associated to a zircon-to-monazite and monazite-to-scheelite phase transitions respectively [48]. In addition to this, Panchal et al. [114] reported some HP Raman spectroscopy experiments in which the monazite phase appears at 6.5 GPa, also using 16:3:1 MEW as PTM. A second phase transition was also reported, not at 11

GPa like previous experiments, but at 18.1 GPa instead. Such results were supported by *ab initio* density functional theory (DFT) calculations, which found that the enthalpy of the monazite phase is lower than that of the zircon phase beyond 5.9 GPa. These calculations also showed that the $BaWO_4$-II-type structure should be the most stable phase beyond 12.4 GPa. In this case, the stability of the scheelite phase is not analyzed.

Therefore, according to all these findings, the zircon-to-monazite phase transition in $NdVO_4$ under high pressure using 16:3:1 MEW as PTM seems to be well confirmed. Nonetheless, some studies have reported that non-hydrostatic stresses can alter either the structural sequence or the transition pressure of some vanadium ternary oxides under compression [115–118]. A good example of this would be $CeVO_4$, which shows different high pressure phases depending on the used PTM [40] i.e. the structure goes from the zircon to the scheelite structure when BN is used as PTM whereas it transforms into a monazite structure under quasi-hydrostatic conditions. Since R = Nd and Sm constitute the boundary in the RVO_4 family of the zircon-to-monazite/scheelite systematic reported in literature, hydrostatic conditions may be of special relevance. Although 16:3:1 MEW is considered to be quasi-hydrostatic below 10 GPa, compounds in the systematic boundary (R = Pr, Nd, Sm) may be extremely sensible to stresses. Therefore, He or Ne gases need to be used in order to optimize the hydrostatic conditions and thus determine which $NdVO_4$ structure is the most stable at high pressures.

In this chapter we present our results reported in Refs. [44] and [46] in which we study the high pressure evolution of $NdVO_4$ under optimal hydrostatic conditions. We performed HP powder XRD experiments up to 25 GPa and Raman spectroscopy measurements up to 20 GPa using He and Ne gases as PTM respectively. We show that, contrary to the results previously reported, there is a zircon-to-scheelite transition around 6.5 GPa. We also found evidence of a second phase transition from scheelite- to a fergusonite-type structure at 20 GPa, probably induced by a mechanical instability. Our findings are supported by *ab initio* DFT calculations.

4.1 Experimental details

Optically clear $NdVO_4$ single-crystals were synthesized by means of the flux growth method [119–121], using a 1:1.923 mol mixture of V_2O_5 and PbO (99% Carlo Elba and Sigma Aldrich respectively). Borax ($Na_2B_4O_7 \cdot 10H_2O$) was used as flux modifier. This allowed to increase the size of the crsytals up to 1 cm long. Platinum crucibles of 4 cm diameter and 6 cm height were filled with both the flux and the precursor (Nd_2O_3, 0.7394 g, purity 99.99%, Sigma Aldrich). These crucibles were sealed with a platinum lid and heated in a programmable oven. The mixture was dehydrated by heating it at 250℃ during 2 hours. Afterwards, temperature was progressively increased during 10 hours up to 1300 ℃ and fixed at that level for 15 hours. In order to promote the growth of the crystals by precipitation and spontaneous nucleation, temperature was the decreased to 950 ℃ at a rate of -1.8 ℃ h^{-1}. Finally, the crucible was taken out of the oven, rapidly reversed (to ease the recovery of the crystals) and let to cool down. After removing the platinum lid, the crucible was submerged in a beaker with hot nitric acid (1.5 M). The excess flux was totally dissolved by stirring and renewing the acid multiple times. The zircon-type structure was confirmed by room conditions XRD measurements. The obtained unit-cell parameters a = 7.333(1)Å and c = 6.438(1) Å are in agreement with previously reported values [50, 51].

Angle-dispersive XRD experiments at high pressure were performed at the European Synchrotron Radiation Facility (ESRF Grenoble, beamline ID15B). Sample compression was carried out using a DAC with 300 μm diameter culets. The sample and some ruby chips were introduced in a 150 μm hole of a stainless-steel gasket, which was preindented to a thickness of 40 μm. During the loading, special care was taken in order to avoid sample bridging and inter-grain stresses. Pressure was determined by the ruby luminescence method. He gas was loaded inside the DAC with the Sanchez Technologies gas loading system available at the ESRF. Helium ensures a fluid medium below 12 GPa and is nearly hydrostatic below 25 GPa [99]. The powder XRD 2D patterns were integrated using the software Dioptas [122]. The integrated patterns were analyzed using

the PowderCell and UnitCell software packages [123, 124].

In the case of the Raman spectroscopy experiments, we used an in-house built setup with a confocal microscope, a 1m focal length monochromator with a 600 groves/mm grating (TRH 1000, JobinYvon), and a thermoelectric-cooled multi-channel CCD detector (Synapse, Horiba). The resolution of the system is 1 cm^{-1} approximately. A scheme of this system is shown in Fig. 3.14 in Chapter 3. The wavenumber scale of the measured spectra were calibrated according to the plasma lines of the He-Ne laser (λ = 632.8 nm). The incident power of the laser light on the sample was 10 mW. For this experiment we used a DAC with culets of 350 μm diameter. Powder sample and ruby chips were loaded in a 150 μm hole drilled in an Inconel gasket, preindented to a 40 μm thickness. Ne gas was loaded in the pressure chamber of the DAC with the Sanchez Technologies apparatus available at the Applied Physics Department of the University of Valencia.

4.2 Simulation details

The simulations used to study $NdVO_4$ were carried out within the framework of the density functional theory (DFT) [125] using the so-called *Vienna Ab initio Simulation Package* (VASP) [126]. The projector augmented wave (PAW) [127, 128] pseudopotential used was provided by the VASP pseudopotentials base. Particularly, we considered a pseudopotential in which the $4f$ electrons are included in the core, since recent works [43] have shown that it is not necessary to include them as valence. The generalized gradient approximation (GGA) with the AM05 prescription [129] was used to describe the exchange-correlation energy. The integration in the Brillouin zone (BZ) was performed using a plane wave basis with a kinetic energy cutoff of 540 eV and a dense k-special points grid for getting accurate results [130]. Optimal structural configurations were obtained by relaxing the external and internal parameters as well as minimizing atomic forces and stresses. As a result, a set of theoretical unit-cell volumes, energies and pressures was obtained.

Lattice dynamics properties were calculated in the harmonic approximation with the Phonopy package [131]. Taking the relaxed primitive cells of the analyzed structures as a starting point and considering their symmetries, this method allows to calculate the Hellman-Feynman forces and the dynamical matrix. Hence, it is possible to derive the frequencies, the eigenvectors and the irreducible representations of the normal modes at the center of the BZ. We used this method to determine the phonon density of states and the dispersion using supercell calculations. The elastic properties of the structures were also determined using the method implemented in the VASP code [132, 133]. The stiffness tensor of the different structures was calculated for the fully optimized structures within the harmonic approximation considering small deformations and their corresponding strains.

The calculations here reported were performed by our collaborators at the University of La Laguna (ULL; Tenerife, Spain) i.e. Alfonso Muñoz, Plácida Rodríguez-Hernández and Isidoro Nieves.

4.3 Powder XRD experiments

Selected integrated powder XRD patters up to 13.3 GPa are shown in Fig.4.1. Below 6 GPa, the pattern can be clearly assigned to a zircon-type structure. Since the cake patterns obtained by the CCD detector show spotty rings as a consequence of a strong preferential orientations in the powder sample, the intensities of the integrated patterns are not reliable. Thus, the atomic positions of the oxygen atoms cannot be refined and only LeBail analyses are possible. A LeBail fitting of this structure at 0.3 GPa is shown in Fig.4.2, for which the χ^2 of the fit is 1.31. The quality of the fitting of other patterns is similar. At 0.3 GPa, the unit-cell parameters of zircon-type $NdVO_4$ obtained after the refinement are $a = 7.3269(2)$ Å and $c = 6.4341(3)$ Å, which are in excellent agreement with other values reported in literature at similar pressures [41, 50].

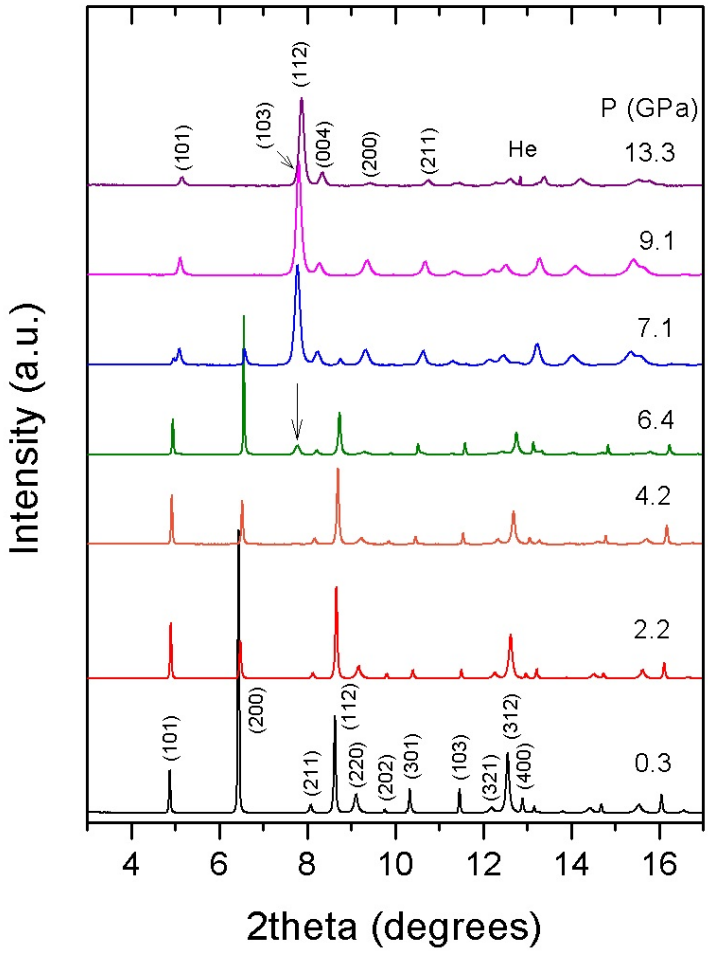

Figure 4.1: Powder XRD patterns of $NdVO_4$ from 0.3 to 13.3 GPa. At the lowest pressure, the zircon (hkl) reflections below 13° are labeled. A new peak arises at 6.4 GPa, which is assigned to the (112) Bragg peak of the scheelite phase. At 13.3 GPa some of the scheelite reflections are labeled. The reflection associated with solid He is indicated.

When compressing the sample beyond 6 GPa, a new phase arises at 6.4 GPa, as can be inferred from the pattern sequence shown in Fig. 4.1. More specifically, the onset of the phase transition, is evidenced by the emergence of a new peak at $2\theta \approx 7.8°$, which is indicated with a vertical arrow at 6.4 GPa. This peak actually corresponds to the (112) reflection of the scheelite-structure (S.G.: $I4_1/a$). For higher pressures, new peaks grow whereas the ones assigned to the zircon phase disappear. The transition pressure is similar to that previously reported in literature, but the high pressure phase is not the monazite- but scheelite-type structure. There is a phase coexistence

of the zircon and scheelite phases up to 8.5 GPa. Beyond such pressure, the scheelite structure appears as a single phase. LeBail refinements of the phase coexistence at 7.1 GPa and the scheelite phase at 9.1 GPa are shown in Fig. 4.2. The peaks associated to the zircon phase during the phase coexistence are too weak in the range 7.1-8.5 GPa, so the zircon structure could not be accurately refined in this range. Therefore, the obtained values in this range for this phase are not included in the analysis.

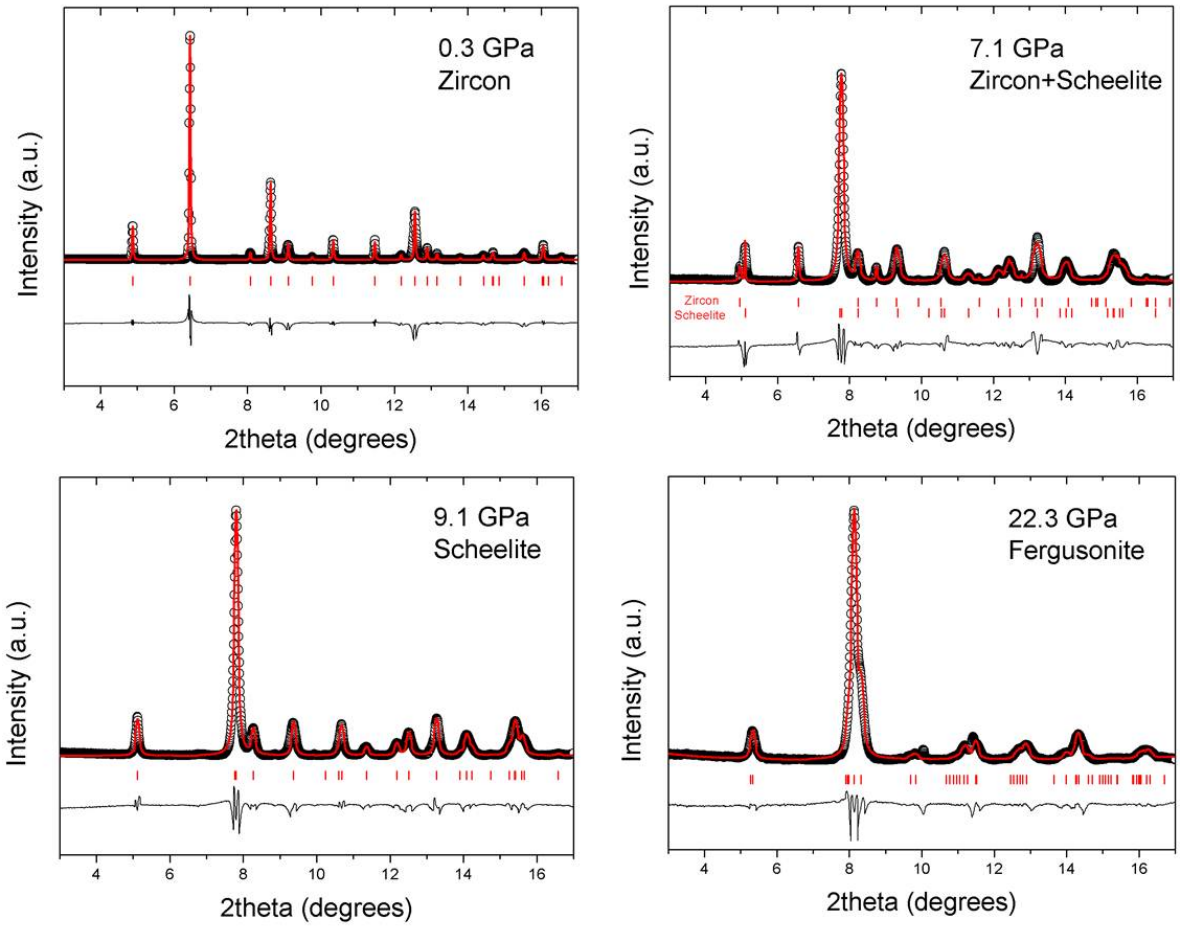

Figure 4.2: LeBail refinement for different structures of NdVO4. The corresponding phases and pressure conditions are indicated in each figure. Experimental data are represented by empty dots; the results of the refinements and the calculated difference are depicted as solid red and black lines, respectively. The refined position of each Bragg reflections is indicated with ticks.

According to the LeBail refinement depicted in Fig. 4.2, the structure found at 9.1 GPa corresponds to a scheelite-type structure whose unit-cell parameters are $a = 5.0376(5)$ Å and $c = 11.4105(7)$ Å. The peaks corresponding to this new phase are broader than those of the zircon phase, probably as a result of the lattice strains and grain cracks induced by the huge volume collapse (10.7% approximately) during the phase transition. The effects of this sharp decrease in the unit-cell volume across the zircon-to-scheelite transition has been studied in $ErVO_4$ [54] as well as in other isostructural compounds such as $TmPO_4$ [134]. Although this broadening is smaller than that observed in other similar experiments with a less hydrostatic PTM, the fact that it takes place even though He is used indicates that this peak broadening is an intrinsic feature of the zircon-to-scheelite phase transition. The induced strains and the change in the grain size

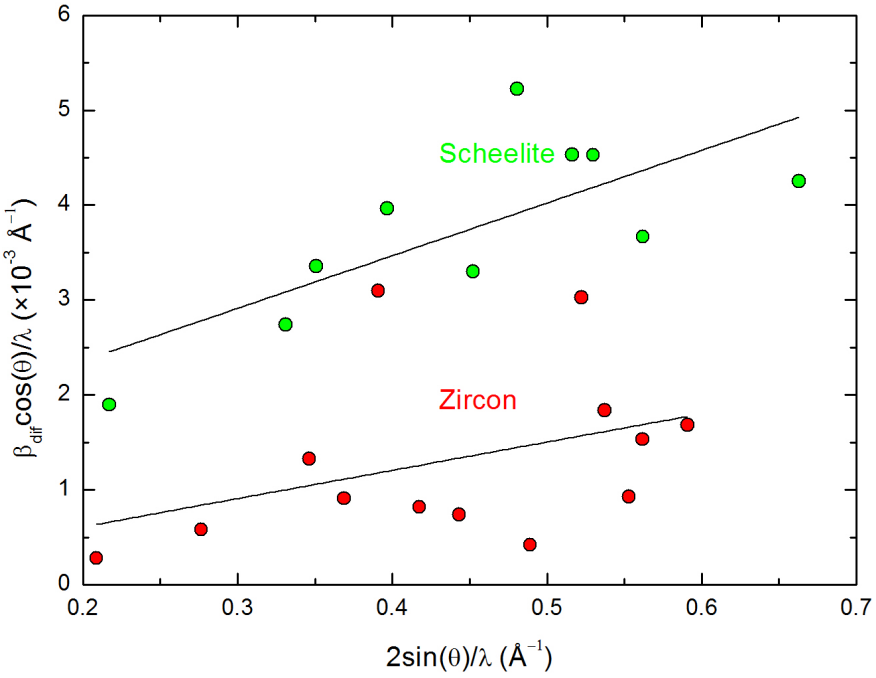

Figure 4.3: Williamson-Hall plot for two XRD patterns of zircon- (red symbols) and scheelite-type (green symbols) $NdVO_4$. The considerable dispersion of the data is related to the spotty character of the XRD patterns.

can be roughly estimated with the kind of analysis proposed by Williamson and Hall [111, 135] (see subsection 3.2.2). The plots for the zircon and scheelite structures of $NdVO_4$ at high pressures are depicted in Fig. 4.3. We chose two XRD patterns of the zircon and scheelite as single phases, avoiding any kind of phase coexistence that might hinder the analysis. The experimental contribution was subtracted by taking the callibrant as reference: $\beta_{dif} = \sqrt{\beta^2 - \beta^2_{callibrant}}$ [135]. We estimated that in the zircon phase of $NdVO_4$ at 4.2 GPa the size of the grain is $t \sim 0.50(5)$ μm, whereas in the case of the scheelite phase at 9.1 GPa the grain size is considerably reduced to $t \sim 0.10(5)$ μm. In other words, grains break as a consequence of the volume sudden decrease. On the contrary, the ξ microstrain parameter increases from $1.2(7) \times 10^{-3}$ in the zircon phase to $6.0(1.8) \times 10^{-3}$ in the scheelite phase, which is also compatible with a huge change in volume. Therefore, both facts contribute to the peak broadening: a grain size five times smaller and a microstrain parameter five times higher.

The scheelite phase of $NdVO_4$ is stable up to 19.9 GPa, with no significant changes in the peaks width under compression, which means that the sample is still under hydrostatic conditions. At higher pressures, there is a clear peak broadening, which is shown in Fig. 4.4 (a). Moreover, there is a peak splitting of some reflections, as it can be observed in Fig. 4.4 (b). The observed changes in the XRD patterns are compatible with a scheelite-to-fergusonite phase transition, which has been reported in other scheelite-type RVO_4 compounds under high pressure [37, 136]. As an example, Fig. 4.4 (b) shows the splitting of the scheelite (101) reflection ($2\theta \approx 5.3°$) into the (101) and (011) reflections of the fergusonite structure. Similar splitting is observed for other peaks too. As an example, the (112) and (103) reflections of the scheelite phase, which correspond to the most intense peak (although the latter is a minor contribution), split into four different contributions: (103), (031), (−121) and (121). Furthermore, another evidence of the scheelite-to-fergusonite phase transition is the shift of the (004) Bragg reflection of the scheelite phase [(040) in the fergusonite phase] towards lower 2θ angles. This means that whereas the b-axis decreases with pressure in the scheelite phase, it grows when it transforms into the c-axis of the

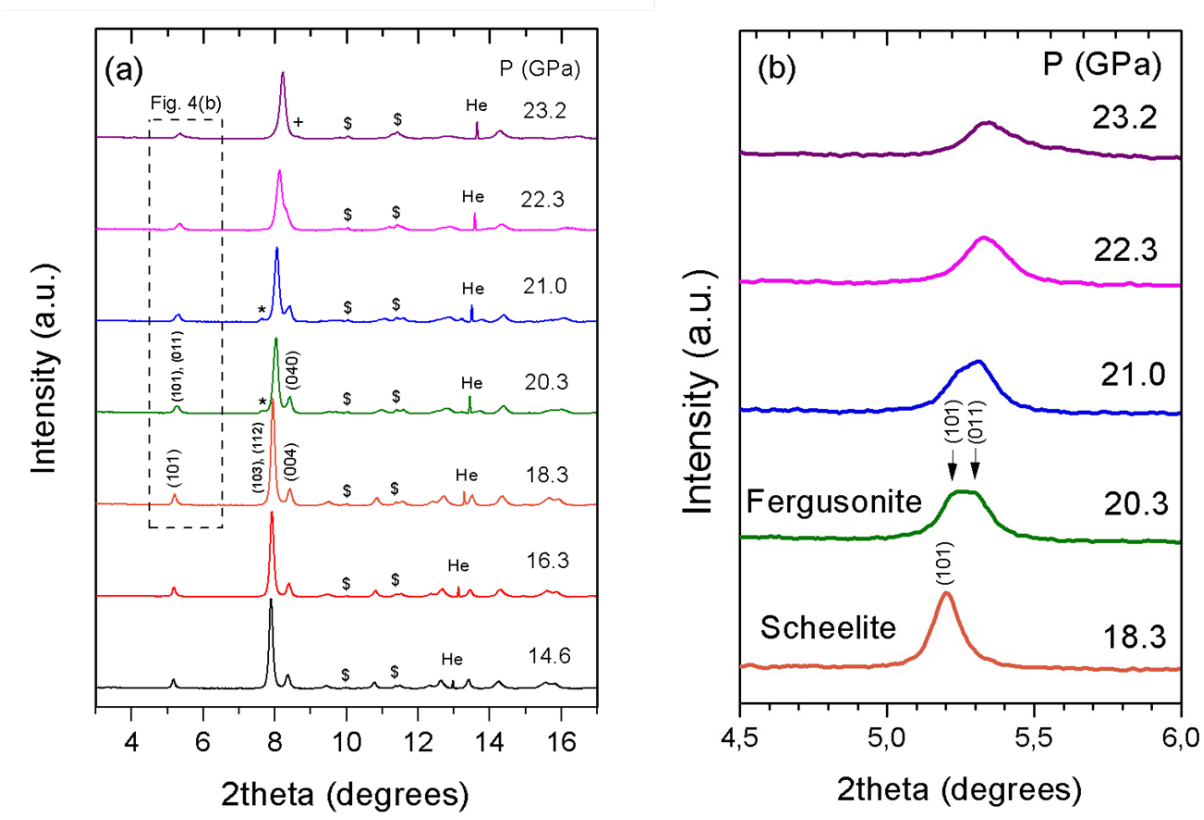

Figure 4.4: (a) Selected powder XRD patterns of NdVO4 from 14.6 to 23.2 GPa. The reflections associated with the solidification of He are identified. The peaks labeled with the symbol "$" correspond to some ruby reflections that came into view just after the recentering of the DAC carried out at 12.5 GPa. The symbols "*" and "+" correspond to the orthorhombic and quasi-amorphous phases of V_2O_5 respectively. The (101) and (112) reflections of the scheelite phase and the (101), (011) and (040) reflections of the fergusonite phase are indicated. (b) Detail of the splitting of the scheelite (101) reflection into the fergusonite (101) and (011) reflections.

fergusonite phase. Fig. 4.2 shows the LeBail profile matching for the fergusonite structure (S. G.: $I2/a$) of $NdVO_4$ at 23.3 GPa. The refined unit-cell parameters are $a = 4.874(2)$ Å, $b = 11.335(6)$ Å and $c = 4.804(4)$ Å and $\beta = 90.40(5)°$. No other phase transitions has been observed up to the maximum pressure achieved in this experiment ($\sim$ 25 GPa).

At the scheelite-to-fergusonite transition pressure, new peaks appear which do not correspond to the fergusonite phase. In particular, a small peak appears at the left hand side of the most intense peak, approximately at $2\theta \approx 7.3°$. This peak is labeled with an asterisk "*" in Fig. 4.4 (a). Some works on RVO_4 under high pressure have reported this peak as the most intense

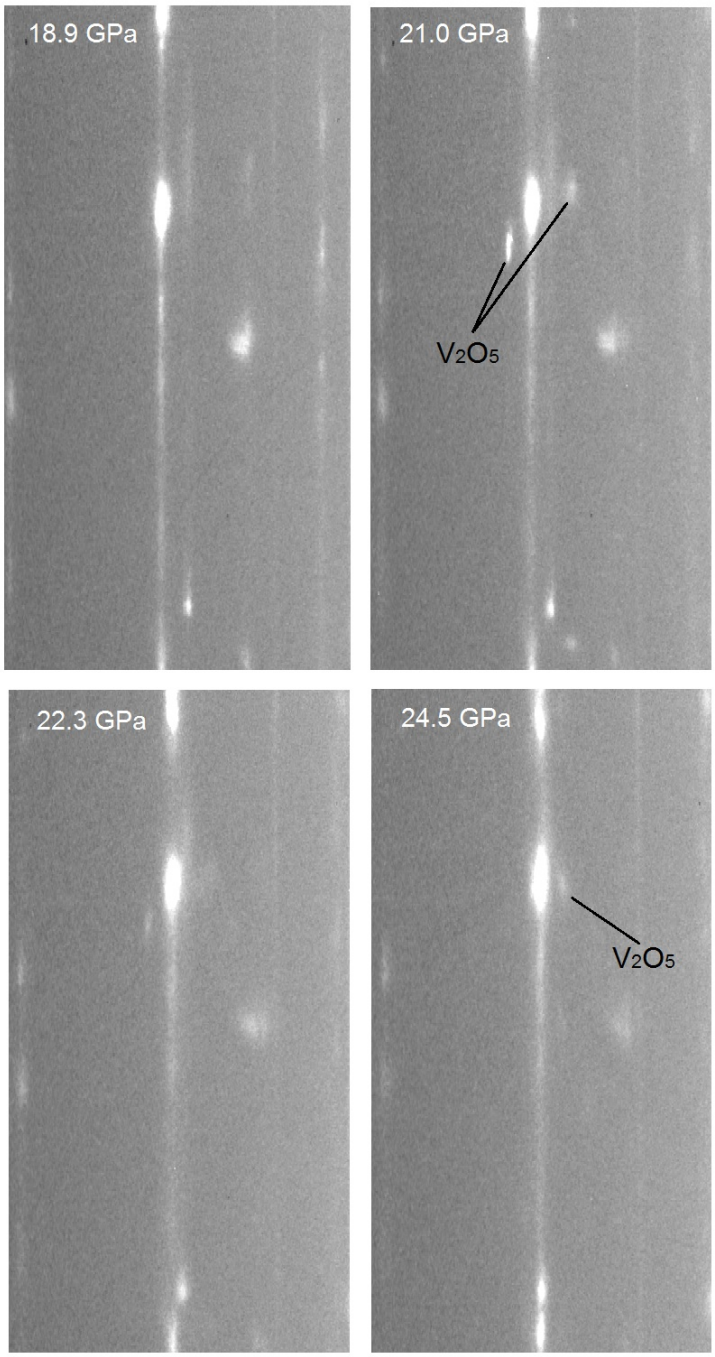

Figure 4.5: Selected un-rolled CCD cake images in the $2\theta \approx 5.6°$- $11.5°$ range at different pressures. At 18.9 GPa the sample is scheelite-type $NdVO_4$. For higher pressures the fergusonite phase is found instead. The spots due to V_2O_5 are indicated. At 21.0 GPa these spots correspond to the orthorhombic phase of vanadium pentaoxide. On the other hand, the spot indicated at 24.5 GPa ($\sim 8.8°$) is assigned to the most intense reflection of the quasi-amorphous phase of V_2O_5 [137].

reflection of orthorhombic V_2O_5 [36, 37], which is produced by a partial decomposition of the sample. According to previous explanations, the decomposition of V_2O_5 units could take place as a consequence of the photoelectric processes induced by a long-time exposition of the sample to X-rays [138]. Nonetheless, the Bragg peaks associated with vanadium pentaoxide are very weak and do not hinder the LeBail refinement of the fergusonite phase XRD patterns. This also indicates that the amount of decomposed V_2O_5 is rather small. Fig. 4.5 shows the appearance and evolution of the reflections associated with vanadium pentaoxide in selected un-rolled CCD cake images. Whereas at 18.9 ° no decomposition is observed, at 21.0 GPa it is possible to observe two of these reflections, which would correspond to the orthorhombic phase. The spot at 8.81° (right hand side of the fergusonite most intense line) is very weak and does not appear in the integrated patterns. These spots become weaker as pressure increases. Then, at the right hand side of the most intense reflection of the fergusonite phase, a weak spot appears, which can be identified as the most intense reflection of quasi-amorphous V_2O_5 [137]. This peak is identified with the symbol "+" in Fig. 4.4. The evolution of these reflections is independent of changes in the patterns associated with the scheelite-to-fergusonite phase transition, which confirms that these reflections do not belong to the $NdVO_4$ sample. The fact that this transition appears just at the transition pressure suggests that the decomposition may be eased by the structural change during the scheelite-to-fergusonite phase transition.

The behaviour of the unit-cell parameters of $NdVO_4$ under high pressure is shown in Fig. 4.6. The linear compressibilities of the zircon-type structure are $\kappa_a = 3.081(8) \times 10^{-3}$ GPa^{-1} and $\kappa_c = 1.556(4) \times 10^{-3}$ GPa^{-1} for the a and c parameters respectively. This non-isotropic behaviour, in which the longest axis is more compressible, is a common feature of zircon-type structures [36, 37, 39, 49, 139]. This fact can be explained as a consequence of the particular packing of the VO_4 and NdO_8 polyhedra in the zircon phase (see sections 1.2 and 1.3 in the Introduction). In particular, the zircon structure is constituted by a succession of alternating edge-sharing VO_4 tetrahedra and NdO_8 dodecahedra distributed parallel to the direction defined by the c-axis. These polyhedral

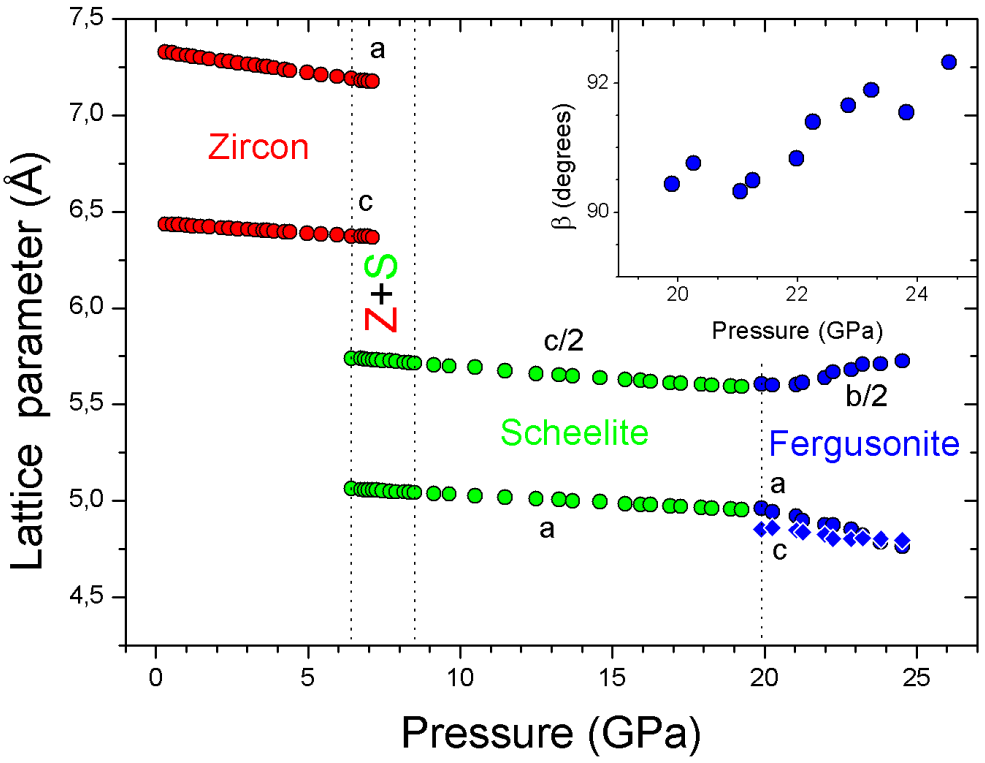

Figure 4.6: Pressure evolution of the unit-cell parameters of $NdVO_4$. Red, green and blue circles represent the experimental data for the zircon, scheelite and fergusonite phases respectively. The *c*-axis of the fergusonite phase is depicted as blue diamonds to avoid confusion. *Inset*: Pressure dependence of the β angle of the fergusonite structure.

chains are laterally attached by edge-sharing NdO_8 dodecahedra along *a*-axis. therefore, the *c*-axis is less compresible than the *a*-axis, since the VO_4 tetrahedra are much less compressible than the NdO_8 dodecahedra, as it has been shown in literature [140]. Additionally, there is a perfect agreement of the extrapolated values of the unit-cell parameters, $a = 7.331$ Å and $c = 6.437$ Å, and the values measured just after the synthesis of the sample.

The zircon-to-scheelite phase transition takes place near 6.4 GPa. The volume collapse associated with this transition is $\sim$ 10.7%. Therefore, according to this huge discontinuity in the unit-cell volume, the transition must be first-order (see section 2.2). As we said before, this volume collapse increases the crystalline disorder, which produces a much broader XRD reflections

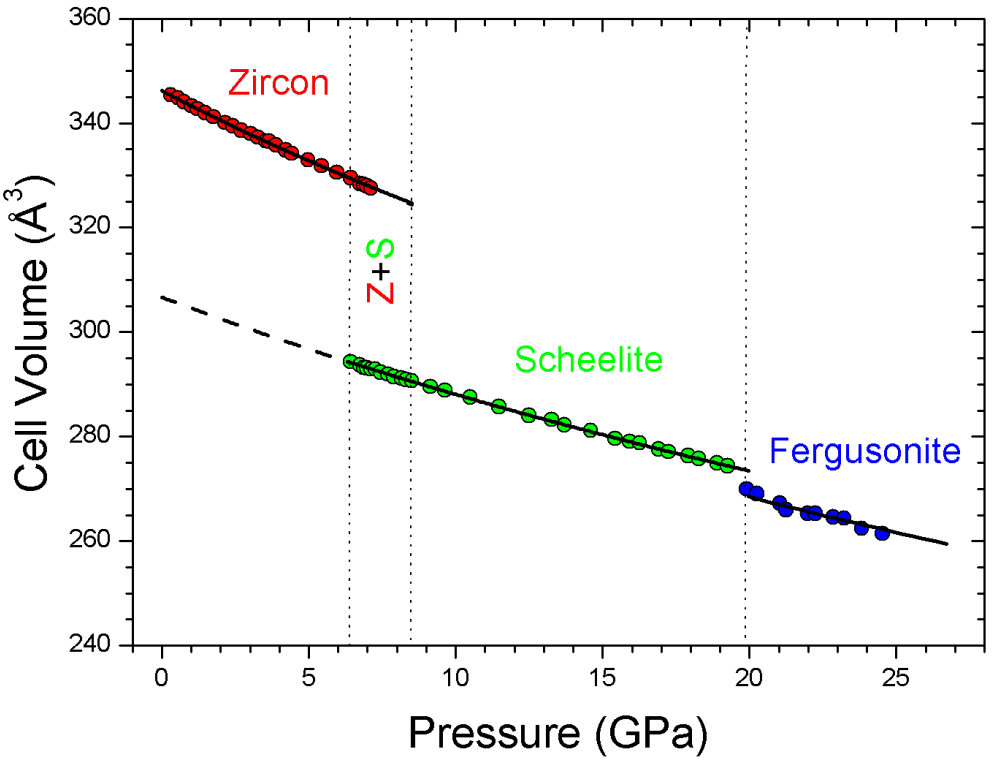

Figure 4.7: Pressure dependence of the unit-cell volume of $NdVO_4$. The red, green and blue circles represent the experimental data for the zircon, scheelite and fergusonite-type structures. The EOS fitted to the experimental data are represented by solid lines. The extrapolation of the EOS at low pressures of the scheelite phase is represented with a dashed line.

for the scheelite structure. Some studies on $ErVO_4$ under high pressure using MEW as PTM have shown that this effect can lead to the inaccurate estimation of the EOS parameters. Nonetheless, we expect that hydrostatic conditions may minimize these effects.

The linear compressibilities of the scheelite phase for the a and c parameters are $\kappa_a = 1.62(2) \times 10^{-3}$ and $\kappa_c = 2.04(3) \times 10^{-3}$ GPa^{-1} respectively. Again, as in the previous phase, we observe an anisotropic behaviour, in which the a lattice parameter is less compressible than c. Similarly to the zircon phase, this anisotropic response to pressure can be explained in terms of the different compressibilities of its constitutive polyhedral units, since the structure of the scheelite phase is also based on the arrangement of VO_4 tetrahedra and NdO_8 dodecahedra. According to the

literature, the zircon-to.scheelite phase transition is irreversible. However, during the experiment, the diamonds of the DAC broke upon compression, so the scheelite phase could not be quenched at low pressures. Nonetheless, we can estimate the values of the lattice parameters at ambient pressure by making a linear extrapolation. By doing so, we obtained the values $a = 5.1143(7)$ and $c = 11.630(3)$ Å, which yield in between of those obtained for $CeVO_4$ and $SmVO_4$ [35, 39], and therefore they can be considered as reasonable.

The evolution of the lattice parameters for the fergusonite phase are also shown in Fig. 4.6. In this case, we observe a small discontinuity between the a-axis of the scheelite structure and the c-axis of the fergusonite phase, which is in contradiction with most observations for similar fergusonite-type oxides. This can be inferred from the sudden splitting of the (101) and (011) peaks of the fergusonite phase in Fig. 4.4 (b) ($2\theta \approx 5.4°$). After such splitting, the a-axis decreases more rapidly than the c-axis in the fergusonite phase. As a consequence of this, both lattice parameters are equal at $\sim$ 23.5 GPa, which can be seen in Fig. 4.6. This can be also be seen in Fig. 4.4 (b), in which we show how the splitting of the (101) and (011) peaks progressively decreases up to 23.5 GPa. On the contrary, the increase of the b-axis and the β angle is similar to other fergusonite-type compounds under high pressure. In fact, the shifting of the (040) Bragg reflection depicted in Fig. 4.4 (a) is a direct consequence if the elongation of the b lattice parameter. This leads to a crossover of the (121) and (040) peaks at 23.5 - 24.5 GPa.

The isothermal compressibility tensor is symmetric and can be described with four independent components i.e. β_{11}, β_{22}, β_{33} and β_{13}, whose expressions are reported in Knight [141]. Considering a linear dependence of the lattice parameters with pressure for the fergusonite phase of $NdVO_4$, the obtained values of the compressibility tensor are $\beta_{11} = 8.8(1) \times 10^{-3}$ GPa^{-1}, $\beta_{22} = -5.47(5) \times 10^{-3}$ GPa^{-1}, $\beta_{33} = 3.12(4) \times 10^{-3}$ GPa^{-1} and $\beta_{13} = 3.57(6) \times 10^{-3}$ GPa^{-1}. The negative value of β_{22} and the positive value of β_{13} are typical of fergusonite-like compounds and can be explained by the elongation of the unique b-axis and the increase in the β monoclinic angle under compression respectively. The symmetric isothermal compressibility tensor can be

diagonalized in order to obtain the directions and magnitudes of the principal axes [141]. The obtained eigenvalues are 10.5(2), −5.47(5), and 1.39(6) GPa−1, whose corresponding eigenvectors are, respectively, $(0.89974, 0, 0.43644)$, $(0, 1, 0)$, and $(0.43644, 0, -0.89974)$. This means that the direction of maximum compressibility is contained within the plane defined by the *a*- and *c*-axes, at 64(2)° with respect to the *c*-axis. Similarly, direction with the smallest compressibility is located within the same plane but perpendicularly oriented.

In addition to this, it is possible to use the volume-pressure data shown in Fig. 4.7 to estimate the isothermal bulk modulus B_0 and its derivative B_0', as well as the zero-pressure unit-cell volume V_0 for the different phases. The fitted EOSs show a maximum misfit lower than 0.05 GPa, which is comparable to the pressure experimental error. This indicates that the pressure behaviour of the crystal is accurately described by this type of EOS. The data corresponding to the zircon and scheelite phases were analyzed with a third order Birch-Murnaghan (BM) EOS, by using the EosFit7 software package. The obtained EOS parameters for these phases are displayed in Table 4.1. With regard to the fergusonite phase, the lack of sufficient data points do not allow an accurate fit to a third order BM EOS. Therefore, we decided to perform the EOS fit assuming $B_0' = 3.4$ as a fixed value, since the scheelite and fergusonite phases show similar compressibilities, as it is shown in Fig. 4.7. The obtained values for V_0 and the bulk modulus B_0 for the fergusonite phase are included in Table 4.1. These values are very similar to those obtained for the scheelite phase, which is a common feature in the scheelite-fergusonite ternary oxides. More specifically, the obtained bulk modulus is identical, which confirms the fact that both structures are equally compressible. In addition to this, both values of V_0 are very similar due to the small change of volume between both phases.

The obtained EOS parameters for the zircon phase are also shown in Table 4.1. We included previously reported data for the sake of comparison. In particular, we show the experimental data reported in Ref. [41] (using 16:3:1 MEW as PTM) and the results of DFT calculations [114]. For $P \leq$ 7.1 GPa, the values of V_0 and the bulk modulus B_0 are quite similar to that given by calculations.

Table 4.1: EOS parameters for the zircon, scheelite and fergusonite phases of $NdVO_4$. for the sake of comparison, we included the calculated and measured values reported in some previous publications.

Phase	PTM	V_0(Å^3)	B_0 (GPa)	B_0'
Zircon [114]	Theory	357.50	124.2	3.66
Zircon [41]	16:3:1 MEW	350.8(9)	148(4)	3.72(2)
Zircon ($P \leq 7.1$ GPa)	He	346.21(6)	121.5(1.9)	2.5(5)
Zircon ($P \leq 6.4$ GPa)	He	346.2(2)	118(2)	3.7(3)
Scheelite	He	306.7(6)	143(8)	3.4(7)
Fergusonite	He	305.5(1.8)	143(12)	3.4 (fixed)

Nonetheless, the value of the bulk modulus second derivative is too small ($B_0' = 2.5(5)$) compared to the calculated value ($B_0' = 3.66$). This huge difference may be attributed to the coexistence of the zircon and scheelite phase beyond 6.4 GPa. This could prevent an accurate analysis of the zircon phase pressure evolution above such pressure. Thus, in order to perform a more accurate EOS analysis, we must consider the data for $P \leq 6.4$ GPa exclusively. As it is shown in Table 4.1, in such case, the obtained values for B_0 and B_0' are in agreement with calculations. In comparison, the experimental values obtained using 16:3:1 MEW as PTM show a less compressible structure, since the bulk modulus is $\sim$ 20% higher than the calculated value, whereas the value reported in this work is only $\sim$ 5% smaller. The small discrepancy between the value of V_0 obtained in this study and the predicted value can be explained by the common tendency of DFT calculations to overestimate unit-cell values.

Since no previous experimental or theoretical data of the sheelite phase of $NdVO_4$ have been published (up to our knowledge), no comparison can be made as in the case of the zircon phase. However, with respect to the zircon phase, the scheelite phase shows a unit-cell volume $\sim$ 11% lower and a bulk modulus $\sim$ 18% higher, which is consistent with the increase in the packing

efficiency associated with first-order reconstructive phase transitions. The extrapolation of the fitted third order BM EOS is depicted in Fig. 4.7 with a dashed line. On the other hand, the scheelite-fergusonite phase transition shows a $\sim$ 1.5% volume collapse, larger than the volume uncertainty associated to measurements. The nature of the scheelite-fergusonite phase transition is still a matter of debates among scholars. For instance, similar results were obtained for $SrWO_4$, in which a 1.5% volume decrease is observed at the transition [142]. Thus, according to this experimental evidence, this transition has been considered a weak first-order martensitic structural transition [1]. On the contrary, no volume discontinuity has been observed in the scheelite-fergusonite phase transition of many orthotungstenates and orthomolybdates at high pressures [144]. In such case, the transition has been considered as a second-order phase transition. The case of $NdVO_4$ seems to correspond to the first kind. Nonetheless, this cannot be said of other orthovanadates such as $BiVO_4$, in which the fergusonite-scheelite phase transition can be definitely classified as ferroelastic second-order [67].

4.4 Raman spectroscopy experiments

As we stated in Chapter 2, the zircon sctructure (S. G.: $I4_1/amd$) has 12 Raman active modes at the center of the BZ i.e. $\Gamma_R = 2A_{1g} + 4B_{1g} + B_{2g} + 5E_g$, according to group theory [63]. Fig. 4.8 shows some selected Raman spectra for $NdVO_4$ upon compression. The different Raman peaks were labeled according to our calculations. With regard to the peak observed near 240 cm^{-1}, it can be labeled as $E_g^{(3)}$ or $B_{1g}^{(2)}$, since their calculated zero-pressure frequencies are relatively close to each other (ω_0 = 231 and 240 cm^{-1}). Even though the calculated value of ω_0 for $B_{1g}^{(2)}$ perfectly agrees with the observed peak position, we decided to label this peak as $E_g^{(3)}$, since the value of the calculated $d\omega/dP$ for this mode is much more coherent with our experimental observations.

[1] In martensitic transformations the displacements of the atoms are simultaneously coordinated so that the translational symmetry of the crystal is preserved along the transition path. These are shear dominant, lattice displacive and diffusionless transitions [143].

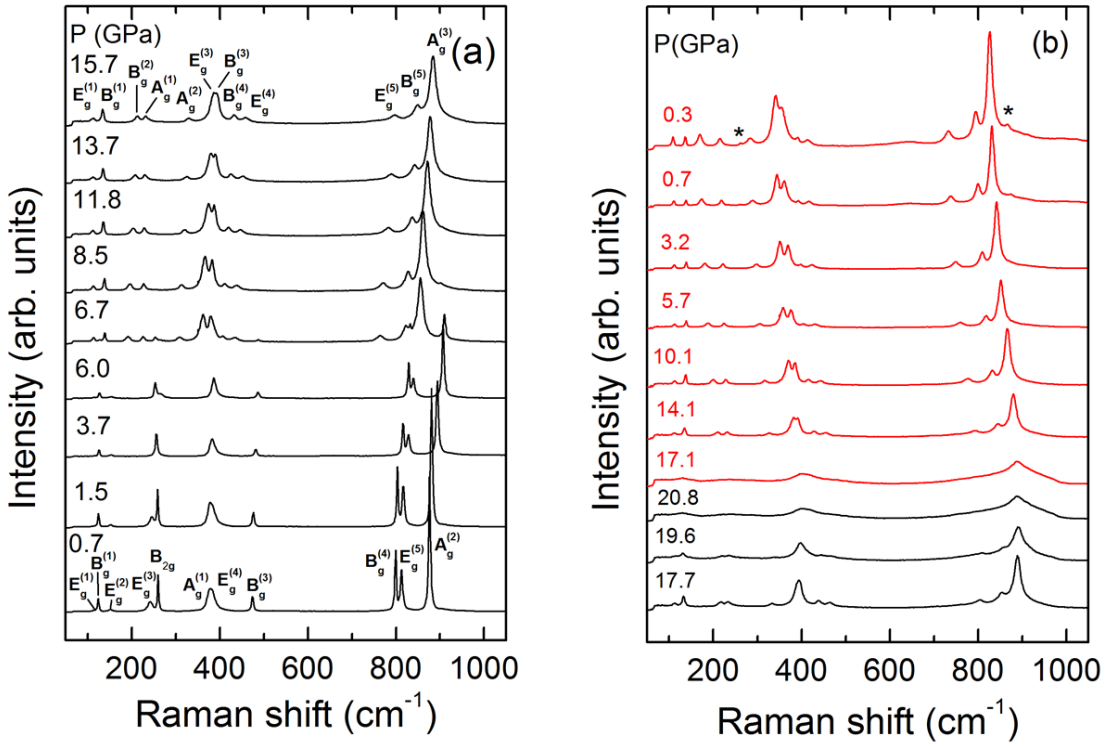

Figure 4.8: Selected Raman spectra for $NdVO_4$ at different pressures. The spectra obtained upon compression and decompression are depicted with black and red solid lines. The Raman peaks indicated with an asterisk do not belong to the scheelite phase, but can be attributed to a zircon-type $NdVO_4$ residual obtained after decreasing pressure.

On the contrary, in Panchal *et al.* [114], the authors reached the opposite conclusion by using the same reasoning. This discrepancy finds its roots not in the calculated values, which are similar to ours, but in the experimental measurements. Thus, only Raman spectroscopy experiments with single-crystals under different orientations can clarify this disagreement. In addition to this, the labelling of the modes $E_g^{(4)}$ and $A_{1g}^{(1)}$ is also different in Panchal *et al.* [114]. While in our study these modes clearly have different $d\omega/dP$ values, in Ref. [114] the pressure evolution of both modes under pressure is very similar, and thus, they are assigned according to the value of the zero-pressure frequency. Apart from these minor discrepancies, in both cases the zircon-type Raman spectra show a large frequency gap between 500 and 800 cm^{-1} approximately, which

can be observed in Fig. 4.8 (a). The modes within the region below 500 cm^{-1} represent the so-called "external modes", which describe the vibration of the rare-earth cation relative to the VO_4 tetrahedra, whereas those beyond 800 cm^{-1} are usually referred as "internal modes" of the vanadium atom inside of the tetrahedra. Although this nomenclature is used in most of literature, in which the modes are identified as R, T and ν, we decided to not make use of it. The reason for this is that, even though the modes at high frequencies can be considered as internal modes of the VO_4 tetrahedra in good approximation, the contribution of the V atom vibrations to the "external modes" is not negligible [67]. In order to be able to distinguish different modes with identical symmetries, we decided to label these with different numerical supra-indexes. As it is shown in Fig. 4.8 (a), the three most intense Raman peaks are in the high-frequency region. The dominating Raman peak $A_g^{(2)}$ corresponds to a symmetric-stretching of the VO_4 tetrahedra, whereas the $E_g^{(5)}$ and $B_{1g}^{(4)}$ modes describe the asymmetric-stretching of these units. On the other hand, the intensities of the modes in the low-frequency region are much weaker, with the only exception of the B_{2g} mode. Only the $B_{1g}^{(2)}$ low-frequency mode is not observed in the Raman spectra, which may be a consequence of its low Raman scattering cross-section. The overlapping with the peaks of the $E_g^{(3)}$ mode, which should be located at similar frequencies, could also hinder its identification. The frequencies of the observed Raman modes at low pressure are shown in Table 4.2.

In the spectra shown in Fig. 4.8 (a), it is clear that there is a qualitative change between 6.0 and 6.7 GPa. Whereas at 6.0 GPa the spectrum corresponds to the zircon structure of $NdVO_4$, it radically changes at the very next pressure. In fact, as we will show, these new spectra can be assigned to the scheelite phase of $NdVO_4$. Therefore, the zircon-to-scheelite transition pressure in this case would be $\sim$ 6.4(3) GPa, which is in perfect agreement with the previous results of our XRD experiments (6.4 GPa, see previous section). In accordance with group theory analysis, the scheelite structure shows 13 Raman active modes at the center of the BZ: $\Gamma_R = 3A_g + 5B_g + 5E_g$ [145, 146]. As in the zircon phase, the assignation of the Raman modes has been made according

to our calculations. In this phase, the spectra is divided in two regions, with a large frequency gap between 480 and 750 cm^{-1}. This similarity with the zircon phase can be explained in terms of the polyhedral constituents, since the modes of the high frequency region can be well approximated to the internal vibrations of the VO_4 tetrahedra. In this region, the symmetric-stretching $A_g^{(3)}$ and the asymmetric stretching modes $B_g^{(5)}$ and $E_g^{(5)}$ are located at 884, 850 and 797 cm^{-1} respectively at 15.7 GPa. The $A_g^{(3)}$ mode constitutes the most intense peak of the spectra. At the same pressure, the observed modes in the region below the frequency gap are $E_g^{(4)}$, $B_g^{(4)}$, $B_g^{(3)}$, $A_g^{(2)}$, $E_g^{(3)}$, $A_g^{(1)}$, $B_g^{(2)}$, $B_g^{(1)}$ and $E_g^{(1)}$, which can be found at 459, 433, 393, 385, 330, 232, 213, 134 and 112 cm^{-1} respectively. Only the $E_g^{(2)}$ mode is not observed in the spectra, probably due to its small Raman cross-section. For pressures higher than 17.7 GPa, there is a progressive broadening of the Raman peaks, which transform into wide bands upon compression. This is compatible with the scheelite-fergusonite phase transition observed in XRD experiments at 19.9 GPa. In this case, according to our Raman measurements, the transition pressure should be in between 17.7 and 19.6 GPa. The fact that the transition pressure is slightly lower in the Raman than in the XRD experiments could be attributed to the hydrostatic differences of Ne and He gases at 20 GPa [99]. This phase transition takes place as a consequence of a mechanical instability that induces a monoclinic distortion of the scheelite phase, leading to the fergusonite structure, as it is explained in the next section. Upon decompression, this transition is reversed between 17.1 and 14.1 GPa, as it is shown in Fig. 4.8 (b). The scheelite phase is recovered at low pressures in a metastable state, revealing the existence of a considerable kinetic barrier between the zircon and scheelite phases of $NdVO_4$. This confirms our previous statement that the zircon-to-scheelite phase is an irreversible first-order transition. Nonetheless, in the spectra corresponding to the recovered sample, two peaks that do not correspond to the scheelite structure can be observed. These are labeled with asterisks in Fig. 4.8 (b). On the contrary, these peaks seem to correspond to the B_{2g} and $A_{1g}^{(2)}$ modes of the zircon phase, which also give rise to the most intense Raman peaks in the low- and high-frequency regions of the spectra, respectively. Thus, a small fraction of the zircon phase is also recovered

at low pressures, although most of the recovered sample is metastable scheelite-type $NdVO_4$.

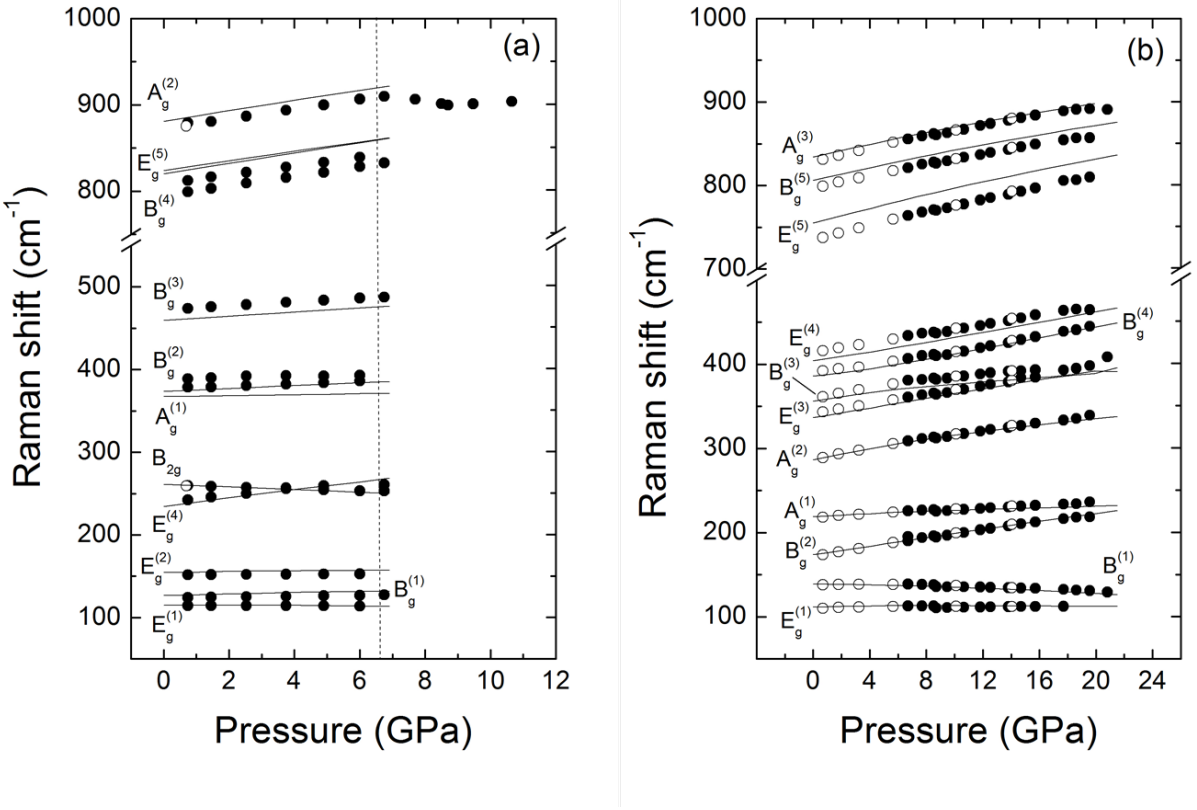

Figure 4.9: Pressure evolution of the frequency of the Raman modes for the (a) zircon and (b) scheelite phases of $NdVO_4$. Experimental data are represented with black (compression) and void (decompression) circles. Solid lines represent theoretical calculations.

The change in frequency of the observed Raman modes under compression and decompression is depicted in Fig. 4.9 for the (a) zircon and (b) scheelite polymorphs of $NdVO_4$. With regard to the zircon phase, the frequency of most of the modes increases with pressure, with the only exception of the B_{2g} mode, whose frequency decreases upon compression. As a result, there is a mode cross-over of this mode and the $E_g^{(4)}$ mode near 3.7 GPa. Beyond that pressure, the frequency of the B_{2g} mode becomes smaller than that of the $E_g^{(4)}$ mode. By performing a linear fitting for both the experimental and calculated values, we could estimate the value of the frequency pressure coefficients at low pressures i.e. $d\omega/dP$. The obtained results for the zircon phase are shown

in Table 4.2.

Table 4.2: Experimental and calculated values of the pressure coefficients, zero-pressure frequencies and Grüneisen parameters of zircon-type $NdVO_4$. The Grüneisen parameters were calculated considering $B_0 = 124.2$ and 118(2) GPa [44] for the theoretical and experimental set of values respectively. For the sake of comparison, we included the values of the zero-pressure frequencies reported in Santos *et al.* [147]. The values indicated with asterisks are labeled as B_{1g} and B_{2g} (261 and 375 cm^{-1} in the table respectively) in Ref. [147], although they should be labeled as B_{2g} and $A_{1g}^{(1)}$ according to our calculations.

	Theory			Experiment			Ref. [147]
Mode	$d\omega/dP$ (cm^{-1}/GPa)	ω_0 (cm^{-1})	γ	$d\omega/dP$ (cm^{-1}/GPa)	ω_0 (cm^{-1})	γ	ω_0 (cm^{-1})
$E_g^{(1)}$	0	115	0	0.00(5)	114	0.00(5)	113
$B_{1g}^{(1)}$	0.75	127	0.77	0.56(8)	124	0.53(1)	123
$E_g^{(2)}$	0.70	155	0.56	0.22(2)	152	0.17(2)	148
$E_g^{(3)}$	4.93	234	2.61	4.17(16)	240	2.05(5)	237
$B_{1g}^{(2)}$	2.86	241	1.48	-	-	-	-
B_{2g}	−1.61	261	−0.77	−1.09(7)	260	−0.49(5)	261*
$E_g^{(4)}$	0.58	367	0.20	0.7(2)	389	0.21(2)	381
$A_{1g}^{(1)}$	1.72	374	0.57	1.44(9)	377	0.45(2)	375*
$B_{1g}^{(3)}$	2.50	459	0.68	2.27(6)	473	0.57(2)	472
$B_{1g}^{(4)}$	6.01	820	0.91	5.53(4)	795	0.82(2)	795
$E_g^{(5)}$	5.50	824	0.83	5.05(6)	809	0.74(2)	808
$A_{1g}^{(2)}$	5.95	881	0.84	5.34(15)	874	0.72(2)	871

On the other hand, all of the observed Raman modes of the scheelite phase harden in the low pressure range, as it is depicted in Fig. 4.9 (b). Similarly to the previous case, we performed a linear fitting in order to obtain the values of $d\omega/dP$, ω_0 and the Grüneisen parameters γ. For such analysis, only the data taken upon pressure release could be used. The obtained values for the cal-

Table 4.3: Experimental and calculated values of the pressure coefficients, zero-pressure frequencies and Grüneisen parameters of scheelite-type $NdVO_4$. The Grüneisen parameters were calculated considering B_0 = 143 and 143(8) GPa [44] for the theoretical and experimental set of values respectively.

	Theory			Experiment		
Mode	$d\omega/dP$ (cm^{-1}/GPa)	ω_0 (cm^{-1})	γ	$d\omega/dP$ (cm^{-1}/GPa)	ω_0 (cm^{-1})	γ
$E_g^{(1)}$	0.48	111	0.62	0.54(9)	110	0.70(5)
$B_g^{(1)}$	−0.13	139	−0.13	0.22(9)	138	0.23(9)
$B_g^{(2)}$	2.46	174	2.02	2.44(5)	173	2.02(12)
$E_g^{(2)}$	2.57	175	1.82	-	-	-
$A_g^{(1)}$	0.60	219	0.34	0.86(3)	219	0.48(3)
$E_g^{(3)}$	2.38	287	1.03	2.53(6)	290	1.08(7)
$A_g^{(2)}$	2.73	337	1.01	2.77	342	1.01(6)
$B_g^{(3)}$	1.60	356	0.56	1.9(1)	365	0.64(5)
$B_g^{(4)}$	3.01	386	0.97	2.83(7)	388	0.91(6)
$E_g^{(4)}$	2.93	404	0.90	2.71(5)	415	0.81(5)
$E_g^{(5)}$	3.81	755	0.63	3.82(5)	737	0.64(4)
$B_g^{(5)}$	3.26	806	0.50	3.12	800	0.48(3)
$A_g^{(3)}$	3.22	834	0.48	3.1(1)	833	0.46(3)

culated and experimentally observed Raman modes of the scheelite phase are shown in Table 4.3. In this case, the agreement between calculations and experimental data is excellent, which reinforces the fact that the scheelite phase is the stable high-pressure polymorph of $NdVO_4$. Beyond the zircon-scheelite transition pressures, only the $E_g^{(1)}$ and $B_g^{(1)}$ modes soften under compression. Upon decompression, the frequency of the former increases, as it should be expected. However, below 3.5 GPa, in the metastability region of the scheelite structure, the opposite behaviour is

observed. As a consequence, its pressure coefficient at zero-pressure is positive. In the case of the $B_g^{(1)}$ mode, its frequency is predicted to decrease under an increasing pressure load. However, at very low pressures, this softening is predicted to be very small, as it is shown in Table 4.3. Experimentally, we observe a very small increase in the frequency of this mode, which yields a small but positive value of $d\omega/dP$. However, this small difference in the sign of the pressure coefficient could be attributed to a minor inaccuracy of calculations. In both cases the value of $d\omega/dP$ is close to zero though. For higher pressures, the tendency of the frequency to decrease upon compression predicted by calculations is empirically correct. In the case of the high-frequency modes $A_g^{(3)}$, $B_g^{(5)}$ and $E_g^{(5)}$, their evolution is directly related to the V–O distance, since these are the internal modes of the tetrahedra. In this case, when compared with the high frequency modes of the zircon phase, these modes have lower $d\omega/dP$ and ω_0 values. This can be explained by small changes in the direction of the vibration and a decrease in the contribution of the V atom to the movement [67] (see subsection 1.3.2 in the Introduction). For instance, with respect to the most intense Raman modes in each phase, the $A_g^{(2)}$ vibration in the zircon phase is exclusively directed along the V–O bond direction, but not in the $A_g^{(3)}$ mode of the scheelite phase.

4.5 *Ab initio* calculations

The calculated energy-volume as well as the enthalpy curves for the zircon, scheelite and monazite phases of $NdVO_4$ are depicted in Fig. 4.10. These curves show how the scheelite is actually a more stable phase at high pressures than the monazite phase. According to enthalphy calculations, the scheelite- and monazite-type structures become more stable than the zircon phase beyond 3.7 and 6.5 GPa respectively. However, the difference between the enthalphy curves of both high-pressure phases is below 1 eV at 6.5 GPa. Therefore, the presence of small stresses within the DAC pressure chamber can trigger the zircon-to-monazite phase transition, like in Refs. [41, 114], where the experiments were carried out using 16:3:1 MEW as PTM. This

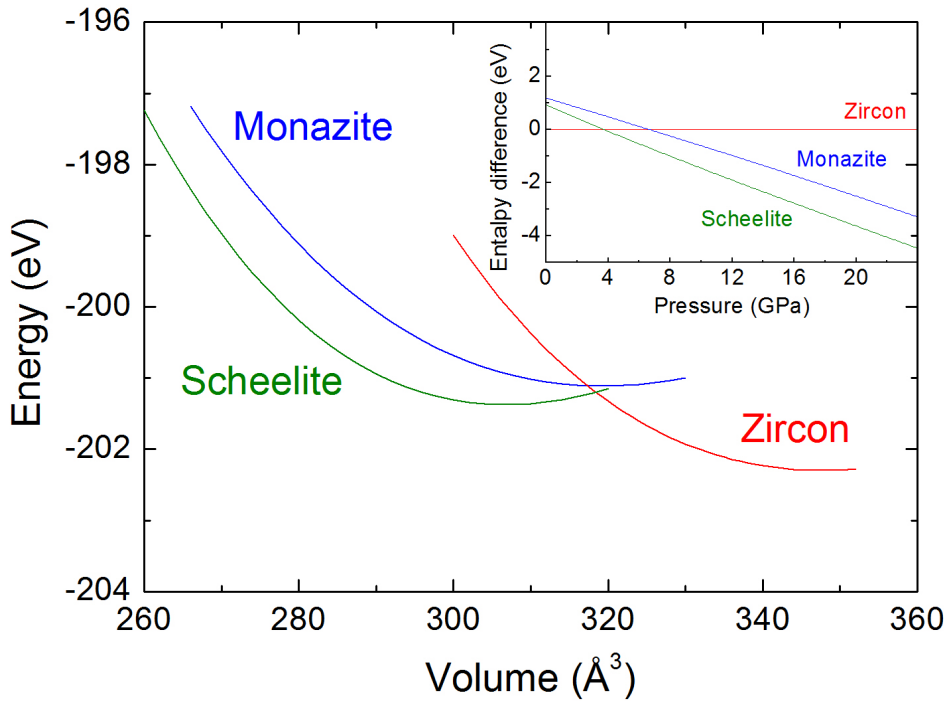

Figure 4.10: Theoretical energy-volume curves (per unit-cell) for the zircon, scheelite and monazite structures of $NdVO_4$. *Inset:* Calculated enthalpy curves (per unit-cell) for these phases assuming $T = 0$K. The zircon phase is taken as reference.

explains why the scheelite phase is only observed when He or Ne gases are used as PTM, since these ensure optimal hydrostatic conditions. Contrary to $NdVO_4$, the monazite phase of $CeVO_4$ is predicted to be the most stable phase at high pressures. Nonetheless, the scheelite phase can be achieved under poor hydrostatic conditions. These facts reveal the relevant role played by the surrounding medium in RVO_4 compounds. Nevertheless, the predicted transition pressure for the zircon-to-monazite phase transformation in $NdVO_4$ is accurately predicted by our calculations. By contrast, the predicted pressure transition for the zircon-to-scheelite transformation is approximately 3 GPa lower than the experimental value. If we discard an eventual underestimation of DFT calculations as a source of error, this considerable difference could be explained as a result of the huge kinetic barrier between both phases. This is a reasonable assumption, since the

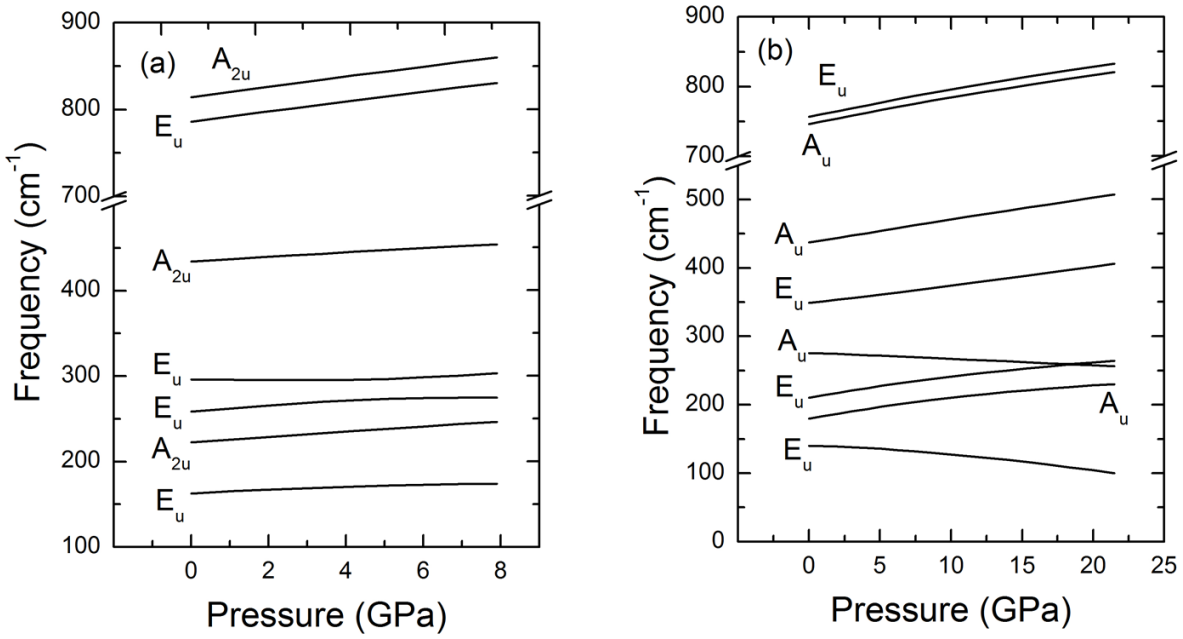

Figure 4.11: Calculated IR modes (TO) for the (a) zircon and (b) scheelite phases of $NdVO_4$.

existence of a large kinetic barrier is coherent with the irreversibility of the zircon-to-scheelite phase transition.

For the sake of completeness, we also provide the calculated IR (only TO modes) and silent modes (Figs. 4.11 and 4.12, respectively) for the zircon and scheelite phases of $NdVO_4$. In the zircon structure, all the IR modes show a positive pressure dependence in the whole range, with the only exception of the E_u mode located at $\sim$ 300 cm^{-1}, whose frequency shows a minimum at $\sim$ 3 GPa. In the scheelite phase, the frequency of only two modes decreases upon compression. These are the E_u and A_u modes, which can be found at $\sim$ 150 and $\sim$ 280 cm^{-1} at zero-pressure conditions, respectively. The partial softening of the A_u mode leads to a frequency crossover with a hard E_u mode at 18.3 GPa. With respect to the silent modes, the most remarkable feature is pressure-induced softening of a B_{1u} silent mode in the zircon phase, which becomes zero at 7.0 GPa, close to the observed transition pressure (6.4 GPa). This suggest a possible influence of this soft mode in the phase transition.

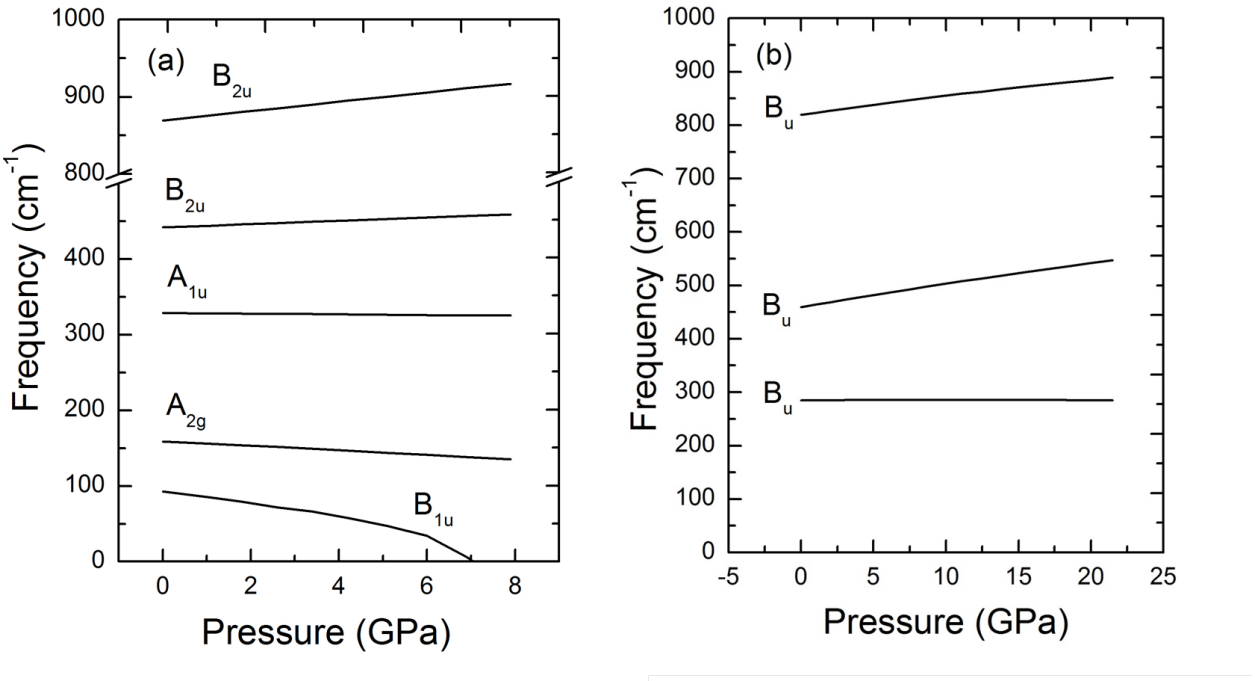

Figure 4.12: Calculated silent modes for the (a) zircon and (b) scheelite phases of $NdVO_4$.

In this regard, the difference between the predicted and the observed transition pressure in the zircon-to-scheelite transformation motivates the study of the different mechanisms that may induce the transition and lower the kinetic barrier. In some compounds under high pressure, soft phonons or instabilities in the stiffness tensor induce second order phase transitions, which are characterized by the absence of volume discontinuities. However, dynamical and mechanical instabilities can also be related to first order phase transitions such as in some layered materials like boron nitride [148] (dynamical buckling) or bulk materials [149, 150]. The soft B_{1u} silent mode depicted in Fig. 4.12 (a) corresponds to rotations of the VO_4 tetrahedra around the direction given by the c-axis. The softening of this mode is directly related to the frequency decrease upon compression observed in the $E_g^{(1)}$ and B_{2g} Raman modes, since these also involve rotations of the VO_4 units around the c-axis. In fact, it has been suggested by Mihailova *et al.* [151] that the softening of this phonon reduces the kinetic barrier in the zircon-to-reidite phase transition

in natural zircon ($ZrSiO_4$). According to these authors, there is a second order phase transition to a lower symmetry version of the zircon structure (called HPLS, S. G.: $I\bar{4}2d$), which a much lower kinetic barrier to the reidite (scheelite) phase. This phase is experimentally identified by the observation of a new peak below 100 cm^{-1}. The reidite phase appears 1.5 GPa after in the Raman spectra. The influence of this phonon in the transition would be discussed in the next chapters in more detail, since it is directly related to the high pressure systematics of the RVO_4 compounds. In our case, no evidence of this second order phase transition is observed. However, the proximity of the observed transition pressure and the pressure at which the calculated B_{1u} silent mode softens may indicate that a similar process to that observed in natural zircon can play a role in the zircon to scheelite phase transition in $NdVO_4$.

In addition to this, we searched for mechanical instabilities by calculating the stiffness tensors of the zircon and scheelite phases. Ab initio calculations allowed us to calculated the C_{ijkl} elements of the matrix at a given pressure P. When the applied load on the solid is not zero, the relationship between additional stresses and strains is given by Eqn. 2.60. The new stiffness tensor **B** can be calculated with Eqn. 2.61, which takes the form expressed in Eqn. 2.63 for hydrostatic pressure. The structure can only be mechanically stable if the **B** stiffness tensor is positive definite. Therefore, if the determinant of the stiffness tensor **B** becomes zero at some pressure, the structure should undergo a spontaneous distortion. The direction of the distortion is given by the eigenvector whose eigenvalue becomes zero.

The theoretical pressure evolution of the stiffness coefficients in the Voigt notation of the zircon and scheelite phases are shown in Fig. 4.13 (a) and (b) respectively; the minima that can be observed in some coefficients at $\sim$ 2.5 GPa in (b) is an artifact of calculations. The zircon structure shows a mechanical instability at 6.2 GPa. At this pressure, one of the matrix eigenvalues becomes zero, which leads to the violation of one of the Born stability criteria for Tetragonal I structures, which includes 422, $\bar{4}2m$ and $4/mmm$ point groups (see Table 2.3). In particular, the condition $B_{66} > 0$ is not fulfilled beyond 6.2 GPa. This mechanical instability is related to the

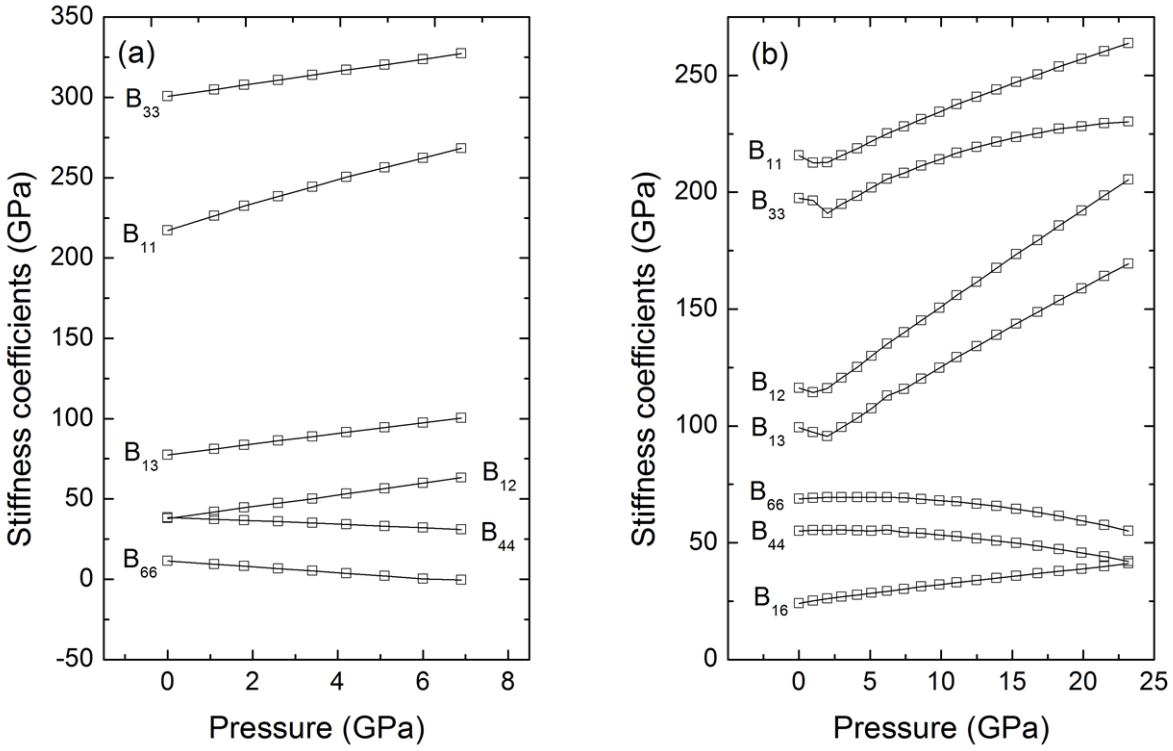

Figure 4.13: Calculated pressure dependence of the stiffness matrix elements for the (a) zircon and (b) scheelite phases of $NdVO_4$.

eigenvector $\eta = (0 \quad 0 \quad 0 \quad 0 \quad 0 \quad 1)$, which describes a pure shear strain of the *ab* plane. This is compatible with the structural relationship between the zircon and the scheelite phases, which involves a shearing of the *ab* plane of the zircon unit-cell [152, 153]. Moreover, some authors have suggested the possible existence of a monoclinic structure between the zircon and scheelite phases in isomorphic chromates [154], even though no experimental proof of this has been reported. Although the mechanical instability (6.2 GPa) is apparently closer to the experimental transition pressure ($P_T = 6.4(3)$ GPa), an overestimation of ~ 0.5 GPa in the pressure at which the B_{1u} silent mode becomes negative (7.0 GPa) is perfectly reasonable for DFT calculations. Thus, since the value of both dynamical and mechanical instabilities are so close to the experimental

transition pressure , it is difficult to discern which of both plays the primary role in lowering the kinetic barrier between the zircon and scheelite phases. With respect to the scheelite phase of $NdVO_4$, the mechanical instability predicted at 22.5 GPa is related to the violation of the Born criterion $2B_{16}^2 < B_{66}(B_{11} - B_{12})$ beyond such pressure (see Table 2.3). The eigenvector associated to this instability is $\eta = (0.5 \quad -0.5 \quad 0 \quad 0 \quad 0 \quad -0.7)$, which corresponds to a monoclinic distortion. This deformation of the unit-cell is perfectly compatible with the scheelite-fergusonite phase transition reported in our XRD and Raman spectroscopy experiments at $\sim$ 19.9 and $\sim$ 19.6 GPa respectively. This mechanism has also been reported for isomorphic compounds as a main cause of the second order transition from scheelite- to fergusonite-type phases [144, 155]. In our case, assuming that the results from our XRD experiments are accurate, this mechanism is also compatible with a weak first order phase transition between both phases.

4.6 Conclusions

In this chapter we presented the results of our experiments on $NdVO_4$ under high pressure in hydrostatic conditions. Firstly, powder XRD experiments up to 24.5 GPa were perform at a synchrotron source, using He gas as PTM. At 6.4 GPa we reported the appearance of a new phase corresponding to a scheelite structure, which remains stable up to $\sim$ 19.9 GPa. These results were confirmed by our Raman spectroscopy measurements using Ne as PTM, in which the Raman spectra corresponding to the scheelite phase arises between 6.0 and 6.7 GPa. Enthalpy calculations also show the scheelite phase as the high-pressure stable phase. The finding of this phase at high pressures and room temperatures establishes a substantial difference with previous experiments using 16:3:1 MEW as PTM, in which the monazite phase appeared over 6.5 GPa. This definitely confirms the huge sensibility to hydrostatic conditions of some ternary oxides upon compression, such as RVO_4 in this case. The possible influence of dynamical or mechanical instabilities in the zircon-to-scheelite phase transition has also been discussed. In addition to this, we also

reported a second phase transition from scheelite- to fergusonite-type $NdVO_4$ between 19 and 20 GPa in our XRD and Raman experiments. According to calculations, this phase transition could be favoured by a mechanical instability that leads to the distortion of the scheelite unit-cell. The EOS of the different polymorphs are also reported, showing good agreements with previously reported calculations. With respect to the Raman spectroscopy experiments, the pressure evolution of the Raman modes of the zircon and scheelite phases under high pressure has been studied, showing excellent agreement with our theoretical predictions.

5 | Gadolinium orthovanadate under high pressure

In the previous chapter, we studied the behaviour of $NdVO_4$ under high pressure conditions by means of XRD and Raman scattering. Now, we follow a similar path towards the characterization of $GdVO_4$. Thus, in this chapter we provide a broad study on the pressure effects on $GdVO_4$, which include XRD, Raman scattering and optical absorption, measurements. In addition to this, experimental results are supported by DFT calculations. This will allow us to discuss the relative stability of the different phases, the identification of the different Raman modes and the role played by stiffness instabilities in the transition processes.

Similarly to other RVO_4 compounds, $GdVO_4$ crystallizes in the zircon structure at ambient conditions and undergoes a zircon-to-scheelite phase transition upon compression. Nonetheless, the phase diagram of this compound has been a matter of debate, since different experiments under different hydrostatic conditions yielded different results. In this regard, Zhang *et al.* [156] reported the existence of a zircon-to-scheelite phase transition at 7.4 GPa by means of Raman spectroscopy and luminiscence experiments on doped $GdVO_4$:Eu^{3+} microcrystals under high pressure, using MEW as PTM. Moreover, metastable scheelite-type $GdVO_4$ samples (as well as many other RVO_4 compounds) were studied by Huang *et al.* [157] at ambient temperature using XRD and Raman spectroscopy measurements. Some discrepancies in the frequencies of the Raman modes can be found in Refs. [156] and [157], which we expect to clarify with our

experimental results. In addition to this, photoluminescence and XRD measurements on doped $GdVO_4Er^{3+}$ under high pressure using silicone oil as PTM were performed by Hong *et al.*[158]. These authors reported a zircon-to-scheelite and a scheelite-to-fergusonite phase transition at 7.4 and 23.1 GPa respectively. In Yue *et al.* [115] un-doped $GdVO_4$ was studied under non-hydrostatic conditions (no PTM was used) by means of XRD experiments. These results showed that the zircon-to-scheelite and scheelite-to-fergusonite phase transitions take place at 5.0 GPa and 31.2 GPa respectively. In the previous chapter, we showed how different hydrostatic conditions can alter the structural sequence of RVO_4 [40, 44] compounds under high pressure. Poor hydrostatic conditions and sample doping can also alter the transition pressure of ternary oxides under high pressure [41, 159–161]. Thus, in order to accurately determine the structural and vibrational properties of $GdVO_4$ under high pressure, we need to perform a systematic study of un-doped $GdVO_4$ under compression. In this chapter we describe the experimental and theoretical results reported in Marqueño *et al.*[49] on $GdVO_4$ under high pressures. We studied $GdVO_4$ under high pressure conditions by means of XRD and Raman spectroscopy experiments up to 16 and 39 GPa respectively. Ar and Ne gases were used as PTM in order to ensure hydrostatic conditions. In this study we also included *ab initio* calculations in which the stability and the atomic positions of different phases are analyzed up to 31 GPa. The EOS and axial compressibilities of the zircon and scheelite phases are analyzed, as well as the phonon frequency-pressure evolution of these two polymorphs. For the sake of completion, we also included the results of optical absorption measurements on a single-crystal $GdVO_4$ under compression up to 16 GPa, which allowed us to determine the pressure dependence of the band gap energy of both zircon and scheelite phases.

5.1 Experimental details

The polycrystalline $GdVO_4$ samples used in XRD and Raman experiments were synthesized by a solid-state reaction of proper amounts of predried Gd_2O_3 and V_2O_5 with 99.9% purity. The

oxides were homogeneously mixed, pelletized and heated at 800 ℃ for 24 h. The sample were cooled afterwards to room temperature. The recovered product was regrounded and heated again at 1100 ℃ for 24 h. On the other hand, the synthesis of $GdVO_4$ single crystals used in the optical absorption measurements is similar to that described for $NdVO_4$ in the previous chapter. Optical clear $GdVO_4$ single-crystals were prepared by the flux growth method in which $Pb_2V_2O_7$ was used as solvent [162]. Appropriate quantities of pure V_2O_5, PbO and $Na_2B_4O_7$ and 99.99% purity Gd_2O_3 were used as starting materials. A mixture of these materials was introduced and sealed in a platinum crucible and heated up to 1270 ℃ for 12 h, and subsequently cooled to 800 ℃. The crucible was then removed and rapidly inverted in order to separate the flux from the crystals. The residual flux was dissolved using hot diluted nitric acid. As a result optical transparent crystals with average dimensions $\sim 3 \times 2 \times 1$ mm^3 were obtained. Both the polycrystalline and single-crystal $GdVO_4$ samples were analyzed at room conditions by means of XRD. The obtained lattice parameters are $a = 7.198(6)$Å and $c = 6.353(3)$Å, which are in perfect agreement with the values reported in literature [115]. The sample did not contain any other phase, impurities or precursor residuals, which confirms the high purity of the obtained crystals.

A DAC with diamond culets of 350 μm diameter was used for the high-pressure angle-dispersive XRD experiments. Powder $GdVO_4$ was introduced in a 150 μm diameter hole drilled on an Inconel gasket, which was previously preindented to $\sim$ 40 μm thickness. Fine copper grains were also loaded in the DAC chamber, whose EOS was used as pressure gauge [163]. Ar gas was loaded as PTM to ensure quasihydrostatic conditions below 20 GPa [99]. The evolution of the Ar peaks in the XRD patterns can be used to confirm the pressure [164] indicated by the Cu Bragg peaks. The loading of the DAC was carried out with special care in order to avoid sample bridging between the diamond anvils and the sample, which would introduce non-hydrostatic stresses [118, 165]. The experiment was carried out at the MSPD-BL04 beamline of the ALBA-CELLS synchrotron [166] (Fig. 3.12) using a monochromatic x-ray beam with $\lambda = 0.4246$Å focused down to 20×20 μm^2 (FWHM). A Rayonix detector located at 240 mm from the sample was used to collect the

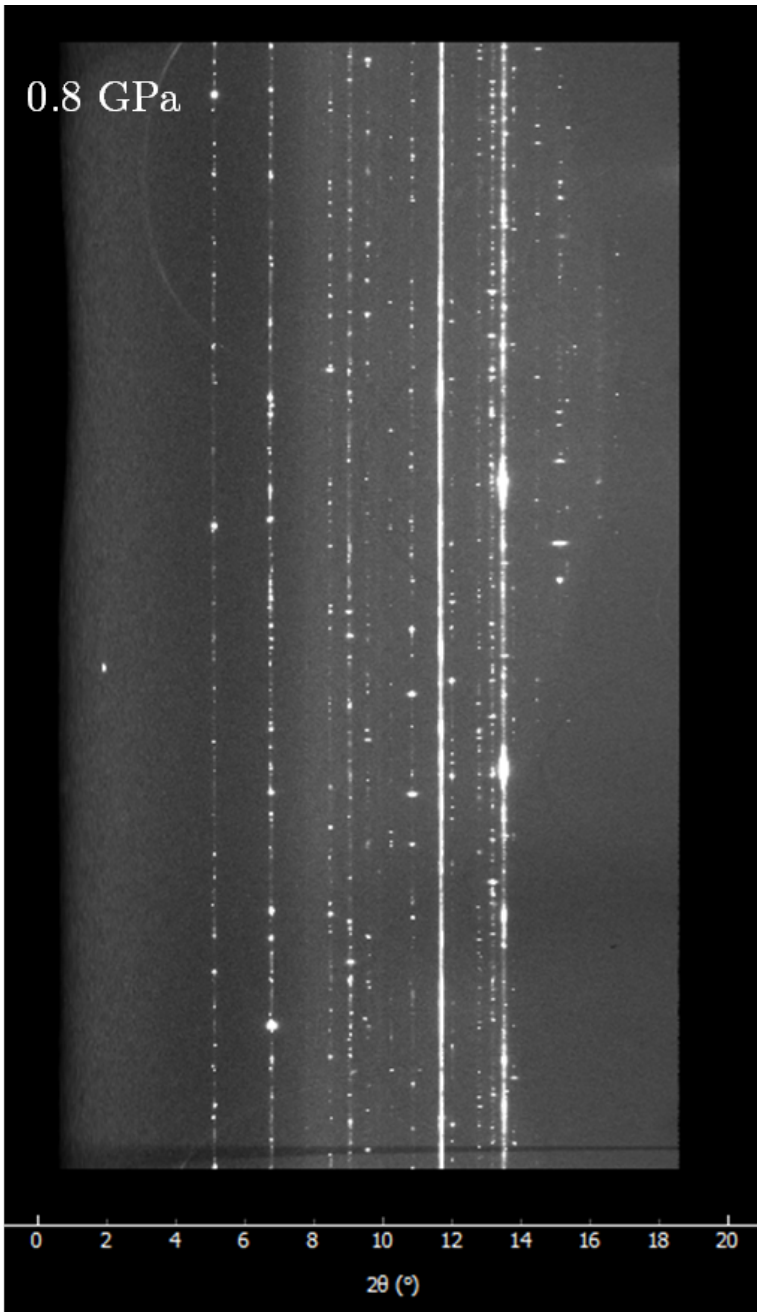

Figure 5.1: Unrolled CCD cake image of zircon-type $GdVO_4$ at 0.8 GPa. The spotty appearance of the Debye rings confirms the existence of preferred orientations in the sample.

XRD patterns. The homogeneity of the Debye rings was improved by using a ±3° rocking angle. The integration of the collected CCD images into 2θ patterns was performed using the Dioptas software [122]. The refinements of the integrated XRD patterns were performed using the PowderCell [123] and FullProf [167] software packages. Preferred orientation effects, which are shown in Fig. 5.1, did not allow to perform Rietveld refinements. Thus, only LeBail refinements were possible. This kind of analysis allows us to study the pressure evolution of the unit-cell parameters and the identification of each of the crystal structures that appear during the experiment.

On the other hand, two different runs were performed in the Raman scattering experiments, with the same DAC than that used in XRD experiments. Steel and rhenium gaskets were used in the first and second runs, respectively. The gaskets were preindented to a 40 μm thickness and subsequently drilled a 200 μm diameter hole. Powder $GdVO_4$ and ruby chips were introduced in the cavity of the DAC, which was loaded with Ne gas as PTM. Pressure was determined by the ruby luminiscence method [100]. The experiments were performed in the setup schematized in Fig. 3.14 and described in subsection 3.3.

Finally, in the optical absorption experiments, small single crystals of size $\sim 80 \times 80$ μm and thickness ~ 10 μm were studied under high pressure in a DAC equipped with IIA-type diamond anvils with a culet size of 480 μm. The sample was loaded in a 200 μm hole drilled in an Inconel gasket previously preindented down to 50 μm. A mixture of 16:3:1 methanol-ethanol-water (MEW) was used as PTM. The pressure of the cavity was measured using the ruby luminiscence method [100]. 16 GPa was the maximum pressure achieved in the experiment. The optical set up consisted in a deuterium lamp, fused silica lenses, reflecting optics objectives and an UV-visible near-infrared spectrometer.

5.2 Simulation details

Theoretical calculations for the different phases of $GdVO_4$ were carried out with the *Vienna Ab Initio Simulation Package* (VASP) [126, 127] in the framework of density functional theory (DFT) [125]. The pseudopotential method and the projector augmented wave scheme (PAW) were used [128]. The generalized-gradient approximation (GGA) with the Perdew-Burke-Ernzerhof (PBE) prescripition [168] was employed to describe the exchange-correlation energy. The Dudarev's GGA+U method [169] was used to describe the highly localized nature of the rare-earth $4f$ electrons, with an effective U value of 3.4 eV. A basis of plane waves up to kinetic energy curoff of 520 eV was used to ensure highly converged results. The integrations on the Brillouin zone (BZ) were performed with a dense Monkhorst-Pack k-special points grid [130]. The structural configurations were completely optimized for a set of selected volumes by minimizing the atomic forces and stresses [170]. The applied optimization criteria were to acieve forces below 0.006 eV/Å and differences among the diagonal elements of the stress tensor smaller than 0.1 GPa. The phonon calculations were carried out at the center of the BZ by means of the small displacement method, which has been reported to yield accurate results when calculating phonons under high pressures [171].

Calculations were performed by our collaborators at University of La Laguna (Tenerife, Spain), Alfonso Muñoz and Plácida Rodríguez-Hernández.

5.3 Powder XRD experiments

Selected powder XRD patterns of $GdVO_4$ upon compression from 0.8 to 16.7 GPa are depicted in Fig. 5.2. The Bragg reflections of the PTM (Ar) and the pressure calibrant (Cu) are indicated within the figure. From ambient pressure to 6.0 GPa the diffraction peaks can be unambiguously assigned to the zircon phase of $GdVO_4$. At 0.8 GPa, the unit-cell lattice parameters are

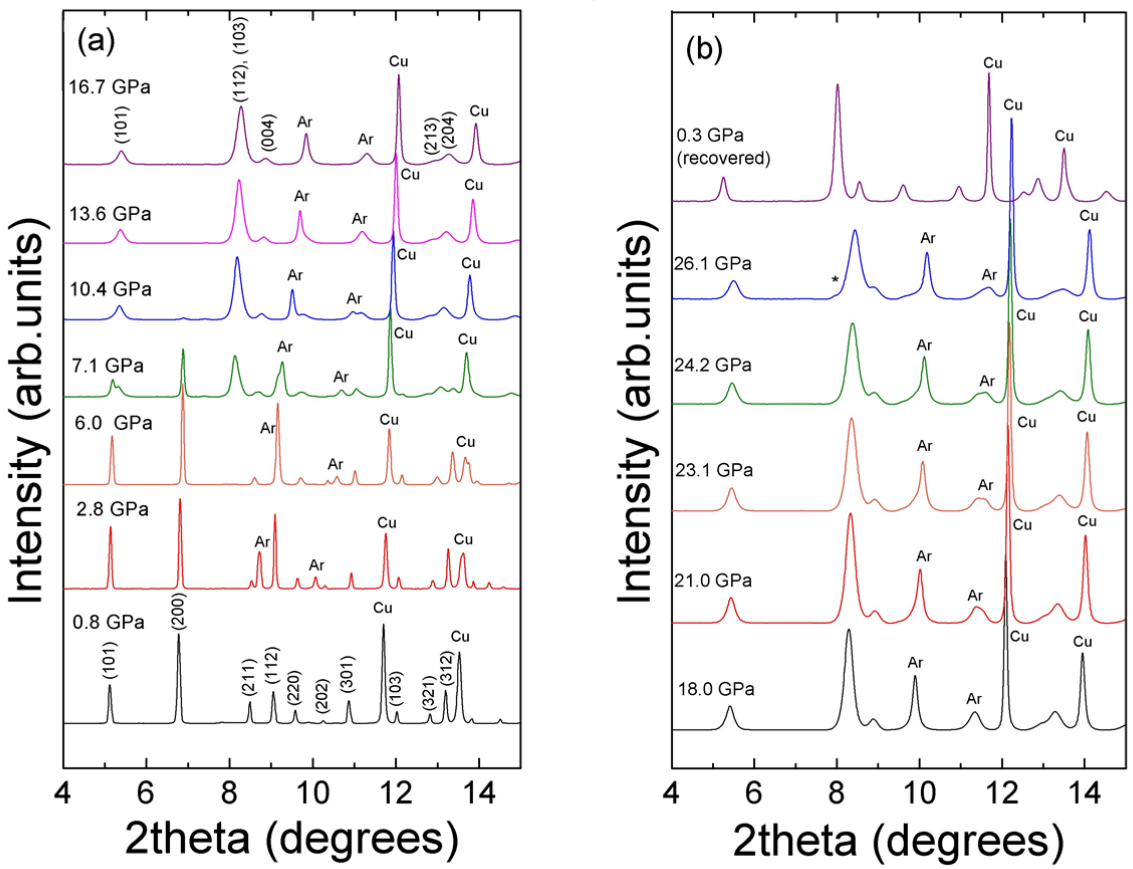

Figure 5.2: Selected powder XRD patterns of $GdVO_4$ at different pressures up to 26.1 GPa. The pattern corresponding to the recovered sample at 0.3 GPa is shown in (b). The Ar and Cu diffraction peaks are indicated. Asterisks identify the Bragg peaks associated with V_2O_5.

$a = 7.186(4)$Å and $c = 6.341(3)$Å, which are similar to the values reported at room conditions [50, 172]. At 7.1 GPa, new Bragg peaks arise in the spectra, which indicates the onset of the zircon-to-scheelite phase transition. Both zircon and scheelite phases of $GdVO_4$ coexists up to 10.4 GPa. The zircon reflections progressively vanish and the scheelite appears as a single phase at 11.6 GPa. For pressures over 8 GPa, the unit-cell lattice parameters of the zircon phase cannot be determined since only the (200) reflection associated with this phase is visible. The scheelite phase lattice parameters at 13.6 GPa are $a = 4.963(4)$Å and $c = 11.023$Å. The broadening of the scheelite peaks with respect to those of the zircon phase can be observed in Fig. 5.2 (a). This

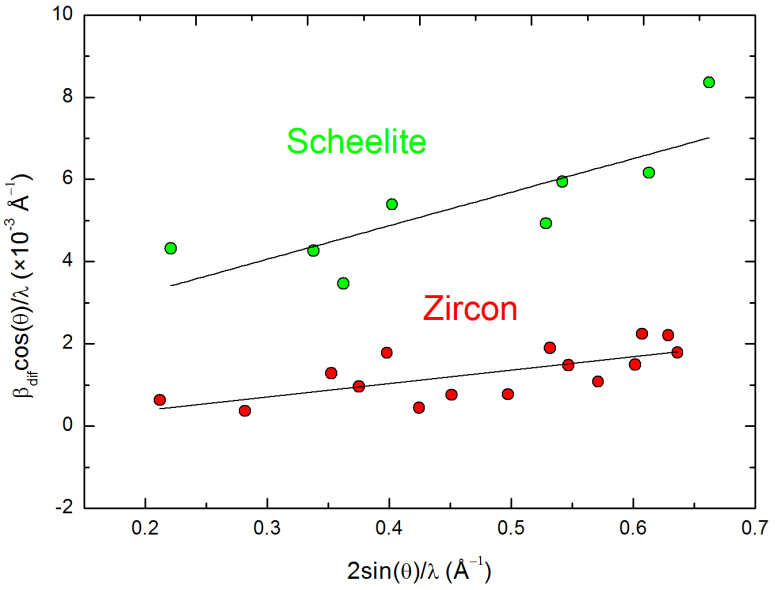

Figure 5.3: Williamson-Hall plot for the zircon (red symbols) and scheelite (green symbols) phases of $GdVO_4$ at 5.2 and 13.2 GPa respectively.

widening can be attributed to the effects of the huge volume collapse at the transition pressure ($\Delta V/V_0 = 10.8\%$). These effects include a reduction in the grain size and a strain increase. This can be easily proof by performing a Williamson-Hall plot [111, 135] (subsection 3.2.2) of two different XRD patterns corresponding to the zircon and scheelite single phases, which is shown in Fig. 5.3. The instrumental contribution to the peak breath was subtracted taking the callibrant (LaB_6) as reference. It is also possible to determine the change in the microstrain parameter ξ before and after the transition, since it must necessarily be related with changes in the sample. As a result, we determined that in the zircon phase at 5.2 GPa the mean grain size and the microstrain parameters are $t_Z \sim 330$ nm and $\xi_Z = 3.3 \times 10^{-3}$ respectively. By contrast, these magnitudes take the values $t_S \sim 60$nm and $\xi_S = 8.2 \times 10^{-3}$ for the scheelite phase at 13.2 GPa, which are coherent with expected consequences of the volume collapse at the phase transition. Similar effects have been reported for $ErVO_4$ [54] and $NdVO_4$ (Chapter 4) under high pressure, in which a partial loss of crystallinity is observed after the zircon-to-scheelite phase transition.

The Bragg peaks associated with the scheelite phase start to broaden for pressures above 20 GPa, as it can be observed in Fig. 5.2 (b). In fact, this structure cannot precisely describe the evolution of the patterns, unless we consider a monoclinic distorted version of the scheelite phase, in particular a fergusonite-type structure (S. G.: $I2/a$, $Z = 4$). Therefore, we can state that there is a scheelite-to-fergusonite phase transition above 20 GPa, which has been reported at similar pressures in other rare-earth orthovanadates [36, 37, 39, 44, 139]. This phase transition has been reported at 31.2 GPa by Yue *et al.* [115] under non-hydrostatic conditions. In our experimental results we observe a small reflection arising at $2\theta \approx 8^{\circ}$, which is labeled in Fig. 5.2(b) with an asterisk. This small Bragg peak cannot be explained by none of the proposed structures for $GdVO_4$ but as the most intense reflection of V_2O_5 [137]. In fact, as we could see in the case of $NdVO_4$ [44], a partial x-ray induced decomposition of V_2O_5 units can take place as a consequence of the photoelectric processes triggered by the interaction of x-rays with the sample. This has been observed for ternary oxides [138], including other RVO_4 compounds [36, 37]. Upon pressure release, the scheelite structure reappears at 21.0 GPa, showing the reversible character of the scheelite-to-fergusonite phase transition. By contrast, the zircon-to-scheelite phase transition can be considered as irreversible, since the scheelite phase was recovered at 0.3 GPa, as it can be observed in Fig. 5.2(b). This is a typical feature of the zircon/scheelite structured compounds, including other related orthovanadates [35–37, 39, 46, 54, 136]. This also reveals the existence of considerable kinetic barriers between both phases.

The pressure evolution of the unit-cell lattice parameters of the diffrent phases of $GdVO_4$ is depicted in Fig. 5.4. In this figure we included our exoerimental and theoretical results, as well as the experimental results reported by Yue *et al.*[115] for the sake of comparison. The difference between our results and calculations is rather small. In adittion to this, our experimental results are much less dispersed than those reported in Ref. [115], since the latter were taken under non-hydrostatic conditions. Moreover, Yue *et al.*[115] reported the onset of the phase transition at 5.0 GPa, whereas according to our results the estimated transition pressure is 6.6(5) GPa.

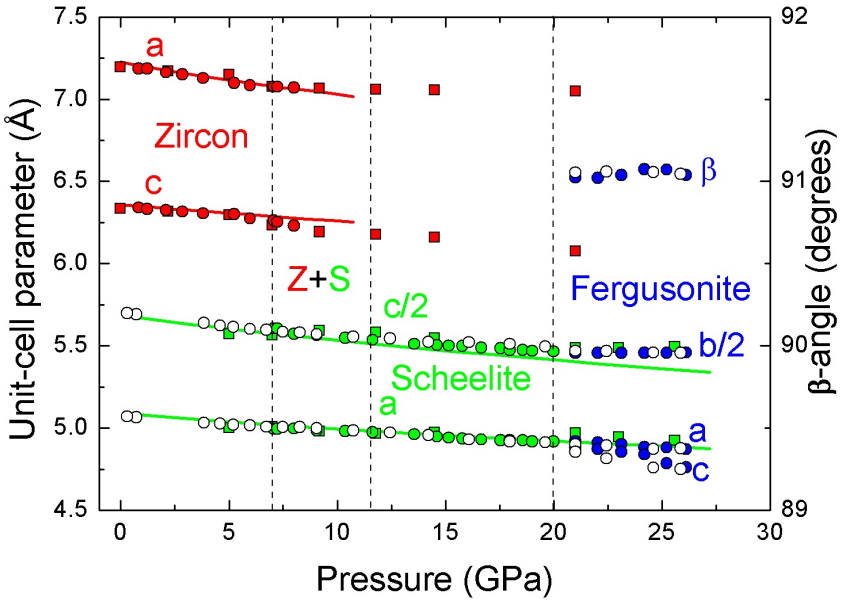

Figure 5.4: Pressure dependence of the unit-cell lattice parameters of the zircon, scheelite and fergusonite phases of $GdVO_4$. The corresponding colors for each phase are indicated in the figure. Circles correspond to our experimental data (Ne as PTM) whereas squares refer to the data reported by Yue *et al.*[115] (no PTM). Solid and empty symbols represent the data taken upon compression and decompression respectively. Solid lines represent the results of our *ab initio* calculations.

This reduction in the transition pressure has been previously reported for other vanadates, such as $HoVO_4$, in which the transition pressure is reduced from 8.2 to 4 GPa under non-hydrotatic conditions [37]. The onset of the zircon-to-scheelite phase transition for $GdVO_4$:Eu^{+3} [156] and $GdVO_4$:Er^{+3}[158] was found below 7.4 GPa, which is good agreement with our results.

The experimental linear compressibilities of the lattice parameters of the zircon phase of $GdVO_4$ are $\kappa_a = 2.6 \times 10^{-3}$ and $\kappa_c = 1.9 \times 10^{-3}$ GPa^{-1}, which are in good agreement with the calculated axial compressibilities $\kappa_a = 2.7 \times 10^{-3}$ and $\kappa_c = 1.6 \times 10^{-3}$ GPa^{-1}. Both experimental and theoretical values show that the a-axis is clearly more compressible than the c-axis. This anisotropic behaviour of the zircon phase can be explained in terms o the particular arrangement of the GdO_8 and VO_4 polyhedra within the structure and their different compressibilities, as we previously explained for $NdVO_4$ (see also sections 1.2 and 1.3). In the case of the scheelite phase,

the experimental axial-compressibilities are $\kappa_a = 1.6 \times 10^{-3}$ and $\kappa_c = 2.7 \times 10^{-2}$ GPa^{-1}. The compressibility of the c-axis was determined for the data points collected below 10 GPa, since these were much less dispersed. The calculated values $\kappa_a = 1.5 \times 10^{-3}$ and $\kappa_c = 2.7 \times 10^{-3}$ GPa^{-1} are reasonably in accordance with the experimental values. In addition to axial compressibilities, we could also estimate the zero-pressure lattice parameters of the scheelite structure. The obtained experimental values are $a_0 = 5.063(2)$ Å and $c_0 = 11.390(12)$ Å, which are similar to the predicted values $a_0 = 5.084$ Å and $c_0 = 11.364$ Å. Again, as in the zircon phase, the scheelite anisotropic compressibility can be explained in terms of the different compressibilities of the GdO_8 and VO_4 polyhedral units. At the scheelite-to-fergusonite phase transition, the monoclinic β angle suddenly increases up to $\sim 91^\circ$ and stays nearly constant up to the maximum pressure achieved ($\sim$ 26 GPa). With regard to the other lattice parameters, these do not show any discontinuity with those of the scheelite phase. The a and the c parameters of the fergusonite phase diverge upon compression, with the former reproducing the tendency of the a parameter of the scheelite phase. The b parameter of the fergusonite phase slightly increases upon compression, which is a common feature of fergusonite structured oxides upon compression [44, 144].

Fig. 5.5 shows the change in the unit-cell volume of the zircon, scheelite and fergusonite polymorphs. The former two were analyzed using a third order BM EOS [173], which allowed to estimate the values of the zero-pressure volumes, the bulk moduli B_0 and its first derivative B_0'. The data corresponding to the fergusonite phase were not sufficient to provide an accurate analysis. The obtained results of the fitting are summarized in Table 5.1, in which we included the calculated values as well as some values reported in literature. The reported results are very similar to those obtained for Eu-doped $GdVO_4$ (10% Eu). With respect to the relative compressibility of the zircon and scheelite phases, there is a 11% increase in the value of the bulk modulus B_0. This fact is coherent with the increase in the packing efficiency after the transition, which is associated with a $\sim$ 10.8% volume collapse. The predicted values for the ambient-pressure volume and the bulk modulus are in good agreement with the results obtained in the experiments.

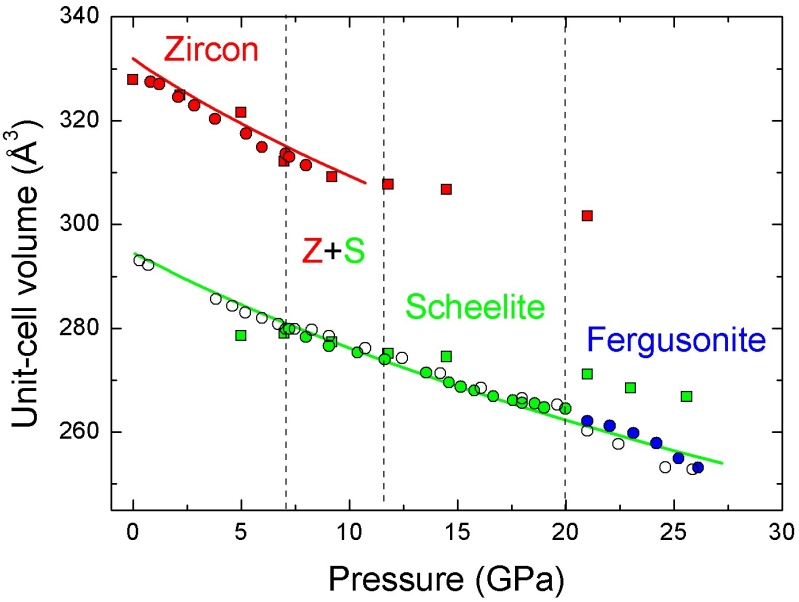

Figure 5.5: Evolution of the unit-cell volume with pressure of the zircon. scheelite and fergusonite phases of $GdVO_4$. The meaning of the symbols is the same than that used in Fig. 5.4.

By contrast, when no PTM is used, the structure seems to be much less compressible, especially during the scheelite phase. Hence, the existence of considerable deviatoric stresses can lead to a substantial increase in the measured value of the bulk modulus. In the case of the experiments reported by Huang *et al.* [157] fo Eu-doped $GdVO_4$, in which silicon oil was used as PTM, the bulk modulus of the zircon phase is lower than that obtained under quasi-hydrostatic conditions. Nonetheless, this fact do not contradict the general tendency, since the associated error bar for the value of B_0 is quite large. In fact, the observed general tendency in many other vanadates consists in a reduction of the bulk compressibility (i.e. larger B_0 values) as non-hydrostatic effects increase [35–37, 174].

As we previously mentioned, the zircon structure can be described as a set of chains of alternating VO_4 tetrahedra and GdO_8 dodecahedra distributed along the *c*-axis direction and edge-sharing GdO_8 dodecahedra along the *a*-axis direction (Fig. 1.1). By contrast, in the scheelite phase the relative positions and orientations of the different polyhedral units change, so that the VO_4

Table 5.1: EOS parameters for zircon- and scheelite-type $GdVO_4$. We included the calculated EOS parameters of the proposed postfergusonite phase (S. G.: *Cmca*)

Phase	PTM	V_0(Å^3)	B_0 (GPa)	B_0'
Zircon (our work, [49])	Theory	331.9	117.3	5.5
Zircon (our work, [49])	Ar	330.0(5)	122(5)	4.2(1.5)
Zircon [157]	Silicon oil	327(2)	102(14)	4 (fixed)
Zircon [115]	None	327(2)	185(28)	4 (fixed)
Scheelite (our work, [49])	Theory	294.5	138.03	3.9
Scheelite (our work, [49])	Ar	293.4(6)	137(2)	6(2)
Scheelite [157]	Silicon oil	289.6(1.4)	137(15)	4 (fixed)
Scheelite [115]	None	283.6(1.4)	379(32)	4 (fixed)
Cmca (our work, [49])	Theory	535.9	110.7	4.5

tetrahedra are no longer edge-shared (Fig. 1.2). Fig. 5.6 shows the calculated evolution of the Gd–O and V–O bond length upon compression for both phases. The GdO_8 dodecahedra are not regular in any of these phases, since there are two different Gd–O distances. Nonetheless, this distortion is reduced by an order of magnitude in the zircon-to-scheelite transition, since both Gd–O distances become much more similar in the scheelite phase. To put it more clearly, the bond-length distortion index of these polyhedral units are ~ 0.03 and ~ 0.003 for the zircon and scheelite phases respectively. The predicted change in the bond distance is compatible with previous reported data on different RVO_4 compounds [37, 174]. On the other hand, the VO_4 tetrahedra are regular in both structures, with a small expansion during the phase transition ($\Delta V/V \sim 4\%$), as it can be deducted from the small increase in the V–O interatomic distance shown in Fig. 5.6. Moreover, this figure also shows that the V–O distance is far less compressible than the Gd–O distances. Therefore, the contribution of the GdO_8 dodecahedra to the pressure-induced volume

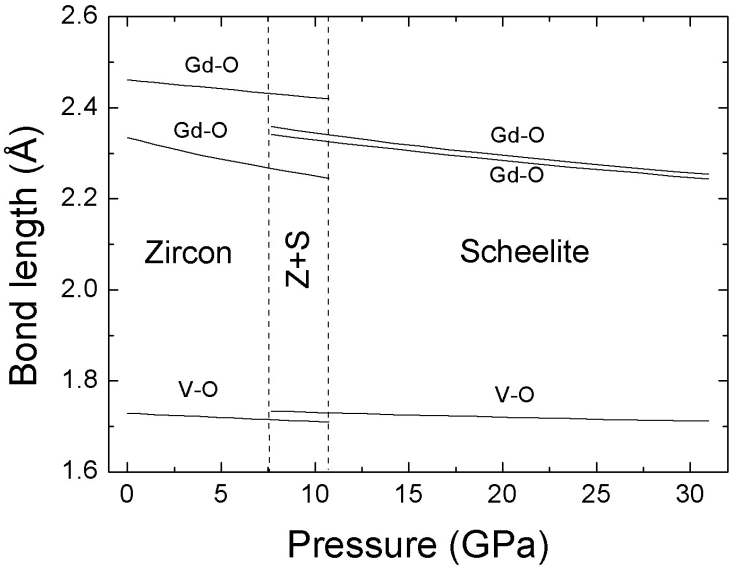

Figure 5.6: Calculated pressure dependence of the Gd–O and V–O bond distance in the zircon and scheelite phases of $GdVO_4$.

change of the crystal is much more significant than that of the VO_4 tetrahedra. This behaviour has been observed in many other isomorphic compounds such as orthomolybdates[175] and orthophosphates [140, 176].

5.4 Raman spectroscopy experiments

As we noted in previous chapters, the zircon structure have twelve Raman-active modes at the center of the BZ ($\Gamma_R = 2A_{1g} + 4B_{1g} + B_{2g} + 5E_g$) [63, 177]. The evolution of the Raman spectra of the zircon phase of $GdVO_4$ at different pressures is shown in Fig. 5.7(a). Even though 12 Raman modes are predicted, only 9 can be actually observed in the spectra. The symmetry of these modes has been assigned according to our calculations and the values reported in literature [64]. As in other zircon-structured compounds, the spectra are divided in two main regions, separated by a large frequency gap between $\sim$ 500-800 cm^{-1}. The modes in the high-frequency region (over 800 cm^{-1}) can be considered as internal vibration modes of the VO_4 tetrahedra in

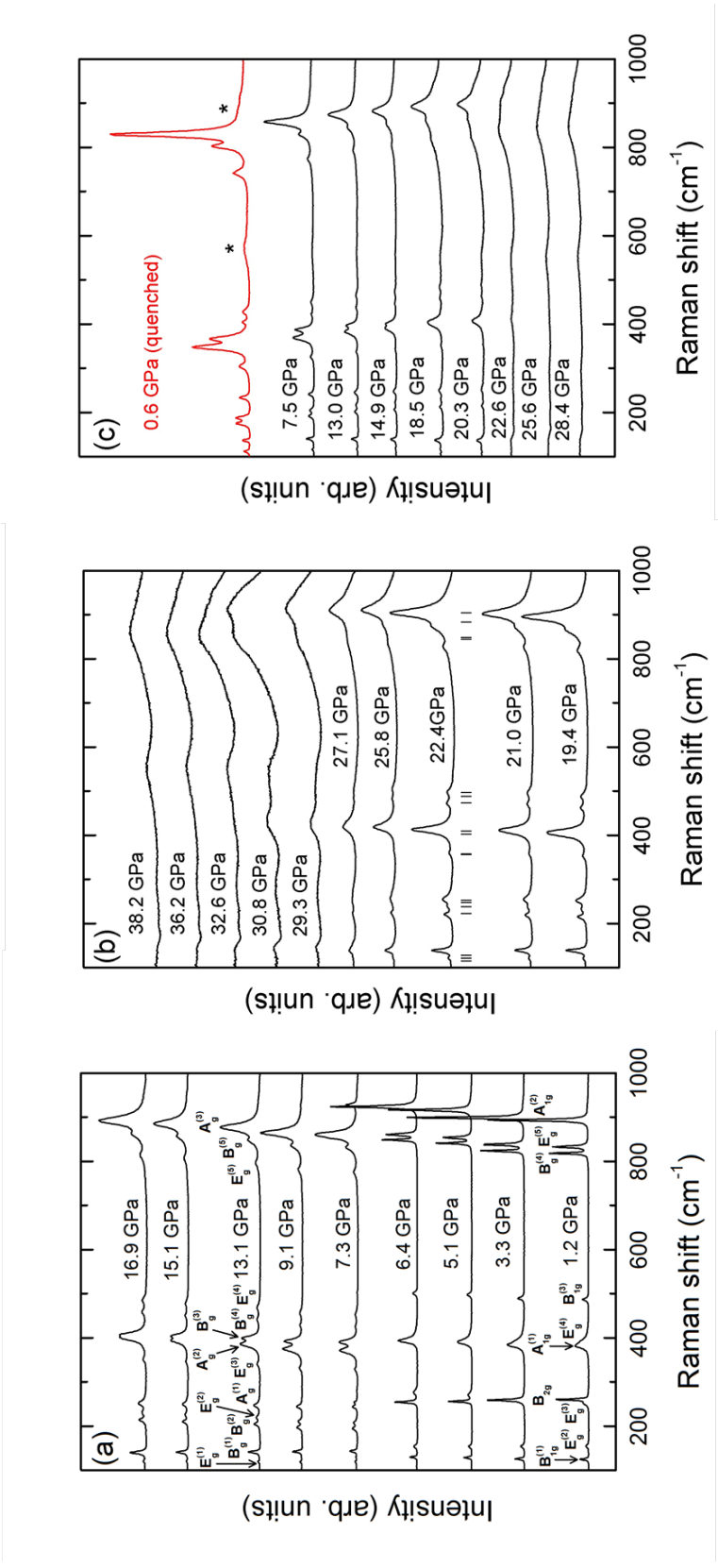

Figure 5.7: Selected Raman spectra of $GdVO_4$ at different pressures. The spectra shown in (a) were obtained in the first run upon compression (steel gasket), while those shown in (b) and (c) correspond to the second run (rhenium gasket). The spectra shown in the latter picture were acquired upon pressure release. The black ticks in (b) represent the calculated Raman peaks for the fergusonite phase observed at 22.4 GPa in the XRD experiments. The spectrum of the recovered sample at 0.6 GPa is shown in red colour in (c). The bands associated to the post-fergusonite phase are denoted by asterisks.

good approximation [67]. The modes with identical symmetries are distinguished with different supra-indexes in order to ease explanations, so that the small (large) indexes correspond to the lower (higher) frequency modes. It must be remarked that this labeling order is the opposite in Marqueño *et al.* [49], but it has been modified so that the same criteria applies to all the Raman experiments reported in this dissertation. The Raman spectra of zircon-type $GdVO_4$ is dominated by the symmetric stretching mode $A_{1g}^{(2)}$ located in the high frequency region at 893 cm^{-1}. In this same region we can also find the $E_g^{(5)}$ and $B_{1g}^{(4)}$ asymmetric-stretching modes at 824 and 818 cm^{-1} respectively. On the other hand, in the low-frequency region, the Raman peak corresponding to the $A_{1g}^{(2)}$ shows an asymmetric profile. According to some polarization works in which different scattering geometries were studied, this line corresponds to the contribution of two different modes [64]. In Ref. [178], the authors suggest that these are the $A_{1g}^{(1)}$ and $E_g^{(4)}$ Raman modes. In fact, our calculations predict a very little difference in their wavenumbers at room pressure (352 and 366 cm^{-1} respectively). Thus, it is reasonable to assume that the observed peak asymmetry is a consequence of the proximity of such Raman modes. The other Raman modes observed at 1.2 GPa in the low-frequency region are the $B_{1g}^{(3)}$, $E_g^{(4)}$, $A_{1g}^{(1)}$ and B_{2g} ones, which are located at 486, 392, 382 and 260 cm^{-1} respectively. The $B_{1g}^{(2)}$ and $E_g^{(1)}$ modes are not observed in the spectra, probably due to their weak Raman scattering cross-section. These peaks can only be identified using $GdVO_4$ single crystals in air (outside of a DAC), under particular scattering geometries [64].

Fig. 5.8 (a) shows the evolution of the Raman frequencies of zircon-type $GdVO_4$ under high pressure. Although our theoretical calculations tend to yield slightly lower frequency values (with differences from 1% to 13%), the predicted behaviour upon compression is in good agreement with our experimental observations. Except for the low-frequency modes $E_g^{(2)}$ and B_{2g} modes, which soften upon compression, most of the Raman modes show a positive (quasi)linear dependence with pressure. In Table 5.2 we shown the experimental and calculated values of the pressure coefficients $d\omega/dP$, the zero-pressure frequency ω_0 and the Grüneisen parameters for each Raman mode, showing good compatibility. The Grüneisen parameters were calculated with the values

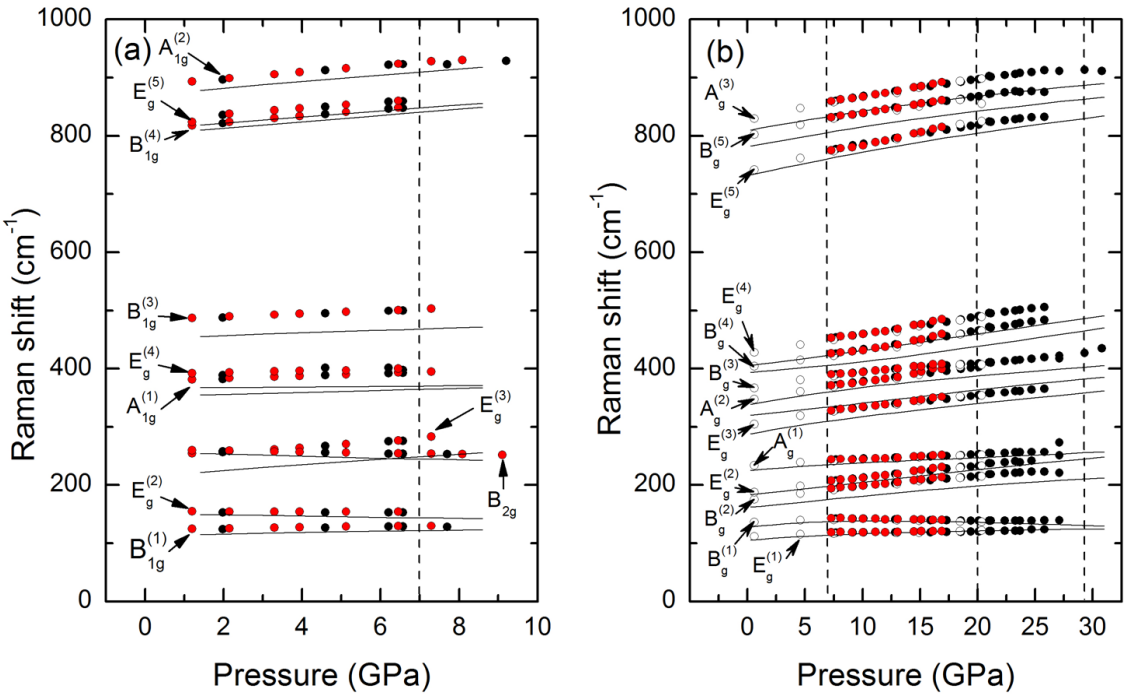

Figure 5.8: Pressure dependence of the frequency of the Raman active modes of (a) zircon- and (b) scheelite-type $GdVO_4$. Red symbols stand for the data obtained during the first run. while black and empty circles represent the data obtained in the second run upon compression and pressure release respectively. Solid lines represent the calculated frequencies. In (b), the data shown after 20 GPa represent the average position of the peaks observed in the spectra. Some of these peaks are not single modes, in particular those associated with E_g modes in the scheelite phase, since the frequency degeneracy is broken in the fergusonite phase.

of B_0 shown in Table 5.1. In the low-frequency region, only the $E_g^{(3)}$ mode shows a comparable pressure dependence. The strong positive linear dependence of this mode and the progressive softening of the B_{2g} mode make that near 3 GPa there is a crossover of these two modes. This is a common feature in zircon-structured compounds, including many other related orthovanadates [38, 46, 54, 179] as well as in Eu-doped $GdVO_4$ [156]. Moreover, the fact that the $E_g^{(3)}$ is the low-frequency mode with the strongest pressure dependence is also a particularity of zircon-type RVO_4 compounds [38, 46, 54, 179]. In order to compare with previously reported results, the data reported in Zhang *et al.* [156] (doped $GdVO_4$ samples) and Voron'ko *et al.* [64] are also included

in Table 5.2. In general, there is a reasonably good compatibility between our data and those reported in Ref. [156], with the only exception of the $E_g^{(2)}$ mode. According to Zhang *et al.* [156], this mode has a small positive pressure dependence, whereas our calculations and experimental results suggest that the frequency of this mode decreases under compression ($d\omega/dP < 0$). Nonetheless, this discrepancy may be attributed to its small absolute value, which is close to zero. Therefore, since in this case the experimental margin of error is comparable to the dispersion of the data, both values can be considered as compatible, even though the sign of the pressure coefficients are different.

Fig. 5.7 (a) shows how there is a striking change in the Raman spectra between 6.4 and 7.3 GPa, which can be associated with the zircon-to-scheelite phase transition. Our previous XRD experiments on $GdVO_4$ under high pressure showed that the phase transition is located at some pressure between 6.0 and 7.1 GPa. Therefore, according to both experiments, a more accurate value of the transition pressure would be 6.8(4) GPa. The Raman spectra shown in Fig. 5.7 (a) show a coexistence of both phases from 7.3 up to 9.1 GPa, in which the zircon phase progressively vanishes as the scheelite phase arises. In our experiments, we observed a subtle change in the colour of the sample just after the transition, which can be associated with a band gap collapse, as we will show in the next subsection. Above 9.1 GPa the scheelite structure appears as a single phase. In accordance with group theory analysis [63], the scheelite phase has thirteen Raman active modes at the center of the BZ ($\Gamma_R = 3A_g + 5B_g + 5E_g$) [145, 146]. In this particular case, all these modes can be observed in the spectra . As in the previous phase, the Raman spectra appears as divided in two regions, with a frequency gap between $\sim$ 550 and 750 cm^{-1}. The symmetry of each mode has been assigned in accordance with our calculations and previous data from the literature [156]. The highest mode in frequency is also the dominating Raman peak in the spectra. This mode correspond to the $A_g^{(3)}$ symmetric-stretching mode of the VO_4 tetrahedra, which can be found in the high-frequency region at 877 cm^{-1} at $P = 13$ GPa. Within the same region, we can also find the asymmetric-stretching modes $B_g^{(5)}$ and $E_g^{(5)}$ at 848 and 796 cm^{-1} respectively. With

Table 5.2: Experimental and calculated values of the pressure coefficients, zero-pressure frequencies and Grüneisen parameters of the Raman-active modes of zircon-type $GdVO_4$. The Grüneisen parameters were obtained considering $B_0 = 117.3$ and 122(5) GPa [49] (see Table 5.1) for the calculated and experimental values respectively. The results reported by Zhang *et al.* [156] and Voron'ko *et al.* [64] for the zircon phase of $GdVO_4$ are also included

	Theory			Experiment			Ref. [156]		Ref. [64]
	$d\omega/dP$	ω_0	γ	$d\omega/dP$	ω_0	γ	$d\omega/dP$	ω_0	ω_0
Mode	(cm^{-1}/GPa)	(cm^{-1})		(cm^{-1}/GPa)	(cm^{-1})		(cm^{-1}/GPa)	(cm^{-1})	(cm^{-1})
$E_g^{(1)}$	1.46	105.3	1.62	–	–	–	–	–	110
$B_{1g}^{(1)}$	1.59	112.8	1.65	1.19(8)	123	1.18(9)	0.9	124	123
$E_g^{(2)}$	−0.96	150.5	−0.75	−0.21(2)	155	−0.17(4)	0.1	156	156
$E_g^{(3)}$	4.86	214.7	2.66	4.7(3)	247	2.32(18)	4.5	245	246
$B_{1g}^{(2)}$	2.66	237.4	1.31	–	–	–	–	–	252
B_{2g}	−1.62	256.4	−0.74	−1.02(2)	261	−0.48(2)	−0.8	263	261
$A_{1g}^{(1)}$	1.75	352.3	0.58	2.16(4)	379	0.72(6)	1.7	384	380
$E_g^{(4)}$	0.51	366.5	0.58	1.4(1)	391	0.49(7)	–	–	438
$B_{1g}^{(3)}$	2.37	451.6	0.62	2.60(4)	484	0.66(3)	2.5	485	483
$B_{1g}^{(4)}$	5.58	801.6	0.82	5.78(2)	811	0.87(4)	5.2	811	809
$E_g^{(5)}$	5.25	811.2	0.76	5.24(2)	827	0.77(3)	5.31	827	825
$A_{1g}^{(2)}$	5.67	870.0	0.76	5.51(14)	887	0.76(4)	5.5	887	884

regard to the modes in the low-frequency region, we could observe the $E_g^{(1)}$ mode at 119 cm^{-1} at this same pressure, which was not previously reported in literature.

The calculated and experimental pressure dependence of the Raman-active modes of the scheelite phase is depicted in Fig. 5.8 (b). The frequency of all these modes has a positive linear dependence with pressure, with the only exception of the $B_g^{(1)}$ mode, which shows a clear non-linear behaviour. The pressure coefficients, zero-pressure frequencies and Grüneisen parameters (considering the bulk modulus values shown in Table 5.1) for scheelite-type $GdVO_4$ are summarized in Table 5.3. Previously reported data by Zhang *et al.* [156] and Huang *et al.* [157] are also included. In general, there is a good agreement between the values reported by Zhang *et al.* [156] and our experimental values, with the only exception of the pressure coefficients of the $E_g^{(4)}$ and $B_g^{(5)}$ modes, which are underestimated in their study. Moreover, the $B_g^{(2)}$ is incorrectly labeled in Ref. [156] as a degenerate E_g mode (as indicated in Table 5.3). The theoretical value of the pressure coefficient of the $B_g^{(5)}$ mode was calculated for $P < 5$ GPa due to its non-linear behaviour. In our case, we could not report an accurate value of $d\omega/dP$ at low pressures, since the data points collected upon decompression are insufficient in such region. It seems reasonably to assume that the value given in Ref. [156] is negative, in contrast to our theoretical value, due to the fact that the authors calculated $d\omega/dP$ by making a linear fit of the whole pressure range in which the scheelite phase is observed. On the other hand, some ω_0 values reported by Huang *et al.* [157], such as those corresponding to the $E_g^{(1)}$, $B_g^{(1)}$ and $B_g^{(2)}$ modes, are quite different from those obtained in our experiments and also from the values reported in Ref. [156]. A possible explanation of these differences may be the presence of precursor impurities or small quantities of zircon-type $GdVO_4$ in the recovered sample synthesized by Huang *et al.* [157].

A particular feature of the Raman spectra shown in Zhang *et al.* [156] is the presence of a Raman peak near 900 cm^{-1} which is not explained and appears at the zircon-to-scheelite phase transition. We believe that the presence of this Raman peak may be ascribed to the existence of V_2O_5 [180] units as a consequence of a small partial decomposition of the sample. In our case,

Table 5.3: Theoretical and experimental values of the pressure coefficients, zero-pressure frequencies and Grüneisen parameters of the scheelite phase of $GdVO_4$. The Grüneisen parameters were calculated considering $B_0 = 138.03$ and 137(2) GPa [44] for the theoretical and experimental set of values respectively. For the sake of comparison, we included previously reported data in Zhang *et al.* [156] and Huang *et al.* [157]. The values indicated with an asterisk are labeled as $T(E_g)$ in Ref. [156]. In the case of the $B_g^{(1)}$ mode, the values with a dagger superscript were obtained for $P < 5$ GPa, since this mode shows a non-linear evolution with pressure. The corresponding experimental values are not shown due to insufficient data below 5 GPa.

	Theory			Experiment			Ref. [156]		Ref. [157]
	$d\omega/dP$	ω_0	γ	$d\omega/dP$	ω_0	γ	$d\omega/dP$	ω_0	ω_0
Mode	(cm^{-1}/GPa)	(cm^{-1})		(cm^{-1}/GPa)	(cm^{-1})		(cm^{-1}/GPa)	(cm^{-1})	(cm^{-1})
$E_g^{(1)}$	0.76	109.5	1.05	0.32(5)	115	0.38(6)	–	–	147
$B_g^{(1)}$	$1.76^{\dagger}$	127.5	$1.90^{\dagger}$	–	140	–	−0.6	140	176
$B_g^{(2)}$	2.45	158.8	2.33	1.95(7)	178	1.50(6)	3.4^{*}	178^{*}	200
$E_g^{(2)}$	2.10	184.1	1.72	2.29(7)	189	1.66(6)	2.1	190	188
$A_g^{(1)}$	0.89	229.3	0.59	0.86(5)	236	0.50(3)	1.0	236	244
$E_g^{(3)}$	2.12	297.1	1.08	2.36(8)	309	1.05(4)	2.8	307	321
$A_g^{(2)}$	2.18	319.5	1.03	2.88(7)	348	1.13(3)	2.3	350	350
$B_g^{(3)}$	2.66	343.4	1.17	1.90(11)	374	0.70(4)	1.0	370	368
$B_g^{(4)}$	2.75	383.8	1.08	3.19(8)	401	1.09(3)	2.6	407	417
$E_g^{(4)}$	2.86	402.5	1.07	3.10(9)	428	0.99(3)	1.7	432	435
$E_g^{(5)}$	3.04	742.8	0.62	3.99(9)	744	0.73(2)	2.8	745	748
$B_g^{(5)}$	2.50	791.5	0.48	2.97(14)	808	0.50(2)	1.6	804	809
$A_g^{(3)}$	3.47	810.9	0.65	3.33(8)	833	0.55(2)	3.2	833	831

we do not report any peaks that may be associated with vanadium pentaoxide. This suggests the idea that non-optimal hydrostatic conditions can induce the partial decomposition of the sample across the phase transition.

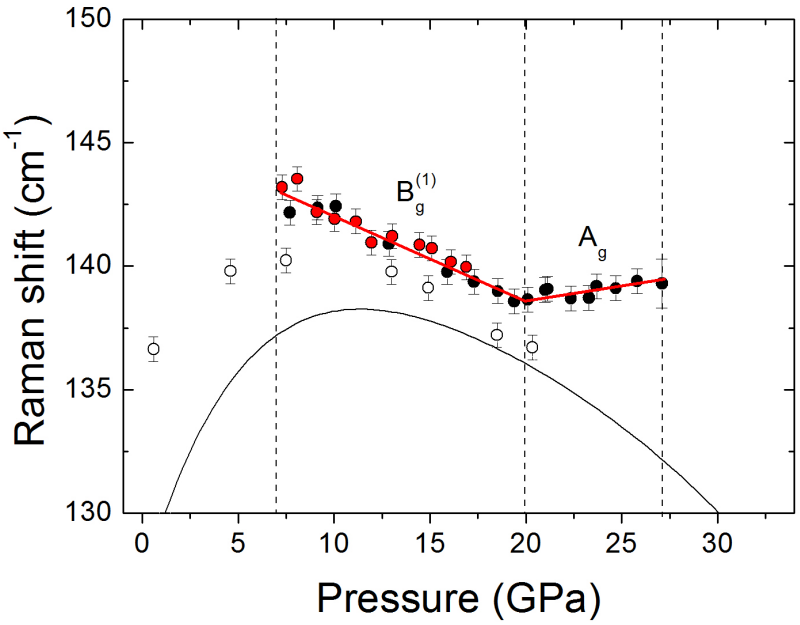

Figure 5.9: Pressure evolution of the frequency of the scheelite $B_g^{(1)}$ mode and its transformation into the A_g mode of the fergusonite phase at $\sim$ 20 GPa. The meaning of the symbols is the same than that used in Fig. 5.8. The black solid line stand for the predicted theoretical behaviour of the $B_g^{(1)}$ mode. Red lines are only a guide to the eye.

The progressive softening under high pressure of the $B_g^{(1)}$ mode of scheelite-type $GdVO_4$ up to 20 GPa is displayed in Fig. 5.9. On the contrary, the frequency of this mode shows a positive pressure dependence beyond such pressure. Several experimental studies have shown that there is no discontinuity between the scheelite $B_g^{(1)}$ mode and the fergusonite A_g mode, but the transformation of one into the other [144]. This is experimentally manifested as a change in the shift direction of the associated Raman peak. In other words, the frequency of the scheelite $B_g^{(1)}$ mode decreases upon compression up to the point in which it transforms into the fergusonite A_g mode, which hardens with pressure. This is actually a characteristic feature of the second-

order scheelite-to-fergusonite phase transition [144]. Therefore, these results and those obtained in our XRD experiments confirm that there is a transition from the scheelite phase to a fergusonite structure of $GdVO_4$. In Fig. 5.7 (b) we compared the obtained spectra at 22.4 GPa and the calculated positions of Raman modes of the fergusonite phase at the same pressure, showing a reasonable agreement between both. The calculation of the Raman frequencies were performed assuming the same structure than that obtained in the XRD refinements at 22.4 GPa, whose unit cell parameters are $a = 4.8933$Å, $b = 10.9367$Å, $c = 4.8160$Å and $\beta = 91.06°$. This transition is characterized by the breaking of the scheelite E_g modes degeneracy due to the lower symmetry of the fergusonite phase, according to our calculations. The consequence of this should be a small splitting of the corresponding Raman peaks. Nonetheless, this effect is actually quite small and cannot be directly observed in our measured Raman spectra. Furthermore, there is an increase of non-hydrostatic effects over 20 GPa (see the hydrostatic limits of Ne in Table 3.1) that hinders a clear observation of any peak splitting, since all of the Raman peaks tend to broaden. In order to avoid any misinterpretation, we decided to follow the behaviour of the peaks over 20 GPa as if they were single. In Fig. 5.8 (b) we represent the evolution of these peaks beyond 20 GPa, which do not necessarily represent one particular mode.

For higher pressures, new changes in the Raman spectrum take place at 29.3 GPa. In fact, for pressures over 32.6 GPa the fergusonite peaks disappear and the Raman spectra are mainly constituted by broad bands. We think that this fact can be attributed to a phase transition towards a new post-fergusonite structure of $GdVO_4$, whose unit-cell is depicted in Fig. 5.10. Similar observations have been reported for other similar compounds. In fact, in Ref. [181], the authors suggest the existence of an orthorhombic post-fergusonite phase (S. G.: *Cmca*) of $TbVO_4$ under high pressure. According to this scenario, there is an increase in the coordination of both Gd and V atoms at the transition, as well as a considerable volume collapse ($\Delta V/V \approx 11.8\%$). In particular, the V coordination increases from 4 to 6, which implies a larger polyhedral unit and therefore a weaker V–O bond. This would induce smaller frequency values of the dominant stretching

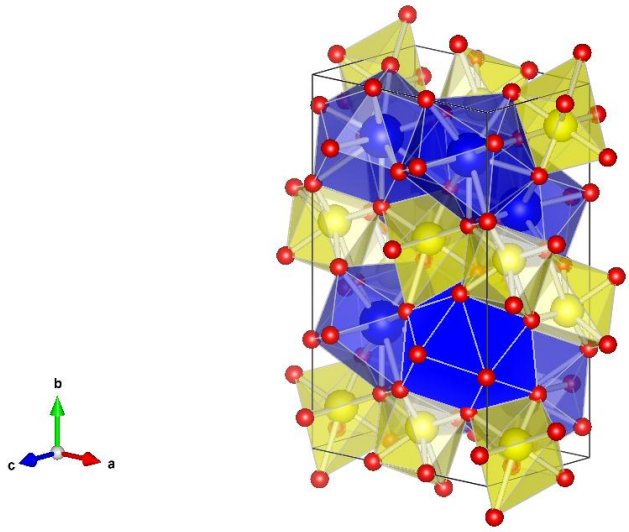

Figure 5.10: Unit-cell of the suggested post-fergusonite phase for $GdVO_4$ (S. G.: *Cmca*, $Z = 8$).

mode. This is compatible with the fact that the most intense band of the post-fergusonite phase appears on the left-hand side of the fergusonite most intense peak, which is associated with the A_g stretching mode. The suggested post-fergusonite phase has 36 modes in the center of the BZ, which, together with the progressive loss of hydrostaticity, can explain the observation of wide bands in the Raman spectra. As a consequence, the pressure evolution of these modes cannot be extracted from the spectra. Even though all of the described facts seem coherent, this is just an hypothetical explanation of our experimental observations. Further experiments and calculations are necessary to elucidate this question. It must be remarked that during the experiment the laser beam used for exciting the ruby was being absorbed by the sample once the third phase transition was achieved. Moreover, the sample was opaque and showed a gray bright colour after the transition. A possible explanation to this is a huge decrease in the band gap energy from the visible region to the near infrared, as happens in $SrCrO_4$ [182]. Nonetheless, the reflectivity of the sample is not enhanced, which indicated that the decrease in the band gap does not imply a pressure-driven metallization, which contradicts previous predictions [32]. Finally, in Fig. 5.7 (c) we show the collected Raman spectra upon decompression. When pressure is released, small

peaks seem to appear at 22.6 GPa and become more visible at 20.3 GPa. Upon pressure release, the bands corresponding to the post-fergusonite phase vanish, whereas the Raman peaks that can be assigned to the scheelite phase reappear. Therefore, it is possible to assume that there is a phase transition near 22.6 GPa, which is extremely close to the scheelite-to-fergusonite transition pressure observed upon compression. Thus, the most reasonable scenario is that the obtained sample after 22.6 GPa corresponds to the scheelite- and not to the fergusonite-type structure of $GdVO_4$. The scheelite phase is recovered in a metastable state at the lowest pressure ($P = 0.6$ GPa), which clearly shows the irreversible character of the zircon-to-scheelite phase transition. In addition to this, the Raman spectra shows two wide bands that could be associated to the post-fergusonite phase, which are labeled with asterisks in Fig. 5.7 (c).

5.5 Optical absorption experiments

As we could see in subsection 1.3.3, most of zircon-type RVO_4 compounds only allow step-like direct transitions. Moreover, the magnitude of the direct band gap for most rare-earth orthovanadates is between 3 and 4 eV at room conditions (see Table 1.10). In this particular case, we carried out optical absorption measurements in zircon-type $GdVO_4$ single crystals under high pressure.

The absorption spectra obtained in the experiments is shown in Fig. 5.11 up to 16 GPa. In optical absorption measurements, the optimal thickness of a single crystal is that for which $\alpha d \sim 3$. Considering that α is of order 10^5 cm^{-1} in direct semiconductors at room conditions, the optimal thickness d should be smaller than 1 μm. Thus, the selected single-crystal is excessively thick for a direct semiconductor ($d = 10$ μm). As a result, the maximum value of the measured absorption coefficients are below 2500 cm^{-1}, which hinders the optical absorption analysis explained in Chapter 3. Consequently, we could only analyze the low-energy tail of the absorption edge at different pressures. However, according to Urbach's rule [183], the absorption edge has an exponential dependence on the photon energy,

$$\alpha = \alpha_0 \exp\left(\frac{E - E_{gap}}{E_U}\right) \tag{5.1}$$

where E_U is the so-called Urbach energy, which is directly related with the steepness of the absorption tail, and α_0 is a constant. By fitting Eqn. 5.1 to the absorption spectra shown in Fig. 5.11 it is possible to estimate the change of the bandgap energy E_{gap} upon compression. The absolute value of E_{gap} cannot be determined with this equation though. Nonetheless, we estimated by linear extrapolation that the value of E_{gap} is 3.83 eV at 1 bar, which is in quite good agreement with the value previously reported by Krumpel *et al.* [75] (E_{gap} = 3.87 eV) at room conditions. As clearly shows Fig. 5.11, the behaviour of the absorption edge is the opposite in the zircon and in the scheelite phases. In particular, the band gap energy tends to grow upon

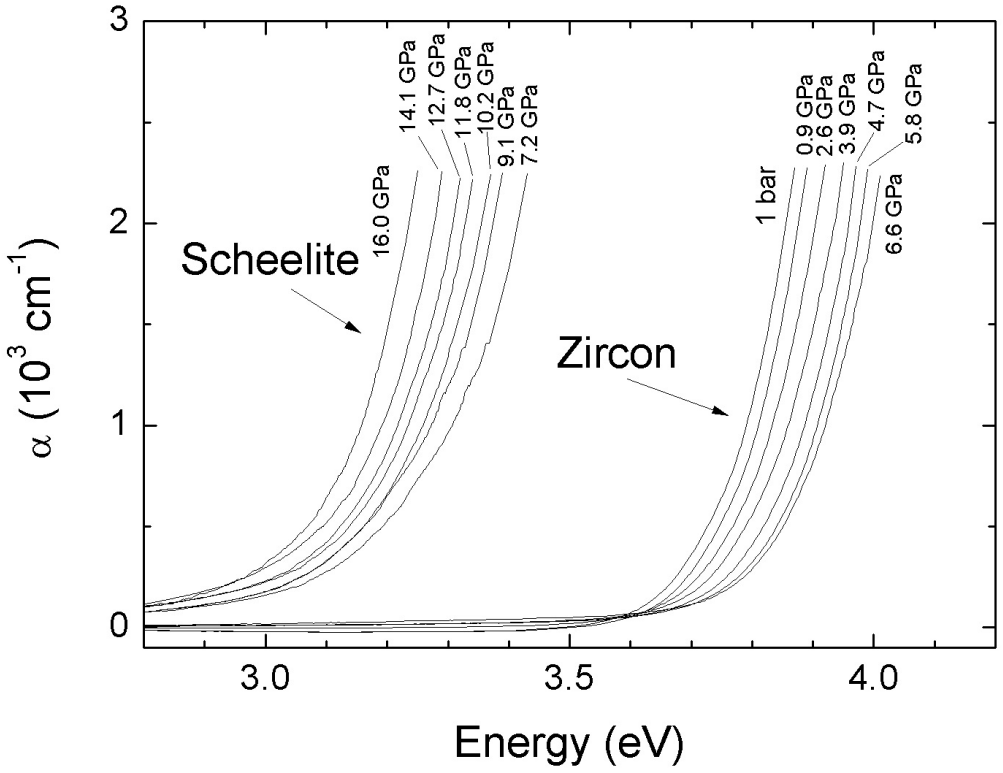

Figure 5.11: Absorption spectra for zircon- and scheelite-type $GdVO_4$ under high pressure.

compression, while it decreases in the scheelite phase. In other words, the band gap widens and narrows in the zircon and scheelite phases respectively. This can be observed in Fig. 5.12. Similar behaviour has been reported by Panchal *et al.* [48] and Bandiello *et al.* [184] for other rare-earth orthovanadates. Here we see that there is a band gap collapse of $\Delta E_{gap} \sim 0.6$ eV at the phase transition ($P \approx 7$ GPa), which is slightly smaller than the band gap collapse observed for other rare-earth orthovanadates, such as those studied in Panchal *et al.* [48] in which $\Delta E_{gap} \sim 1$ eV. This explains the colour change of the sample at ~ 7 GPa observed during our previous Raman scattering experiments. In both phases, the band gap energy follows a linear dependence with pressure, which allows to obtain the value of dE_{gap}/dP by fitting a linear function to the data. For the zircon phase we obtain $dE_{gap}/dP = 21.1(7)$ meV/GPa, which is compatible with the values obtained for zircon-type $YbVO_4$, YVO_4 and $LuVO_4$ [48]. By contrast, we found a negative pressure dependence of the band gap energy in the scheelite phase, in particular, $dE_{gap}/dP = -18.4(3)$ meV/GPa. This value compatible with other reported values on scheelite-type YVO_4, $YbVO_4$, $TbVO_4$ and $DyVO_4$ [32, 48].

The calculated band-structure of zircon-type $GdVO_4$ has been previously reported by Huang *et al.* [72]. These authors suggest a direct band-gap at the Γ point with a theoretical value of 2.77 eV. In general, DFT calculations tend to yield lower values of the E_{gap} than those experimentally observed. In the particular case of RVO_4 compounds, these calculations tend to underestimate the band gap energy by ~ 1 eV [48]. Thus, the difference between the calculated value reported in Ref. [72] and the experimental results (3.83 and 3.87 eV in our work [49] and Ref. [75] respectively) is acceptable. Furthermore, Huang *et al.* [72] also reported that the upper part of the valence band is mainly composed of O $2p$ states, with a very small hybridization with the $5d$ orbitals of Gd. On the other hand, the main contribution to the lower part of the conduction band is constituted by antibonding V $3d$–O $2p$ states. Thus, the broadening of the band gap in zircon-type $GdVO_4$ can be associated with the reduction of the V–O bond distance in the VO_4 tetrahedra. A possible contribution of the rare-earth atom $4f$ orbitals to the valence or the conduction band has also been

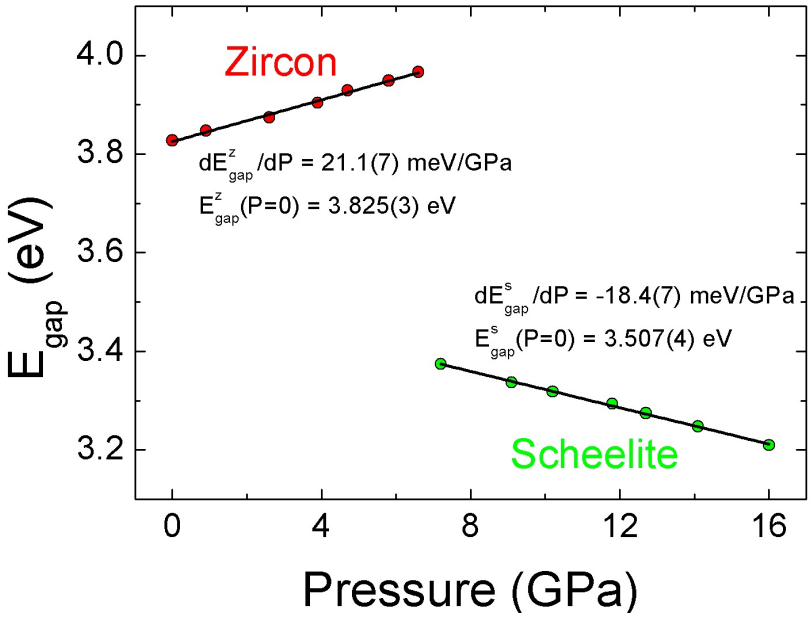

Figure 5.12: Pressure dependence of the band gap energy of zircon- (red circles) and scheelite-type (green circles) $GdVO_4$. Solid lines represent a linear fit to both sets of data. The obtained parameters are included within the figure.

a matter of debate in literature [185]. However, according to the density of states calculated by Huang *et al.*[72] for the band-structure of zircon-type $GdVO_4$, $4f$ electrons do not have a relevant contribution to the upper part of the valence band nor the lower part of the conduction band. In fact, these electrons are highly localized and remain practically unaffected upon compression in the current range i.e. up to 16 GPa.

By contrast, the calculated electronic band structure of scheelite-type $GdVO_4$ has not been reported in literature up to our knowledge. Nonetheless, some authors [48] have suggested that, for similar RVO_4 compounds, pressure may induce a weak hybridization of the O $2p$ and V $3d$ with the s orbitals of the rare-earth cation. This would explain the band gap collapse observed in the transition as well as the negative pressure dependence of E_{gap} with pressure ($dE_{gap}/dP = -18.7(7)$ meV/GPa). In addition to this, the small expansion of the VO_4 tetrahedra at the transition may also contribute to the band gap collapse.

5.6 *Ab initio* calculations

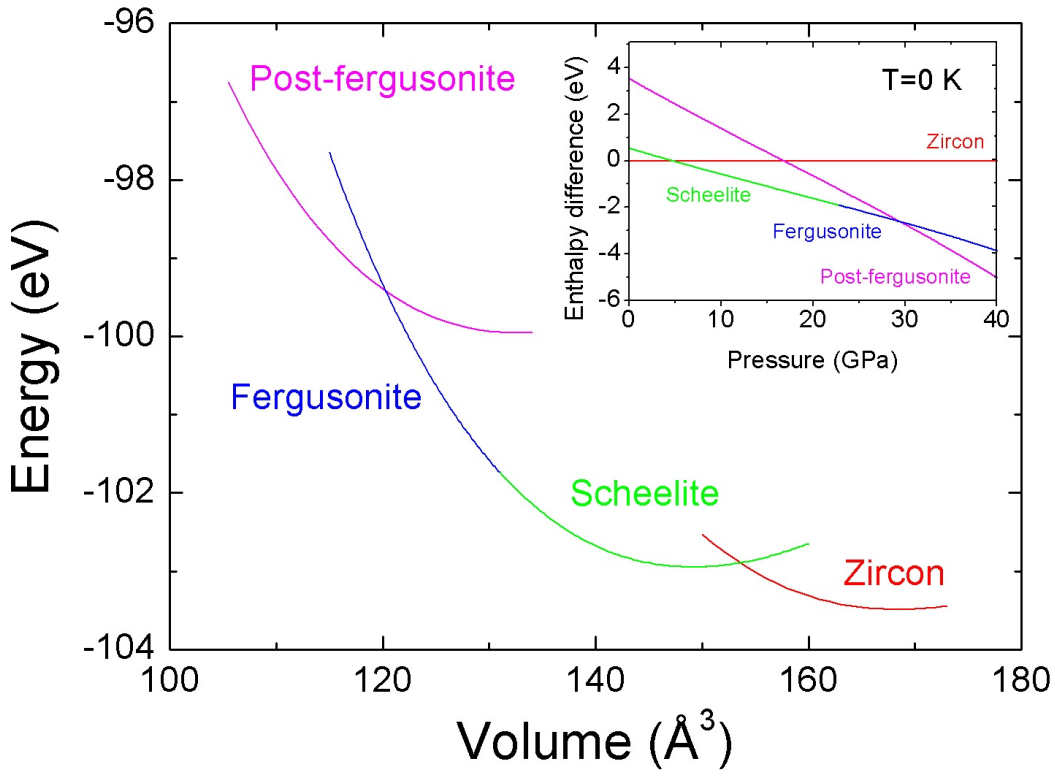

Figure 5.13: Theoretical energy-volume curves for different phases of $GdVO_4$. Energies are given per unit-cell. In the case of the post-fergusonite phase, the energy of the unit-cell has been divided by 2, since it has twice the number of atoms than the rest. *Inset:* Calculated pressure dependence of the enthalpy of the same $GdVO_4$ phases considering $T = 0$ K. The zircon phase is taken as a reference.

The calculated E-V curves for the different studied polymorphs of $GdVO_4$ is shown in Fig. 5.13. The theoretical pressure evolution of the enthalpy of these phases is shown in the inset of the figure, in which the zircon phase is taken as a referrence. Calculations were performed assuming $T = 0$ K. The structural parameters of these different structures of $GdVO_4$ are shown in Table 5.4. The enthalpy curves displayed in the inset of Fig. 5.13 show that the zircon-to-scheelite phase transition is predicted to take place at 4.8 GPa. Moreover, according to the energy-volume curves, which are also shown in Fig. 5.13, this transition should involve a huge volume collapse

of 10.9%, which is in agreement with our experimental observations. This is also coherent with the first-order reconstructive nature of the zircon-to-scheelite phase transition. The structural relationships between these phases, as well as different transition mechanism has been proposed in literature [151, 152, 186–188] for natural zircon ($ZrSiO_4$). These studies have shown that the reconstructive nature of the transition is directly related with the existence of a considerable kinetic barriers, which must be surpassed so that the transition can take place. Since our calculations do not contain any information about the particular kinetics of the transition, it is reasonable to assume that the predicted experimental transition pressure will be underestimated. In fact, whereas the transition should happen at 4.8 GPa according to our DFT calculations, we experimentally observe the appearance of the scheelite phase at 6.8(4) GPa. With respect to the post-fergusonite phase, the suggested structure (S.G.: *Cmca*) would appear at 29 GPa, which is compatible with the transition pressure observed in our Raman scattering experiments.

Lattice dynamics calculations of the zircon and scheelite phases of $GdVO_4$ were performed in order to support our Raman scattering experiments and to evaluate the dynamical stability of both structures. We also provide the frequencies of the infrared (IR) active (only the TO modes) and silent modes of both structures, which are shown in Fig.5.14 and Fig. 5.15 respectively. With regard to the IR active modes, all of them have a positive dependence on pressure in the zircon phase, with the only exception of the E_u mode located at $\sim$ 300 cm^{-1}, which is approximately constant, with less than a 1% of variation. In the scheelite phase, only the E_u and A_u modes located at $\sim$ 150 and 250 cm^{-1} at 0 GPa soften upon compression. As a result, there is a mode crossover of the latter with the hard E_u mode (located near 250 cm^{-1} at 0 GPa) around 21 GPa. With respect to the silent modes of the zircon phase, two of them harden, another remain constant and two soften as pressure increases. Moreover, the B_{1u} mode, which has the lowest frequency of all, shrinks to zero at $\sim$ 8.2 GPa, near the transition pressure. This mode correspond to pure rotations of the VO_4 tetrahedra around the direction defined by the *c*-axis. The fact that the dynamical instability at 8.2 GPa is so close to the transition pressure $\sim$ 7 GPa suggest that this

Table 5.4: Calculated structural parameters of different phases of $GdVO_4$. The fergusonite structure was calculated by assuming the unit-cell parameters obtained at 22.4 GPa in our XRD experiments as fixed, since this structure reduces to scheelite in our calculations.

Atom	Site	x	y	z
Zircon (S.G.: $I4_1/amd$) at 0 GPa; $a = b = 7.22610$ Å, $c = 6.35814$ Å				
O	16h	0	−0.06618	0.79907
V	4b	0	0.25	0.375
Gd	4a	0	0.75	0.125
Scheelite (S.G.: $I4_1/a$) at 14.1 GPa; $a = b = 4.96269$ Å, $c = 10.96299$ Å				
O	16f	0.65091	0.50346	0.29159
V	4a	0	0.25	0.125
Gd	4b	0	0.25	0.625
Fergusonite (S.G.: $I2/a$) at 22.4 GPa; $a = 4.89330$ Å, $b = 10.93670$ Å, $c = 4.81600$ Å, $\beta = 91.06°$				
O_1	8f	0.00104	0.21022	0.15253
O_2	8f	0.90564	0.45963	0.24678
V	4e	0.25	0.87632	0
Gd	4e	0.25	0.37511	0
Post-fergusonite (S.G.: $Cmca$) at 31.8 GPa; $a = 7.37379$ Å, $b = 12.23432$ Å, $c = 4.91467$ Å				
O_1	8f	0	0.08762	0.07106
O_2	8d	0.65227	0	0
O_3	8f	0	0.20808	0.50645
O_4	8e	0.25	0.34707	0.25
V	8f	0	0.41012	0.21704
Gd	8e	0.25	0.15843	0.25

mode could trigger the zircon-to-scheelite transition by lowering the kinetic barrier. This idea has been previously suggested by Mihailova *et al.* [151] for the zircon-to-reidite phase transition observed in $ZrSiO_4$. In fact, this behaviour is also predicted for many other zircon-type rare-earth orthovanadates [35, 181] and orthophosphates [134]. These ideas are discussed in more detail in Chapter 7.

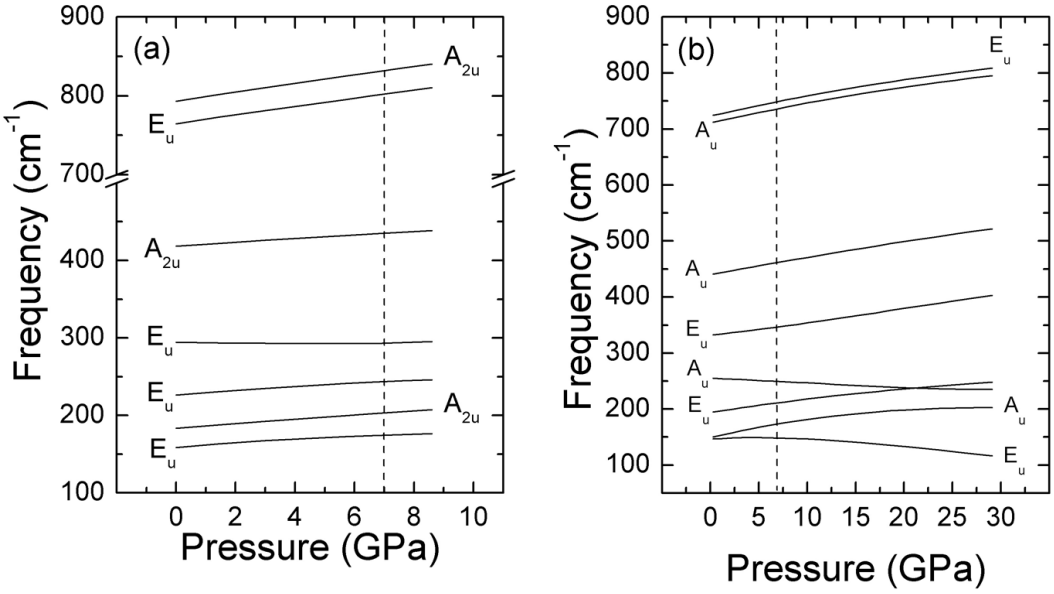

Figure 5.14: Calculated frequencies of the IR active modes (TO) of (a) zircon- and (b) scheelite-type $GdVO_4$.

Besides the vibrational structure of the zircon and scheelite phases of $GdVO_4$, we also performed calculations in order to study their elastic properties. The non-zero elastic constants of are summarized in Tables 5.5 and 5.6, in which we included the experimental and theoretical values of other RVO_4 compounds for the sake of comparison. With regard to the zircon phase, the calculated stiffness tensor elements at ambient pressure are quite similar, although apparently slightly underestimated, compared to the other RVO_4 compounds. On the other hand, the elastic constants calculated for scheelite-type $GdVO_4$ are put into comparison with previous reported values of $SmVO_4$ and $GdVO_4$ using the GGA+U and LSDA+U approximations [35, 157]. These

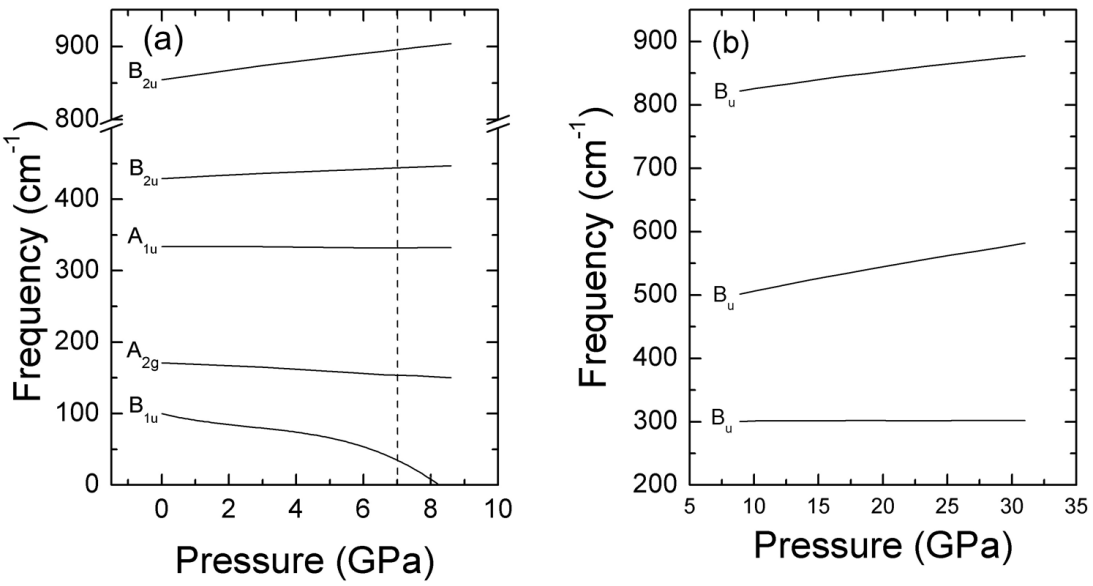

Figure 5.15: Calculated silent modes of (a) zircon and (b) scheelite-type $GdVO_4$

calculations were carried out using the VASP and CASTEP software packages respectively. It is clear that the obtained values for $SmVO_4$ and $GdVO_4$ in Ref. [35] and in our work [49] are in better agreement than the results reported in Ref. [157] for both compounds.

In order to seek for any kind of mechanical instability of either the zircon or the scheelite phases of $GdVO_4$, we also calculated the pressure evolution of the stiffness tensor elements assuming hydrostatic conditions. The results are shown in Fig. 5.16 for (a) zircon- and (b) scheelite-type $GdVO_4$. In both cases there is a mechanical instability at high pressures, as it can be inferred from the insets of Figs. 5.16 (a) and (b), where the lowest eigenvalue of the stiffness tensor shrinks to zero at a certain pressure, i.e., the matrix is not positive definite beyond that point. In particular, these instabilities take place at 9.6 GPa and 22.8 GPa for the zircon and scheelite phases respectively. Regarding the former, the condition $B_{66} < 0$ is not fulfilled over 9.6 GPa [89, 91, 94, 95]. This mechanical instability should not have any physical relevance in the transition process, since it take place when the zircon phase is nearly nonexistent, as it is shown in our experiments. With respect to the scheelite phase, the Born criterion $2B_{16}^2 < B_{66}(B_{11} - B_{12})$ [89, 91, 94, 95] does

Table 5.5: Theoretical and experimental stiffness tensor elements of different zircon-type rare-earth orthovanadates at ambient pressure.

	$SmVO_4$	$GdVO_4$	$TbVO_4$	$DyVO_4$	$HoVO_4$	$ErVO_4$
Elastic constant	[35]	(our work, [49])	[189]	[189, 190]	[191]	[192]
	Theoretical		Experimental			
C_{11}	212	227.2	240(2)	242(2)	246.4 (230K)	256.6(5.1)
C_{12}	37	45.6	55(3)	50(4)	–	53(3)
C_{13}	76	83.9	–	–	–	79(6)
C_{33}	286.6	297.8	–	–	310.5 (190 K)	313(6)
C_{44}	40.8	43.5	–	–	48.5 (250 K)	50.1(1.0)
C_{66}	13.6	16.5	13.1(2.0)	15.0(0.5)	16.07 (250 K)	17.7(0.9)

Table 5.6: Calculated stiffness tensor elements of different scheelite-type rare-earth orthovanadates at ambient pressure.

	$SmVO_4$	$SmVO_4$	$GdVO_4$	$GdVO_4$
Elastic constant	[35]	[157]	(our work, [49])	[157]
C_{11}	218	192	229.5	279
C_{12}	114.4	77	115.5	146
C_{13}	99.5	92	97.9	129
C_{33}	196.3	187	200.5	251
C_{44}	53.4	57	54.9	79
C_{66}	68.1	96	69.8	85
C_{16}	−21.8	−56	−22.5	−22

not stand beyond 22.8 GPa. The direction of deformation can be deducted from the eigenvector associated to the eigenvalue that becomes negative beyond 22.8 GPa, since this is proportional to the induced strain vector. At 23.7 GPa, the very next calculated pressure after 22.8 GPa, the eigenvector associated with the instability is $(-0.4195 \quad 0.4195 \quad 0 \quad 0 \quad 0 \quad 0.8050)$. This eigenvector corresponds to a distortion within the *ab* plane of the unit-cell. The immediate consequence of this is a decrease of the γ angle, and a contraction and expansion of the a and b lattice parameters respectively. The described changes are perfectly compatible with a monoclinic distortion of the scheelite phase, which leads to the fergusonite-type structure. Thus, calculations strongly support the fact that there is a scheelite-to-fergusonite phase transition in $GdVO_4$ at $\sim$ 20 GPa.

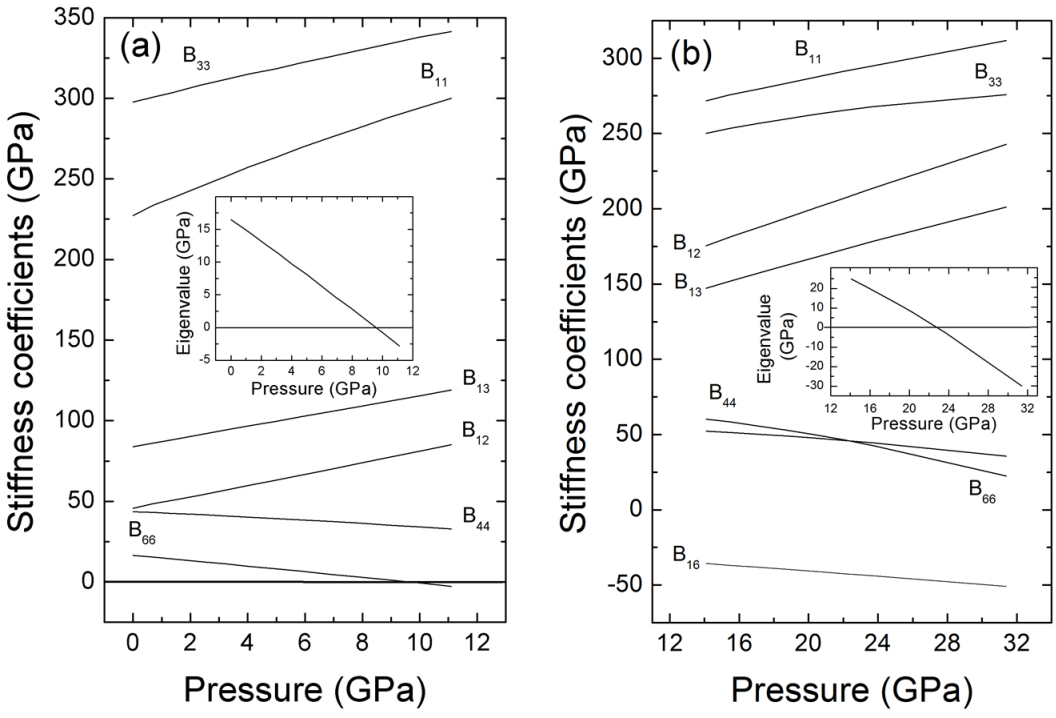

Figure 5.16: Theoretical stiffness matrix elements vs pressure for (a) zircon- and (b) scheelite-type $GdVO_4$. *Inset:* Pressure evolution of the lowest eigenvalue. Mechanical instabilities take place when this eigenvalue becomes zero. This happens at 9.6 and 22.8 for the zircon and scheelite phases respectively.

Table 5.7: Theoretical elastic moduli B, E and G (GPa), the B/G ratio, and Poisson's ratio ν in the Voigt, Reuss and Hill approximations for the zircon and scheelite phases of $GdVO_4$ at zero pressure. We included the values reported by Huang *et al.* [157] for the scheelite structure of $GdVO_4$.

Phase	Approximation	B	E	G	ν	B/G
Zircon	Voigt	131.0	148.5	56.6	0.311	2.31
	Reuss	126.1	105.3	38.7	0.361	3.26
	Hill	128.5	127.2	47.6	0.335	2.70
Scheelite	Voigt	142.5	155.8	59.1	0.318	2.41
	Reuss	141.1	147.3	55.5	0.326	2.54
	Hill	141.8	151.6	57.3	0.322	2.47
	Hill [157]	149	198	75	0.320	2.40
	Experimental [157]	140	175	68	0.290	2.10

Table 5.7 shows the calculated bulk (B), Young (E) and shear (G) moduli as well as the Poisson's ratio ν of zircon- and scheelite-type $GdVO_4$. Each of these quantities can be calculated by combining the elastic constants of the stiffness tensor under different approximations. In particular, we included the obtained values under the Voigt [193], Reuss [194] and Hill [195] approximations[1]. The theoretical and experimental values given in Huang *et al.* [157] for the scheelite phase are also shown in the table for the sake of comparison. According to Pugh [196], it is possible to establish an empirical relationship between the elastic moduli and the plastic properties of materials, which is expressed as the B/G ratio (see Table 5.7). In such study the following criterion is

[1]The bulk modulus and the shear modulus can be estimated according to the following approximations:
(1) Voigt: $B_V = (C_{11}+C_{22}+C_{33})/9+2(C_{12}+C_{13}+C_{23})/9$; $G_V = (C_{11}+C_{22}+C_{33}-C_{12}-C_{13}-C_{23})/15+(C_{44}+C_{55}+C_{66})/5$.
(2) Reuss: $B_R = [(S_{11}+S_{22}+S_{33})+2(S_{12}+S_{13}+S_{23})]^{-1}$; $G_R = [4(S_{11}+S_{22}+S_{33})-4(S_{12}+S_{13}+S_{23})+3(S_{44}+S_{55}+S_{66})]^{-1}$, where S_{ij} are the elements of the compliance tensor, defined as the inverse of the stiffness tensor ($[S] = [C]^{-1}$). The Hill approximation is the arithmetic mean of the values obtained under the Voigt and Reuss approximations:
(3) Hill: $B_H = (B_R + B_V)/2$; $G_H = (G_R + G_V)/2$.
In all cases, the Young's modulus E and the Poisson's ratio ν can be estimated as $E = 9BG/(3B + G)$ and $\nu = (3B - 2G)/(6B + 2G)$, respectively.

proposed: a material can be considered ductile if $B/G > 1.75$ and fragile otherwise. In our case, both zircon and scheelite phases of $GdVO_4$ can be considered ductile at zero pressure, with very similar B/G values in both cases.

For the sake of completeness, we also included the calculated Birch-Murnaghan EOS parameters for the post-fergusonite phase (S. G.: *Cmca*) proposed in this work, which are shown in Table 5.1. A particular feature that may attract our attention, is the fact that the bulk modulus of this post-fergusonite phase is smaller than that of the scheelite phase. In other words, the post-fergusonite phase would be more compressible, which is in apparent contradiction with the increase in density and packing efficiency in this phase. Some possible explanations have been given for such cases. For instance, in has been proposed that a smaller bulk modulus could be explained by a localized-to-delocalized electronic transition in the f electrons of the rare-earth cation. This phenomenon has been observed in pure rare-earths under high pressure conditions [197]. The consequence of such delocalization would be a weaker Gd–O bond, which leads to a higher compressibility. Nonetheless, these scenarios are just hypothetical and further experiments are required to elucidate this question.

5.7 Conclusions

In this section we presented our experimental and theoretical results on $GdVO_4$ under high pressures. XRD, Raman scattering and optical absorption experiments at high pressures show that there is a zircon-to-scheelite phase transition at 6.8(4) GPa. For these two phases we reported the calculated and experimental Birch-Murnaghan EOS parameters and the pressure dependence of the Raman active modes. We also included the theoretical behaviour of the IR and silent modes under high pressure for the zircon and scheelite phases. We predicted a dynamical instability at 8.2 GPa, near the experimental transition pressure, which suggest a possible influence of a soft silent phonon in the transition mechanism. The optical absorption measurements clearly showed

the band gap collapse during the transition, which explains the subtle change in the sample colour observed during the Raman experiments. We also found a scheelite-to-fergusonite phase transition near 20 GPa, which is induced by a mechanical instability according to our calculations. In our Raman scattering experiments we also confirmed the existence of a post-fergusonite phase over 29 GPa. We proposed an orthorhombic structure with *Cmca* symmetry as a possible candidate for this post-fergusonite structure, which is more stable than the scheelite phase over 29 GPa in our DFT calculations. This phase becomes opaque to light, which may be due to a small band gap in the IR region. Upon decompression, the scheelite phase reappears at 22.9 GPa and is recovered at low pressures, showing the irreversible character of the zircon-to-scheelite phase transition. A small fraction of post-fergusonite seems to remain in the recovered sample.

6 | Praseodymium orthovanadate under high pressure

In this chapter we present our results on the behaviour of $PrVO_4$ under high-pressure conditions. The results here presented have been published in Marqueño *et al.* [43] and [46]. Previously to such works, the behaviour of $PrVO_4$ at high pressures and room temperature has been studied, although many questions remained unanswered. This compound has been studied by means of Raman scattering experiments under high pressure by Errandonea *at al.* [65]. These authors compressed a powder $PrVO_4$ sample in a DAC loaded with 16:3:1 MEW as PTM, which is quasi-hydrostatic below ~ 10 GPa. According to the changes in their Raman spectra, a zircon-to-monazite phase transition takes place near 6 GPa. The monazite phase remains stable up to the maximum pressure reached in their experiments (17.2 GPa) and it Fis recovered at ambient conditions in a metastable state after decompression. In the same work, these authors report the XRD pattern of a recovered $PrVO_4$ sample after compressing it under non-hydrostatic conditions up to 12 GPa in a Paris-Edinburgh large-volume press cell. A monazite structure was recovered, reinforcing the idea of a zircon-to-monazite phase transition at high pressures. On the other hand, Bandiello *et al.* [42] performed powder XRD high-pressure experiments on $PrVO_4$. in which they reported a second phase transition to a post-monazite structure near 14 GPa. Since these experiments were performed with MEW as PTM, they are not hydrostatic beyond ~ 10 GPa. Moreover, the proposed structure for the post-monazite phase, which is a monoclinic $BaWO_4$-II-

type phase according to the authors, cannot explain their experimental observations. Their DFT calculations at $T = 0$ K show that there is a phase transition at 11 GPa, which is in agreement with their observations. However, there are considerable discrepancies in the predicted and observed lattice parameters. For instance, whereas they found $\beta = 90.71°$and $a = 11.557(7)$ Å in their experiments, these values are $\beta = 96.20°$and $a = 12.45$ Å according to calculations. Thus, these facts indicate that new experiments under better hydrostatic conditions as well as more accurate DFT calculations needed to be performed to properly determine the post-monazite crystalline structure.

In our study, we carried out high pressure powder XRD experiments using a more hydrostatic PTM (Ne gas). We also performed a more systematic and varied search for post-monazite candidate structures. In particular, we included other different polymorphs in our calculations and evaluated their stability and also their compatibility with our experimental observations. Powder XRD experiments confirmed the onset of the zircon-to-monazite phase transition at 5-5.9 GPa and the existence of a second phase transition at 12.2 GPa. In addition, we could show that the compressibility of the monazite phase is affected by hydrostaticity. We identified the post-monazite phase as a monoclinic $PbWO_4$-III-type structure (S.G.: $P2_1/n$), which is perfectly compatible with our experimental observations. Furthermore, our DFT calculations showed that the scheelite phase is energetically competitive with the monazite phase, suggesting that the observation of one phase or the other could depend on kinetic effects, an thus on temperature. Therefore, we performed different syntheses at high pressures ($P = 7$ GPa) and high temperatures ($T = 600$ - 1000℃) in a Paris-Edinburgh large press cell during different time lapses. The recovered sample was a mixture of zircon- and scheelite-type $PrVO_4$. The latter was recovered in a metastable phase and is not observed in high pressure experiments at room temperature. The recovered sample with the largest scheelite phase proportion was studied under compression by means of Raman scattering experiments, showing a reversible phase transition to a $PbWO_4$-III-type phase at 16.8(4) GPa. The pressure evolution of the Raman active modes were evaluated.

6.1 Experimental details

Polycrystalline $PrVO_4$ samples were prepared by the solid-state reaction method introducing proper amounts of predried Pr_6O_{11} and V_2O_5 (Alfa-Aesar) in a Pt crucible. The homogeneous sample was heated up to 600 ℃ for 24h and subsequently reground and pelletized. The obtained pellets were heated again up to 900 ℃ for 24h and at 1100 ℃ for another 12h. The recovered samples were characterized at room conditions via XRD, using a Panalytical X-pert Pro diffractometer using Cu $-K_\alpha$ radiation. These experiments confirmed a zircon structure whose lattice parameters are $a = 7.3618(2)$ Å and $c = 6.4634(3)$ Å, which are in good agreement with the values previously reported in literature [51].

The zircon-type $PrVO_4$ powder samples were studied by means of angle dispersive XRD experiments in the MSPD beamline the ALBA-CELLS synchrotron [166] (Fig. 3.12). The sample was compressed using a DAC with diamond culets of 350 μm diameter. The powder sample and some ruby chips were introduced in a 150 μm diameter hole drilled on a rhenium gasket preindented to a 40 μm thickness. The pressure within the chamber was determined by the ruby luminescence method [100]. Ne gas was loaded in the DAC as PTM, which ensures a hydrostatic liquid medium below 5 GPa and remains quasi-hydrostatic up to 20 GPa [99]. For the XRD measurements we used a monochromatic x-ray beam with a wavelentgth $\lambda = 0.4642$ Å, focused down to 20×20 μm^2 FWHM. The x-ray patterns were collected using a bidimensional Rayonix CCD. The collected images were integrated and transformed into I vs. 2θ patterns using the DIOPTAS software [122]. Structural refinements were carried out with the UNITCELL and PowderCell software packages. Preferred orientations in the sample lead to spotty cake images, which hinders the structural analysis concerning the relative intensities of the Bragg peaks. Thus, Rietveld refinements could not be performed but only Le Bail analysis.

The high-pressure and high-temperature syntheses of the scheelite phase of $PrVO_4$ were performed in a Paris-Edinburgh large press cell, which is shown in Fig. 3.17 (a) in Chapter 3. A com-

pacted powder sample of $PrVO_4$ was introduced in a compacted boron nitride tube, which acts as PTM. This was subsequently introduced in a cylindrical graphite oven, with two molybdenum disks on its bases as the electrodes of the heating system. The whole capsule was then introduced in a pyrophyllite gasket, which was previously treated at 1223 K for 1 h 30min. A Teflon ring was added around the gasket to prevent lateral extrusion of the material. This also improved the the pressure-load efficiency. An scheme of this assembly is depicted in Fig. 3.18. The pressure of the sample was raised by a hand-operated hydraulic pump, which raised the oil pressure and moved the piston. The oven was heated by a computer-controlled electrical power supply. The P-T conditions of the sample were measured and controlled by using the oil-pressure/sample-pressure and electrical-power/temperature calibration curves, whose estimated error is below 5%. Three different syntheses were performed at 7 GPa at 600, 800 and 1000 ℃ for 1 h. The synthesis at 7 GPa and 800 was repeated afterwards for 6 h in order to increase the scheelite proportion in the recovered sample. In this second run, we decided to heat up the sample below 1000 ℃ in order to avoid temperature-induced decomposition. The compression of the sample was carried out in 2-2.5 GPa steps up to 7 GPa. After reaching this pressure, temperature was linearly increased during 10 min from ambient to the target temperature and kept at that temperature for 1h (6h in the latter case). After this time lapse, the sample was quenched to ambien temperature and decompressed during few hours. The product was then recovered at room conditions. The sample was then characterized *ex situ* using XRD at ambient conditions on a Bruker B8 Advance diffractometer configuration using Cu–K_α radiation. The lattice parameters as well as the atomic positions were refined by the Rietveld method (subsection 3.2.2) using the program GSAS-II [198]. By doing so we could also estimate the relative amount of zircon and scheelite phases.

The sample with a higher scheelite/zircon phase composition ratio ($\sim$ 80/20) was studied by means of Raman spectroscopy under high pressure. The sample load was identical to that used in XRD experiments (same DAC, powder sample, Ne as PTM, ruby as pressure gauge, etc.), but with an Inconel gasket instead of a rhenium one. For the Raman scattering experiments, we

used the same in-house built setup than in the previous experiments with $NdVO_4$ and $GdVO_4$. A description of the system can be found in subsection 3.3.

6.2 Simulation details

Ab initio calculations were performed in order to better understand the influence of pressure on $PrVO_4$. Computational simulations were carried out with the *Vienna Ab initio Simulation Package* (VASP) [126, 127] within the framework of the density functional theory (DFT). The projector augmented wave (PAW) [128] pseudopotentials of Pt, V and O were provided by the VASP pseudopotential base. The $4f$ electrons of the Pr atom were assumed as core electrons. The exchange-correlation energy was described by the generalized-gradient approximation (GGA) with the AM05 prescription [129, 199]. A basis of plane waves up to a kinetic energy cutoff of 540 eV and a dense Monkhorst-Pack k-special points grid [130] to carry out the integrations in the Brillouin zone (BZ), which ensures highly converged results. The structural configurations of a set of selected unit-cell volumes were optimized by minimizing the forces on the atoms and the stress matrix. The convergence criteria used implied forces were smaller than 0.006 eV/Å and differences among the diagonal components of the stress tensor below 0.1 GPa. $T = 0$ K was assumed for these simulations. Therefore, transition pressures can be estimated by analyzing the enthalphy curves of the different polymorphs.

The effects of considering the $4f$ electrons of the Pr atom as valence instead of core electrons. The resulting effect on the value of the transition pressures was rather small though. For instance, the calculated transition pressures in the zircon-to-scheelite phase are 3.6 and 3.7 GPa considering the $4f$ electrons in the core and in the valence band, respectively.

Temperature effects were also considered in some particular cases. In order to introduce such effects, lattice-dynamics calculations have been carried out using the PHONOPY software package and scripts. A complete description of how to obtain the thermodynamic properties in the

harmonic and quasi-harmonic approximations are given in Togo and Tanaka [131]. Using the same software, it is also possible to calculate the lattice-dynamical properties in the harmonic approximation. This allowed to obtain the Hellman Feynman forces and the dynamical matrix to derive the frequencies, the eigenvectors and the irreducible representations of the normal vibration modes at the BZ zone-center. The phonon density of states as well as the phonon dispersion were calculated using supercells. The elastic properties of the crystal were also studied by using the method implemented in the VASP code [132]. The elastic constants (i.e. the stiffness tensor) of the solid were calculated in the harmonic approximation for the fully optimized structures, through small distortions, which give rise to small strains in different directions.

Calculations were performed by our collaborators at University of La Laguna (Tenerife, Spain), Alfonso Muñoz and Plácida Rodríguez-Hernández.

6.3 Powder XRD experiments

Some selected powder XRD patterns of $PrVO_4$ at different pressures are shown in Fig. 6.1. The (a) and (b) pictures show the changes in the XRD patterns of $PrVO_4$ under compression (pressure ranges 1.4-11.0 and 11.0-20.7 GPa respectively) whereas (c) shows the behaviour of the sample upon pressure release (from 20.7 to 0.2 GPa). According to our Le Bail refinements, the unit-cell lattice parameters of the zircon phase at 1.4 GPa are $a = 7.333(3)$ Å and $c = 6.454(3)$ Å. The highest pressure at which the zircon structure is observed pure is 5 GPa. At 5.9 GPa, which is the very next pressure, the XRD pattern looks strikingly different, which reveals the onset of a phase transition. This new phase can be undoubtedly identified as a monazite-type structure. Upon compression, we observe the coexistence of both zircon and monazite phases up to 11 GPa. The monazite phase finally appears as a single phase at this pressure. In addition to this, some extra Bragg peaks appear at 5.9 GPa, which are associated to the pressure-induced solidification of the Ne gas used as PTM. These are labeled as "Ne" in the figure. Beyond 6.3 GPa, the reflections

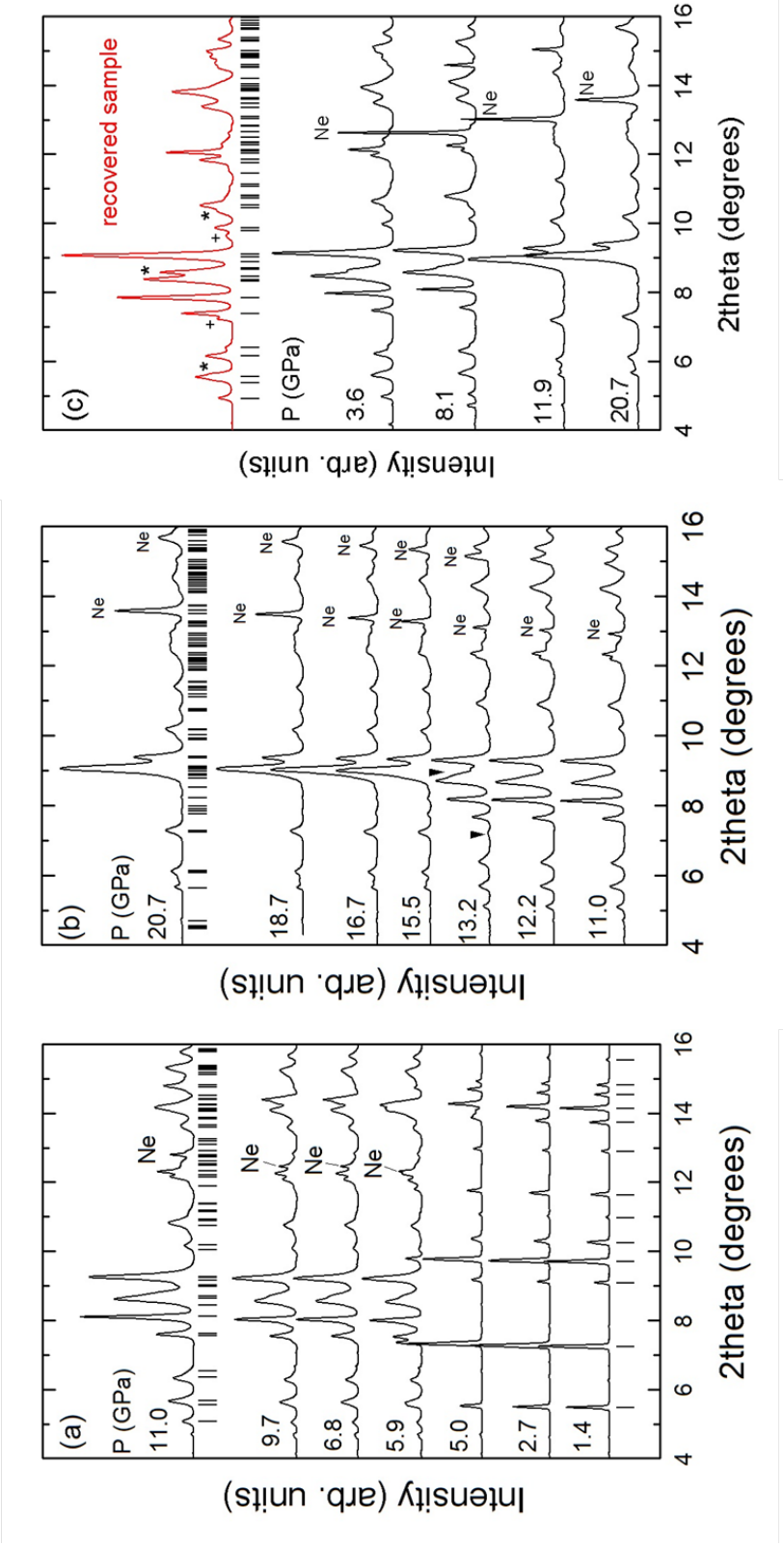

Figure 6.1: Selected powder XRD patterns of $PrVO_4$ at different pressures and ambient temperature (λ = 0.4642 Å). The position of the Bragg peaks for the zircon (1.4 GPa), monazite (11.0 GPa and recovered phase) and the $PbWO_4$-III phases of $PrVO_4$ are depicted as black vertical ticks. Black triangles at (b) indicate the emergent peaks of the $PbWO_4$-III structure at 13.2 GPa. The XRD pattern of the recovered sample at 0.2 GPa id depicted in red colour. The Bragg reflections labeled with the "*" and "+" symbols cannot be explained with a monazite structure and have been tentatively assigned to the scheelite and zircon structures respectively.

associated with the zircon phase are weak and insufficient to refine the lattice parameters. Thus, the structure could only be analyzed for pressures lower than 6.3 GPa. The refined unit-cell parameters of the monazite structure at 11.0 GPa are $a = 6.744(8)$, $b = 6.975(14)$ and $c = 6.492(5)$ Å and $\beta = 104.22(5)^\circ$. This transition confirms the results reported by Errandonea *et al.* [65] and Bandiello *et al.*[42]. A volume collapse of $\Delta V/V_0 \approx 8.4\%$ takes place at 5.9 GPa, reflecting the first-order nature of the transition. The structure remains stable upon further compression up to 12.2 GPa, as it is shown in Fig. 6.1 (a).

As it is displayed in Fig. 6.1 (b), beyond 12.2 GPa new Bragg reflections appear in the XRD patterns, while those associated to the monazite phase begin to disappear. Above 15.5 GPa, the monazite phase is no longer visible. On the contrary, the new high pressure phase is stable up to the maximum pressure reached in the experiments ($P = 20.7$ GPa). Similar behaviour has been observed in $CeVO_4$ under high pressure, in which two phase transitions are observed at 5.6 (zircon-to-monazite) and 14.7 GPa (monazite-to-post-monazite) [39]. The authors suggest a post-barite-type structure (S.G.: $P2_12_12_1$, $Z = 4$) such as the one observed in $BaSO_4$ and $PbSO_4$ [200, 201]. On the contrary, in the case of monazite-type $LaVO_4$, Errandonea *et al.* [45] reported XRD and Raman scattering measurements under high pressure, showing that there is a phase transition to a $BaWO_4$-II structure (S. G.: $P2_1/n$, $Z = 8$) below 12 GPa. As it has been previously mentioned, Bandiello *et al.* [42] proposed a $BaWO_4$-II-type structure for $PrVO_4$, which showed some inconsistencies with the measured unit-cell lattice parameters. Here, several high pressure structures were considered as post-monazite candidate structures. From all of those considered, we decided to propose one similar to the $PbWO_4$-III phase (S.G.: $P2_1/n$, $Z = 8$), which according to Richter *et al.* is formally isomorphic to the $BaWO_4$-II phase. However, we decided to name this new phase "$PbWO_4$-III" instead of "$BaWO_4$-II" because the former is associated with a smaller monoclinic distortion ($\beta \sim 90^\circ$) which barely changes with pressure. In our *ab initio* calculations we could verify that the structure proposed by Bandiello *et al.* [42] corresponded to a free energy local minimum, whereas our candidate structure is associated with an absolute minimum. Thus,

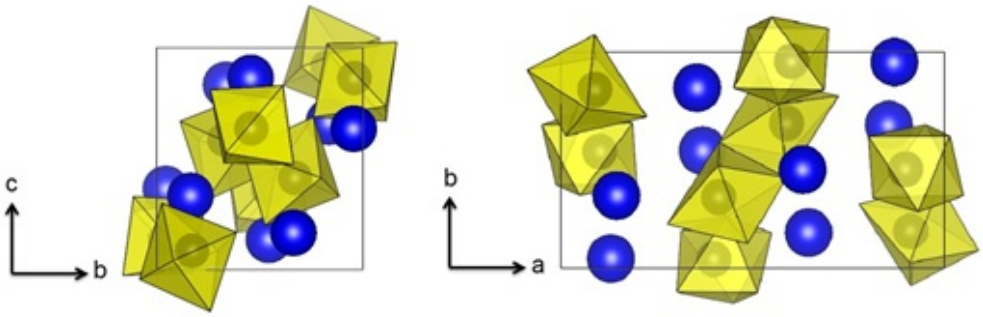

Figure 6.2: Unit-cell of the $PbWO_4$-III phase of $PrVO_4$ under different projections. The Pr atoms and the VO_6 units are represented as blue spheres and yellow polyhedra. The V atoms are represented as dark spheres within the yellow polyhedra.

the proposed structure is the most stable phase beyond the transition pressure. The unit-cell of the $PbWO_4$-III-type phase is depicted in Fig. 6.2. This kind of structure can also be considered as a distorted version of the post-monazite phase of $CeVO_4$. Actually, both crystal structures are related via group-subgroup transformations. The reasons that support the assignment ot the $PbWO_4$-III structure to the post-monazite phase are manifold:

(i) This phase is the most stable of all the considered phases according to our DFT calculations, as it is shown in the *Ab initio* calculations section.

(ii) The predicted transition pressure (P_{theo} = 11.1 GPa) is compatible with our experimental observations (P_{exp} = 12.7(8) GPa).

(iii) The simulated XRD pattern of the calculated structure is qualitatively similar to the experimental pattern at the same pressure (Fig 6.3).

(iv) The predicted pressure dependence of the unit-cell lattice parameters is in good agreement with the experimental data obtained from XRD measurements

(v) This phase is isomorphic to the high pressure post-monazite phase of $LaVO_4$.

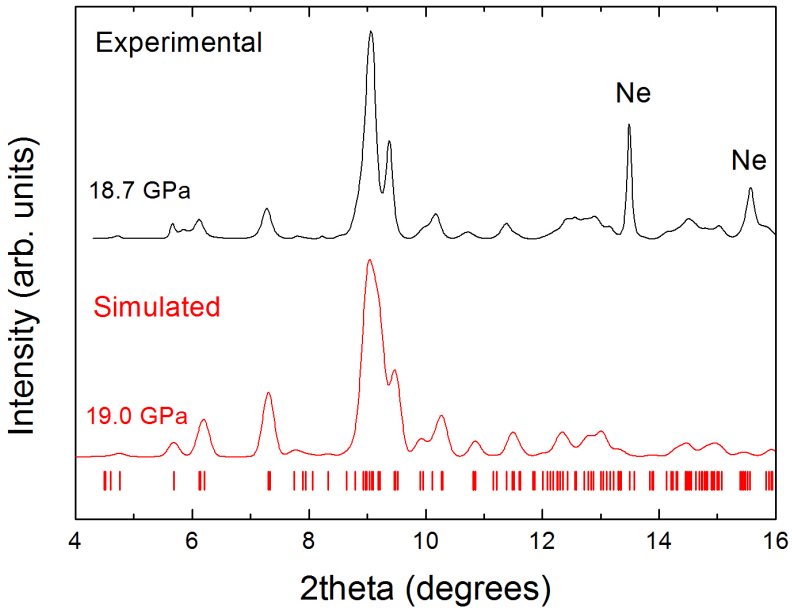

Figure 6.3: Visual comparison of the experimental (black line) and simulated (red line) XRD patterns of the $PbWO_4$-III phase of $PrVO_4$ at $\sim$ 19 GPa (λ = 0.4642 Å). The calculated Bragg peak positions are depicted as red vertical ticks. In the simulated patter we assumed a Gaussian width of w = 0.05. The predicted lattice parameters and atomic positions at 19 GPa are summarized in Table 6.1.

The monazite-to-$PbWO_4$-III phase transition shows a noticeable large volume collapse of $\Delta V/V_0 \approx 8.8\%$ at 14.4 GPa, which is similar to the volume change in the first phase transition. The refined $PbWO_4$-III phase lattice parameters at 16.7 GPa are a = 11.681(11) Å, b = 6.496(4) Å, c = 6.865(8) Å and β = 90.42(4)°. It must be remarked that in this new high-pressure phase, the VO_4 tetrahedra that are present in the previous crystal structures no longer exist, since the vanadium coordination increases from 4 to 4+2 during the transition. In other words, the VO_4 tetrahedra of the monazite phase transform into the slightly distorted VO_6 octahedra that are part of the $PbWO_4$-III structure. This can be observed in Fig. 6.2. The calculated atomic positions for the $PbWO_4$-III phase are compiled in Table 6.1.

Upon decompression, the monazite-type phase reappears at pressures below 11.9 GPa and is finally recovered at room conditions in a metastable state. Thus, while the second phase transition is reversible, the first is not. A similar behaviour has been reported for other orthovanadates

Table 6.1: Theoretical atomic positions for the $PbWO_4$-III structure ($S.G.: P2_1/n$, $Z = 8$)of $PrVO_4$ at 19 GPa. The unit-cell lattice parameters are $a = 11.5608$, $b = 6.3821$, $c = 6.8746$ Å and $\beta = 90.365$ °.

Atom	x	y	z
O_1	0.4091	0.4752	0.8004
O_2	0.3016	0.8889	0.2641
O_3	0.4507	0.8359	0.9745
O_4	0.4507	0.8359	0.9745
O_5	0.4315	0.2395	0.3116
O_6	0.3134	0.1734	0.9817
O_7	0.4867	0.1132	0.6695
O_8	0.4117	0.5823	0.4571
V_1	0.4116	0.3282	0.5864
V_2	0.3986	0.0408	0.1366
Pr_1	0.3547	0.8363	0.6666
Pr_2	0.3695	0.5442	0.1355

such as $CevO_4$ and $LaVO_4$ [39, 45]. This can be seen in the XRD pattern of the recovered sample near ambient pressure, which is shown in Fig. 6.1 (c). The refined lattice parameters of the recovered monazite phase are $a = 7.008(5)$ Å, $b = 7.198(11)$ Å, $c = 6.610(8)$ Å, and $\beta = 104.85(5)°$. The difference between these values and those reported in Ref. [40] range from 0.5 to 1.0%. Some of the Bragg peaks in the recovered XRD pattern could not be explained with a monazite-type phase, but with the zircon and scheelite structures (labeled with the symbols "*" and "+" respectively in Fig. 6.1 (c)). The tentative values of their unit-cell parameters at 0.2 GPa are $a \sim 7.353$ Å and $c \sim 6.510$ Å for the zircon phase and $a \sim 5.140$ Å and $c \sim 11.892$ Å for the scheelite phase. Hence, it is reasonable to suggest that a minor quantity of scheelite-type $PrVO_4$ appears below 11.9 GPa, just when the second phase transition is reversed, and another small

fraction of the sample returns to the zircon structure, which is the most stable phase at ambient conditions. These hypotheses cannot be fully confirmed, since the recovered XRD pattern does not show enough Bragg reflections that could be assigned to these phases. Nonetheless, the suggested scenario is coherent with the results obtained in our high-pressure-high-temperature experiments, which are shown in the next section of this chapter.

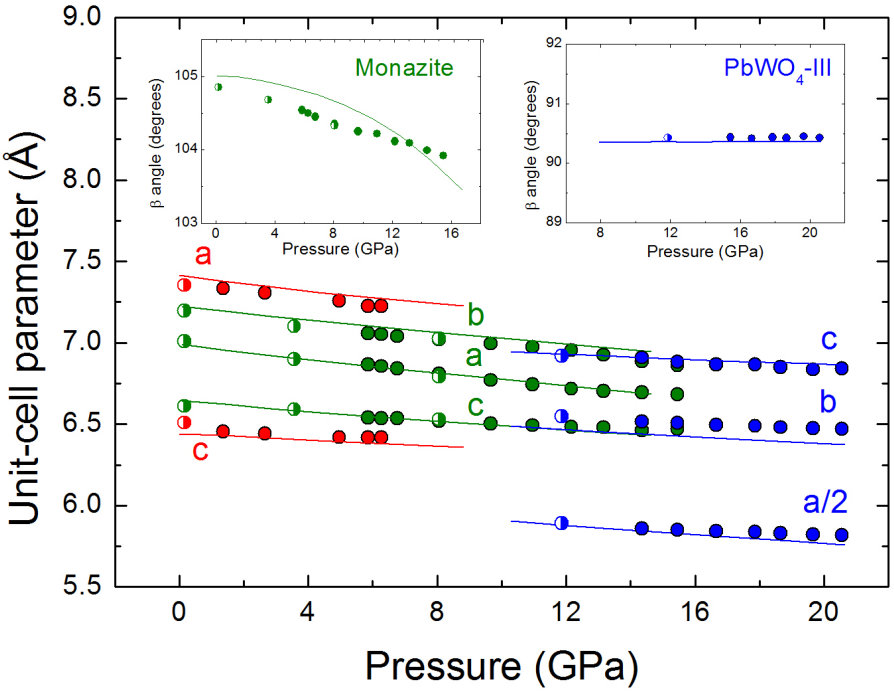

Figure 6.4: Unit-cell parameters vs pressure for the zircon (red), monazite (green) and $PbWO_4$-III (blue) phases of $PrVO_4$. Experimental data and calculations are represented with circles and solid lines respectively. The data collected upon pressure release are depicted as semi-void circles. The insets of the figure represent the evolution of the monoclinic angle β for the monazite and $PbWO_4$-III phases.

Fig. 6.4 shows the pressure dependence of the theoretical and experimental lattice parameters for zircon-, monazite- and $PbWO_4$-III-type $PrVO_4$. The linear compressibilities of the experimental and calculated values of the lattice parameters are summarized in Table 6.2. In the case of the $PbWO_4$-III phase, there is an excellent agreement between the calculated and experimental values, which supports the hypothesis of this phase as the post-monazite structure of $PrVO_4$.

The compressibility of the lattice parameters is anisotropic for all three polymorphs, although κ is very similar for the a, b and c axes in the $PbWO_4$ phase. Regarding the monazite phase, the compressibilities of the a and b axes are similar, whereas the c parameter is nearly half compressible than the former two. These values are qualitatively compatible with those reported for other monazite-type rare-earth orthovanadates such as $LaVO_4$ [45] and $CeVO_4$ [39]. Calculations on rare-earth orthophosphates such as $LaPO_4$, $CePO_4$ and $PrPO_4$ also yield compatible results [140]. The linear compressibility of the b parameter obtained in our experimental analysis is in much better agreement with theoretical predictions than the value reported in Ref. [42] which is 50% higher, as it is shown in Table 6.2. This may be a consequence to the different hydrostatic conditions over 10 GPa in the experiments, since Bandiello *et al.* [42] used a 16:3:1 MEW mixture as PTM whereas Ne gas was used in our case. The monazite-type structure is described in detail in section 1.2 (Fig. 1.3). A difference between experiments and calculations with regard to the monazite phase is that, although in both cases a decrease of the monoclinic β angle is observed, the dependence with pressure is more or less constant with pressure in the former whereas it shows a non-linear behaviour in the latter. From our experimental data, we obtained a pressure coefficient of $-6.1(2)\times10^{-2}$ °/GPa and a zero-pressure angle 104.87(2)°after performing a linear fitting. This tendency has also been experimentally verified in both $LaVO_4$ and $CeVO_4$ [39, 45]. As we stated before, in the $PbWO_4$-III phase all axes show similar compressibilities. Another particularity of this phase is that the monoclinic angle β remains more or less constant upon compression, with a measured value of $\sim 90.4°$. Calculations do correctly predict this behaviour.

Fig. 6.5 shows the experimental and calculated pressure dependence of the unit-cell volume of the different observed phases. The experimental data corresponding to the zircon and monazite phases were fitted to a second-order and a third-order BM EOS. The former analysis allow us to compare our data with that reported by Bandiello *et al.* [42]. In the latter case, we decided to fix the value of the bulk modulus derivative to the theoretical value in order to improve the reliability of the fit, since it is known that there is a correlation of B_0 and B_0'. On the other hand,

Table 6.2: Linear compressibilities of the unit-cell parameters of each $PrVO_4$ polymorph observed in the high pressure-room temperature XRD experiments. In the zircon and monazite phases, the values of κ were obtained at ambient conditions, whereas in the case of $PbWO_4$-III these values are estimated at $\sim$ 11.5 GPa.

Phase		κ_a	κ_b	κ_c	κ_β
		$(\times 10^{-3})$ GPa^{-1}	$(\times 10^{-3})$ GPa^{-1}	$(\times 10^{-3})$ GPa^{-1}	$(\times 10^{-4})$ GPa^{-1}
Zircon	Ref.[42]	3.1(1)	–	1.29(4)	–
	Our work [43]	3.03(5)	–	1.30(4)	–
	Theory	2.75	–	1.49	–
Monazite	Ref.[42]	3.4(1)	4.3(1)	2.1(3)	6.8(2)
	Our work [43]	3.0(1)	2.8(1)	1.5(2)	5.8(1)
	Theory	3.03	2.82	2.02	2.71
$PbWO_4$-III	Ref. [42]	0.5(1)	1.7(2)	1.7(2)	2.0(5)
	Our work [43]	1.36(9)	1.31(1)	1.4(1)	0.03
	Theory	1.36	1.31	1.46	0.10

we used a second-order BM EOS to fit the experimental data of the $PbWO_4$-III phase due to the fact that the predicted value of B_0' is close to 4. In Table 6.3 we included our experimental and theoretical results as well as those reported by Ref. [42] for the sake of comparison. In general, the zircon and monazite phases have very similar bulk moduli B_0. The value of the bulk modulus of the zircon phase reported in Ref. [42] and in our experiments is very similar, while that of the monazite phase is clearly underestimated by Bandiello *et al.* [42]. This can be explained in terms of the deterioration of the hydrostatic conditions provided by MEW over $\sim$ 10 GPa [99]. In any case, the reported values for the zircon and monazite phases in our experiments [43] and in Ref.

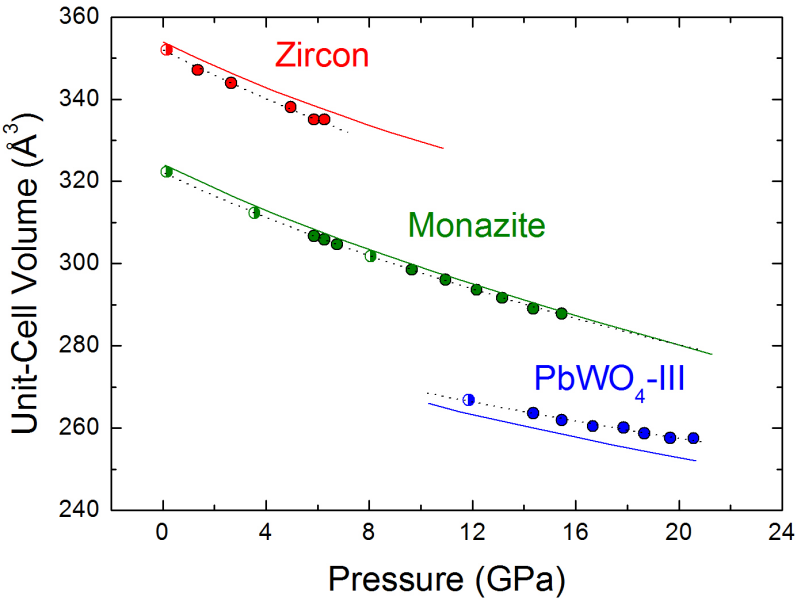

Figure 6.5: Unit-cell volume vs. pressure for zircon-, scheelite- and $PbWO_4$-III-type $PrVO_4$. Experimental and calculated data are represented as in Fig. 6.4. The spotted lines represent the EOS fitted to the data.

[42] are both compatible with calculations. The $PbWO_4$-III structure shows an increase of $\sim$ 50% in the value of B_0 with respect to the previous phases, which may be associated to the change in coordination of the vanadium atom from 4 to 4+2. In this case, the experimental value of the bulk modulus B_0 is $\sim$ 25% higher than the calculated value for the same structure. This disagreement in the experimental and predicted compressibility may arise form the scarcity of experimental points at the highest pressures (when this phase is observed as single). The calculated value of the EOS parameters of the scheelite phase are included for completion.

6.4 Scheelite phase synthesis and characterization

Our experiments at room-temperature and high-pressure as well as those reported in Refs. [42] and [65] confirm that zircon-type $PrVO_4$ transforms into a monazite-type structure upon compression at $\sim$ 5.5 GPa. Nonetheless, several experiments reported in literature have shown

Table 6.3: BM EOS parameters of zircon-, monazite-, scheelite- and $PbWO_4$-III-type $PrVO_4$.

Phase	Range		V_0 (Å^3)	B_0 (GPa)	B_0'
Zircon	Ref. [42]	Experiment	350.4(3)	120(3)	4.0 (fixed)
	Our work [43]	Experiment	351(3)	117(4)	4.0 (fixed)
	($P < 6.5$ GPa)		352(4)	110(6)	5.8 (fixed)
		Theory	354.0	114.2	5.8
Monazite	Ref. [42]	Experiment	321(4)	95(6)	4.0 (fixed)
	Our work [43]	Experiment	322(3)	108(5)	4.0 (fixed)
	($P < 15.5$ GPa)		321.9(3)	114.8(1.4)	3.1 (fixed)
		Theory	324.0	111.2	3.1
$PbWO_4$-III	Ref. [42]	561(4)	147(6)	4.0 (fixed)	
	Our work [43]	Experiment	566(3)	175(15)	4.0
	($P > 11$ GPa)	Theory	568.09	136.4	3.9
Scheelite	Our work [43]	Theory	312.1	139.4	4.1

that the scheelite phase of other RVO_4 compounds with larger and smaller cations (R = Ce and Nd) can be achieved under compression [40, 44, 202]. Furthermore, our *ab initio* calculations show that the scheelite phase is energetically competitive with the monazite phase at high pressures, which encourage us to carry out the synthesis of the scheelite phase of $PrVO_4$. In order to obtain such structure, we performed four different syntheses at 7 GPa: at 600, 800 and 1000 ℃ during 1 h and at 800 for 6 hours. Fig. 6.6 shows the XRD patterns of the recovered samples which were synthesised at 7 GPa and 800 ℃ for 1 and 6 hours. The recovered pattern is composed of different Bragg

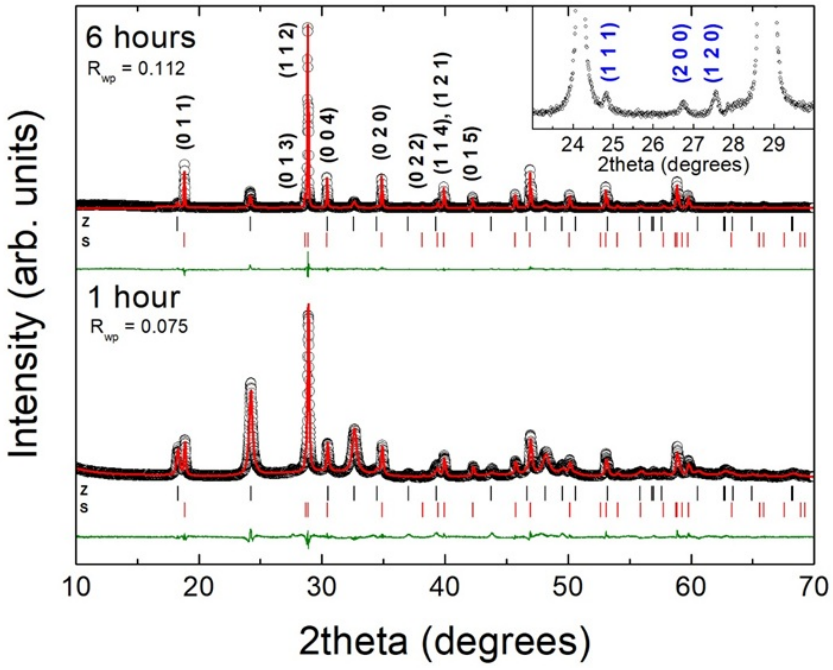

Figure 6.6: Powder XRD patterns of the recovered samples at ambient conditions after their synthesis at 7 GPa and 800 ℃ for 1 and 6 hours (47 and 78% of scheelite phase, respectively). White dots represent the experimental data and red solid lines stand for the refined patterns. The green lines at the bottom of each pattern represent the difference between these two. Black and red ticks indicate the positions of the Bragg reflections of the zircon and scheelite phases respectively. The reflections of the scheelite phase of $PrVO_4$ are labeled with their respective (*hkl*) Miller indices in the upper pattern. *Inset*: Bragg reflections of a remaining tiny fraction of monazite-type $PrVO_4$.

reflections that can be assigned to a mixture of both zircon and scheelite phases. The combined effects of temperature gradients during the synthesis process as well as the existence of kinetic barriers between these two structures [151, 187, 188] produce an heterogeneous composition in the recovered sample, with a different zircon/scheelite relative composition in different parts of it. Nonetheless, these effects can be overcome by performing syntheses for longer periods of time, so that more parts of the system can reach the fully stable phase. In fact, as it is shown in Fig. 6.6, longer time lapses lead to a higher degree of homogeneity and a larger proportion of scheelite phase. It must be remarked that, as it can be seen in this picture, the Bragg reflections associated to the zircon phase are much more broad than those corresponding to the scheelite phase. This could be explained as a direct consequence of the internal strains of the zircon phase that take

place during the zircon-to-scheelite phase transition.

Besides the zircon and scheelite phases, some weak reflections can be observed in the region $2\theta \approx 25\text{-}30^{\circ}$, which cannot be explained with these two structures. This can be seen in the inset of Fig. 6.6. We found that a monazite phase with unit-cell parameters $a = 6.920$ Å, $b = 7.406$ Å, $c = 6.551$ Å and $\beta = 105.4^{\circ}$is compatible with the existence of such reflections. According to our Rietveld refinements, this structure is found in a relative proportion of ~ 2 wt %. The corresponding (hkl) Miller indices of the reflections associated with the monazite structure are depicted in blue in the inset of Fig. 6.6. Although the suggestion of the monazite phase in order to explain the weak reflections seems quite reasonable, we must emphasize that this is only an hypothesis, since there are not enough reflections in the pattern to completely verify it. Nonetheless, the presence of a minor residual of this phase in the final result is coherent with the experimental procedure that we followed during the synthesis. As we previously explained, the original sample was compressed at 7 GPa at room temperature and temperature was increased once this pressure has been achieved. We expect a partial transition from zircon to monazite at high pressures before the heating process. As the temperature of the sample is increased, this fraction of the monazite phase should undergo a phase transition to the scheelite phase, which is presumably the most stable phase at 7 GPa. This would be a consequence of the system overcoming the kinetic barriers through thermal motion of the atoms.

The XRD patterns of the recovered sample were refined according to the Rietveld method. The obtained results are shown in Table 6.4. In this table we included the lattice parameters of both zircon and scheelite structures, the atomic positions of the oxygen atoms in the scheelite unit-cell (the position of the praseodymium and vanadium atoms are fixed by symmetry constraints), the relative amount of each phase and the R_{wp} fitting parameter. As it was expected, the refined values of the unit-cell lattice parameters for scheelite-type $PrVO_4$ lie in between of those obtained for the same phase of $NdVO_4$ [43] and $CeVO_4$ [39, 202] after being decompressed. With respect to the zircon/scheelite relative amounts, the refinements revealed that the scheelite proportion

decreases as temperature increases. By contrast, the scheelite phase was quite abundant (~ 80%) in the recovered product when the synthesis time duration was extended to 6 hours. In our argumentation, we assumed that the scheelite phase, not the monazite structure, is the most stable polymorph at 7 GPa, but it is necessary to heat up the sample in order to surpass kinetic barriers. Nonetheless, our results could also indicate that the scheelite phase may be more stable than the monazite phases at high-temperature conditions due to entropic effects [203]. However, as we will show latter in the *ab initio* calculations section, entropic effects barely change the relative stability of these two high pressure structures.

Table 6.4: Refined parameters (Rietveld method) of the recovered scheelite phase at ambient conditions. All syntheses were performed at 7 GPa. The temperature of each synthesis is indicated in the first row.

Synthesis conditions	600℃ (1 h)	800℃ (1 h)	1000℃ (1 h)	800℃ (6 h)
a (Å)	5.1437	5.1463	5.1447	5.1436
c (Å)	11.7489	11.7533	11.7750	11.7488
V (Å)	310.84	311.28	311.01	310.83
O (x)	0.2324	0.2300	0.2307	0.2348
O (y)	0.1166	0.1245	0.1295	0.1202
O (z)	0.0458	0.0468	0.0429	0.0470
R_{wp}	0.092	0.075	0.098	0.108
Zircon-scheelite Phase fraction (%)	46-54	53-47	65-35	20-78(+2% monazite)

Thus, we should consider the influence of kinetic barriers in order to explain our experimental observations. If we assume that the scheelite polymorph is the most stable phase at 7 GPa (as our theoretical predictions found), the appearance of such phase would be necessarily precluded by a huge kinetic barrier. In Fig. 6.7, we suggest a qualitative energetic diagram for explaining all these facts in a qualitatively way. In this scheme, the relative energetic positions of the different

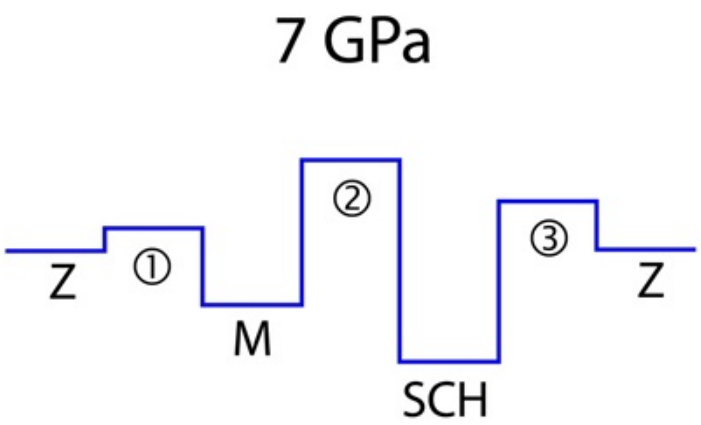

Figure 6.7: Qualitative energy scheme of the kinetic barriers between the zircon (Z), monazite (M) and scheelite (SCH) phases at 7 GPa (synthesis pressure).

structures were set in accordance with our *ab initio* calculations. The energetic barriers between each phase (Z= zircon, M= monazite and SCH = scheelite) are labeled with numbers. At room-temperature conditions, the size of the barrier 1 in the M to Z direction explains why the monazite phase is recovered in a metastable state at low pressures upon pressure release. However, thermal energy is still too low to surpass barrier 2. As it is shown in Table 6.4, at 600 ℃ this barrier can be surpassed and the scheelite phase can be achieved. That is to say, the thermal energy must be nearly tripled so that the sample can transform into the scheelite phase (54%). However, the kinetics of the phase transition are still low, since 6 hours are needed to have a clearly dominant scheelite phase relative amount (78%). When the sample is quenched to room temperature, the scheelite phase remains trapped in its energy local minimum, thanks to the kinetic barrier effect. By contrast, if the sample is heated at even higher temperatures (near 1000 ℃), there is an enhancement of the monazite-to-scheelite transformation but, however, thermal energy is high enough to trigger the back-transformation to zircon, which leads to increased amounts of zircon in the final product (Z/SCH = 65/35 %).

6.5 Raman scattering experiments on the scheelite phase

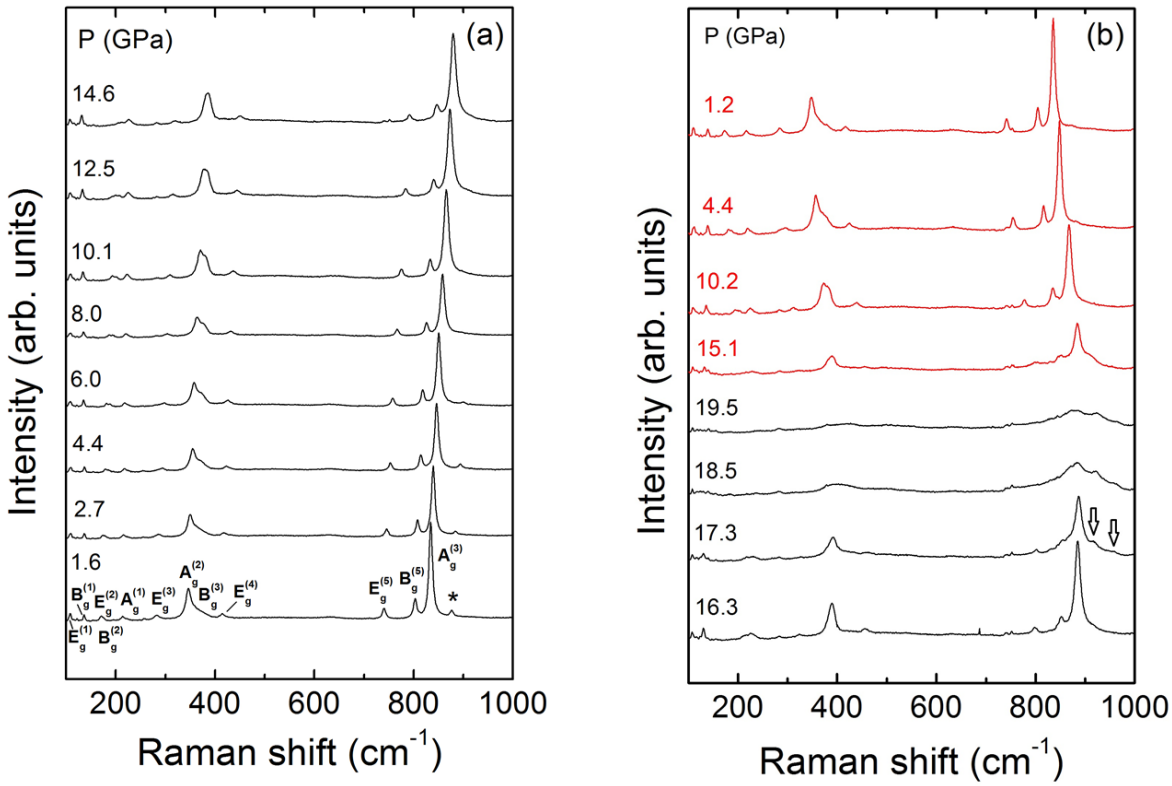

Figure 6.8: Selected Raman spectra of scheelite-type $PrVO_4$ at different pressures. The black and red spectra represent the data collected upon compression and decompression respectively. The Raman peak indicated with an asterisk correspond to the most intense peak of zircon-type $PrVO_4$. The arrows in the Raman spectra at 17.3 GPa point to the new Raman peaks of a post-scheelite phase, which could be associated to the $PbWO_4$-III phase.

For our high-pressure Raman scattering experiments, we decided to study the recovered sample with the highest scheelite proportion (78%). Selected Raman spectra of this sample upon compression are depicted in Fig. 6.8 (a). The general appearance of the Raman peaks in the spectra follows the typical distribution of scheelite structured compounds. In particular, the spectra is clearly divided in two frequency regions, with a frequency gap between them from ~ 450 and 700 cm^{-1}. All the modes predicted by calculations were observed in the experimental patterns,

with the only exception of the $B_g^{(4)}$ mode, predicted at 380 cm^{-1} at zero pressure. The symmetry of each mode was assigned in accordance with calculations. In our case, four Raman peaks can be observed in the high frequency region. The three most intense peaks can be attributed to the internal vibration modes of the VO_4 tetrahedra, while the small peak at the highest frequency (labeled with an asterisk in Fig. 6.8) correspond to the most intense Raman mode of the zircon phase. This is a direct consequence of the small zircon relative amount in the studied sample, which is $\sim$ 20% according to our XRD refinements (see Table 6.4). As pressure is increased, the Raman peak assigned to the zircon phase disappears above 6.0 GPa. This can be explained in terms of the zircon-to-monazite phase transition observed in the XRD experiments on zircon-type $PrVO_4$ at high pressures [42, 43, 65]. However, the peaks associated with the monazite phase are extremely weak here, so they are not observed during the experiment. As it is shown in Fig. 6.8 (b), substantial changes in the Raman spectra take place above 16.3 GPa approximately. At higher pressures, the Raman peaks associated to the scheelite phase considerably broaden and decrease in intensity. Moreover, new peaks arise at higher frequencies, at the left-hand side of the scheelite $A_g^{(3)}$ mode at 17.3 GPa, which are indicated by arrows. These observations are compatible with the onset of a phase transition from scheelite- to $PbWO_4$-III-type $PrVO_4$, which is predicted to take place at 15.2 GPa according to our *ab initio* calculations. At 18.5 GPa the spectrum consists of a set of broad peaks and bands, which hinder an accurate identification of the different Raman active modes. After achieving 19.5 GPa, the applied load was progressively decreased to ambient pressure. At 15.0 GPa, the Raman spectra associated with the scheelite phase reappeared, which reveals the reversible character of this transition. The scheelite phase was finally recovered near room pressure in a metastable state. No other phases were identified in these conditions.

Fig. 6.9 shows the pressure dependence of the Raman active modes of the scheelite phase. As expected, all modes have a positive quasi-linear dependence with pressure, except for the $E_g^{(1)}$ and $B_g^{(1)}$ modes, which are found at the lowest frequencies. Our calculations predict that the frequency of the $E_g^{(1)}$ mode increases from ambient pressure to a maximum at $\sim$ 4.5 GPa. Upon

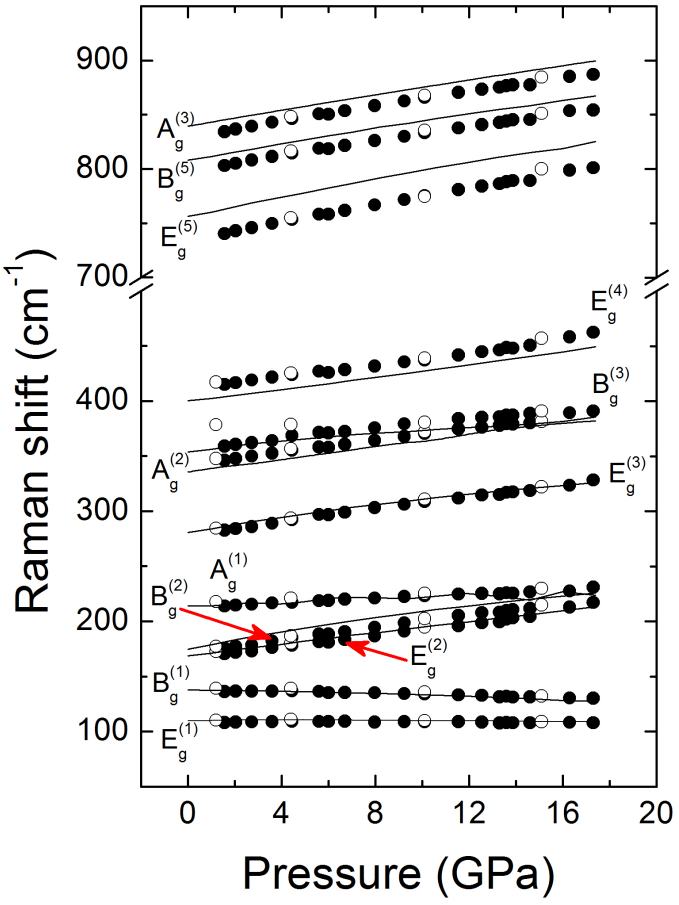

Figure 6.9: Pressure evolution of the frequencies of the Raman active modes of the scheelite phase of $PrVO_4$. The experimental data collected upon compression and decompression are represented by black and void circles respectively. Solid lines stand for the calculated data.

further compression, the behaviour is the opposite. This predicted pressure dependence is well reproduced by our experimental data. Regarding the $B_g^{(1)}$ mode, there is a small frequency decrease at low pressures which enhances upon further compression. In general, our experimental data reproduce this negative pressure dependence, with the only exception of a few points at very low pressures, which show a weak frequency increase. Nonetheless, this minor disagreement is compatible with the accuracy of the DFT calculations or the detector data resolution. Theoret-

ical and empirical values of the pressure coefficients and frequencies at zero-pressure and the corresponding Grüneisen parameters are shown in Table 6.5. In general, the obtained values are quite similar to those obtained for scheelite-type $NdVO_4$ and $GdVO_4$ (shown in Tables 4.3 and 5.3 respectively), although some pressure coefficients of scheelite-type $PrVO_4$ are slightly larger. Since all these phases show similar compressibilities and unit-cell volumes, the differences in the Grüneisen parameters with other RVO_4 compounds may be attributed to differences in the electronic density distribution.

6.6 *Ab initio* calculations

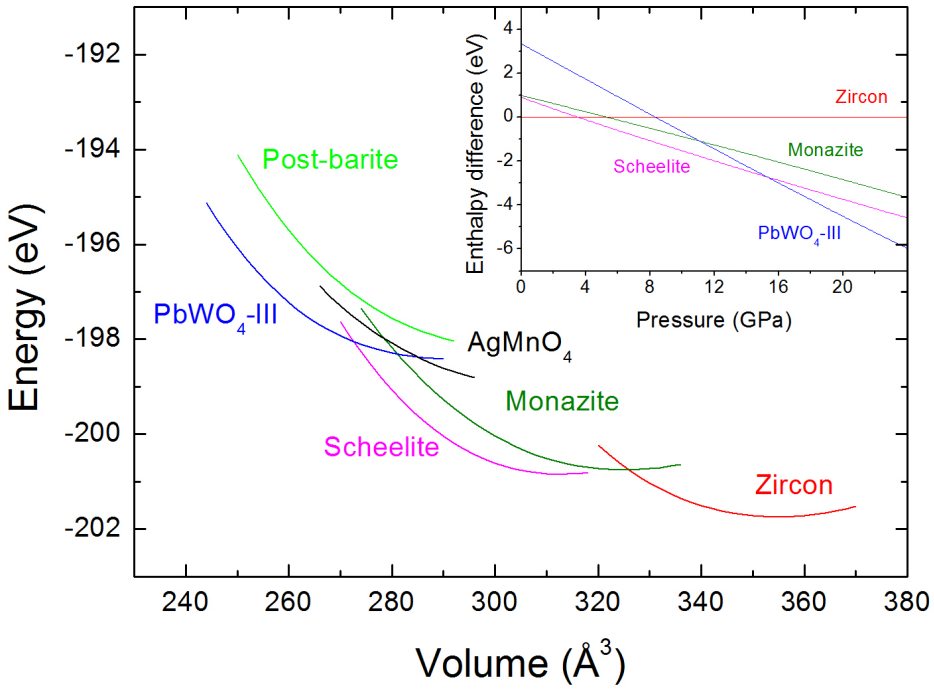

Figure 6.10: Calculated energy-volume curves for different phases of $PrVO_4$. *Inset:* theoretical pressure dependence of the enthalpy of the structures experimentally observed ($T = 0$ K). The zircon phase is taken as a reference.

Table 6.5: Calculated and experimental pressure coefficients, zero-pressure frequencies and Grüneisen parameters of the Raman active modes of scheelite-type $PrVO_4$. The value of the bulk modulus used for estimating the Grüneisen parameters was $B_0 = 139$ GPa for both sets of data.

	Theory			Experiment		
Mode	$d\omega/dP$ (cm^{-1}/GPa)	ω_0 (cm^{-1})	γ	$d\omega/dP$ (cm^{-1}/GPa)	ω_0 (cm^{-1})	γ
$E_g^{(1)}$	0.32	110	0.40	0.31(9)	108	0.4(1)
$B_g^{(1)}$	−0.23	138	−0.23	0.16(7)	136	0.16(7)
$E_g^{(2)}$	2.56	169	2.11	2.70(2)	166	2.26(2)
$B_g^{(2)}$	4.20	175	3.33	3.1(4)	171	2.5(3)
$A_g^{(1)}$	0.99	214	0.64	1.34(9)	212	0.88(6)
$E_g^{(3)}$	2.60	283	1.28	3.1(1)	278	1.55(3)
$A_g^{(2)}$	2.74	337	1.13	3.17(4)	341	1.29(2)
$B_g^{(3)}$	2.67	354	1.05	2.43(2)	355	0.95(1)
$B_g^{(4)}$	1.96	382	0.71	–	–	–
$E_g^{(4)}$	2.52	400	0.88	3.3(1)	410	1.12(3)
$E_g^{(5)}$	4.48	756.8	0.82	4.5(1)	733	0.85(2)
$B_g^{(5)}$	3.79	807	0.65	4.08(14)	797	0.71(1)
$A_g^{(3)}$	3.60	840	0.60	4.02(6)	828	0.67(1)

Theoretical energy-volume curves of different structures of $PrVO_4$ are displayed in Fig. 6.10. In this case we included the experimentally observed phases as well as the post-barite and $AgMnO_4$ [201, 204] phases for the sake of comparison. The calculated pressure evolution of enthalpy of the experimentally observed polymorphs is shown in the inset of such figure, with the zircon phase as a reference. With regard to the relative stability of the scheelite and monazite phases, calculations suggest that the former is the most stable structure after the zircon phase. Accordingly,

the predicted transition pressures at $T = 0$ K are 3.5 and 5.2 GPa for the zircon-to-scheelite and zircon-to-monazite phase transformations. Nonetheless, both curves are extremely close to one another, so that the enthalpy differences per atom are of the same order of thermal energy at 300 K. Thus, we decided to include thermal effects in order to investigate the role of temperature in the relative position of the Gibbs free energy curves for the zircon, scheelite and monazite phases. These calculations were carried out in the framework of the quasi-harmonic approximation.

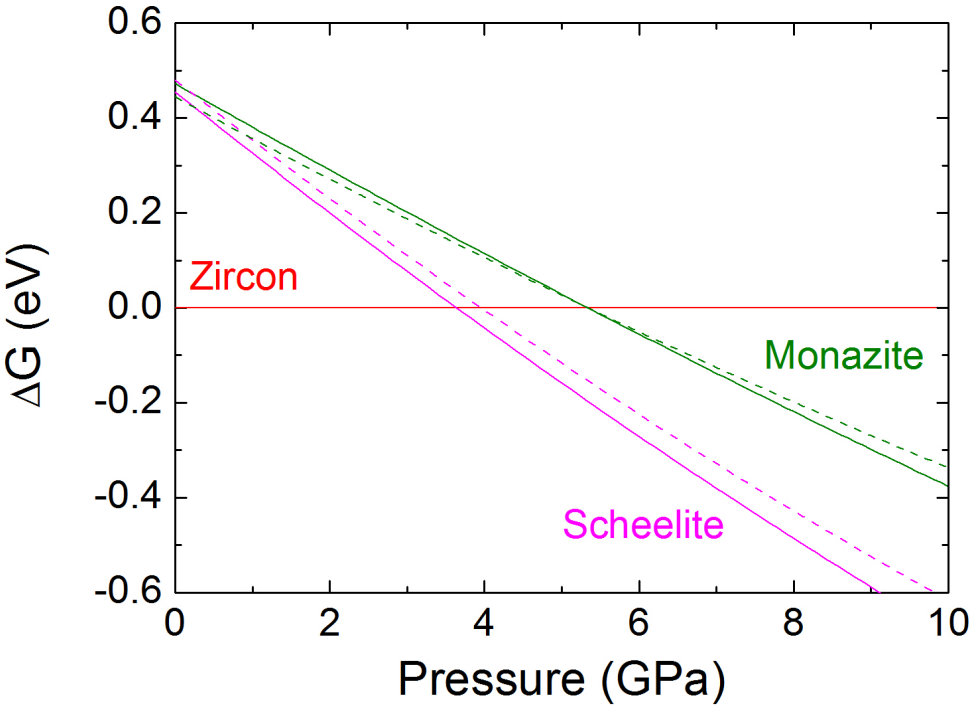

Figure 6.11: Theoretical Gibbs free energy difference of zircon-, scheelite- and monazite-type $PrVO_4$ upon compression at 300 (solid lines) and 700 K (dashed lines). The zircon phase has been taken as reference.

The Gibbs free energies of these three polymorphs calculated at 300 and 700 K for different pressures are shown in Fig. 6.11 (the zircon phase is taken as a reference). In both cases, the theoretical transition pressures are quite similar to those calculated assuming zero-temperature conditions, that is to say, neglecting the entropic effects (inset of Fig. 6.10). In fact, the zircon-to-scheelite and zircon-to-monazite predicted transition pressures at 300 K are 3.7 and 5.3 GPa

respectively (3.5 and 5.2 GPa at $T = 0$). At high-temperatures (700 K) these values are 4.0 and 5.4 GPa, which are also quite similar. In essence, entropic effects are not critical for calculating the transition pressures for these structures. Similarly to the $T = 0$ case, the difference between the Gibbs free energy curves of the scheelite and monazite phases is of the same order of thermal energy at 300 K. Thus, calculations predict a similar stability between both phases. Thus, in cases such as $CeVO_4$ [48] and $NdVO_4$ [44, 114], hydrostatic effects are crucial in order to obtain one phase or another at high pressures. Furthermore, if both high-pressure structures show similar stability, the existence of kinetic barriers can definitely alter the observed transition sequence. In fact, some studies [187] have quantified the kinetic barrier between the zircon and scheelite phases of $ZrSiO_4$ to be 80 kJ/mol ($\sim$ 0.83 eV/molecule), which is a highly enough value to considerably modify the expected transition pressure. Another feature that is worth mentioning, is that DFT calculations tend to underestimate the zircon-to-scheelite phase transition by $\sim$ 1-2 GPa in zircon-structured compounds [49, 151, 205]. It must be remarked that DFT calculations predict a very similar stability of the scheelite and monazite phases at high pressures, so that they are unable to undoubtedly distinguish which one is actually the stable polymorph at such conditions. Moreover, this issue only comes at worse when we take into account the existence of kinetic barriers, hydrostaticity and the difficulty of dealing with rare-earth $4f$ orbitals in calculations.

The obtained results for our Gibbs free energy calculations can be useful in order to infer the sign of the slope for the zircon-scheelite and zircon-monazite phase boundaries in the $P - T$ diagram. In fact this can be inferred from the changes in ΔG depicted in Fig. 6.11. According to the definition of the Gibbs free energy, the difference between the calculated ΔG curves at T_1 and T_2 can be expressed as

$$\Delta_{zx} = \Delta G_{T2} - \Delta G_{T1} = -(S_x - S_z)(T_2 - T_1) \tag{6.1}$$

where $x = S$ or M for the scheelite and monazite phases directly. According to the results shown in Fig. 6.11, Δ_{ZS} and $T_2 - T_1 > 0$, since $T_2 = 700$ K and $T_1 = 300$ K. Therefore, $S_S < S_Z$. By contrast,

the monazite ΔG curves are very similar at 300 and 700 GPa. Hence we can state that $\Delta_{ZM} \sim 0$ and $S_Z \sim S_M$. Thus, $S_Z \sim S_M > S_S$ according to our reasoning. In this sense, $PrVO_4$ does not follow the general tendency in which larger entropy values are associated with higher symmetry phases [206], which would require that $S_Z > S_S > S_M$. As we showed in Chapter 2, the Clausius-Clapeyron equation (Eqn. 2.13) establishes the relationship between the phase boundary line slope in the $P - T$ diagram with the changes in entropy and volume at this boundary. We can rewrite this relationship from as

$$\frac{dP}{dT} = \frac{\Delta S}{\Delta V} = \frac{S_x - S_Z}{V_x - V_Z} \tag{6.2}$$

Since $V_Z > V_M > V_S$ and $S_Z \sim S_M > S_S$, then $(dP/dT)_{ZS} > 0$ and $(dP/dT)_{ZM} \sim 0$. In other words, the slope of the zircon-scheelite phase boundary is positive whereas the boundary between the zircon and monazite phases should follow a weak temperature dependence.

The reported high-pressure and room-temperature XRD experiments confirm the existence of a monazite-to-$PbWO_4$-III phase transition at 12.7(5) GPa, which is still visible at 11.9 GPa upon pressure release. The calculated transition pressure according to the enthalpy-pressure curves of Fig. 6.10 is 11.1 GPa, which is compatible with the experimental value. Moreover, these calculations also predict the transformation of the scheelite phase into the $PbWO_4$-III near 15.5 GPa. This is compatible with the observation of a phase transition between 16.3 and 17.3 GPa in our Raman scattering experiments on scheelite-type $PrVO_4$ under high pressures. However, many scheelite structured RVO_4 compounds show a scheelite-to-fergusonite phase transition upon compression. In this case, we think that $PrVO_4$ is an exception to this. In fact, as we proved for scheelite-type $NdVO_4$ and $GdVO_4$, this transition is associated with a mechanical instability related to the stiffness tensor. Similarly to those cases, we calculated the stiffness tensor of scheelite-type $PrVO_4$ at different hydrostatic pressures. The pressure evolution of the elastic constants is depicted in Fig. 6.12. The obtained results predict that the mechanical instability that should lead to the

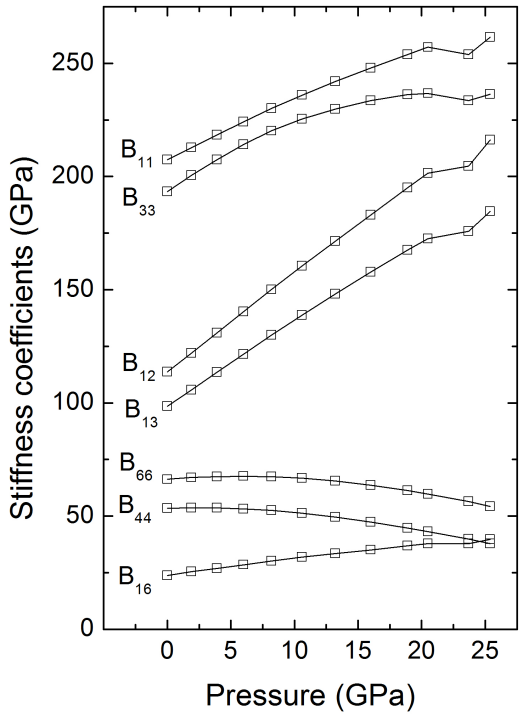

Figure 6.12: Theoretical pressure behaviour of the stiffness tensor elements of scheelite-type $PrVO_4$

fergusonite phase, defined by the eigenvector $\eta \approx (0.5 \quad -0.5 \quad 0 \quad 0 \quad 0 \quad 0.7)$, takes place at 23.3 GPa, far beyond the transition pressure observed during the experiment. Thus it is reasonably to assume that the observation of the fergusonite phase is precluded by the transformation of the scheelite into the $PbWO_4$-III structure at lower pressures.

6.6.1 Polyhedral contribution to compressibility

In order to evaluate the different contribution of the polyhedral units to the compressibility of the zircon and monazite phases, we also calculated the pressure evolution of their volumes, which is shown for both structures in Fig. 6.13 for normalized volumes. Both structures can be described as an arrangement of VO_4 tetrahedra and PrO_x polyhedral units (where $x = 8$ and 9 for

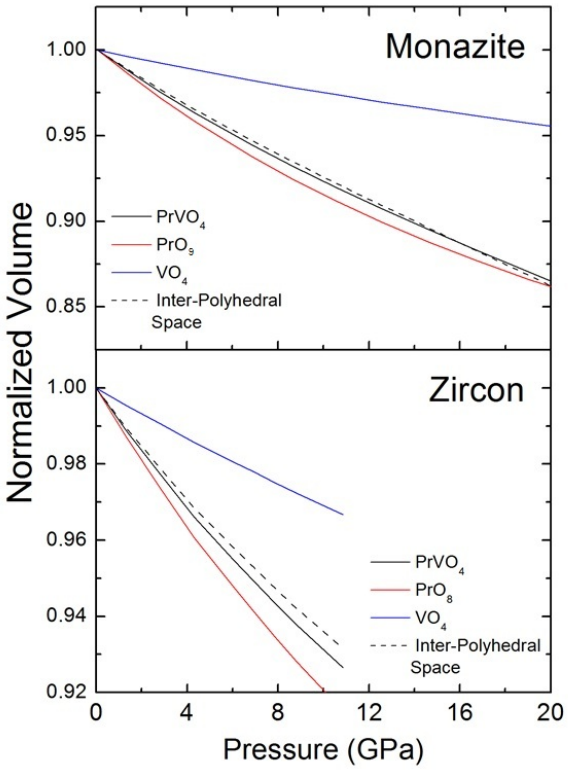

Figure 6.13: Theoretical pressure evolution of the constitutive polyhedral units of the zircon and monazite phases of $PrVO_4$.

zircon- and monazite-type $PrVO_4$ respectively). As can be deducted from this figure, the PO_x units and the void space between polyhedral units (referred as inter-polyhedral space in the figure) constitute the main contribution to the whole unit-cell volume decrease upon compression. This theoretical data were fitted to a third order BM EOS, in order to compare the bulk modulus of each polyhedron. The obtained results are summarized in Table 6.6. In this case we observe that the VO_4 are much less compressible than the PrO_x units. In fact $B_0 \sim 300$ GPa for the former whereas $B_0 < 100$ GPa for the PrO*x* units. In fact, PrO_x polyhedra show a similar compressibility to the $PrVO_4$ phase. These values are in good agreement with previously reported calculations on zircon-type $PrVO_4$ [156]. According to Recio *et al.* [207], the value of the bulk modulus in some oxides can be expressed as a combination of the different contributions to compressibility

Table 6.6: Calculated EOS parameters of the unit-cell of zircon- and monazite-type $PrVO_4$ and their respective polyhedral constituents.

Phase		V_0(Å^3)	B_0 (GPa)	B'_0
Zircon	$PrVO_4$	354.0	114.2	5.8
	PrO_8	27.2	98.2	5.0
	VO_4	2.6	290.0	5.0
	Inter-Polyhedral Space	245.2	123.8	5.9
Monazite	$PrVO_4$	324.0	111.2	3.1
	PrO_9	32.3	85.2	6.0
	VO_4	2.6	341.5	11.5
	Inter-Polyhedral Space	184.7	123.7	1.6

of the constitutive polyhedra. This is coherent with the anisotropic compressibility observed in the studied structures, since this is a direct consequence of the particular arrangement o such polyhedral units within the crystal.

In order to estimate the relative contribution of each element to the total compressibility, we have to consider the total volume of the unit cell as the sum of the different polyhedral elements within, as well as the inter-polyhedral space between them. In particular $V = 4V_{VO4} + 4V_{PrOx} + V_{IP}$ in the case of zircon and monazite phases. If we take the basic definition of compressibility $\kappa = (-1/V)(\partial V/\partial P)_T$ it is possible to demonstrate that the compressibility of the whole unit cell can be estimated as

$$\kappa = \frac{1}{V}(4V_{VO4} \cdot \kappa_{VO4} + 4V_{PrOx} \cdot \kappa_{PrOx} + V_{IP} \cdot \kappa_{IP}) \tag{6.3}$$

Since the compressibility is the inverse value of the bulk modulus ($B = 1/\kappa$), it is possible to tentatively estimate the relative contribution of each polyhedron using the reported EOS bulk moduli in Table 6.6. Hence, the PrO_8 polyhedra and the inter-polyhedral space are, respectively,

responsible of the 36 and 63% of the total compressibility of the zircon phase at ambient pressure. On the other hand, the relative contribution of the PrO_9 units and the inter-polyhedral space are 49 and 50% in the monazite phase. A particular feature of both structures is that the relative contribution of the VO_4 tetrahedra to the oxide compressibility is only $\sim$ 1%. This behaviour is analogue to that observed for other isomorphic compounds, such as the rare-erth orthophosphates like $CePO_4$ and $PrVO_4$ [140].

6.7 Conclusions

In this chapter we reported an extensive study of $PrVO_4$ under high pressure, in which we provided experimental and theoretical results. In our XRD experiments at high pressures and ambient temperature, a zircon-to-monazite phase transition was confirmed at 5.5(4) GPa. Beyond 12.2 GPa we found a second transition to a post-monazite phase, which we identified with a $PbWO_4$-III-type structure. This candidate phase showed a striking good compatibility with the experimental results, in contrast to previous phases proposed in literature [42]. Experimental and calculated linear compressibilities and EOS were also reported, showing good agreement. This was possible thanks to the optimal hydrostatic conditions provided by Ne gas, which was used as PTM. Theoretical predictions found the cited phase transitions at 5.3 and 11.1 GPa, which are in agreement with the experimental observations. However, calculations also predicted that the scheelite phase is energetically competitive at high pressures. For this reason we decided to perform several syntheses at high pressures and high temperatures in a Paris-Edinburgh large press cell. As a result we obtained a mixture of both zircon and scheelite phases at ambient conditions. The relative amount of scheelite in the recovered sample was considerably increased with the synthesis duration. The refined parameters of the scheelite phase at ambient conditions were reported. These results revealed the relevance of kinetic barriers in the transition mechanisms of $PrVO_4$ under high pressure. The scheelite-type $PrVO_4$ samples were analyzed afterwards by

means of Raman scattering experiments under high pressure. The pressure dependence of the Raman modes shows good compatibility with calculations. At 16.7 GPa we found a reversible phase transition to a post-scheelite structure, which we identified as the $PbWO_4$-III-type phase in accordance with calculations. No hints of a scheelite-to-fergusonite phase transition were observed, in contrast to many other scheelite structured $R VO_4$ compounds.

7 | Transition mechanisms in RVO_4 compounds

The zircon-to-scheelite phase transition has been widely studied in literature, specially in the case of natural zircon ($ZrSiO_4$), where the high-pressure phase, usually referred as reidite, is isomorphic to the scheelite structure. In 1986, Kusaba *et al* [153] proposed a zircon-scheelite transformation mechanism in $ZrSiO_4$ under shock compression based in two consecutive processes. In the first process there is a shearing of the zircon structure, which increases the density of the crystal by $\sim$ 10%. More specifically, a deformation of the zircon unit-cell along the base diagonal occurs, so that the [110] direction in this phase transforms into the [001] direction in the scheelite structure. Once the crystal is transformed into a quasi-scheelite structure, a small readjustment of the SiO_4 tetrahedra takes place, which leads to the scheelite structure final configuration. Nonetheless, this explanation has been proved to be insufficient for explaining the large kinetic barriers associated with the transition. In a later publication, Flórez *et al.* [187] explored this two steps mechanism proposed by Kusaba *et al.* [153] by means of DFT calculations. In their work, they studied the size of the activation barrier through different transition pathways. A more favourable monoclinic $C2/c$ transition path was found, whose associated activation energy was 80 kJ/mol. According to their explanations, two Zr−O bonds are broken and two new Zr−O bonds appear, so that the cation coordination is preserved. In fact, this would be a consequence of the tilting of the SiO_4 tetrahedra, since these structures change from sharing the

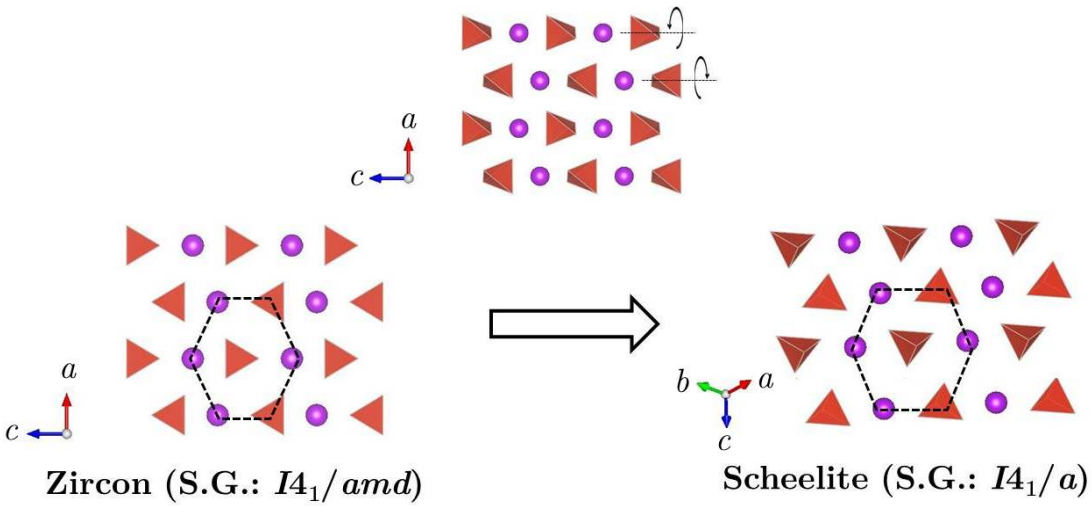

Figure 7.1: Selected hexagonal layers of the zircon (left) and scheelite (right) phases. The vibration pattern of the B_{1u} silent soft mode is represented in the upper part of the figure, between both phases. This mode correspond to a rotation of the VO_4 tetrahedra around the c-axis direction.

O–O edge with the ZrO_8 bidisphenoid in the zircon phase to a O corner in the scheelite structure. This process is in fact the main responsible for hindering the phase transformation at room temperature. The SiO_4 remain unaltered during this process i.e. there is no Si–O bond breaking or formation. Thus, according to these results, the second step of the process proposed by Kusaba *et al.* [153] would not be a simple readjustment, since the transition necessary involves oxygen displacements and the breaking and formation of Zr–O bonds. However, in recent years, new transition mechanisms that we should explore have been proposed.

The structure of both zircon and scheelite phases can be described as a set of alternating hexagonal layers, such as the ones depicted in Fig. 7.1, where two isolated layers of each phase are compared. Both layers show very similar atomic configurations with one remarkable difference though: the relative position of the VO_4 tetrahedra. The fact that the change in the relative position of the VO_4 tetrahedra requires, at least in some degree, the rotation of this units during the transition suggests that maybe there is a possible influence of the B_{1u} silent soft mode in the transition mechanism, since this mode consists of pure rotations of the VO_4 tetrahedra. In fact, some studies on zircon-type RVO_4 compounds have pointed to the proximity of the observed

zircon-to-scheelite transition pressure and the predicted pressure at which the B_{1u} silent mode softens [35, 37, 46, 49]. In fact, we showed in previous chapters that our DFT calculations predict the softening of this mode at pressures near the transition point, as it is depicted in Figs. 4.12 and 5.15 (a) for zircon-type $NdVO_4$ and $GdVO_4$ respectively [46, 49]. Fig. 7.2 shows the calculated softening of the B_{1u} silent mode for other RVO_4 compounds. As it is shown in the figure, this mode shrinks to zero at pressures between 7 and 9 GPa, close to the observed transition pressures. The silent nature of the soft mode precludes the use of conventional techniques like Raman or IR spectroscopy to characterize the evolution of this mode upon compression and its influence in the transition mechanism. Nonetheless, the frequency decrease driven by pressure observed in some Raman active modes like B_{2g} [46, 49, 65] is directly related to the progressive softening of the B_{1u} silent mode, since the former involves the rotation of the tetrahedra around the c-axis direction. Finally, the relationship between the softening of the B_{1u} silent mode and the zircon-to-scheelite phase transition was theoretically elucidated by Stangarone *et al.* [208] for $ZrSiO_4$. The phase transition mechanism proposed for this authors was experimentally confirmed by Mihailova *et al.* by means of Raman scattering experiments under high pressure. According to these studies, in between the zircon ans scheelite phases, there is a tetragonal structure similar to the zircon phase, but with the VO_4 tetrahedra rotated in accordance with the vibration pattern of the B_{1u} mode. This phase has a lower symmetry than the zircon phase and it is referred as HPLS (*High-Pressure Low-Symmetry*) by the authors. In their experiments, this phase is observed as single in a very narrow range of pressures and in coexistence with the scheelite phase upon further compression. The calculations reported by these authors predict that the scheelite phase is more stable than the zircon phase above 9.1 GPa, since beyond this pressure, the former has a lower Gibbs free energy, although considerably larger pressures are needed to experimentally observe the scheelite structure. However, the soft B_{1u} silent mode should become negative beyond 20 GPa. This dynamical instability leads to the so-called HPLS metastable phase, which we previously described. According to the authors, the activation barrier is considerably lowered by

the apparition of this intermediate phase, which triggers the emergence of the scheelite structure at the very next pressures. As it is shown below, our systematic analysis of the data reported in literature shows that this kind of mechanism also applies to the small cation RVO_4 compounds (R = Nd-Lu).

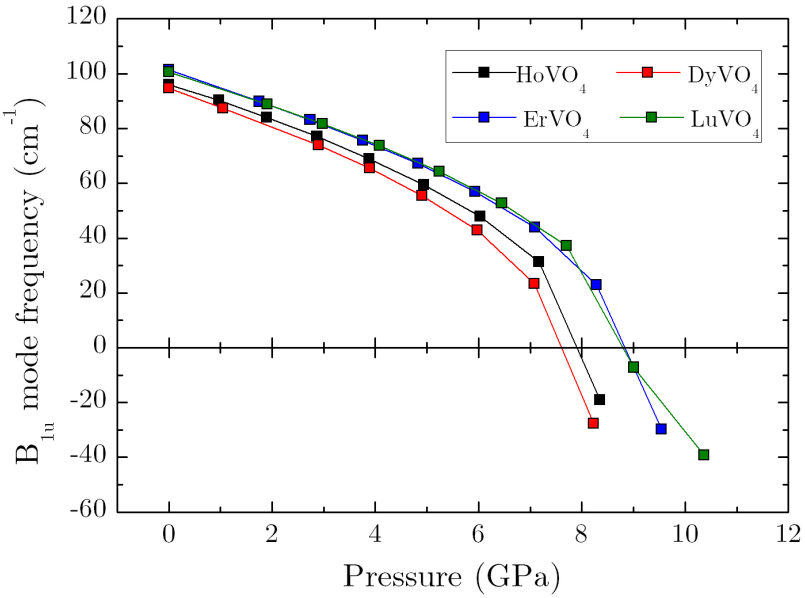

Figure 7.2: Predicted softening of the B_{1u} silent mode for different zircon-type rare-earth orthovanadates under high pressure.

On the other hand, the zircon-to-monazite phase transition observed in large cation RVO_4 compounds (R = Ce, Pr, Nd) cannot be explained in terms of this dynamical instability. Thus, we decided to calculate the pressure evolution of the stiffness tensor associated with the zircon phase for each case in order to look for possible mechanical instabilities. As a matter of example, Fig. 7.3 shows the change in the non-zero elements of the stiffness tensor for zircon-type $PrVO_4$. The inset of the figure shows how the smallest eigenvalue of the tensor becomes zero at 5.1 GPa. Thus, the structure is mechanically unstable beyond that pressure, since the stiffness tensor is no longer positive definite. As a consequence of this, there is a violation of one of the Born criteria associated with tetragonal I structures, which are shown in Table 2.3 in Chapter 2. In particular,

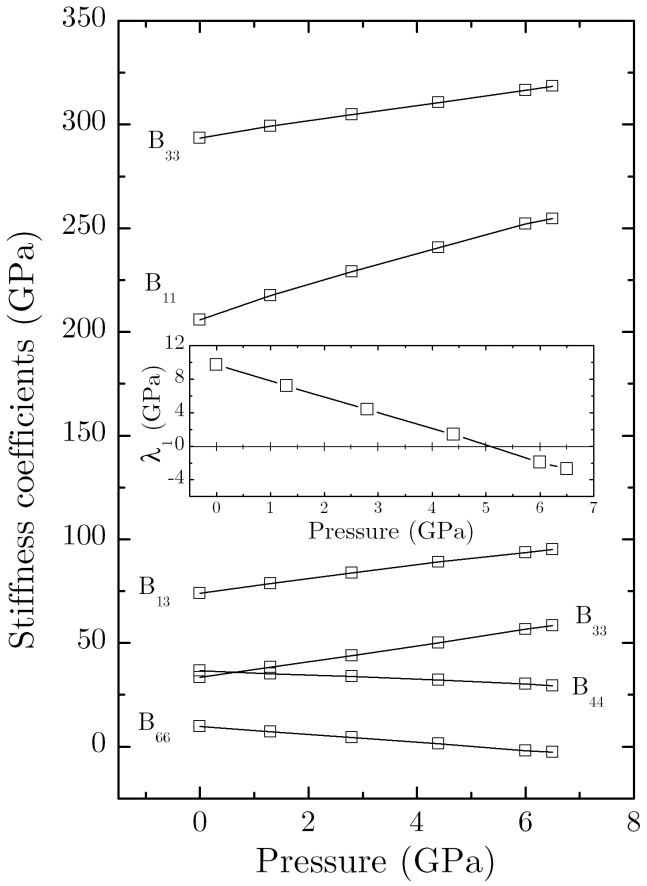

Figure 7.3: Pressure dependence of the non-zero stiffness tensor elements in zircon-type $PrVO_4$.

the B_{66} element of the matrix is not positive beyond 5.1 GPa. The spontaneous distortion associated with this instability is described by a strain vector proportional to the eigenvector whose eigenvalue shrinks to zero. In this case, this vector is $(0 \quad 0 \quad 0 \quad 0 \quad 0 \quad 1)$, which describes a pure shear strain within the *ab* plane of the zircon unit-cell. In other words, this vector corresponds to a monoclinic deformation along the *ab* base diagonal. We think that this mechanism can help to diminish the activation barrier between the zircon and monazite phases. This is coherent with the zircon and monazite structural relationships, since the transition from one to another requires

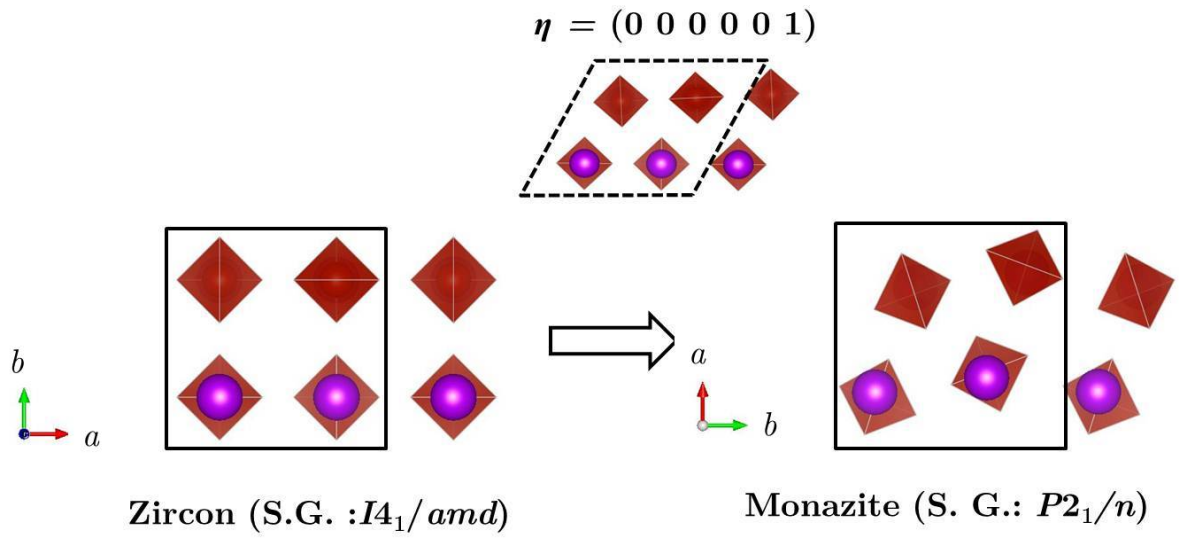

Figure 7.4: Structural relationship between the zircon (left) and monazite (right) structures. The associated monoclinic distortion of the zircon phase is depicted in the upper part of the figure.

some shift of the planes perpendicular to the b-axis, as it is shown in Fig. 7.4. Thus, it is reasonable to assume that this kind of mechanical instability could trigger the zircon-to-monazite phase transition.

Once we have discussed the mechanisms involved in the dynamical and mechanical instabilities, we are able to understand their influence on the whole family of RVO_4 compounds. We summarize in Fig. 7.5 the experimental pressure ranges of observation for the zircon and monazite/scheelite phases of the whole RVO_4 family, either pure or in coexistence. The lanthanum symbol is denoted with an asterisk since here we are dealing with metastable zircon-type $LaVO_4$. Experimentally, $LaVO_4$, $CeVO_4$, $PrVO_4$ and, depending on hydrostatic conditions, $NdVO_4$ transform into the monazite phase at high pressures, while, by contrast, the compounds with smaller rare-earth cations transform into the scheelite phase. The phase coexistence is extended to larger pressure ranges at the sides of the diagram, for metastable zircon-type $LaVO_4$, $CeVO_4$ on one side and for the lanthanides laying in between Dy and Lu (both inclusive) on the other side.

The obtained results of our theoretical calculations are also shown in Fig. 7.5. Magenta and green circles stand for the predicted transition pressures for the zircon-to-monazite and zircon-

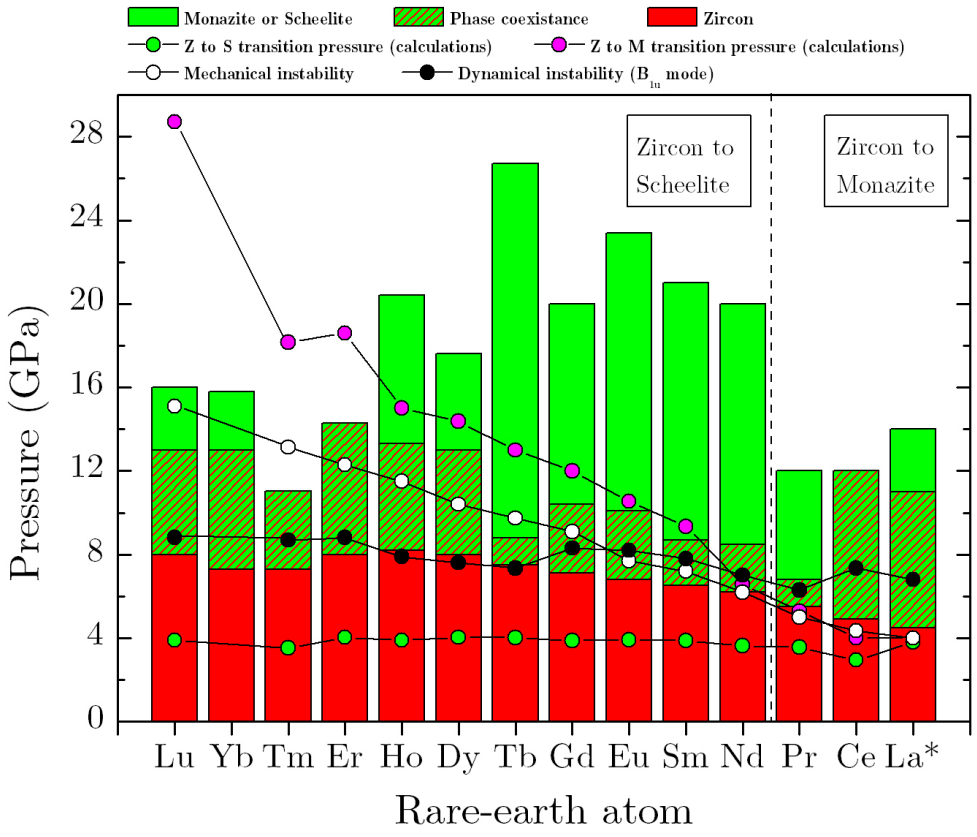

Figure 7.5: Experimental transition pressures of the RVO_4 family (R = Lu - La) represented as vertical bars [35, 37, 40–44, 48, 49, 54, 61, 62, 117, 209, 210]. The obtained results in our *ab initio* calculations are represented with symbols. The legend over the figure indicates the meaning of the bar colours and the symbols. The Lanthanum symbol "La" has been labeled with an asterisk to remark that here we are dealing with metastable zircon-type $LaVO_4$.

to-scheelite transformations respectively, according to their relative enthalpies. According to experimental observations, the stable phase of $LaVO_4$ at room conditions is the monazite structure. Thus, the fact that our *ab initio* calculations found the zircon phase as thermodynamically stable at low pressures indicates that the predicted zircon-to-monazite transition pressures are probably slightly overestimated. Nonetheless, the predicted tendency of the zircon-to-monazite transition pressure to decrease with the size of the rare-earth atom is completely coherent with experimental observations. On the contrary, the zircon-to-scheelite transition pressure is predicted to have a very weak dependence on the type of rare-earth cation. This different behaviour

of the transition pressures with the rare-earth atomic number explains why both monazite and scheelite phases can only be achieved in RVO_4 compounds where R = Ce, Pr, Nd, in which the calculated enthalpies are similar one to each other, whereas only the scheelite structure can be obtained for the compounds with smaller cations. The predicted pressure at which the dynamical instability associated to the softening of the B_{1u} mode takes place is depicted in Fig. 7.5 as black circles. In general, this pressure barely changes with the atomic number. Similarly, the pressure at which the zircon structure is mechanically unstable is indicated with void circles. This pressure clearly decreases from $\sim$ 15 GPa in $LuVO_4$ to $\sim$ 4.5 in mestastable zircon-type $LaVO_4$.

At first sight, the most striking feature in Fig. 7.5 is the fact that the zircon-to-scheelite phase transition is observed at higher pressures that those predicted by DFT enthalpy calculations. On the contrary, the experimental zircon-to-scheelite transition pressures show a considerable good compatibility with the pressure at which the dynamical instability should occur, with differences of $\sim$ 1 GPa. Thus, it seems that the transition pressure in these compounds is governed by the softening of the B_{1u} silent mode, similarly to the mechanism described for natural zircon by Stangarone *et al.* [208] and Mihailova *et al.* [151]. To be more precise, the kinetic barrier between the zircon and scheelite phases is lowered by this particular mechanism.

On the other hand, there is a coincidence between the predicted and experimental zircon-to-monazite phase transition with the pressure at which the zircon phase becomes mechanically unstable for R = Nd-La. The existence of kinetic barriers between the zircon and monazite phases has been experimentally demonstrated, since the latter is recovered in a metastable state at ambient conditions after releasing the pressure load [41–43, 144]. We believe that the phase transition from the zircon to the monazite phase for R = La-Nd is triggered by the mechanical instability associated to the monoclinic distortion shown in Fig. 7.4. The pressure evolution of metastable zircon-type $LaVO_4$ nanostructures [62] constitutes a perfect example for this actually. In fact, according to the experiments reported by Yuan *et al.* [62], the zircon phase remains stable up to $\sim$ 4.5 GPa. At higher pressures the monazite phase appears in coexistence with the zircon phase,

which progressively vanishes. The observed transition pressure matches with the pressure at which the zircon phase is mechanically unstable which suggests that this mechanism reduces the activation barrier between both phases. With regard to $CeVO_4$, the zircon-to-monazite phase transition is empirically observed at $\sim$ 4.9 GPa [39], probably triggered by the mechanical instability predicted at 4.4 GPa. In this case, the scheelite phase cannot be observed at room temperatures, since the dynamical instability that should lead to it is predicted at higher pressures. In the case of $PrVO_4$, both monazite and scheelite phases are thermodynamically competitive at high pressures according to enthalpy calculations. In fact, whereas the former is found at high pressures and room temperature, the latter can only be synthesized at high pressures and high temperatures [43], as we previously showed. The explanation for this would be analogue to that used for $CeVO_4$. Even though both phases are relatively equally stable, only the monazite phase is observed at room conditions, since the mechanical instability precedes the softening of the B_{1u} mode.

The boundary that divides the family in these two groups is constituted by $NdVO_4$, since the monazite phase cannot be obtained at high pressures for smaller rare-earth atoms than Nd. Upon compression, zircon-type $NdVO_4$ transforms into the scheelite phase when hydrostatic conditions are optimal [44]. Otherwise, the monazite phase appears instead [41]. As it is shown in Fig. 7.5, the dynamical and mechanical instabilities should occur at more or less the same pressure, also in coincidence with the zircon-to-monazite calculated transition pressure. This is coherent with the observation of the monazite phase under poor hydrostatic conditions, since these tend to lower the pressure at which the mechanical instability happens. With regard to the RVO_4 compounds with R = Sm, Eu and Gd, both instabilities are also close in pressure, but the monazite phase cannot be observed experimentally because the enthalpy of the scheelite phase is clearly lower.

It must be remarked that, apparently, the range of coexistence of the zircon and scheelite phases increases as the difference between the pressures at which the dynamical and mechanical instabilities are predicted to happen. In other words, the pressure at which the monoclinic

distortion should take place is extremely close to the upper limit of the zircon-scheelite coexistence. According to our previous explanation, the apparition of the monazite phases is triggered by the mechanical instability for large rare-earth cation. However, for small rare-earth atoms the enthalpy of the monazite phase is considerably larger than that of the scheelite structure. Therefore, it seems that the monoclinic distortion induced by the mechanical instability favors the completion of the zircon-to-scheelite phase transformation.

In this chapter, we have gathered the experimental data reported in literature and our calculations, which allowed us to describe how the pressure induced phase transitions of $R\mathrm{VO}_4$ compounds are not only affected by differences in the enthalpy of the studied polymorphs, but also by a complex interrelation between dynamical and mechanical instabilities. These mechanisms help to lower the activation barrier between the zircon and the monazite/scheelite phases and thus, they determine the experimental transition pressures. We believe that this approach to the systematics of $R\mathrm{VO}_4$ compounds under high pressures can be also applied to other families of compounds.

8 | The Jahn-Teller effect in Terbium Orthovanadate

Some zircon-type rare-earth oxides have shown to undergo a second order phase transition at low temperatures, driven by a cooperative Jahn-Teller distortion. This led to exhaustive studies on their vibrational, optical and magnetic properties as well as on their structural evolution at low temperatures [26, 27, 211–215]. With regard to $R\mathrm{VO_4}$ compounds, the cooperative Jahn-Teller effect has been observed to take place in $\mathrm{TbVO_4}$ and $\mathrm{DyVO_4}$ below 33 K and 14 K [27], respectively. $\mathrm{TmVO_4}$ orthovanadate has also shown this kind of behaviour, but at much lower temperatures (below 2.15 K) [25, 216, 217].

In the zircon structure unit-cell we can find two rare-earth cations on D_{2d} sites related by an inversion center. At room conditions, the crystal field leads to pseudo-degenerated electronic levels, which split into more separated states when the zircon structure gets distorted. The direction of the distortion and the associated splitting of the electronic levels are both schematically shown in Fig. 2.8 (Chapter 2). In particular, the cooperative Jahn-Teller effect observed in these compounds is caused by the coupling of the nearly degenerated electronic states and a singly degenerated lattice mode [28].

According to several studies on $\mathrm{TbVO_4}$ [27, 28, 216], this compound undergoes a second order phase transition at low temperatures from a zircon to a zircon-like orthorhombic phase whose space group is $Fddd$. The orthorhombic distortion is associated with the Raman-active B_{2g} mode

in $TbVO_4$, which is the most strongly coupled vibration to the low-lying electronic levels of the rare-earth cation ($E \otimes B_{2g}$). During this transition the point symmetry of the terbium cation changes from D_{2d} ($\bar{4}m2$-dodecahedral) to D_2 (222-distorted dodecahedral). The temperature evolution of the unit-cell parameters were reported by Will *et al.* [218] and Kazei *et al.* [219] by means of XRD measurements at low temperatures on single-crystals and powder, but the structure was not fully refined. The crystal structure of the low-temperature phase was finally solved by Kirschbaum *et al.* [215] via single-crystal XRD measurements. These authors showed that a twinning of the crystal takes place in this transition and verified the reduction in the site symmetry of the Tb cation.

In this chapter we characterize the temperature evolution of the $TbVO_4$ bandgap energy from 13.5 K to ambient conditions by means of optical absorption measurements. This allowed us to determine the effects of the Jahn-Teller distortion on the bandgap of $TbVO_4$. Moreover, we explored the phase boundaries between the zircon and the distorted phase of $TbVO_4$ in the low temperature range using powder XRD measurements at high pressures. Our experiments determine that pressure considerably raises the transition temperature, since it eases the orthorhombic distortion of the structure.

8.1 Experimental details

$TbVO_4$ single crystals were obtained by the flux growth method. A 1:1.923 mol. mixture of V_2O_5 and PbO (99% and 99.9%) plus borax ($Na_2B_4O_7{\cdot}10H_2O$, > 99%) was used as the flux. Borax was added as a flux modifier, in order to increase the size of the crystals. Tb_2O_3 (99.99%) was added as the crystal precursor. All the reagents were in form of fine powders. Platinum crucibles were filled with the flux and the precursor, sealed with a platinum lid, and put in a programmable oven. To dehydrate the mixture, the temperature was ramped up at 0.6 ℃/hour and kept at 250 ℃ for 2 hours. Afterwards, the temperature was kept fixed for 15 hours at 1300 ℃, after a gradual

increment at a rate of 105 ℃/hour. During this step, the flux melts and acts as a solvent for Tb_2O_3. The temperature was then slowly decreased until 950 ℃ (−1.8 ℃/hour), in order to promote the formation of the crystals by precipitation and spontaneous nucleation. The crucible was then removed from the oven, rapidly reversed (to facilitate the recovery of the crystals) and allowed to cool down to room temperature. Subsequently, the platinum lid was removed and the crucible was immersed in hot nitric acid (1.5 M), which was continuously stirred and renewed multiple times until the complete dissolution of the flux. Finally, the clean crystals were washed with deionized water and recovered using a paper filter.

Polycrystalline samples of zircon-type $TbVO_4$ were synthesized by the solid-state reaction method by mixing appropriate quantities of pre-dried Tb_2O_3 (Indian Rare Earth Ltd. 99%) and V_2O_5 (Alfa-Aesar 99%). An homogeneous mixture of the precursors was compacted into pellets, which were heated at 800 ℃ for 24 h and cooled to ambient temperature afterwards. The recovered pellets were reground and heated at 1100 ℃ during 24 h. The obtained samples were characterized by means of XRD in a Panalytical X-pert Pro diffractometer using Cu−$K\alpha$ radiation. The zircon-type structure was confirmed by the measured XRD patterns, with unit-cell lattice parameters $a = 7.166(7)$Å and $c = 6.317(6)$Å. These values are compatible with those reported in literature [215].

A $TbVO_4$ single-crystal of $\sim 10\ \mu$m thickness with plane parallel faces was placed in the sample holder of a cryostat, which allows to cool down the sample by using a cold finger through which liquid Helium circulates. A vessel equipped with transparent windows was placed around the sample holder in order to provide the vacuum conditions necessary to preclude water condensation and the formation of ice crystals. The temperature of the sample was determined by a thermocouple attached to the sample holder. The sample was cooled down at the lowest temperature (13.5 K) and subsequently warmed up using a resistive heater. Temperature was stabilized by a digital temperature controller, so that the spectra measurements were taken upon sample warming. The optical absorption measurements were carried out using a system with a deu-

terium lamp as a light source. Since the size of the vessel precludes the use of objective lenses, the light beam was focused on the sample through a system of concave mirrors with no chromatic dispersion. A schematic representation of this experimental setup is depicted in Fig. 3.16 (Chapter 3).

The high pressure angle-dispersive XRD meausrements were performed at the MSPD-BL04 beamline at the ALBA-CELLS synchrotron [166], using a DAC with a diamond culet size of 300 μm. A polycrystalline $TbVO_4$ powder sample wass introduced, together with some ruby chips, inside a 150 μm hole drilled in a stainless-steel gasket preindented to a thickness of 40 μm. Pressure of the sample was determined by the ruby luminescence method [100]. Silicon oil was loaded inside of the hole as PTM, since this medium does not solidify at low temperatures. The whole DAC was introduced in a pumped He cryostat, which allowed to cool down the sample down to a minimum of 15 K. The temperature of the sample was measured with a thermocouple attached next to the DAC. The cryostat was introduced in a vessel equipped with x-ray transparent windows. Vacuum conditions were ensured in order to avoid the formation of ice crystals. The temperature of the sample was regulated by a computer-controlled resistive heater. An incident monochromatic beam with wavelength $\lambda = 0.4246$ Å focused down to 20×20 μm^2 was used to characterize the sample. The diffraction patterns were collected using a Rayonix two-dimensional CCD detector. The cake patterns were integrated using the DIOPTAS software program [122]. Preferred orientations in the XRD patterns precluded the refinement of the atomic positions in the unit-cell. However, the evolution of the unit-cell parameters could be studied by performing LeBail analysis [105]. Integrated XRD patterns were analized using the UNITCELL [124] and PowderCell [123] software packages. With the same setup, two succesive runs consisting in cooling down the sample and warming it up were carried out at a series of different pressures.

8.2 Optical absorption experiments

Fig. 8.1 shows the transmittance spectra of $TbVO_4$ at different temperatures from 280 to 13.5 K. As it can be observed in the figure, there is a considerable shift in the transmission edge from 280 to 100 K, whereas the spectra taken at 100, 60 and 35 K are barely different. In other words, the bandgap energy shows a negative temperature dependence that becomes stronger upon warming. On the other hand, the transmission edge of the spectrum taken at 13.5 K is slightly displaced towards higher energies, which points to a bandgap energy increase in the distorted structure of $TbVO_4$, after the Jahn-Teller distortion takes place at $\sim$ 30 K.

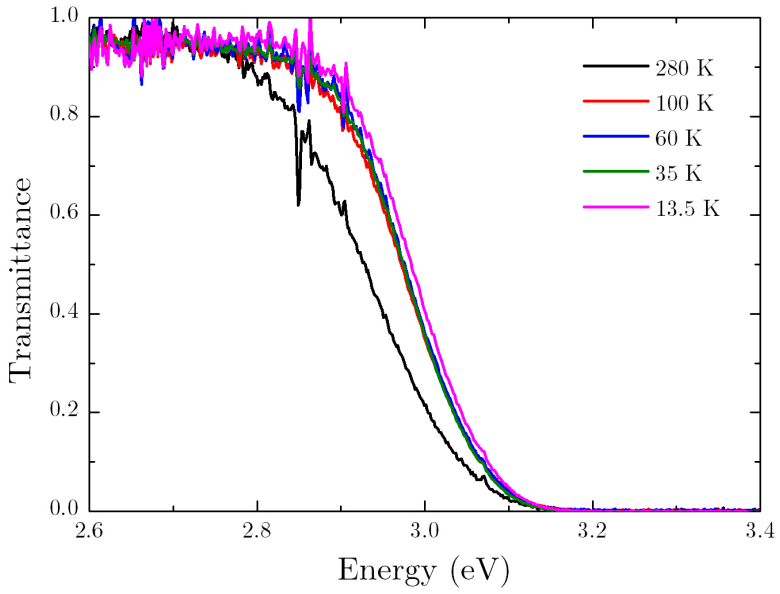

Figure 8.1: Transmittance spectra of $TbVO_4$ at different temperatures.

The absorption coefficient for each temperature can be calculated using the expression shown in Eqn.3.25, where the transmittance data obtained in the experiment is taken as $\langle T \rangle$. An approximate value of R is obtained using the expression 3.23, where we took an estimated value of $\bar{n} \approx 2.1$ according to the calculations and experiments reported of other zircon-type RVO_4 com-

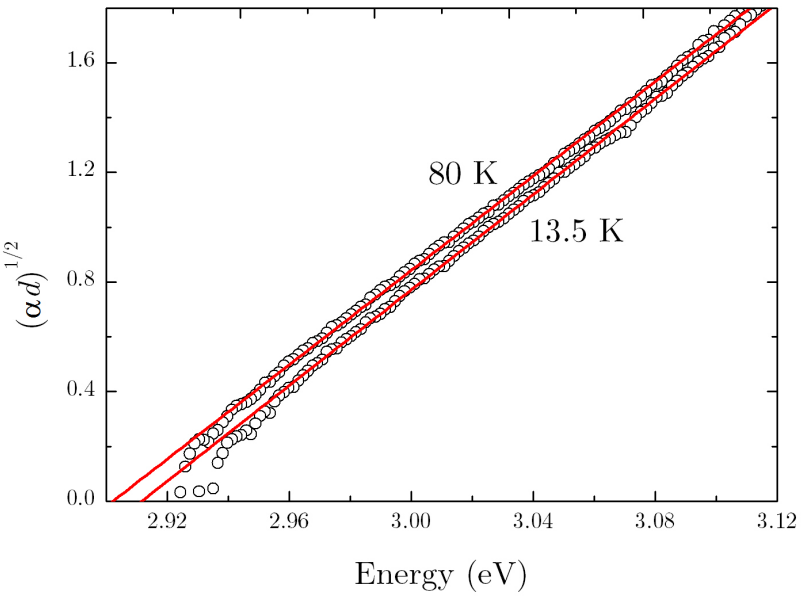

Figure 8.2: Square root of αd vs. photon energy at 80 and 13.5 K (zircon and orthorhombic phases of $TbVO_4$ respectively). Circles stand for the experimental data while solid red lines represent the linear fit for each series.

pounds [72, 220]. The variation of R with the photon energy in this range can be considered small. After doing so, we plotted $(\alpha d)^{1/2}$ (since the exact thickness d of the single-crystal was unknown) as a function of the energy of the incident photons, as it is shown in Fig. 8.2 for the zircon and orthorhombic phases at 80 and 13.5 K respectively. The linear dependence of the absorption edge with energy is clear for both phases, showing the indirect character of the electronic bandgap (see Eqn. 2.85). In this case, phonon absorption contribution is too weak to be observed. Thus, only the phonon emission contribution is relevant in our analysis. The indirect nature of the electronic bandgap is in agreement with the DFT calculations reported in the Materials Project website by Persson [221]. In particular, whereas the minimum of the conduction band is located at the Γ point, the maximum of the valence band is slightly shifted in the $\Gamma \rightarrow Z$ direction. Many RVO_4 compounds [68, 69, 222–224] are predicted to show this weak indirect bandgap nature. The energy of the bandgap can be estimated by performing a linear fit to the $(\alpha d)^{1/2}$ vs. E experi-

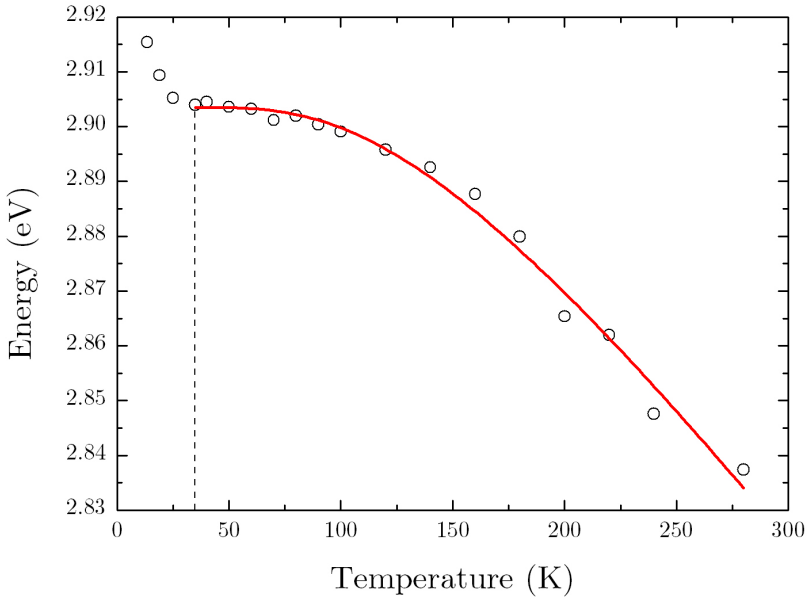

Figure 8.3: Evolution of the bandgap energy (plus the energy of the assistant phonon E_p) of $TbVO_4$ with temperature. Circles represent the experimental data, while the red solid line stands for the obtained fit to a Bose-Einstein function for $T > 30$ K. The vertical dashed line indicates the transition temperature.

mental data, as it is shown in Fig. 5.11. The intercept of the fitted line should give an estimation of the value of $E_{gap} + E_p$, where E_p is the energy of the phonon that assists the interband transition. Since the phonon absorption contribution is not observed we could not quantify the value of E_p. However, this magnitude is not expected to change during the experiment, so the observed variation in the energy can be entirely attributed to the changes in E_{gap}.

The obtained results from this analysis are depicted in Fig. 8.3, where we show the behaviour of the bandgap of $TbVO_4$ from 13.5 to 280 K. For temperatures higher than 30 K, the temperature dependence of the bandgap energy follows a tendency that can be described with a Bose-Einstein function [225, 226],

$$E_{gap}(T) = E_{gap}(0) - \frac{2A}{\exp\left(\hbar\Omega/k_B T\right) - 1} \tag{8.1}$$

where $\hbar\Omega$ is the average phonon energy and A describes the strength of the interaction. The

argument inside the exponential part can also be expressed as Θ/T, with Θ as the associated temperature of the average phonon ($\hbar\Omega = k_B\Theta$). The solid red line in Fig. 8.3 represent the result of the performed fit. The obtained parameters are $A = 112(8)$ meV, $\hbar\Omega = 36(3)$ meV ($\Theta = 420(40)$ K) and $E_{gap}(0) = 2.903(5) - E_p$ eV. Assuming that $E_p \approx 25$ meV, then $E_{gap}(0) \approx 2.878$ eV. The predicted value of $E_{gap}(0)$ in Ref. [221] is 2.990 eV, which is similar to our value. This small discrepancy is compatible with the typical error associated to DFT calculations.

Table 1.10 (Introduction, Chapter 1) shows the experimental (obtained near room conditions in optical absorption measurements) and theoretical values reported in literature. In general, the experimental results reported in Panchal *et al.* [48] for several vanadates and in our work on $GdVO_4$ (Ref. [49], Chapter 5) are $\sim$ 1 eV higher than the predicted value, which is attributed in to the tendency of DFT calculations to severely underestimate the size of the bandgap. On the contrary, in our case, the estimated value of the bandgap of $TbVO_4$ at 0 K is compatible with calculations. Although some assumptions were made in order to get the experimental value, these cannot explain the $\sim$ 1 eV difference with the experimental values of the other compounds. With respect to our previous work on $GdVO_4$, a possible explanation to the higher value of E_{gap} may be the fact that in the experiments, only the Urbach's tail of the absorption spectra could be analyzed, whereas in the case of $TbVO_4$ we could measure the whole absorption edge.

Regarding the behaviour of the bandgap below 30 K, Fig. 8.3 shows that the tendency of E_{gap} to be constant at low temperatures does not hold. On the contrary, the bandgap energy increases when temperature decreases under 33(2) K. This is coherent with the second order phase transition induced by the cooperative Jahn-Teller distortion that takes place at similar temperatures [215]. According to our results, in the low temperature orthorhombic phase of $TbVO_4$, there is a broadening of the electronic bandgap. In other words, the increase in the separation of the electronic degenerated states, which is shown in Fig. 2.8 (b) (Chapter 2), leads to an increase of the size of the bandgap. According to electronic band calculations in zircon-type $TbVO_4$ [221], the major contribution to the density of states (DOS) in the maximum of the valence band and

the minimum of the conduction band are $2p$−O and $3d$−V orbitals respectively. By contrast, the only significant contributions to the electronic DOS of the rare-earth cation are found at low energies in the valence band and at very high energies over the conduction band. Moreover, these contributions correspond to s and d orbitals. The $4f$ electrons of the rare-earth cations are highly localized in narrow bands at much lower energies [72]. In other words, calculations predict that the changes in the size of the bandgap are mostly related to variations in the VO_4 tetrahedra. Moreover, high-pressure experiments on zircon-type orthovanadates showed that the compression of the tetrahedra leads to a widening of the bandgap. Thus, the observed widening of the bandgap at low temperatures cannot be explained in terms of the contraction of the VO_4 units, since, according to Kirschbaum *et al.* [215], the V−O bond length of $TbVO_4$ is 1.714(4) Å at ambient conditions (zircon phase) and 1.720(5) Å at 22 K (orthorhombic phase). Therefore, the increase in the band gap energy below 33 K may be attributed to an increase in the intensity of the electron-phonon interaction.

8.3 Low-Temperature-High-Pressure XRD experiments

Fig. 8.4 show some selected powder XRD patterns of $TbVO_4$ collected at different temperatures and pressures. The reason why these patterns were not collected by following isobars or isotherms is purely experimental. As the DAC is cooled down, the materials that constitute this device contract, so that the pressure of the chamber increases as temperatures fall down. On the other hand, the piston of the cell gets stuck at low temperatures, so that pressure cannot be increased or released. Thus, it is only possible to follow diagonal lines in the Temperature-Pressure phase diagram. The powder XRD pattern at room temperature and 0.9 GPa can be undoubtedly assigned to a zircon-type structure whose lattice parameters are $a = 7.158(3)$ Å and $c = 6.317(4)$ Å, which are slightly smaller than those reported in Ref. [215] at ambient conditions. In the first run the sample was cooled down to 15 K and compressed to 6.7 GPa. As it is depicted in Fig.

8.4, subtle changes take place between 200 K, 2.1 GPa and 100 K, 4.8 GPa. There is a general broadening of the Bragg peaks, which is specially evident for those located at $2\theta \sim 13.3°$. At 15 K and 6.7 GPa the splitting of the peaks become more obvious. This new phase is perfectly compatible with the orthorhombic structure (S.G.: *Fddd*) that should arise as a consequence of the cooperative Jahn-Teller distortion. At 15 K and 6.7 GPa, the unit-cell lattice parameters are $a = 10.194(2)$ Å, $b = 9.864(5)$ Å and $c = 6.274(3)$ Å, which are also similar, although smaller, than those reported at 22 K and zero pressure by Kirschbaum *et al.* [215]. The sample was warmed up to 250 K and 1.6 GPa. During this process the broadening of the peaks progressively reduces

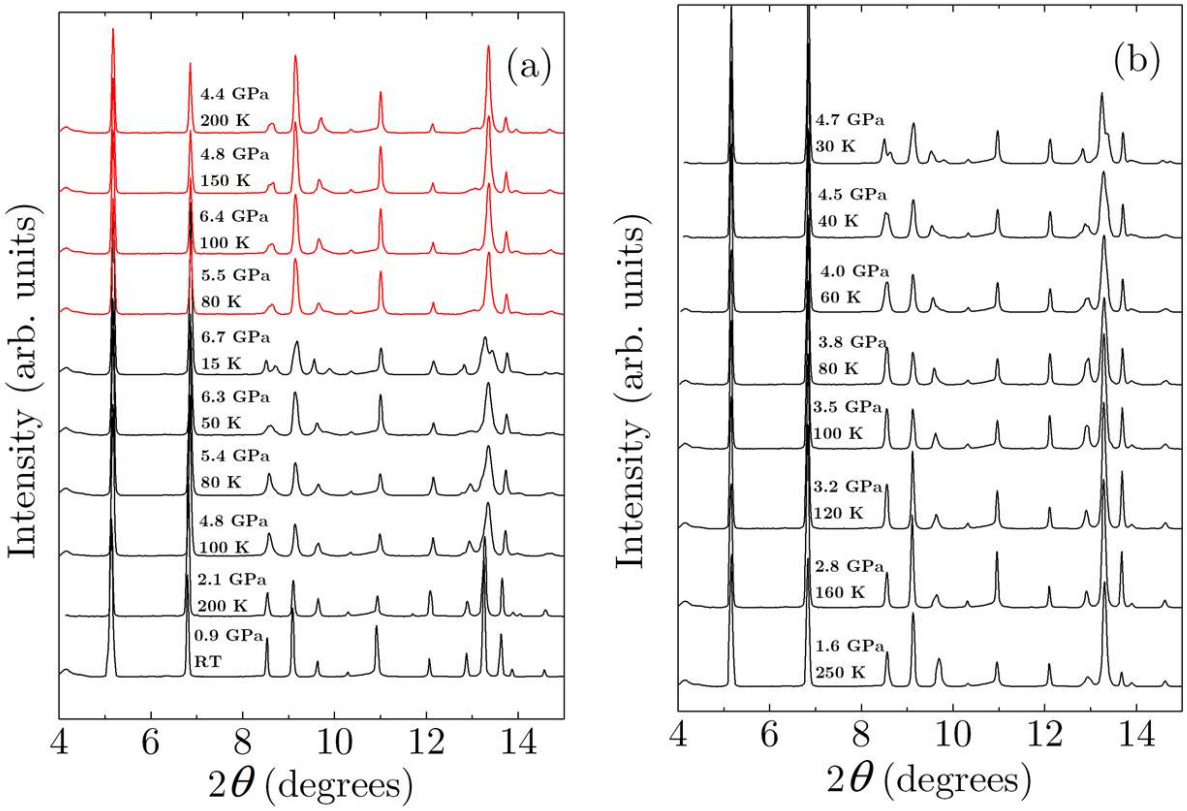

Figure 8.4: Selected XRD patterns of $TbVO_4$ at different temperatures and pressures. Black and red solid lines stand for those patterns collected upon cooling and warming respectively.

and the zircon structure is recovered again. Due to the existence of preferred orientations in the sample, variations in the width and intensity of the reflections hinder the identification of the reverse phase transition to the zircon structure. Nonetheless, it is clear that at 250 K and 1.6 GPa the peaks are not split. The sample was cooled again from these conditions down to 30 K. This process was carried out in smaller temperature steps than in the first run, which lead to smaller pressure increments. In fact, at 30 K we reached a pressure of 4.7 GPa, whereas the same pressure was achieved in the first run at 100 K.

The distortion associated to the phase transition from zircon to the orthorhombic phase is not evident at the beginning of the phase transition (Fig. 8.4). The temperature and pressure of the phase transition are then determined by the evolution of the unit-cell parameters. It is possible to relate the zircon (S.G.: $I4_1/amd$) and orthorhombic (S.G.: $Fddd$) structures by group-subgroup relationships. In particular, the a and b lattice parameters of the orthorhombic phase are taken as the base diagonals of the tetragonal zircon structure, which correspond to the directions associated to the vibration pattern of the B_{2g} mode. On the other hand, the c axis is the same for both structures. Thus, in the zircon-to-orthorhombic phase transition the the unit-cell parameters transform as $a \rightarrow a/\sqrt{2}$, $b/\sqrt{2}$ and $c \rightarrow c$. Hereon, we will use a' and b' for $a/\sqrt{2}$ and $b/\sqrt{2}$ respectively. In Fig. 8.5 we represented the evolution of the unit-cell lattice parameters and the pressure of the sample against temperature for the data collected in the first (a) and second (b) experimental runs upon cooling. We decided to establish temperature as the variable in the horizontal axis and represent pressure in the lower part of the figures. It must be remarked that each of the lattice parameters data points were obtained at a certain temperature and pressure. In fact, in the lower part of both Fig. 8.5 (a) and (b), we see that the pressure load applied on the sample has a quasi-linear dependence with temperature. Regarding the evolution of the unit-cell parameters, we can observe that, in both cases, there is a splitting of the a lattice parameter of the zircon phase into the a' and b' lattice parameters of the orthorhombic phase. Actually, whereas the former slightly increases, the latter shortens as temperature goes down and pressure

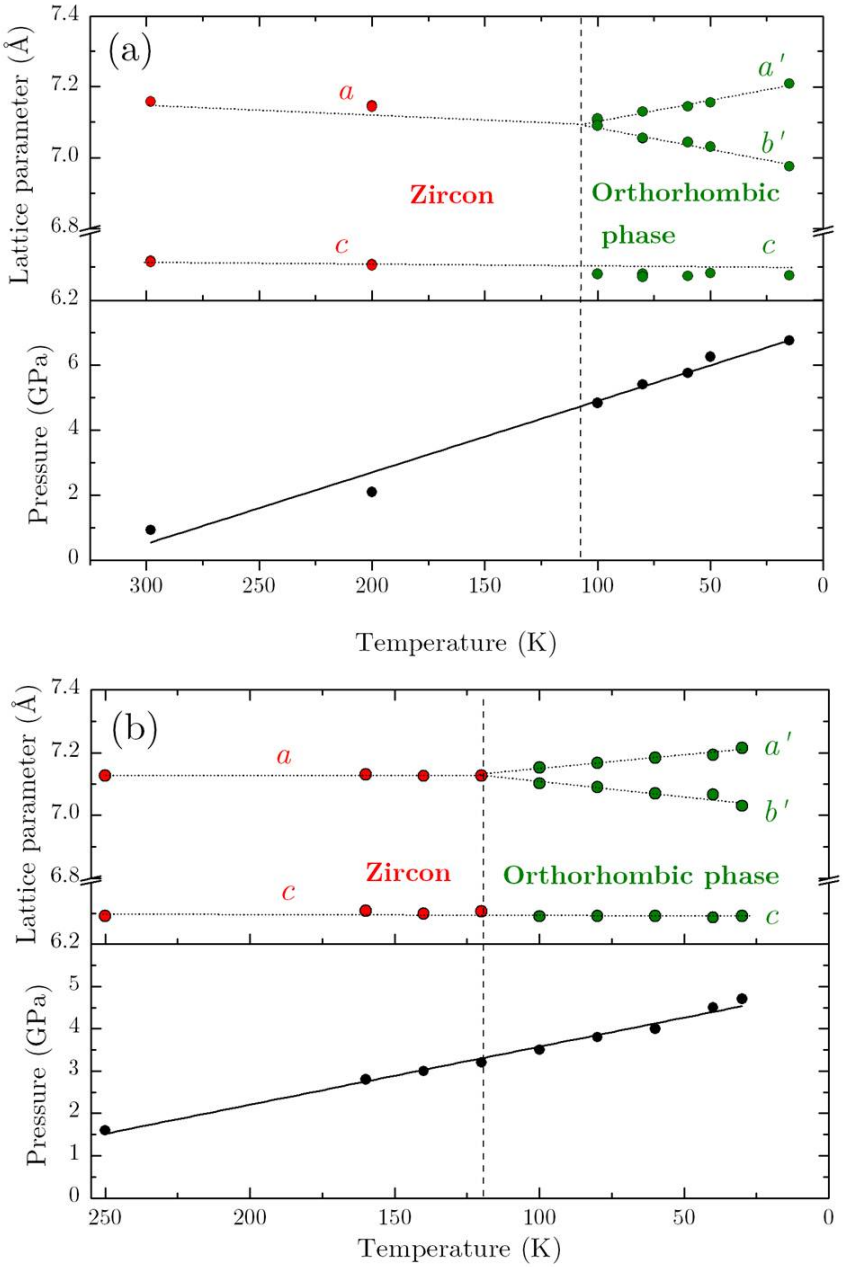

Figure 8.5: Temperature and pressure evolution of the unit-cell parameters of $TbVO_4$ during the first (a) and second (b) experimental runs. Red and green circles represent the experimental data for the zircon and orthorhombic phases respectively. For the latter phase $a' = a/\sqrt{2}$ and $b' = b/\sqrt{2}$. Dashed lines are a guide to the eye. Black dots represent the evolution of pressure with temperature in each case. A linear fit to the data is represented by a black solid line.

increases. This allows to estimate the temperature and pressure conditions at which the phase transition occur. In particular, the phase transition is estimated to take place at 107(10) K and 4.8 GPa, according to the data collected during the first run. A similar analysis for the data collected during the second run suggests that the phase transition can also happen at 120(11) K and 3.2 GPa. In contrast to the other lattice parameters, the c-axis shows no relevant variation during the phase transition. All these changes are consistent with the second order character of the transition, since no discontinuity is observed.

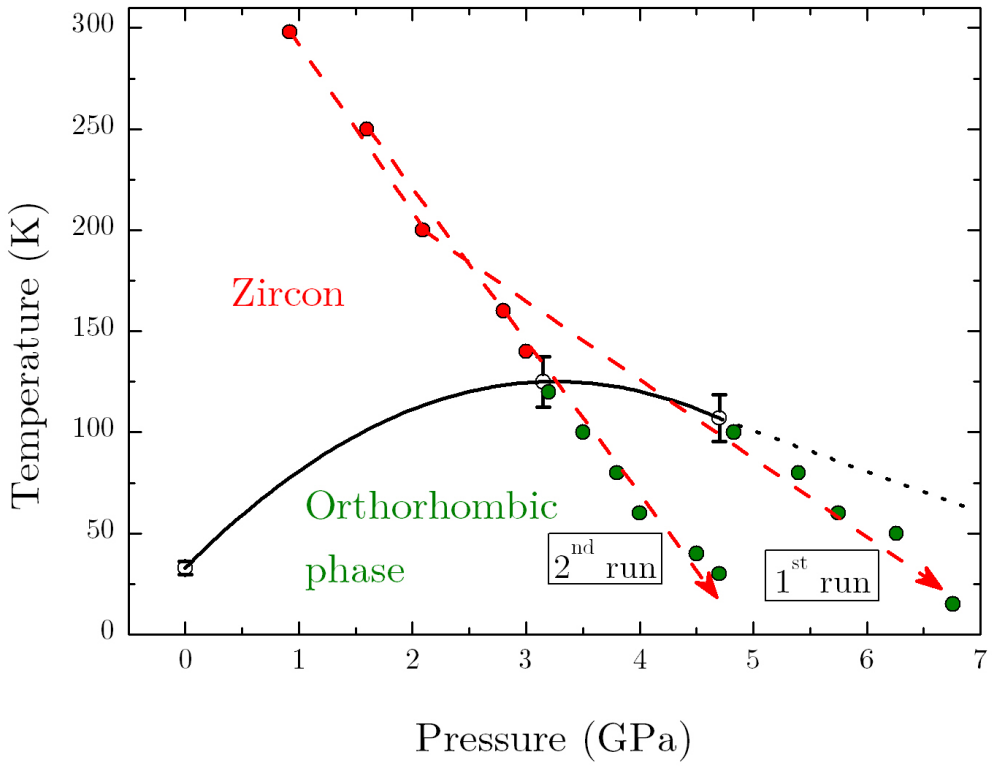

Figure 8.6: Tentative $P-T$ phase diagram of $TbVO_4$. Red and green circles represent the measurements at which the zircon and orthorhombic phases were found, respectively. Red dashed lines indicate the path followed during the two different experimental runs. Void circles represent the estimated transition points whereas the solid line stands for a quadratic fit to these data. The black dotted line represents the hypothetical phase line for higher pressures.

With these two points at the zircon-orthorhombic phase boundary and the one already known at zero pressure and 33 K, we can tentatively draw a sketch of the $P - T$ phase diagram, as it is depicted in Fig. 8.6. In this case we fitted a quadratic function to the three available data points. Assuming that the proposed phase boundary is more or less correct, we would expect a considerable increase in the transition temperature with pressure up to $\sim$ 3 GPa. Qualitatively, we can see that high pressure conditions favour the Jahn-Teller distortion at considerably higher transition temperatures. A possible explanation to this is that high pressures induce a much stronger crystal field effect on the rare-earth cation, which promotes the splitting of the associated electronic levels. In addition to this, Raman scattering experiments on $TbVO_4$ under high pressure showed that the frequency of the B_{2g} mode decreases upon compression [181]. Therefore, it is possible that this partial softening of this mode at high-pressures could also contribute to the Jahn-Teller distortion at higher temperatures.

8.4 Conclusions

In this chapter we have characterized the bandgap of zircon-type $TbVO_4$ at low temperatures. Our optical absorption experiments on $TbVO_4$ thin single crystals revealed that this compound has an indirect gap whose behaviour at low temperatures can be described with a Bose-Einstein function down to 35 K. At lower temperatures there is a progressive increase in the size of the bandgap, which is associated with the Jahn-Teller distortion that leads to an orthorhombic structure below 33 K [27, 215]. We also performed XRD measurements of $TbVO_4$ at low temperatures and high pressures. In the first run, we observed that the Jahn-Teller effect takes place at 107(10) K and 4.8 GPa, whereas in the second one, the transition was observed and 120(11) K and 3.2 GPa. These transition temperatures are much higher than that observed at zero pressure (T = 33 K), which is coherent with the mechanisms that are involved in the distortion. A tentative $P - T$ phase diagram has also been proposed.

9 | Conclusions

In this dissertation we have explained in detail the obtained results of our experiments on different RVO$_4$ compounds under high pressures. These results have been supplemented with DFT *ab initio* calculations, which allowed a better understanding of the underlying physical phenomena.

We started in Chapter 4 by showing our results on NdVO$_4$ at high pressures under quasi-hydrostatic conditions. Our XRD and Raman scattering measurements (using He and Ne gases as PTM respectively) confirmed the onset of a zircon-to-scheelite phase transition near 6.5 GPa. This constitutes a huge difference with previous studies in which the monazite phase was found as the stable high pressure phase [41, 114]. The possible influence of dynamical or mechanical instabilities has also been discussed. A second phase transition from scheelite to a fergusonite phase was reported to take place at $\sim$ 20 GPa in both kinds of experiments. According to our calculations, the transition takes places as a consequence of a mechanical instability that leads to a monoclinic distortion of the fergusonite phase. The obtained results confirmed the considerable influence of hydrostatic conditions on RVO$_4$ under compression. The EOS and the pressure evolution of the Raman modes were also reported, showing good agreement with theoretical calculations.

In Chapter 5 we provided a systematic study on GdVO$_4$ under high pressures. XRD and Raman spectroscopy experiments showed that this compounds transforms from a zircon to a scheelite structure below 7 GPa. The EOS of these polymorphs, as well as the pressure evolution of the Raman modes were reported, showing good agreement with calculations. The softening of the

B_{1u} silent mode was predicted to take place at 8.2 GPa, near the observed phase transition. As we lately proved, the softening of such phonon is directly involved in the transition process. The zircon-to-scheelite phase transition was confirmed by optical absorption measurements, which showed a band gap collapse at the transition pressure. This explains the change in the sample colour during the transition. A second order phase transition is observed at $\sim$ 20 GPa, in which the scheelite phase transforms into a fergusonite phase. Calculations predict this transition at similar pressures, which takes place as a consequence of a mechanical instability. In the Raman experiments, a third phase is observed over 29 GPa. We proposed a structure with a *Cmca* symmetry, although further experiments are needed in order to fully assess the correct structure. The scheelite phase is recovered at ambient conditions in a metastable form, showing the irreversible character of the first phase transition.

On the other hand, in Chapter 6 we studied the polymorphism of $PrVO_4$ under high pressures and high temperatures. We first performed XRD measurements under high pressures and room temperatures, using Ne gas as PTM. A first zircon-to-monazite phase transition was confirmed at 5.5 GPa, in line with previous studies [42]. A second order phase transition was reported to take place beyond 12.2 GPa. We proposed a $PbWO_4$-III phase as a candidate structure, which showed an outstanding good compatibility with experimental observations, in contrast to previously suggested structures [42]. *Ab initio* enthalpy calculations predicted these transitions at 5.3 and 11.1 GPa, which definitely agrees with the experiments. Moreover, calculations predict that a mechanical instability takes place at similar pressures than the zircon-to-monazite phase transition, suggesting a possible influence of this mechanism in the trasnsformation process. Theoretical calculations also predicted that the scheelite phase is energetically competitive with the monazite phase. Thus, we decided to perform several syntheses in the Paris-Edinburgh large press cell at high pressures and high temperatures. As a result we obtained a mixture of both zircon and scheelite phases at ambient conditions. The proportion of scheelite phase was hugely increased with longer heating lapses (80% after 6h). The lattice parameters as well as the atomic

positions in the scheelite phase were refined. These experiments showed the great relevance of kinetic barriers in RVO$_4$ compounds. The obtained scheelite-type PrVO$_4$ samples were analyzed under high pressures by means of Raman scattering experiments. These experiments showed a reversible phase transition to a PbWO$_4$-III structure at 16.7 GPa, which is in agreement with theoretical predictions.

A more general approach to the zircon-to-scheelite/monazite phase transition systematic is given in Chapter 7. By gathering the experimental data reported in literature and our calculations we were able to unveil the mechanisms that underlay these high pressure transformations in RVO$_4$ compounds. Previously to our study, the structural systematics of RVO$_4$ was rationalized in terms of the rare-earth cation size and the relative stability of the high pressure phases was discussed in accordance with enthalpy calculations. However, the role played by dynamical and mechanical instabilities is often left out of the scope. By contrast, our calculations showed that the activation barrier of the zircon-to-scheelite phase transition is lowered by the softening of the B_{1u} silent mode (dynamical instability). Moreover, the zircon-to-monazite phase transition is triggered by a mechanical instability related to the stiffness tensor. In fact, this leads to a monoclinic distortion of the zircon phase, which is compatible with the required atomic displacements of the phase transition. The complex interplay between these two phenomena explains the observed transition pressures as well as the observed systematic. In this case, the described mechanisms were studied for the RVO$_4$ family. Nonetheless, we believe that our study constitutes a particular example that may be applied to many other ternary oxides and related compounds.

By the end of this dissertation in Chapter 8, we studied the cooperative Jahn-Teller effect in TbVO$_4$ at low temperatures. Optical absorption measurements of a thin single crystal at low temperatures and ambient pressure revealed that zicon-type TbVO$_4$ has an indirect gap of $\sim$ 2.8 eV. Upon cooling, the band gap of TbVO$_4$ slightly increases from 280 to $\sim$ 100 K. Between 100 and 35 K the band gap remains more or less constant. This behaviour is well described by the Bose-Einstein function. However, between 35 and 30 K, the band gap increases as temperature is

lowered. This is in agreement with the second order phase transition induced by the Jahn-Teller distortion at 33 K. XRD experiments at low temperatures and high pressures revealed that the transition temperature can be considerably increased upon compression. In fact, two points at the $P-T$ phase diagram were determined: (1) 120(11) K and 3.2 GPa and (2) 107(10) K and 4.8 GPa. Thus, high pressure conditions tend to favour the Jahn-Teller distortion, increasing the transition temperature from 33 K at zero pressure to a maximum of 120(11) K.

To sum up, we have studied some RVO$_4$ compounds under extreme pressure and temperature conditions. In our studies we could identify at least six different polymorphs: zircon, monazite, scheelite, fergusonite, PbWO$_4$-III (formally isomorphic to BaWO$_4$-II) and the orthorhombic phase of TbVO$_4$ at low temperatures. Some of these structures, like the scheelite and monazite can be quenched at ambient conditions in a metastable state. Different kinds of experimental techniques, such as XRD, Raman scattering and optical absorption, were used to characterize the samples. The observed results were complemented with DFT *ab initio* calculations, which allowed us to better interpret our observations. In addition to this, we studied the zircon-to-scheelite/monazite transition systematic in these compounds by gathering experimental data from literature and our theoretical calculations. We concluded that the systematic of these compounds can be explained in terms of competing dynamical and mechanical instabilities, which opens the possibility of performing similar analyses on other different ternary oxide families.

Bibliography

1. Hummel, R. E. *Understanding materials science: history, properties, applications* (Springer, 1998).
2. McMillan, P. F. *Nature Materials* **4,** 715–718 (2005).
3. Bridgman, P. W. *The resistance of 72 elements, alloys and compounds to 100,000 kg/cm2* (Harvard University Press, 2013).
4. Bassett, W. A. *High Press. Res.* **29,** 163–186 (2009).
5. Dubrovinskaia, N. *et al. Sci. Adv.* **2,** e1600341 (2016).
6. Balasubramaniam, V. & Farkas, D. *Food Sci. Tech. Inter.* **14,** 413–418 (2008).
7. Oelkers, E. H. & Montel, J.-M. *Elements* **4,** 113–116 (2008).
8. Dou, R. *et al. Crystals* **8,** 55 (2018).
9. Zhang, X., Lin, J., Mikhailik, V. & Kraus, H. *Astropart. Phys.* **79,** 31–40 (2016).
10. Errandonea, D. & Garg, A. B. *Prog. Mater. Sci.* **97,** 123–169 (2018).
11. Voloshina, O. *et al. Nucl. Instrum. Methods Phys. Res. Sect. A* **664,** 299–303 (2012).
12. Fujimoto, Y. *et al. Nucl. Instrum. Methods Phys. Res. Sect. A* **635,** 53–56 (2011).
13. Kang, J. H. *et al. Solid S Commun.* **133,** 651–656 (2005).
14. Zhang, C. *et al. Opt. Lett.* **31,** 1435–1437 (2006).

15. Nadimi, M., Waritanant, T. & Major, A. *Laser Physics Letters* **15,** 055002 (2018).

16. Mahapatra, S., Madras, G. & Guru Row, T. *Ind. Eng. Chem. Res.* **46,** 1013–1017 (2007).

17. Oshikiri, M., Ye, J. & Boero, M. *J. Phys. Chem. C* **118,** 8331–8341 (2014).

18. Wang, T. *et al. ACS Sustain. Chem. Eng.* **2,** 2253–2258 (2014).

19. Young, A. & Schwartz, C. *Acta Crystallogr.* **15,** 1305–1305 (1962).

20. Laves, F., Young, A. & Schwartz, C. *Acta Crystallogr.* **17,** 1476–1477 (1964).

21. Muller, J. & Joubert, J. *J. Solid State Chem.* **14,** 8–13 (1975).

22. Kanamaru, F., Shimada, M., Koizumi, M. & Asai, T. *Rev. Phys. Chem. Jap.,* 180–184 (1975).

23. Stubican, V. & Roy, R. *Zeitschrift für Kristallographie-Crystalline Materials* **119,** 90–97 (1964).

24. Cooke, A., Martin, D. & Wells, M. *Solid State Commun.* **9,** 519–522 (1971).

25. Cooke, A., Swithenby, S. & Wells, M. *Solid State Comm.* **10,** 265–268 (1972).

26. Elliott, R. *et al. J. Phys. C Solid State Phys.* **4,** L179 (1971).

27. Elliott, R. J., Harley, R., Hayes, W. & Smith, S. *Proceedings of the Royal Society of London. A. Mathematical and Physical Sciences* **328,** 217–266 (1972).

28. Gehring, G. & Gehring, K. *Rep. on Prog. Phys.* **38,** 1 (1975).

29. Hazen, R. & Mariathasan, J. *Science* **216,** 991–993 (1982).

30. Mariathasan, J., Hazen, R. & Finger, L. *Phase Trans.* **6,** 165–173 (1986).

31. Jayaraman, A. *et al. J. Phys. Chem. Solids* **48,** 755–759 (1987).

32. Duclos, S. J. *et al. J. Phys. Chem. Solids* **50,** 769–775 (1989).

33. Wang, X. *et al. Phys. Rev. B* **70,** 064109 (2004).

34. Manjón, F. *et al. Phys. Rev. B* **69,** 165121 (2004).

35. Popescu, C. *et al. J. Phys. Condens. Matter* **28,** 035402 (2016).

36. Garg, A. B. *et al. J. Phys. Condens. Matter* **26,** 265402 (2014).

37. Garg, A. B. *et al. J .Phys. Condens. Matter* **26,** 265402 (2014).

38. Rao, R. *et al. J. Solid State Chem.* **182,** 1879–1883 (2009).

39. Errandonea, D., Kumar, R., Achary, S. & Tyagi, A. *Phys. Rev. B* **84,** 224121 (2011).

40. Panchal, V. *et al. Phys. Rev. B* **84,** 024111 (2011).

41. Errandonea, D. *et al. Mat. Res. Bull.* **50,** 279–284 (2014).

42. Bandiello, E. *et al. Inorg. Chem.* **59,** 18325–18337 (2020).

43. Marqueño, T. *et al. Phys. Rev. B* **103,** 134113 (2021).

44. Marqueño, T. *et al. J. Phys. Condens. Matter* **31,** 235401 (2019).

45. Errandonea, D. *et al. J. Phys. Chem. C* **120,** 13749–13762 (2016).

46. Marqueño, T. *et al. J. Phys. Condens. Mat.* (2021).

47. Garg, A. B., Errandonea, D., Rodríguez-Hernández, P. & Muñoz, A. *J. Phys. Condens. Mat.* **29,** 055401 (2016).

48. Panchal, V. *et al. J. Appl. Phys.* **110,** 043723 (2011).

49. Marqueño, T. *et al. Phys. Rev. B* **100,** 064106 (2019).

50. Milligan, W. O. & Vernon, L. W. *J. Phys. Chem.* **56,** 145–147 (1952).

51. Chakoumakos, B. C., Abraham, M. M. & Boatner, L. A. *J. Solid State Chem.* **109,** 197–202 (1994).

52. Mullica, D. F. *et al. Inorg. Chim. Acta* **248,** 85–88 (1996).

53. Range, K.-J. & Meister, H. *Acta Crystallogr. Sect. C* **46,** 1093–1094 (1990).

54. Ruiz-Fuertes, J. *et al. Inorg. Chem.* **57,** 14005–14012 (2018).

55. Beall, G., Boatner, L., Mullica, D. & Milligan, W. *J. Inorg. Nucl. Chem.* **43,** 101–105 (1981).

56. Mullica, D. *et al. Inorg. Chim. Acta* **95,** 231–236 (1984).

57. Mullica, D., Grossie, D. A. & Boatner, L. *Inorg. Chim. Acta* **109,** 105–110 (1985).

58. Clavier, N., Podor, R. & Dacheux, N. *J. Europ. Ceram. Soc.* **31,** 941–976 (2011).

59. Richter, P., Kruger, G. & Pistorius, C. *Acta Crystallogr. Sect. B* **32,** 928–929 (1976).

60. Kawada, I., Kato, K. & Fujita, T. *Acta Crystallogr.* **30,** 2069–2071 (1974).

61. Wang, X. *et al. J. Alloys Comp.* **875,** 159926 (2021).

62. Yuan, H. *et al. J. Phys. Chem. C* **119,** 8364–8372 (2015).

63. Dresselhaus, M. S., Dresselhaus, G. & Jorio, A. *Group theory: application to the physics of condensed matter* (Springer Science & Business Media, 2007).

64. Voron'ko, Y. K. *et al. Phys.Solid State* **51,** 1886–1893 (2009).

65. Errandonea, D., Achary, S. N., Pellicer-Porres, J. & Tyagi, A. K. *Inorg. Chem.* **52,** 5464–5469 (2013).

66. Errandonea, D. *et al. J. Alloys Compd.* **577,** 327–335 (2013).

67. Pellicer-Porres, J. *et al. Phys. Rev. B* **98,** 214109 (2018).

68. Persson, K. *Materials Data on YVO_4 (SG:141) by Materials Project* (2014). doi:10.17188/1193956.

69. Persson, K. *Materials Data on $LuVO_4$ (SG:141) by Materials Project* (2014). doi:10.17188/1193773.

70. Persson, K. *Materials Data on $NdVO_4$ (SG:141) by Materials Project* (2014). doi:10.17188/1193511.

71. Anonymous. *Materials Data on $GdVO_4$ (SG:141) by Materials Project* (2014). https://materialsproject.org/materials/mp-22024/.

72. Huang, Z. *et al. J. Alloys Compd.* **538,** 56–60 (2012).

73. Jain, A. *et al. APL Mater.* **1,** 011002 (2013).

74. https://materialsproject.org/.

75. Krumpel, A. H. *et al. J. Phys. Condens. Matter* **21,** 115503 (2009).

76. Banerjee, C. *et al. J. Hazard. Mater.* **280,** 63–70 (2014).

77. Wei, X. *et al. J. Appl. Phys.* **107,** 103107 (2010).

78. Krumpel, A. H., Boutinaud, P., van der Kolk, E. & Dorenbos, P. *J. Lumin.* **130,** 1357–1365 (2010).

79. Tang, X., Ding, Z. & Zhang, Z. *J. Lumin.* **122,** 66–69 (2007).

80. Reitz, C., Smarsly, B. & Brezesinski, T. *ACS Appl. Nano Mater.* **2,** 1063–1071 (2019).

81. Monsef, R., Ghiyasiyan-Arani, M. & Salavati-Niasari, M. *J. Environ. Manage.* **230,** 266–281 (2019).

82. Kang, X. *et al. Langmuir* **29,** 1286–1294 (2013).

83. Potter, S. & Ehlers, E. G. *Encyclopedia Britannica* Nov. 2019. https://www.britannica.com/science/phase-state-of-matter.

84. Umantsev, A. *Field theoretic method in phase transformations* (Springer, 2012).

85. Poirier, J.-P. *Introduction to the Physics of the Earth's Interior* (Cambridge University Press, 2000).

86. Katsura, T. & Tange, Y. *Minerals* **9,** 745 (2019).

87. Murnaghan, F. D. *Amer. J. Math.* **59,** 235–260 (1937).

88. Recio, J. M., Menéndez, J. M. & De la Roza, A. O. *An introduction to high-pressure science and technology* (CRC Press, 2016).

89. Wallace, D. C. *Thermodynamics of Crystals* (Dover Publications, 1998).

90. Landau, L. *et al. Theory of Elasticity: Volume 7* (Elsevier Science, 1986).

91. Nye, J. F. *et al. Physical properties of crystals: their representation by tensors and matrices* (Oxford university press, 1985).

92. Wang, J. *et al. Phys. Rev. B* **52,** 12627 (1995).

93. Karki, B., Ackland, G. & Crain, J. *J. Phys. Condens. Mat.* **9,** 8579 (1997).

94. Born, M., Huang, K. & Lax, M. *Amer. J. Phys.* **23,** 474–474 (1955).

95. Mouhat, F. & Coudert, F. X. *Phys. Rev. B* **90,** 224104 (2014).

96. Fox, A. *Optical Properties of Solids* (Oxford University Press, 2001).

97. Bersuker, I. B. *The Jahn-Teller Effect* (Cambridge University Press, 2006).

98. Dove, M. T. *Structure and dynamics: an atomic view of materials* (Oxford University Press, 2003).

99. Klotz, S., Chervin, J. C., Munsch, P. & Le Marchand, G. *J. Phys. D* **42,** 075413 (2009).

100. Mao, H. K., Xu, J. A. & Bell, P. M. *J. Geophys. Res.* **91,** 4673–4676 (1986).

101. Dorogokupets, P. & Dewaele, A. *High Press. Res.* **27,** 431–446 (2007).

102. Fei, Y. *et al. Proc. Nat. Acad. Sci.* **104,** 9182–9186 (2007).

103. Wilson, A. & Prince, E. *International Tables for Crystallography Vol. C, Mathematical, Physical and Chemical Tables* 1999.

104. Als-Nielsen, J. & McMorrow, D. *Elements of modern X-ray physics* (John Wiley & Sons, 2011).

105. Le Bail, A. *Powder Diffraction* **20,** 316–326 (2005).

106. Will, G. *J. Appl. Crystallogr.* **12,** 483–485 (1979).

107. Pawley, G. *J. Appl. Crystallogr.* **14,** 357–361 (1981).

108. Langford, J. & Louer, D. *J. Applied Crystallogr.* **24,** 149–155 (1991).

109. Young, R. A. *The Rietveld method* (1993).

110. Pecharsky, V. & Zavalij, P. *Fundamentals of powder diffraction and structural characterization of materials* (Springer Science & Business Media, 2008).

111. Williamson, G. K. & Hall, W. H. *Acta metallurgica* **1,** 22–31 (1953).

112. Ibach, H. & Lüth, H. *Solid-state physics: an introduction to principles of materials science* (Springer Science & Business Media, 2009).

113. Aroyo, M. I. *et al. Bulg. Chem. Commun.* **43,** 183–197 (2011).

114. Panchal, V. *et al. J. Phys. Chem. Solids* **100,** 126–133 (2017).

115. Yue, B. *et al. Phys. Rev. Lett.* **117,** 135701 (2016).

116. Tschauner, O., Ushakov, S. V., Navrotsky, A. & Boatner, L. A. *J. Phys. Condens. Matter* **28,** 035403 (2016).

117. Garg, A. B. *et al. J. Phys. Condens. Matter* **26,** 265402 (2014).

118. Errandonea, D., Muñoz, A. & Gonzalez-Platas, J. *J. Appl. Phys.* **115** (2014).

119. Feigelson, R. *J. Am. Ceram. Soc.* **51** (1968).

120. Garton, G. & Smith, S. *J. Cryst. Growth* **13-4** (1972).

121. Wanklyn, B. M. *J. Cryst. Growth* **7** (1970).

122. Prescher, C. & Prakapenka, V. B. *High Press. Res.* **35,** 223–230 (2015).

123. Kraus, W. & Nolze, G. *J. Appl. Cryst.* **29,** 301–303 (1996).

124. Holland, T. & Redfern, S. *J. Appl. Cryst.* **30,** 84–84 (1997).

125. Hohenberg, P. & Kohn, W. *Phys. Rev* **136,** B864 (1964).

126. Kresse, G. & Furthmüller, J. *Phys. Rev. B* **54,** 11169 (1996).

127. Kresse, G. & Joubert, D. *Phys. Rev. B* **59,** 1758 (1999).

128. Blöchl, P. E. *Phys. Rev. B* **50,** 17953 (1994).

129. Armiento, R. & Mattsson, A. E. *Phys. Rev. B* **72,** 085108 (2005).

130. Monkhorst, H. J. & Pack, J. D. *Phys. Rev. B* **13,** 5188 (1976).

131. Togo, A. & Tanaka, I. *Scr. Mater.* **108,** 1–5 (2015).

132. Le Page, Y. & Saxe, P. *Phys. Rev. B* **65,** 104104 (2002).

133. Chetty, N., Muoñz, A. & Martin, R. M. *Phys. Rev. B* **40,** 11934 (1989).

134. Stavrou, E. *et al. Phys. Rev. B* **85,** 024117 (2012).

135. Mote, V., Purushotham, Y. & Dole, B. *J. Theor. Applied Phys.* **6,** 1–8 (2012).

136. Garg, A. B. *et al. J. Appl. Phys.* **106,** 063513 (2009).

137. Arora, A., Sato, T., Okada, T. & Yagi, T. *Phys. Rev. B* **85,** 094113 (2012).

138. Pravica, M. *et al. Appl. Phys. Lett.* **103,** 224103 (2013).

139. Mittal, R. *et al. J. Phys. Condens. Matter* **20,** 075223 (2008).

140. Errandonea, D. *et al. J. Phys. Condens. Matter* **30,** 065401 (2018).

141. Knight, K. S. *Phys. Chem. Miner.* **37,** 529–533 (2010).

142. Santamaria-Perez, D. *et al. Inorg. Chem.* **55,** 10406–10414 (2016).

143. Christian, J., Olson, G. & Cohen, M. *Le Journal de Physique IV* **5,** C8–3 (1995).

144. Errandonea, D. & Manjón, F. J. *Mater. Res. B.* **44,** 807–811 (2009).

145. Manjón, F. *et al. Phys. Rev. B* **74,** 144111 (2006).

146. Nicol, M. & Durana, J. F. *J. Chem. Phys.* **54,** 1436–1440 (1971).

147. Santos, C. *et al. J. Appl. Phys.* **101,** 053511 (2007).

148. Segura, A. *et al. J. Phys. Chem. C* **123,** 17491–17497 (2019).

149. Majewski, J. & Vogl, P. *Phys. Rev. B* **35,** 9666 (1987).

150. Ozoliņš, V. & Zunger, A. *Phys. Rev. Lett.* **82,** 767 (1999).

151. Mihailova, B. *et al. Phys. Chem. Minerals* **46,** 807–814 (2019).

152. Kusaba, K., Syono, Y., Kikuchi, M. & Fukuoka, K. *Earth Planet. Sci. Lett.* **72,** 433–439 (1985).

153. Kusaba, K., Yagi, T., Kikuchi, M. & Syono, Y. *J. Phys. Chem. Solids* **47,** 675–679 (1986).

154. Mishra, A. *et al. Phys. Rev. B* **81,** 104109 (2010).

155. Errandonea, D. *EPL (Europhys. Lett.)* **77,** 56001 (2007).

156. Zhang, C. *et al. J. Phys. Chem. C* **114,** 18279–18282 (2010).

157. Huang, Z., Zhang, L. & Pan, W. *Inorg. Chem.* **51,** 11235–11237 (2012).

158. Hong, F. *et al. Appl. Phys. Lett.* **110,** 021903 (2017).

159. Garg, A. B., Errandonea, D., Rodríguez-Hernández, P. & Muñoz, A. *J. Phys. Condens. Matter* **29,** 055401 (2016).

160. Panchal, V. *et al. Phys. Rev. B* **83,** 064111 (2011).

161. Bandiello, E. *et al. J. Phys. Chem. C* **123,** 30732–30745 (2019).

162. Goutaudier, C. *et al. Materials research bulletin* **33,** 1457–1465 (1998).

163. Dewaele, A., Loubeyre, P. & Mezouar, M. *Phys. Rev. B* **70,** 094112 (2004).

164. Errandonea, D. *et al. Phys. Rev. B* **73,** 092106 (2006).

165. Errandonea, D. *Cryst. Res. Tech.* **50,** 729–736 (2015).

166. Fauth, F., Peral, I., Popescu, C. & Knapp, M. *Powder Diffr.* **28,** S360–S370 (2013).

167. Rodríguez-Carvajal, J. *Laboratoire Leon Brillouin (CEA-CNRS)* (2001).

168. Perdew, J. P., Burke, K. & Ernzerhof, M. *Phys. Rev. Lett.* **77,** 3865 (1996).

169. Dudarev, S. *et al. Phys. Rev. B* **57,** 1505 (1998).

170. Topsakal, M., Leighton, C. & Wentzcovitch, R. *J. Appl. Phys.* **119,** 244310 (2016).

171. Parlinski, K. *See: http://wolf. ifj. edu. pl/phonon* (2008).

172. Szczeszak, A. *et al. Inorg. Chem.* **53,** 12243–12252 (2014).

173. Birch, F. *J. Appl. Phys.* **9,** 279–288 (1938).

174. Paszkowicz, W. *et al. J. Alloys Compd.* **648,** 1005–1016 (2015).

175. Errandonea, D., Kumar, R. S., Ma, X. & Tu, C. *Journal of Solid State Chemistry* **181,** 355–364 (2008).

176. Lacomba-Perales, R., Errandonea, D., Meng, Y. & Bettinelli, M. *Phys. Rev. B* **81,** 064113 (2010).

177. Guedes, I. *et al. J. Appl. Phys.* **90,** 1843–1846 (2001).

178. Sanson, A. *et al. Phys. Rev. B* **86,** 214305 (2012).

179. Manjón, F. *et al. Phys. Rev. B* **81,** 075202 (2010).

180. Grzechnik, A. *Chem. Mat.* **10,** 2505–2509 (1998).

181. Errandonea, D. *et al. J. Alloys Compd.* **577,** 327–335 (2013).

182. Hakeem, M. A. *et al. Inorg. Chem.* **57,** 7550–7557 (2018).

183. Urbach, F. *Phys. Rev.* **92,** 1324 (1953).

184. Bandiello, E., Sánchez-Martín, J., Errandonea, D. & Bettinelli, M. *Crystals* **9,** 237 (2019).

185. Dolgos, M. R. *et al. J. Solid State Chem.* **182,** 1964–1971 (2009).

186. Nyman, H., Hyde, B. & Andersson, S. *Acta Crystal.* **40,** 441–447 (1984).

187. Flórez, M., Contreras-García, J., Recio, J. & Marques, M. *Phys. Rev. B* **79,** 104101 (2009).

188. Smirnov, M., Mirgorodsky, A., Kazimirov, V. Y. & Guinebretière, R. *Phys. Rev. B* **78,** 094109 (2008).

189. Melcher, R. i. in *Phys. Acoust.* 1–77 (Elsevier, 1976).

190. Sandercock, J. *et al. J. Phys. C: Solid State Phys.* **5,** 3126 (1972).

191. Goto, T., Tamaki, A., Fujimura, T. & Unoki, H. *J. Phys. Soc. Jpn* **55,** 1613–1623 (1986).

192. Hirano, Y. *et al. J. Amer. Ceram. Soc.* **85,** 1001–1003 (2002).

193. Voigt, W. *Lehrbuch der kristallphysik:(mit ausschluss der kristalloptik)* (BG Teubner, 1910).

194. Reuss, A. *Z. Angew. Math. Mech* **9,** 49–58 (1929).

195. Hill, R. *Proc. Phys. Soc. A* **65,** 349 (1952).

196. Pugh, S. *Lond. Edinb. Dubl. Philos. Mag. J. Sci.* **45,** 823–843 (1954).

197. Errandonea, D., Boehler, R. & Ross, M. *Phys. Rev. Lett.* **85,** 3444 (2000).

198. Toby, B. H. & Von Dreele, R. B. *J. Appl. Crystal.* **46,** 544–549 (2013).

199. Mattsson, A. E. *et al. J. Chem. Phys.* **128,** 084714 (2008).

200. Santamaría-Pérez, D. *et al. Phys. Rev. B* **84,** 054102 (2011).

201. Santamaria-Perez, D. *et al. Inorg. Chem.* **58,** 2708–2716 (2019).

202. Range, K.-J., Meister, H. & Klement, U. *Zeitschrift für Naturforschung B* **45,** 598–602 (1990).

203. Cazorla, C. & Errandonea, D. *Phys. Rev. Lett.* **113,** 235902 (2014).

204. Boonstra, E. *Acta Crystallogr. Sect. B* **24,** 1053–1062 (1968).

205. Gonzalez-Platas, J. *et al. Inorg. Chem.* **59,** 6623–6630 (2020).

206. Lin, S.-K. *J. Chem. Inf. Comput. Sc.* **36,** 367–376 (1996).

207. Recio, J. *et al. Phys. Rev. B* **63,** 184101 (2001).

208. Stangarone, C. *et al. Amer. Miner.* **104,** 830–837 (2019).

209. Errandonea, D. *et al. Phys. Rev. B* **79,** 184104 (2009).

210. Bandiello, E. *et al. Inorg. Chem.* **59,** 4882–4894 (2020).

211. Bleaney, B., Pfeffer, J. & Wells, M. *J. Phys. Condens. Mat.* **9,** 7469 (1997).

212. Harley, R., Lyons, K. & Fleury, P. *J. Phys. C Solid State Phys.* **13,** L447 (1980).

213. McPherson, J. & Wang, Y.-L. *J. Phys. Chem. Solids* **36,** 493–499 (1975).

214. Hutchings, M., Scherm, R., Smith, S. & Smith, S. *J. Phys. C Solid State Phys.* **8,** L393 (1975).

215. Kirschbaum, K., Martin, A., Parrish, D. A. & Pinkerton, A. A. *J. Phys. Condens. Matter* **11,** 4483 (1999).

216. Harley, R., Hayes, W. & Smith, S. *J. Phys. C Solid State Phys.* **5,** 1501 (1972).

217. Segmüller, A., Melcher, R. & Kinder, H. *Solid State Comm.* **15,** 101–104 (1974).

218. Will, G., Gobel, H., Sampson, C. & Forsyth, J. *Phys. Lett. A* **38,** 207–208 (1972).

219. Kazei, Z., Kolmakova, N., Sidorenko, A. & Takunov, L. *Phys. Solid State* **40,** 1513–1515 (1998).

220. Terada, Y. *et al. J. Crystal Growth* **167,** 369–372 (1996).

221. Persson, K. *Materials Data on $TbVO_4$ (SG:141) by Materials Project* Nov. (2014). doi:10.17188/1193944.

222. Persson, K. *Materials Data on $PrVO_4$ (SG:141) by Materials Project* Nov. (2014). doi:10.17188/1193993.

223. Persson, K. *Materials Data on $TmVO_4$ (SG:141) by Materials Project* Nov. (2014). doi:10.17188/1193851.

224. Persson, K. *Materials Data on $DyVO_4$ (SG:141) by Materials Project* Nov. (2014). doi:10.17188/1193485.

225. Lautenschlager, P., Garriga, M., Logothetidis, S. & Cardona, M. *Phys. Rev. B* **35,** 9174 (1987).

226. Birkett, M. *et al. APL Materials* **6,** 084901 (2018).